I N A U G U R A L - D I S S E R T A T I O N

Submitted to the
Combined Faculty of Mathematics, Engineering and Natural Sciences
Heidelberg University, Germany
for the degree of
Doctor of Natural Sciences (Dr. rer. nat.)

presented by
Martin Schröter
born in Hohenmölsen

Oral examination: July 21th, 2022

Development of next-generation fluorinated block copolymers and bottom-up assembly of biomimetic cell interaction modules

Referees:

Prof. Joachim P. Spatz

Institute for Molecular Systems Engineering
Ruprecht Karl University of Heidelberg

Max Planck Institute for Medical Research
Heidelberg

Prof. (apl) Reiner Dahint

Physical-Chemical Institute
Ruprecht Karl University of Heidelberg

Nature uses only the longest threads to weave her patterns, so that each small piece of her fabric reveals the organization of the entire tapestry.

(Richard P. Feynman)

Who knows the ways of the universe? Accident? Or destiny? That is the secret.

(Master Oogway)

Abstract

The construction of individual synthetic cells has been developed to achieve processes ranging from recapitulating cell division to mechanosignalling. Taken a step further, another promising implementation of synthetic cell research is the construction of artificial tissues comprising synthetic cells. These artificial tissues have the potential to form a communication network between the synthetic cells to transmit and respond to chemical or mechanical signals. In conjunction with natural tissue, this functioning could support signal transduction and thus aid in creating hybrid systems that will ultimately influence the fundamental understanding of tissue form and functioning.

In this thesis, I described the first steps towards building an artificial tissue that consists of giant unilamellar vesicles (GUVs)-based synthetic cells. In the process of charge-mediated GUV production, block copolymer surfactants consisting of PEG and PFPE were used to stabilize water-in-oil droplets that provide the charged scaffold to generate GUVs in the first place. These polymer-based surfactants have a major impact on the overall GUV production yield which is currently recognized as the major technical challenge in the field. Therefore, the first part of my thesis is dedicated to comparing different synthesis routes to achieve surfactants with desired properties. Subsequently, several functional surfactants have been synthesized: 1) a positively charged surfactant that allows electrostatically-mediated GUV formation; 2) a photoliable surfactant, which should enable a light-induced GUV release from water-in-oil droplet templates; and 3) a fluorescent surfactant for labeling the surfactant layer.

In the second part of this thesis, I focused on introducing biomimetic interactions between GUVs as well as between GUVs and natural cells. Towards this end, a pH-mediated generation of GUVs with improved release efficiency was explored. These GUVs were biofunctionalized and used for the bottom-up assembly of biomimetic cell adhesion and interaction modules: 1) mimicking epithelial cell interactions through the implementation of adherens junctions between GUVs via E-cadherin proteins; 2) GUV-substrate adhesion through the reconstitution of integrins in the GUVs membrane; and 3) implementation of droplet-based microfluidics for the reconstitution of actin cytoskeleton within GUVs to move towards linking intercellular mechanical signaling and synthetic cell mobility for future applications. Additionally, I showed how adherens junctions and substrate adhesion could be mimicked by DNA-mediated interactions. Finally, a hybrid system consisting of synthetic and natural cells was constructed and analyzed with respect to the interaction between GUVs and HEK cells.

Through the use of newly synthesized surfactants, droplet-based microfluidics, and pH-mediated GUV assembly and their efficient biofunctionalization , I was able for the first time to build an extensive network of synthetic cells and hybrid cellular system. This research establishes the foundation for reliable and reproducible production of large numbers of stable populations of GUV-based synthetic cells with pre-determined biomimetic functions and represents a substantial step towards building an artificial tissue. In future, mechanical and biochemical signal transduction can be potentially enabled by transmembrane linkages to the cytoskeleton, leading to the implementation of the advanced bioinspired hybrid cellular systems for biomedical applications.

Zusammenfassung

Die Konstruktion einzelner synthetischer Zellen wurde entwickelt, um biologische Prozesse nachzubauen, die von der Zellteilung bis zur Mechanosignaltransduktion reichen. Ein weiterer interessanter Schritt in der Forschung mit synthetischen Zellen ist der Aufbau eines künstlichen Gewebes bestehend aus synthetischen Zellen. Dieses künstliche Gewebe hat das Potenzial, ein Kommunikationsnetz zwischen den synthetischen Zellen zu bilden, um chemische oder mechanische Signale zu übertragen und auf äußere Einflüsse zu reagieren. In Verbindung mit natürlichem Gewebe könnte diese Eigenschaft die Signaltransduktion unterstützen und so zur Schaffung hybrider Systeme beitragen, die letztlich das grundlegende Verständnis von Gewebeform und -funktion verbessern können.

In dieser Arbeit habe ich die ersten Schritte zum Aufbau eines künstlichen Gewebes beschrieben, das aus synthetischen Zellen auf der Basis von mikrometergroßen, unilamellaren Vesikeln (engl. *giant unilamellar vesicles*, GUVs) besteht. Im Prozess der ladungsvermittelten GUV-Produktion wurden Blockcopolymer-Tenside, bestehend aus PEG und PFPE, zur Stabilisierung von Wasser-in-Öl-Tropfen verwendet, die eine geladene Oberfläche zur Erzeugung von GUVs bilden. Diese polymerbasierten Tenside haben dadurch einen großen Einfluss auf die Gesamtausbeute der produzierten GUVs, die derzeit als eine der größten technischen Herausforderungen auf diesem Gebiet gilt. Daher widmet sich der erste Teil meiner Arbeit dem Vergleich verschiedener Synthesewege, um Tenside mit den benötigten Eigenschaften zu erhalten. Anschließend wurden mehrere funktionelle Tenside synthetisiert: 1) ein positiv geladenes Tensid, das eine elektrostatisch vermittelte GUV-Bildung ermöglicht; 2) ein photolabiles Tensid, das eine lichtinduzierte Freisetzung der GUVs aus Wasser-in-Öl-Tröpfenchen zulassen soll; und 3) ein fluoreszierendes Tensid zur direkten Visualisierung der Tensidschicht.

Im zweiten Teil dieser Arbeit konzentrierte ich mich auf die Einführung biomimetischer Interaktionen zwischen GUVs sowie zwischen GUVs und natürlichen Zellen. Zu diesem Zweck wurde eine pH-vermittelte Erzeugung von GUVs mit verbesserter Freisetzungseffizienz untersucht. Diese GUVs wurden biofunktionalisiert und für den Bottom-up-Aufbau von biomimetischen Zelladhäsions- und Interaktionsmodulen verwendet: 1) Nachahmung epithelialer Zellinteraktionen durch die Implementierung von Adherens Junctions zwischen GUVs über E-Cadherin-Proteine; 2) GUV-Substrat-Adhäsion durch die Rekonstitution von Integrinen in der GUV-Membran; und 3) Implementierung von

tröpfchenbasisierter Mikrofluidik für die Rekonstitution des Aktin-Zytoskeletts innerhalb von GUVs, um eine Verbindung zwischen interzellulärer, mechanischer Signalübertragung und synthetischer Zellmobilität für zukünftige Anwendungen herzustellen. Darüber hinaus habe ich gezeigt, wie GUV-GUV-Interaktionen und Substratadhäsion durch DNA-vermittelte Wechselwirkungen nachgeahmt werden können. Schließlich wurde ein Hybridsystem aus synthetischen und natürlichen Zellen konstruiert und im Hinblick auf die Interaktion zwischen GUVs und HEK-Zellen analysiert.

Im zweiten Teil dieser Arbeit konzentrierte ich mich auf die Einführung biomimetischer Interaktionen zwischen GUVs sowie zwischen GUVs und natürlichen Zellen. Zu diesem Zweck wurde eine pH-vermittelte Erzeugung von GUVs mit verbesserter Freisetzungseffizienz untersucht. Diese GUVs wurden biofunktionalisiert und für den Bottom-up-Aufbau von biomimetischen Zelladhäsions- und Interaktionsmodulen verwendet. Dazu gehörten: 1) Nachahmung epithelialer Zellinteraktionen durch die Implementierung von Adherens Junctions zwischen GUVs über E-Cadherin-Proteine; 2) GUV-Substrat-Adhäsion durch die Rekonstitution von Integrinen in der GUV-Membran; und 3) Implementierung von tröpfchenbasisierter Mikrofluidik für die Rekonstitution des Aktin-Zytoskeletts innerhalb von GUVs, um eine Verbindung zwischen interzellulärer, mechanischer Signalübertragung und synthetischer Zellmobilität für zukünftige Anwendungen herzustellen. Darüber hinaus habe ich gezeigt, wie GUV-GUV-Interaktionen und Substratadhäsion durch DNA-vermittelte Wechselwirkungen nachgeahmt werden können. Schließlich wurde ein Hybridsystem aus synthetischen und natürlichen Zellen konstruiert und im Hinblick auf die Interaktion zwischen GUVs und HEK-Zellen analysiert.

Durch den Einsatz neuartiger synthetisierter Tenside, tröpfchenbasierter Mikrofluidik und pH-vermittelter GUV-Produktion, und ihrer effizienten Biofunktionalisierung konnte ich zum ersten Mal ein umfangreiches Netzwerk synthetischer Zellen und ein hybrides Zellsystem aufbauen. Diese Forschungsarbeit bildet die Grundlage für die zuverlässige und reproduzierbare Herstellung einer großen Anzahl an synthetischen Zellen auf Basis von GUVs mit vorbestimmten biomimetischen Funktionen und stellt einen wesentlichen Schritt auf dem Weg zum Aufbau eines künstlichen Gewebes dar. In Zukunft kann die mechanische und biochemische Signaltransduktion möglicherweise durch Transmembranverbindungen zum Cytoskelett ermöglicht werden, was zur Umsetzung fortschrittlicher bioinspirierter hybrider Zellsysteme für biomedizinische Anwendungen führt.

Table of contents

Abstract

Zusammenfassung

Table of contents **i**

Acknowledgments **v**

Acronyms **vii**

List of Figures **xi**

1 Introduction **1**

1.1 Synthetic cells, the base towards artificial life 1

1.2 Adhesion modules in natural cells 2

1.2.1 Cell junctions 2

1.2.2 Cell-matrix adhesion 4

1.2.3 Actin cytoskeleton 5

1.3 GUV generation methods 5

1.3.1 Lipid film formation 6

1.3.2 Emulsion transfer 6

1.3.3 Water-in-oil droplet-based 7

1.4 Droplet-based microfluidics 7

1.4.1 Physical background 8

1.4.2 Microfluidics devices 9

1.5 Fluorinated block copolymer surfactants 11

1.5.1 Physicochemical properties 11

1.5.2 Synthesis of fluorinated block copolymer surfactants 12

1.5.3 Charge-mediated GUV formation 13

1.5.4 Other surfactants in droplet-based microfluidics 14

1.6 Synthetic cell modifications 14

1.6.1 DNA based modules 16

2 Motivation **17**

3 Materials and Methods **19**

3.1 Instruments 19

3.2 Software 19

3.3 Materials 19

3.3.1 Chemicals 19

3.4 Synthesis 24

3.4.1 Esterified triblock surfactant PFPE 7000-PEG 1500-PFPE 7000 **1** 24

3.4.2 Amidated triblock surfactant PFPE 7000-JA 800-PFPE 7000 **2** 25

3.4.3 PEG 1500 ditosylate **3** 26

3.4.4 PEG 1500 diazide **4** 27

3.4.5 PFPE 7000 chloride and propargyl PFPE 7000 **5** 28

3.4.6 Clicked triblock surfactant PFPE7000-PEG1500-PFPE7000 **6** . 30

3.4.7 PEG 600 ditosylate **7** 32

3.4.8 PEG 600 diazide **8** 33

3.4.9 N,N,N-trimethylprop-2-yn-1-aminium bromide **9** 34

3.4.10 N3-PEG600-TAB **10a** 35

3.4.11 Positively charged, clicked diblock surfactant PFPE7000-PEG600-TAB **11** 36

3.4.12 4-(Azidomethyl)-3-nitrobenzoic acid **12** 38

3.4.13 PEG 1500 bis(4-(azidomethyl)-3-nitrobenzoate) **13** 39

3.4.14 Photoliable, clicked triblock surfactant PFPE7000-NB-PEG1500-NB-PFPE7000 **14** 40

3.4.15 Propargyl rhodamine B **15** 42

3.4.16 N3-PEG600-RhodB **16a** 43

3.4.17 Fluorescent, clicked diblock surfactant PFPE7000-PEG600-RhodB **17** 44

3.4.18 Other synthesis instructions 46

3.5 Methods 46

3.5.1 Analytical methods 46

3.5.2 Generation of synthetic cells 49

3.5.3 Computational methods 57

4 Results **63**

4.1 Synthesis of functional fluorinated block copolymer surfactants 63

4.1.1 Comparison of different surfactant synthesis approaches 63

4.1.2 Surfactant purification 69
4.1.3 Synthesis of functionalized surfactants 72
4.2 Synthetic cells adhesion interactions 87
4.2.1 pH-mediated construction of negatively charged GUVs 87
4.2.2 GUV-GUV interaction 92
4.2.3 GUV-substrate adhesion 98
4.2.4 Reconstitution of actin cytoskeleton 105
4.2.5 DNA-mediated adhesion in GUV-based synthetic cells 107
4.2.6 Hybrid system 110

5 Summary and Outlook 117
5.1 Summary and Conclusions 117
5.1.1 Synthesis of functional fluorinated block copolymer surfactants . 117
5.1.2 Synthetic cells adhesion interactions 120
5.2 Outlook 124
5.2.1 Surfactant modifications 124
5.2.2 Towards artificial tissue 125

6 Appendix I
6.1 Spectra I
6.1.1 Mass spectrometry II
6.1.2 NMR spectroscopy IV
6.1.3 Microscopy XVIII

Bibliography XLVII

Scientific Contribution LXXV

Acknowledgments

First, I would like to thank my supervisor and mentor Prof. Joachim Spatz for all his support and guidance over the last years. Especially, I am very thankful for rising my interest in microfluidics and synthetic cells. Thank you for giving me the opportunity to work in this amazing group. I am very grateful for all the offered possibilities, the well-equipped laboratories and the freedom to explore ideas I developed interest in.

Further, I would like to thank Prof. Rainer Dahint for taking his time to reviewing my doctoral thesis.

I would like to express my gratitude to my daily supervisor, Dr. Ilia Platzman. Look, without your constant scientific support, helpful discussions and the ideas and inspiration you gave, this thesis would not have been possible.

Im Weiteren möchte ich meinen Eltern Annegret und Dietmar danken, die mich von meinem ersten Chemiebaukasten bis hin zum Abschluss meiner Doktorarbeit immer und bedingungslos unterstützt haben. Ohne euer Durchhaltevermögen mit mir wäre das alles nicht möglich gewesen, weshalb ich euch über alles dankbar bin. Auch möchte ich mich bei meiner Schwester Madlen und meinem Schwager Torsten bedanken für das Verständnis, dass sie für mich in den stressigen letzten Jahren gehabt haben. Und natürlich möchte ich meine beiden Nichten Nele und Lara nicht vergessen, die es immer geschafft haben, mir ein Lächeln ins Gesicht zu zaubern.

More, I would like to thank my colleagues and collaborators, Dr. Félix Lussier and Dr. Jacqueline De Lora, for their constant discussion and support. Thank you for being able to count in your expertise and creativity.

I would also like to thank the students I supervised along the way. You have helped me to develop new ideas, look at details easily ignored, and reminded me how fascinating science can be. Anna-Lena, Sarah, Tobias, Dominik, Christina und Luise, thank you.

As well, I would like to thank Jacqueline, Désirée, Andy, Ana, Klaus, Julia and Anastassiya for taking their time for proof reading my thesis. And especially I thank you, Ana and Andy, for joining the last night proof reading party! Without you, it would have been very lonely.

I would also like to thank the Spatz group for being amazing. In front of all, I want to thank our technicians, enabeling the research from the background Carmen, Conny, Sabine, Raimund, Annette and Felix. Further all my office mates for inspiring discussion and improving my time at work. Espacially I would like to thank Conny and Désirée for all their scientific and mental support. And all the other members of the Spatz group. It was a great time with you all and I always look back on it with a smile. :)

Also, I would like to thank my friends. Sarina, Klaus, Tobi and Christoph, who made my chemistry studies incredibly better. Chrissy, David, Fabsch and Manu, who make my life a bit more colorful. Simon and Sophie, for sharing the same board game enthusiasms. And all the other, I am so grateful that you exist and for your support.

A special thanks goes to my underwater hockey team from TCO Weinheim, which helps me to keep the balance between work and life, even if it's not always that easy.

Last but not least, I would like to thank the Max Planck Society and in special the Max Planck Institute for Medical Research. Without the administrative and scientific support, the daily research life would be much harder. In particular, I would like to thank Dr. Sebastian Fabritz and Ulrike Mersdorf for their support.

Acronyms

n-BuLi	*n*-butyllithium.
*p*TsCl	*p*-toluenesulfonyl chloride.
AB	actin buffer.
ADP	adenosine diphosphate.
Alox	aluminium oxide.
AMP	adenosine 5'-monophosphate.
ANBA	4-azidomethyl-3-nitrobenzoic acid.
APB	actin polymerization buffer.
APTMS	(3-Aminopropyl)trimethoxysilane.
ATP	adenosine triphosphate.
ATR	attenuated total reflection.
aTS	amidated triblock surfactant.
BCML	block copolymer micelle nanolithography.
BEP	2-bromo-1-ethyl-pyridinium tetrafluoroborate.
BNBA	4-bromomethyl-3-nitrobenzoic acid.
brine	saturated sodium chloride solution.
BSA	bovine serum albumin.
cDICE	continuous droplet interface crossing encapsulation.
CMC	critical micelle concentration.
CS	commercially available surfactant.
cTS	clicked triblock surfactant.
CuAAC	copper(I)-catalyzed azide-alkyne cycloaddition.
DCM	dichlormethane.

DGS	1,2-dioleoyl-sn-glycero-3-succinate.
DIPEA	*N*,*N*-diisopropylethylamine.
DLS	dynamic light scattering.
DMAP	4-(dimethylamino)pyridine.
DMEM	Dulbecco's modified Eagle's medium.
DMF	dimethylformamide.
DNA	deoxyribonucleic acid.
DOBAQ	N-(4-carboxybenzyl)-N,N-dimethyl-2,3-bis-(oleoyloxy)propan-1-aminium.
DOPC	1,2-dioleoyl-sn-glycero-3-phosphocholine.
DOPE	1,2-dioleoyl-sn-glycero-3-phosphoethanolamine.
DOPG	1,2-dioleoyl-sn-glycero-3-phospho-(1'-rac-glycerol).
DOPS	1,2-dioleoyl-sn-glycero-3-phospho-L-serine.
DOTAP	1,2-dioleoyl-3-trimethylammonium-propane.
dsGUV	droplet-stabilized giant unilamellar vesicles.
ECM	extracellular matrix.
EDC HCl	1-ethyl-3-(3-dimethylaminopropyl)carbodiimide hydrochloride.
eDICE	emulsion droplet interface crossing encapsulation.
EDTA	ethylenediaminetetraacetic acid.
ESI	electrospray ionization.
eTS	esterified triblock surfactant.
F-actin	filamentous actin.
FBS	fetal bovine serum.
fluoDS	fluorescent diblock surfactant.
FRAP	fluorescence recovery after photobleaching.
FRET	Förster resonance energy transfer.
FTIR	fourier transform infrared spectroscopy.
G-actin	globular actin.
GFP	green fluorescent protein.
GUV	giant unilamellar vesicle.

HaCaT	cultured human keratinocyte.
HEK	human embryonic kidney.
HEPES	4-(2-hydroxyethyl)-1-piperazineethanesulfonic acid.
His tag	polyhistidine tag.
HLB	hydrophilic-lipophilic balance.
IFT	interfacial tension.
LB	lysogeny broth.
MS	mass spectrometry.
NaOH	sodium hydroxide.
NASA	National Aeronautics and Space Administration.
NHS	*N*-hydroxysuccinimide.
NMR	nuclear magnetic resonance spectroscopy.
NTA	nitrilotriacetic acid.
OD	optical density.
OLA	octanol-assisted liposome assembly.
PBS	phosphate-buffered saline.
PCA	principal component analysis.
PDMS	polydimethylsiloxane.
PEG	polyethylene glycol.
PFO	*1H,1H,2H,2H*-perfluoro-1-octanol.
PFPE	perfluoropolyether.
PLL	poly-L-lysine.
plTS	photoliable triblock surfactant.
PNIPAM	poly(N-isopropylacrylamide).
posDS	positively-charged diblock surfactant.
PURE	protein synthesis using recombinant elements.
PVA	polyvinyl alcohol.
SEC	size-exclusion chromatography.
SM	sphingomyelin.

SNARE	soluble N-ethylmaleimide-sensitive-factor attachment receptor.
SPR	surface plasmon resonance.
SUV	small unilamellar vesicle.
TAB	N,N,N-trimethylprop-2-yn-1-aminium bromide.
THF	tetrahydrofurane.
TLC	thin-layer chromatography.
TMA	trimethylamine.
TRI-silane	N^1-(3-Trimethoxysilylpropyl)diethylenetriamine.
Tris	tris(hydroxymethyl)aminomethane.
Vertrel	1,1,1,2,3,4,4,5,5,5-decafluoropentane.
w/o	water-in-oil.
w/o/w	water-in-oil-in-water.

List of Figures

1.1 Schematic illustration of adherens junctions, gab junctions and tight junctions. . . . 3
1.2 Schematic illustration of inactivated integrin conformation and quaternary structural transitions after inside-out signalling or outside-in signalling. . . . 4
1.3 Schematic illustration of dynamic polymerisation and depolymerisation of actin filaments. . . . 5
1.4 Schematic illustration of GUV generation using a lipid film, by emulsion transfer and based on w/o droplet. . . . 6
1.5 Schematic illustration of PDMS device productions. . . . 9
1.6 Schematic illustration of droplet production device. . . . 10
1.7 General chemical structure of a fluorinated triblock copolymer surfactant consisting of PEG (hydrophilic) and PFPE (hydrophobic). . . . 11
1.8 Different synthesis routes towards fluorinated triblock copolymer surfactant. . . . 12
1.9 Schematic illustration of GUV generation using droplet-based microfluidics. . . . 13
1.10 Already established reconstituted cell modules into synthetic cells using proteins or DNA mimics. . . . 15

3.1 As part of an partition experiment to determine the concentration of PFPE in surfactants, calibration curves under different conditions where calculated. . . . 47
3.2 Stepwise description of the process of constructing GUVs. . . . 51
3.3 Stepwise illustration of cell detection in hybrid system experiment. . . . 58
3.4 Stepwise illustration of GUV detection in hybrid system experiment. . . . 60

4.1 Three synthesis approaches to synthesize triblock copolymer surfactants consisting of PEG and PFPE blocks. . . . 64
4.2 Synthesis route for producing cTS **6**. . . . 66

4.3 Analysis of the the surfactants eTS **1**, aTS **2** and cTS **6**. 68
4.4 Analysis of eTS **1** and aTS **2** surfactants properties following their purification with amine functionalized silica gel. 71
4.5 Overview of the chemical structures of the functionalized surfactants synthesized in this thesis. 73
4.6 Synthesis of positively charged diblock surfactant posDS **11**. 75
4.7 Transfer assay and pendant drop measurements of posDS **11**. 76
4.8 Representative confocal images of dsGUVs obtained with different sodium chloride concentration and the released GUVs. 77
4.9 Quantitative MS analysis of the lipid composition in process of giant unilamellar vesicle (GUV) formation. 78
4.10 Laminin-111 assembly at the periphery of positively charged w/o droplets prepared via droplet-based microfluidics. 79
4.11 Synthesis of the photoliable triblock surfactant plTS **14**. 80
4.12 Light-induce cleavage mechanism of the PFPE-PEG bond in the photoliable triblock surfactant (plTS) **14** and IFT measurements. 82
4.13 Synthesis of the rhodamine B labeled fluorescent surfactant fluorescent diblock surfactant (fluoDS) **17**. 84
4.14 Representative confocal images and FRAP analysis of droplets stabilized by 2.5 mM cTS **6** with 5 mol% fluoDS **17**. 85
4.15 Schematic illustration and representative confocal images of the pH-mediated GUVs formation. 88
4.16 Zeta potential measurements of vesicles consisting of different lipid composition. 89
4.17 Effect of Krytox addition on the pH values within the droplets and the pH-mediated droplet-stabilized giant unilamellar vesicless (dsGUVs) formation. 91
4.18 Biotin/streptavidin-mediated adherens junction of GUVs. 93
4.19 Representative fluorescence confocal images of His-tagged GFP interactions with PEGylated and not PEGylated GUVs and in presence and absence of nickel(II) ions 94
4.20 Schematic step-wise representation of GUV functionalization with E-cadherin. 95
4.21 Representative confocal images of E-cadherin-mediated adherens junction dependence on nickel(II) ions, E-cadherin, and calcium ions. 97
4.22 Schematic illustration of the complimentary DNA-mediated fusion of GUVs with integrin-reconstituted proteoliposomes. 99

4.23 Comparative UV/Vis spectra of SUVs, Triton X-100, and integrin reconstituted proteoliposomes before and after SEC purification. 99
4.24 Zeta potential measurements of differently charged SUVs before and after integrin reconstitution. 100
4.25 SPR measurements of the adhesion of integrin-reconstituted proteoliposomes. 101
4.26 Schematic representation and representative fluorescence confocal images of the DNA-mediated vesicle fusion. 102
4.27 Representative fluorescence confocal images of XZ plane of the integrin $\alpha_{\mathrm{IIb}}\beta_3$ reconstituted GUV adhesion on a fibrinogen coated surface and respective control experiments. 104
4.28 Actin cytoskeleton reconstitution within GUV-based synthetic cells. . . 106
4.29 Schematic representation of the DNA-mediated assembly of adherens junctions between the GUV-based synthetic cells. 108
4.30 Schemes and representative confocal images of DNA-mediated surface adhesion. 109
4.31 Schematic illustration and representative confocal image of the hybrid system experiment. 111
4.32 Representative confocal images of hybrid system experiment after detecting cell area and GUVs. 112
4.33 Violin plots showing the number and ratio of GUVs and adhesive GUVs depending on the experimental conditions in the hybrid experiment. . . 114
4.34 PCA of the hybrid system with respect to the dependence of detected GUVs, adhesive GUVs and cell area on different parameters. 116

5.1 Pendent drop measurements of triblock copolymer surfactant containing PEG and PFPE of different molecular masses. 124

6.1 ESI-MS spectrum of N,N,N-trimethylprop-2-yn-1-aminium bromide **9**. . II
6.2 ESI-MS spectrum of 4-(azidomethyl)-3-nitrobenzoic acid **12**. III
6.3 ^{1}H-NMR of esterified triblock surfactant PFPE 7000-PEG 1500-PFPE 7000 **1**. IV
6.4 ^{1}H-NMR of amidated triblock surfactant PFPE 7000-JA 800-PFPE 7000 **2**. V
6.5 ^{1}H-NMR of PEG 1500 ditosylate **3**. VI
6.6 ^{1}H-NMR of PEG 1500 diazide **4**. VII
6.7 ^{1}H-NMR of propargyl PFPE 7000 **1**. VIII
6.8 ^{1}H-NMR of licked triblock surfactant PFPE7000-PEG1500-PFPE7000 **6**. IX
6.9 ^{1}H-NMR of PEG 600 ditosylate **7**. X

6.10 ^{1}H-NMR of PEG 600 diazide **8**. XI
6.11 ^{1}H-NMR of N3-PEG600-TAB **10**. XII
6.12 ^{1}H-NMR of Positively charged, clicked diblock surfactant PFPE7000-PEG600-TAB **11**. XIII
6.13 ^{1}H-NMR of 4-(azidomethyl)-3-nitrobenzoic acid **12**. XIV
6.14 ^{1}H-NMR of PEG 1500 bis(4-(azidomethyl)-3-nitrobenzoate) **13**. XV
6.15 ^{1}H-NMR of photoliable, clicked triblock surfactant PFPE7000-NB-PEG1500-NB-PFPE7000 **2**. XVI
6.16 ^{1}H-NMR of Krytox with different concentrations. XVII
6.17 Fluorescent microscope images of Liss Rhodamine-labeled GUVs. . . . XVIII
6.18 Confocal Z-stack (XZ- and YZ-projection) images of Liss Rhodamine-labeled GUVs. XIX
6.19 Fluorescent microscope images of Liss Rhodamine-labeled GUVs with nickel(II) ions. XX
6.20 Confocal Z-stack (XZ- and YZ-projection) images of Liss Rhodamine-labeled GUVs with nickel(II) ions. XXI
6.21 Fluorescent microscope images of Liss Rhodamine-labeled GUVs with calcium ions. XXII
6.22 Confocal Z-stack (XZ- and YZ-projection) images of Liss Rhodamine-labeled GUVs with calcium ions. XXIII
6.23 Fluorescent microscope images of Liss Rhodamine-labeled GUVs with nickel(II) and calcium ions. XXIV
6.24 Confocal Z-stack (XZ- and YZ-projection) images of Liss Rhodamine-labeled GUVs with nickel(II) and calcium ions. XXV
6.25 Fluorescent microscope images of Liss Rhodamine-labeled GUVs with E-cadherin. XXVI
6.26 Confocal Z-stack (XZ- and YZ-projection) images of Liss Rhodamine-labeled GUVs with E-cadherin. XXVII
6.27 Fluorescent microscope images of Liss Rhodamine-labeled GUVs with E-cadherin and nickel(II) ions. XXVIII
6.28 Confocal Z-stack (XZ- and YZ-projection) images of Liss Rhodamine-labeled GUVs with E-cadherin and nickel(II) ions. XXIX
6.29 Fluorescent microscope images of Liss Rhodamine-labeled GUVs with E-cadherin and calcium ions. XXX
6.30 Confocal Z-stack (XZ- and YZ-projection) images of Liss Rhodamine-labeled GUVs with E-cadherin and calcium ions. XXXI
6.31 Fluorescent microscope images of Liss Rhodamine-labeled GUVs with E-cadherin, nickel(II) ions and calcium ions. XXXII

6.32 Confocal Z-stack (XZ- and YZ-projection) images of Liss Rhodamine-labeled GUVs with E-cadherin, nickel(II) ions and calcium ions. XXXIII
6.33 Fluorescent microscope images of ATTO 488-labeled GUVs. XXXIV
6.34 Fluorescent microscope images of ATTO 488-labeled GUVs with nickel(II) ions. XXXV
6.35 Fluorescent microscope images of ATTO 488-labeled GUVs with calcium ions. XXXVI
6.36 Fluorescent microscope images of ATTO 488-labeled GUVs with nickel(II) and calcium ions. XXXVII
6.37 Fluorescent microscope images of ATTO 488-labeled GUVs with E-cadherin.XXXVIII
6.38 Fluorescent microscope images of ATTO 488-labeled GUVs with E-cadherin and nickel(II) ions. XXXIX
6.39 Fluorescent microscope images of ATTO 488-labeled GUVs with E-cadherin and calcium ions. XL
6.40 Fluorescent microscope images of ATTO 488-labeled GUVs with E-cadherin, nickel(II) and calcium ions. XLI
6.41 Fluorescent microscope images of Liss Rhodamine-labeled GUVs. . . . XLII
6.42 Confocal Z-stack (XZ- and YZ-projection) images of Liss Rhodamine-labeled GUVs. XLIII
6.43 Fluorescent microscope images of Liss Rhodamine-labeled GUVs with palindromic DNA. XLIV
6.44 Representative confocal images of Liss Rhodamine-labeled GUVs with palindromic DNA. XLV
6.45 Confocal Z-stack (XZ- and YZ-projection) images of Liss Rhodamine-labeled GUVs with palindromic DNA. XLVI

Chapter 1

Introduction

1.1 Synthetic cells, the base towards artificial life

What is life? From chemists, who seek to understand the mechanism behind how inorganic molecules were converted into organic material and biomolecules,[1–3] to NASA, who is searching for extraterrestrial life and therefore defined a ladder of life detection[4,5] — scientists from different fields explore this question. In contrast, there is synthetic biology research, where scientists are trying to rebuild a cell from scratch, coining the term, “synthetic cells”.[6,7]

To understand the mechanisms of life and how cells are "living", synthetic biology research uses two different approaches. For the top-down approach, the complexity of a natural system is reduced by removing or replacing compartments.[8] In contrast, for the bottom-up approach a natural system is constructed from discrete parts using natural or synthetic compartments to implement biomimicking functionalities. A synthetic cell can be synthesized in many different ways. Natural functionalities which have been defined as inevitable for life can be either achieved via integration of natural components in the synthetic cell,[9–11] or by replacement of natural functionalities by artificial building blocks (e.g. polymers).[12]

In my work, I aimed to construct synthetic cell communities that would mimic a biological tissue such as the epidermis. Therefore, I used synthetic cells based on GUVs (vesicle radius greater than 1 μm), which were produced by droplet-based microfluidics. These GUVs were equipped with various adhesion modules to form a GUV network, which will enable signal transduction and communication between the synthetic cells in future work. In this thesis, I could show for the first time a hybrid system consisting of synthetic and natural cells and confirm the interactions between GUVs and natural cells.

In the following chapter, I will describe the functionalities of natural adhesion modules in cells and give an overview of different ways to generate GUVs. In detail, I will

discuss the droplet-based microfluidic approach, with state-of-the-art of fluorinated block copolymer surfactants, and summarize the synthetic cell research in the direction of implementing adhesion modules and building artificial tissue. The following descriptions of functionalities in the cellular system focus on eukaryotic cells.

1.2 Adhesion modules in natural cells

In natural tissues, cells communicate with each other through chemical cues or mechanically via molecular interactions. Molecular-based communication channels are various and transmit information via transmembrane proteins, or higher-order molecular assemblies, using so-called adhesion modules. These modules can be further classified into cell-cell interactions or cell-matrix adhesion.[13,14] Cell-cell interactions allow the formation of cell assemblies with structures that support specific biological functions. Cell-matrix adhesion enables cells to migrate and plays a crucial role in biological processes like wound healing. The three main types of cell-cell interactions are adherens junctions, gap junctions and tight junctions.[15,16] These adhesion modules consist of multiprotein complexes and are summarised under the definition: cell junctions. Mentioned for completeness, cells interact between each other also via the release of messenger substances of one cell and the corresponding receptor proteins in the membrane of another cell, like signal transduction between synapses.[17] The adhesion of cells with the extracellular matrix (ECM) is mediated mainly by the integrin protein family.[13,18] To transduce messages like forces into the cell, the junction needs to be connected to the inside of the cell. In adherens junctions, tide junctions and the integrin-mediated matrix adhesion this connection is transmitted via multiprotein complexes to the actin cytoskeleton. Through these connections, signals are transmitted across the cell membrane and, using genetic feedback mechanisms, the interactions can be controlled from the inside of the cell.[19,20]

1.2.1 Cell junctions

Cell junctions are a classification of intercellular adhesion modules consisting of a multiprotein complex. Part of cell junctions are: 1) adherens junctions mediating the cell-cell adhesion between epithelial and endothelial cells to enable the formation of cell assemblies, for example (Figure 1.1A);[21,22] 2) gap junctions connecting the cytosol of cells for chemo-signal transduction (Figure 1.1B);[23] and 3) tight junctions sealing the epithelium preventing the uncontrolled diffusion of molecules (Figure 1.1C).[24]

The main components of adherens junctions are transmembrane glycoproteins called cadherins.[25,26] The cadherin superfamily is divided into five subtypes, with the classic

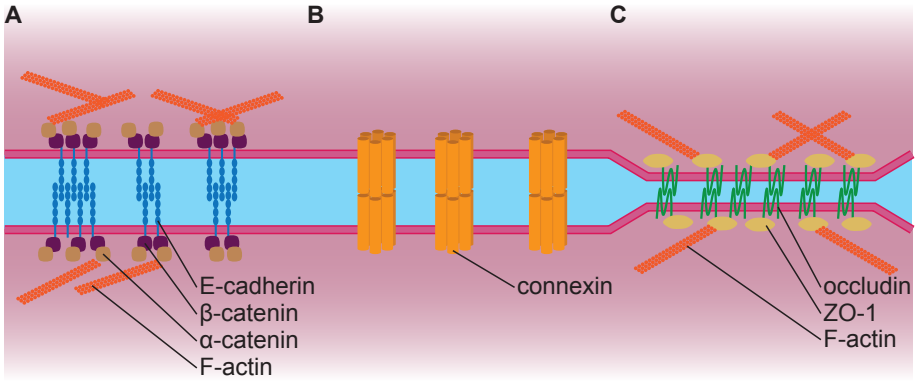


Figure 1.1: Schematic illustration of adherens junctions (A), gab junctions (B) and tight junctions (C). Adapted and modified from Kutova *et al.*[16]

cadherins subtype being of particular interest.[27,28] The classic cadherins are further subdivided into type I, for example the epithelial cadherins (E-cadherins) and the neural cadherins (N-cadherins), and type II, for example vascular-endothelial cadherins (VE-cadherins).[29,30] The extracellular region of classic cadherins mediate calcium ion-dependent homophilic adhesion, but only the first two of the five extracellular domains are involved in this interactions.[31–33] Through the cell membrane, the intracelluar region of classic cadherins is connected via a protein complex consisting of β-catenin, α-catenin and p120-catenin with the actin cytoskeleton.[34] Through this connection, the classic cadherins regulate the local cytoskeleton, intracellular signaling, and gene transcription.[35,36] The classic cadherin-mediated adhesion is highly dynamic, allowing regulated attachment and detachment of cell assemblies, such as in the epithelial-mesenchymal transition.[37–39] Therefore, modifications of classic cadherins, especially of E-cadherins, are correlated with tumor metastasis.[40]

Gap junctions are transmembrane connections between cells providing direct intercellular communication.[23] This connection is constructed by hexamers of the connexin protein family forming a hemichannel called connexon.[41] Two connexons of adjacent cells form a channel directly linking the cytosol of both cells. Through this channel, ions and small molecules pass with a charge and size dependency of 0.2 to 1.0 kDa.[42–44] Gap junctions, thus, enable chemical communication, by small second messenger molecules like calcium ions and cyclic AMP, electrical communication between cells, as in nervous and cardiovascular tissues, and nutrient transport in poorly perfused tissues like the retina.[45]

Tight junctions produce strong interactions in cells from the epithelium, on the one hand preventing diffusion, and in contrast controlling passage of ions and dissolved molecules.[19,46,47] This junction is formed by the transmembrane proteins occludin and claudins family.[48,49] Occludin and the members of the claudin family are tetraspanin proteins containing two extracellular loops, but they do not share sequence

similarities.[49–52] Intracellularly, the proteins are bound to the actin cytoskeleton via ZO proteins, especially ZO-1.[53] It was demonstrated that ZO-1 has a binding pocket for α-catenin and could therefore be the link between adherens junctions and tight junctions. However, the necessary simultaneous binding of actin and α -catenin has not yet been proven.[54,55]

1.2.2 Cell-matrix adhesion

The ECM provides a support structure for cells consisting of a mixture of matrix proteins, like fibronectin, collagens and laminins, and soluble proteins, like growth factors.[56] Cell adhesion on matrix proteins is mediated by integrins by a dynamic mechanism.[57] The members of this transmembrane protein family are heterodimers consisting of an α and a β subunit.[45] In particular, integrins $\alpha_{\mathrm{IIb}}\beta_3$ and $\alpha_{\mathrm{v}}\beta_3$ are well studied in terms of their activation and clustering and especially $\alpha_{\mathrm{IIb}}\beta_3$ is used for synthetic cell research.[11,58]

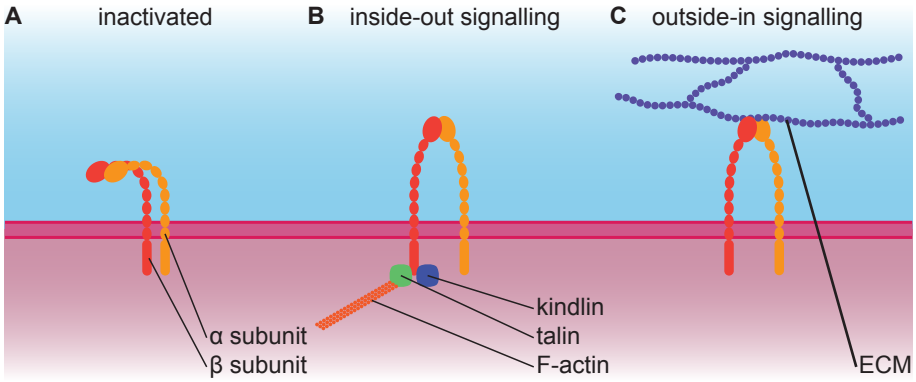


Figure 1.2: Schematic illustration of inactivated integrin conformation (A) and quaternary structural transitions after inside-out signaling (B) or outside-in signaling (C). Adapted and modified from Cheah *et al.*[59]

Integrins are allosteric proteins, meaning they make a quaternary structural transition dependent on ligand concentration.[57,60] They have a closed, bent conformation in which they are inactivated (Figure 1.2A), and an open/ extended conformation after activation. The change in the quaternary structure can either be triggered by intracellular activators kindlin and talin binding to a particular portion of the protein (inside-out signalling, Figure 1.2B), or by ECM ligand binding to specific amino acid sequences in the matrix (outside-in signalling, Figure 1.2C).[58,59] In addition, the integrin $\alpha_{\mathrm{IIb}}\beta_3$ binding pocket can be activated by manganese(II) ions.[61,62]

1.2.3 Actin cytoskeleton

The cytoskeleton is a dynamic filamentous network consisting of actin, microtubules and other structural protein filaments.[63] It is responsible for the mechanical stability of the cell and defines its shape.[64] Therefore, the cytoskeleton has a crucial role in cell migration and also supports the molecule transport inside the cell.[65,66]

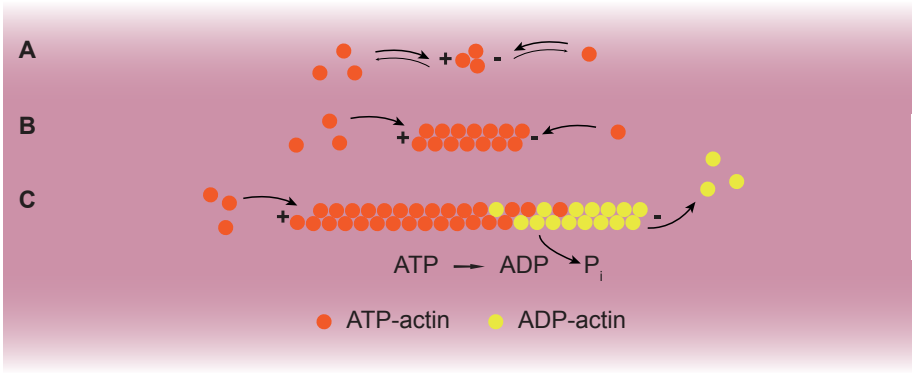


Figure 1.3: Schematic illustration of dynamic polymerisation and depolymerisation of actin filaments. Adapted and modified from Nürnberg *et al.*[67]

In particular, the highly conserved actin is well explored.[68] The dissolved actin monomers are called globular actin (G-actin) and carry an adenosine triphosphate (ATP) molecule. For filament polymerisation, three G-actin form a trimer as a nucleating point for the polymerisation, followed by further G-actin monomers binding onto this trimer, forming filamentous actin (F-actin) (Figure 1.3A). The two ends of the F-actin grow at different rates due to a conformational change: the fast growing end is called the plus end and the slow growing end is called the minus end (Figure 1.3B). The carried ATP hydrolyses to adenosine diphosphate (ADP), reducing the binding affinity of actin monomers to their neighbours. This increases the dissociation rate on the minus end (Figure 1.3C). If the polymerisation at the plus end and the depolymerisation on the minus end are equally fast, the actin filament will reach a static length, even though there is a net flux of subunits through the polymer.[67]

1.3 GUV generation methods

For the generation of GUVs, different methods were developed using various properties of lipids, solvent solubilities, and charge interactions.[69–75] I sorted the most used methods into three different groups: 1) methods using dried lipid films for GUV generation (Figure 1.4A); 2) methods where water droplets were transferred through lipid layers (Figure 1.4B); 3) methods where water-in-oil (w/o) droplets were generated as a template for GUV generation (Figure 1.4C).

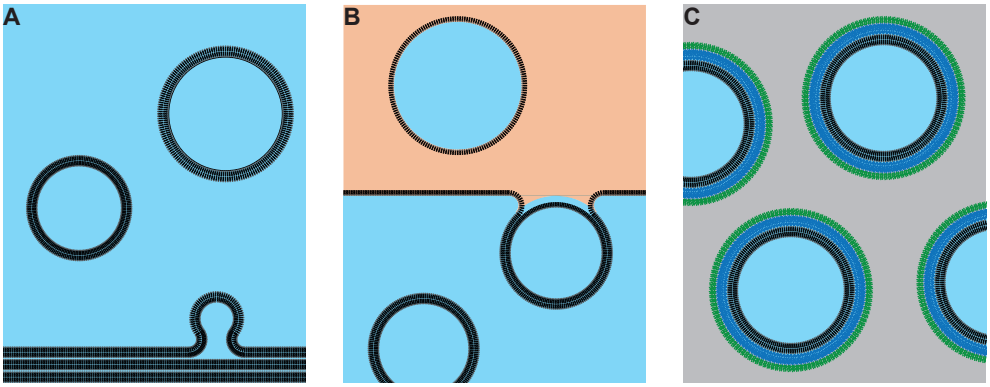


Figure 1.4: Schematic illustration of GUV generation using a lipid film (A), by emulsion transfer (orange: oil phase, blue: aqueous phase, B) and based on w/o droplet (gray: fluorinated oil phase, C). Adapted and modified from Beales *et al.*[76]

1.3.1 Lipid film formation

GUVs can be generated by hydration of dried lipid films. The simplest is the gentle hydration method.[77–79] Here, a layer of water is placed on the dried lipid film. As the lipid film swells, GUVs of various sizes gradually detach.[80] The process can be supported by an external electrical field, called electroformation method.[79,81,82] This decreases inter-membrane attraction inducing instability of lipid binding.[83] For hydrogel-assisted hydration methods, the dried lipid film is created on top of a dried hydrogel, for example an agarose or PVA gel.[69,84–86] The hydrogel supports the swelling process increasing the GUV generation rate.

In terms of methodology, the freeze-thaw cycle method differs. Here, the dried lipid film is hydrated and extruded into small unilamellar vesicles (SUVs) (vesicle radius smaller than 100 nm) to obtain monodisperse vesicles. In several cycles, the solution is alternately frozen in liquid nitrogen and then rapidly thawed, only to be frozen again. In this process, the lipid membrane is destabilized and the vesicles fuse.[87,88]

1.3.2 Emulsion transfer

Generally, for this method group the lipids are dissolved in an organic oil, like mineral oil or silicon oil. Combing this oil solution with an aqueous phase, a lipid monolayer is formed on the interface. If a second water phase with a lipid monolayer is transferred through this monolayer at the water-oil interface, a vesicle with a lipid bilayer is formed. In the inverted emulsion method, a w/o emulsion with the inner GUV buffer in organic oil containing lipids is generated and placed above the previously described water/oil system. While under centrifugation, the emulsion is transferred through the oil-water interface, causing of a density gradient between inner GUV buffer and the oil phase or the outer aqueous phase, forming a GUV.[89,90] For the continuous droplet

interface crossing encapsulation (cDICE) method, the water-oil system was placed in a round vessel that is constantly rotating. Using a cannula, the inner buffer was constantly added dropwise and due to centrifugal forces, transferred through the oil-water interface.[91,92] During the process, monodisperse GUVs are created where the size can be controlled by the inner buffer flow rate or rotation speed. A modification of this method is the emulsion droplet interface crossing encapsulation (eDICE) method, where instead of a constant flow through the cannula, a pre-produced w/o emulsion was added into the rotating vessel.[93]

For another transfer method of GUV production, two water reservoirs are separated by a lipid bilayer film. Either by pulsed microfluidic or acoustic jetting a water drop can be transferred through the lipid bilayer film creating a GUV.[94,95]

1.3.3 Water-in-oil droplet-based

For GUV generation using w/o droplets, an aqueous solution containing SUVs is used to produce droplets in a fluorinated oil. To stabilize the water droplet against fusion, amphiphilic polymer surfactants are added to the oil phase, forming a surfactant layer on the water-oil interface. Due to charge-mediated interactions between the surfactants and the SUVs, a lipid bilayer self assembles and dsGUVs are formed. By destabilizing the droplets shell, the GUVs can be released.[96,97] These droplets can either be produced by microfluidics,[75,98,99] emulsification,[100] or shaking.[101,102] The droplet-based microfluidic method is mainly used for GUV generation in this thesis and therefore described in detail in the next chapter.

With special microfluidic devices it is possible to create water-in-oil-in-water (w/o/w) droplets for octanol-assisted liposome assembly (OLA). In this case, 1-octanol containing the lipids is used. Octanol dewetts from the double emulsion, forming a separate oil droplet and leaving GUV.[103,104]

1.4 Droplet-based microfluidics

Microfluidic technology allows manipulation and control of fluid flows in the microliter to femtoliter scale through micrometer sized channels. The changed behaviour of fluids on micrometric scales compared to macro scales, due to differences in physical properties, enables the use of microfluidics in engineering, physics, chemistry, biochemistry, nanotechnology, and biotechnology.[105–110]

The sub-field of droplet-based microfluidics uses immiscible fluids to create an emulsion, creating individual reaction containers. For the creation and manipulation of droplets, different microfluidic devices were designed.[111–115]

1.4.1 Physical background

Miniaturizing the channels to micrometer scale changes more then just the dimensions. For macroscopic fluid systems, the flow is mostly affected by gravity and inertial forces whereas for microfluidic systems, surface tension and viscous forces dominate.[116] The reason for this difference is the change in surface-to-volume ratios towards higher importance where the surface increasing changes the dependency on surface-associated forces.[106,117] The two forces, inertial and viscous forces, are set in relation by the dimensionless Reynolds number Re:

$$Re = \frac{\rho * \nu * L}{\eta}$$

where ρ is the density of the fluid, ν the flow velocity, L the linear scale of the system and η the dynamic viscosity.[118] If Re is less than 2000, the behaviour of the flow changes from turbulent to laminar flow.[119] In a turbulent flow, chaotic eddies, vortices, and other flow instabilities occur. Laminar flow, instead, is characterized by smooth, constant fluid movement. By decreasing the dimensions of a channel during the transition from macroscopic fluid systems to microfluidic systems, L and therefore also Re decrease. Therefore, it is possible in laminar flow to have adjacent layers in a side-by-side flow without mixing (apart from diffusion).[118]

Whether advection or diffusion mass transfer predominates can be calculated with the help of the Péclet number Pe:

$$Pe = \frac{\nu * L}{D}$$

where D is the diffusion coefficient.[120] For a Pe much bigger than 1, convection predominates diffusion.

The surface tension describes the behaviour of fluids to minimize their surface free energy due to the stronger interactions between liquid molecules than with the molecules in the air.[121] The interfacial tension describes the same system but instead for immiscible liquid-liquid surfaces and, therefore, is the driving force in the stability of droplets and emulsions.[122,123]

To distribute the pressure caused by minimizing the surface free energy evenly, a liquid-air or liquid-liquid system tends to curve the surface respectively the interface. This pressure can be described by the Young-Laplace equation

$$\Delta p = \gamma * (\frac{1}{R_1} + \frac{1}{R_2})$$

where Δp is the Laplace pressure, γ the surface or interfacial tension, and R_1 and R_2 are the principal radii of curvature.[124] For a spherical droplet, R_1 and R_2 are equal and will be combined under R from now on.

Due to the small radii of the droplets generated by microfluidics, the Δp increases and thus the fusion of the droplets is promoted by Ostwald ripening and coalescence.[125–128] By using surfactants, the γ is reduced, which can increase the stability of the droplets.[129]

Pendent drop tensiometry can be used to determine the surface and interfacial tension of fluids. Therefore, the shape of a pendent drop surrounded by air or an immiscible liquid is analysed.[122] This shape is dependent on the Laplace pressure Δp to minimize the surface area as well as the gravity.[130] Therefore, the droplet is deformed and it is not possible to solve the Young-Laplace equation analytically which is only possible for spherical droplets. Instead, the Young-Laplace equation is solved numerically by correlation with the dimensionless Bond number Bo:

$$Bo = \frac{\Delta\rho * g * R_0^2}{\gamma}$$

where $\Delta\rho$ is the density difference between the two phases, g is the gravity constant, and R_0 the characteristic radius of the droplet.[122]

1.4.2 Microfluidics devices

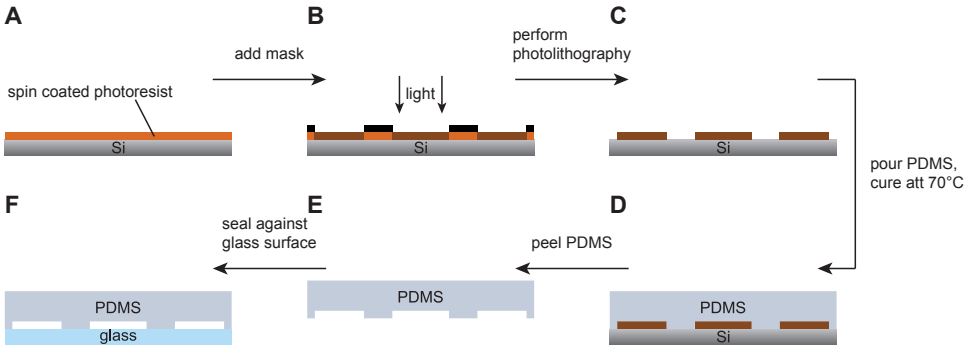


Figure 1.5: Schematic illustration of PDMS device productions. Photoresist is spin coated on a silicon wafer (A) and through a photomask light is used to polymerise photoresist (B). After removing unpolymerised photoresist (C), PDMS monomer mixed with curing agent is poured and polymerised at 70 °C (D). The peeled off PDMS mold (E) and a glass surface are activated in plasma and sealed against each other (F). Adapted and modified from McDonald *et al.*[131]

For the production of microfluidics devices, molds made of polydimethylsiloxane (PDMS) in particular has become widely used.[131–133] Therefore, photolithography is used to create a negative print of the microfluidics channel structure on a silicon wafer (Figure 1.5). A mixture of PDMS monomers and curing agent is added and polymerised. Afterwards, the PDMS mold can be cut out and peeled from the silicon wafer. To seal the PDMS chip on glass, both contact surfaces of PDMS and glass needs to be activated. Therefore, they are treated with plasma. During the process, the free electrons reacting with the surrounding material cleaning the glass surface and oxydizing the methyl groups in the dimethylsiloxane subunits to hydroxyl groups. After attaching the activated surfaces together, the hydroxyl groups from the PDMS mold reacts with the glass forming Si-O-Si bridges to bind the PDMS mold covalently on glass.[134]

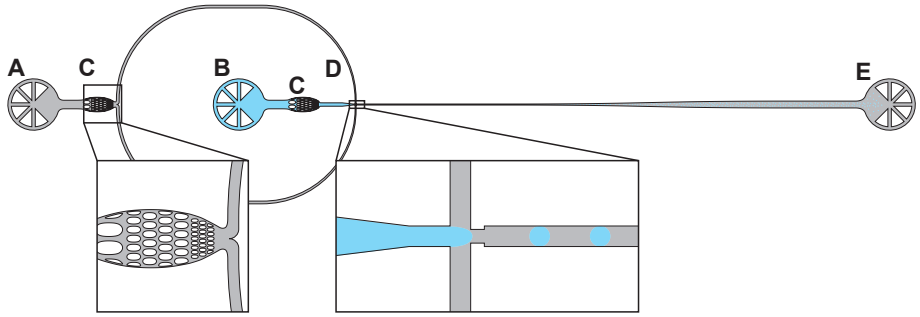


Figure 1.6: Schematic illustration of droplet production device. Through the inlets fluorinated oil (gray, A) and water (blue, B) are injected into the device. To prevent clogging, the fluids are first filtered (C). On the cross junction, the water layer is cut by the oil layer creating monodisperse droplets (D). Afterwards, the w/o droplets were collected from the outlet (E). The device structure was designed by Dr. Christoph Frey.

For the production of w/o droplets, one of the simplest designs has two channel inlets, one for the oil channel (Figure 1.6A) and one for the water channel (Figure 1.6B). These two channels are joining on a cross junction, where the water phase is cut by the oil phase into droplets (Figure 1.6D). Afterwards, the w/o droplets can be collected from the outlet (Figure 1.6E).[135,136] The size and production rate depends on the microfluidic chip dimensions, as well as the flow rate and viscosity of both fluids. So it is possible to produce droplets with a production rate up to multiple kHz.[113] The structure of a droplet production device could be further modified, for example with two parallel water channels inlets mixing on the cross junction to start processes inside a droplet,[11] or by adding a further water channel from the outside to produce w/o/w droplets.[103,104]

Beside droplet production, several different devices were designed for like droplet incubation, droplet reinjection or picoinjection.[137–142]

1.5 Fluorinated block copolymer surfactants

Due to the high Laplace pressure, w/o droplets would fuse instantly after production to reduce the surface free energy.[118] The droplets could be stabilized by reducing the interfacial tension between water and fluorinated oil by using surfactants. These are amphiphilic molecules and, thus, accumulate on the interface between two immiscible fluids reducing the interfacial tension.[143]

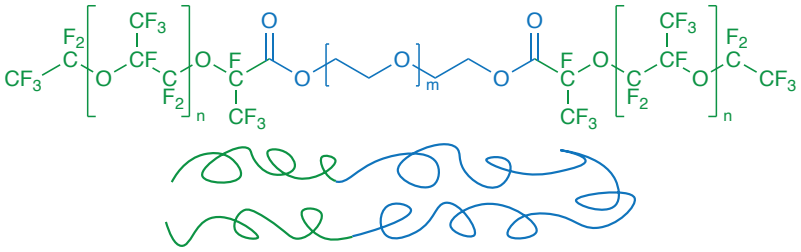


Figure 1.7: General chemical structure of a fluorinated triblock copolymer surfactant consisting of PEG (blue, hydrophilic) and PFPE (green, hydrophobic).

In case of droplet-based microfluidics, fluorinated block copolymer surfactants are the most common (Figure 1.7).[144] The triblock surfactant consists of one hydrophilic polyethylene glycol (PEG) block and two hydrophobic perfluoropolyether (PFPE) blocks, providing the amphiphilic property. Together with Krytox, PFPE with one terminal carboxylic acid group, it is possible to create charge-mediated self-assembly of a lipid bilayer in the water-oil interface.[96]

1.5.1 Physicochemical properties

Surfactants preferentially adsorb at interfaces, where they find the most energetically favorable conditions due to their bipartite structure, in case of droplet-based microfluidics on the fluorinated oil-water interface. As they can form strong interactions between both phases, the inferfacial tension decreases.

The amount of how much the interfacial tension is reduced depends on the amount of surfactants attached to the interface. As soon as the interface is concentrated, addition of surfactant do not decrease the interfacial tension further more. Instead the surfactant molecules form micelles and this concentration is called critical micelle concentration (CMC).[145] For fluorinated block copolymer surfactants, the CMC is around $150\,\mathrm{mmol/m^3}$.[146,147]

If a block copolymer can act as a surfactant depends on the size ratio between hydrophilic and hydrophobic block. The hydrophilic-lipophilic balance (HLB) describes the hydrophilic and hydrophobic degree of a nonionic surfactants:

$$HLB = 20 * \frac{H_W}{H_W + L_W}$$

where H_W is the molecular weight of the hydrophilic block and L_W of the hydrophobic block.[148,149] The HLB value can be between 0 and 20, where it is 0 for a completely hydrophobic and 20 for a completely hydrophilic molecule. To stabilize w/o droplets, a surfactant should have a HLB value between 4 to 6.[148]

1.5.2 Synthesis of fluorinated block copolymer surfactants

The fluorinated block copolymer surfactant is mostly used as a triblock surfactant consisting of PEG and PFPE. For the synthesis of the triblock surfactant, PEG and PFPE must be combined, and three different synthetic routes are of particular interest: 1) with esterification, 2) with amidation or 3) with copper(I)-catalyzed azide-alkyne cycloaddition (CuAAC). As starting material for the PFPE block is commonly Krytox used, a PFPE with one end functionalized by a carboxylic acid group.

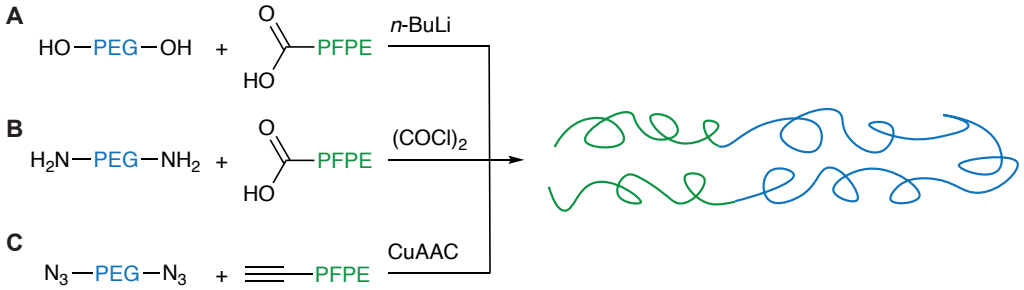


Figure 1.8: Different synthesis routes towards fluorinated triblock copolymer surfactant by esterification using n-BuLi activation of PEG (A), by amidation using oxalyl chloride to activate PFPE (B), or by CuAAC click reaction (C). Hydrophilic parts are labeled in blue, hydrophobic in green.

The first method to combine PEG and Krytox is an esterification using n-butyllithium (n-BuLi) (Figure 1.8A). Therefore, PEG is deprotonated by n-BuLi under inert conditions to receive the lithiated PEG. Under these strong alkaline conditions, Krytox is added and the lithiated oxygen of PEG can attack the carboxyl carbon of Krytox. In the process, a hydroxide ion is split off because of the basic system. Afterwards, the esterified triblock surfactant is obtained.[150]

For an alternative method, diamine PEG and Krytox are amidated by Krytox activation (Figure 1.8B). To achieve this, the carboxylic acid of Krytox is turned into acid chloride using oxalyl chloirde under inert conditions. Due to its higher reactivity, the acid chloride can react with the amine groups of diamine PEG. After this amidation, the amidated triblock surfactant can be isolated.[139]

Both reactions just described proceed via the generation of a reactive, metastable intermediate reacting with the other polymer. Due to the high reactivity and the slow reaction kinetics caused by high molecular masses, side reactions can occur and decrease the efficiency of these synthesis.[151,152] Using stable starting materials for the reaction can prevent side reactions. An example is a CuAAC click reaction (Figure 1.8C). Therefore, diazide PEG and propargyl PFPE are mixed with copper(I) ions catalysing the 1,3-dipolar cycloaddition.[153] The clicked surfactant can easily be seperated after finalizing the reaction.[154]

1.5.3 Charge-mediated GUV formation

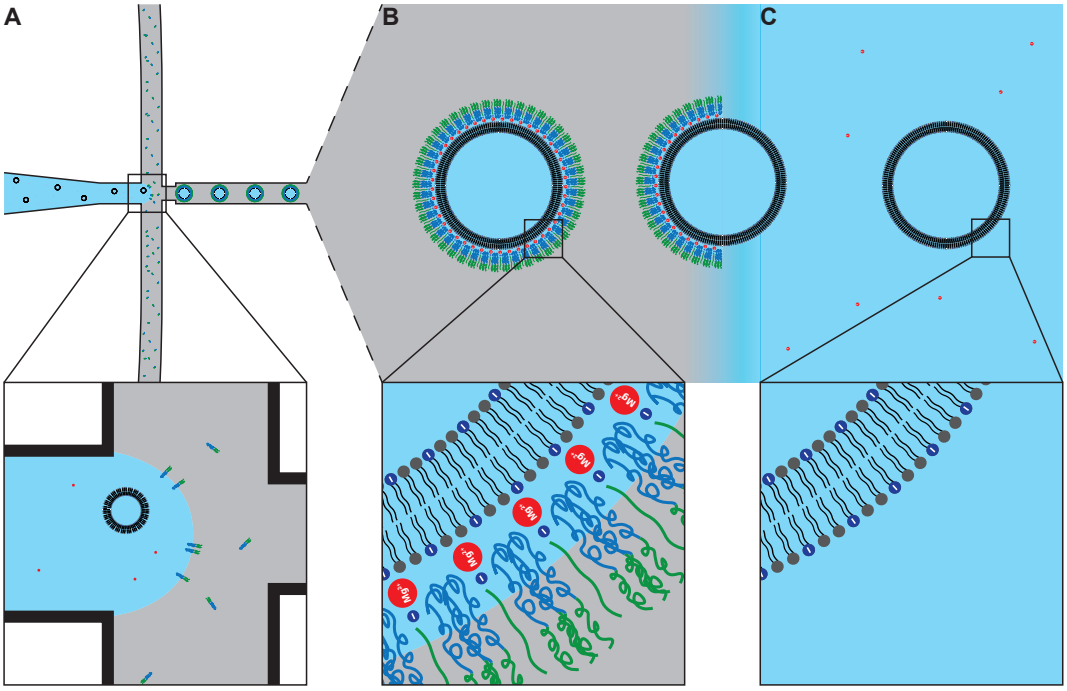


Figure 1.9: Schematic illustration of GUV generation using droplet-based microfluidics. A: W/o droplets are produced on the cross junction of a microfluidic device (grey: fluorinated oil phase, blue: aqueous phase). B: dsGUV formation by charge mediated sequential attraction of magnesium ions first, followed by attraction of the negatively charged SUVs. C: By adding a destabilizing surfactant, the droplets fuses with the buffer phase releasing the GUVs.

To generate GUVs using droplet-based microfluidics, first droplets containing negatively charged SUVs and magnesium ions must be produced using a fluorinated oil phase with dissolved fluorosurfactant and Krytox (Figure 1.9A).

After the droplet production, fluorosurfactant and Krytox adsorb on the water-oil interface to stabilize the droplet against fusion by decreasing the interfacial tension. Here, the hydrophilic part of Krytox is the carboxylic acid group and on the droplet

interface, this functional group is deprotonated inducing a negative charge. The magensium ions are attracted by the negative charge and, in turn, attract the negatively charged SUVs forming a coordination complex.[96,101,155,156] This lipid self-assembly forms a lipid bilayer and, thus, a dsGUV (Figure 1.9B).

To transfer dsGUVs into an aqueous system, the droplets need to be destabilized by adding a destabilizing surfactant, like *1H,1H,2H,2H*-perfluoro-1-octanol (PFO), in excess. This surfactant is too small to efficiently decrease the surface tension. Therefore the surface free energy is increasing, explaining why the droplets start to fuse and the GUVs are released (Figure 1.9C).

1.5.4 Other surfactants in droplet-based microfluidics

Beside triblock copolymer surfactants, differently structured surfactants were also designed, like diblock surfactants. Haller *et al.* could show that using a mixture of triblock and diblock surfactant consisting of PEG and PFPE with the same molecular ratio between the hydrophilic and hydrophobic blocks reduces the interfacial tension more efficiently.[96]

Another example is the branching of the PEG block. These dendronized fluorosurfactants are able to stabilize the droplet further. In addition, they a reducing the amount of small molecules, which are transported between droplets.[157]

In contrast to chemical and biological inert surfactants, functionalized ones are able to introduce a specific property into the water-oil interface. For example, the functionalization of surfactants with gold nanoparticles enables the coating with thiol-containing ligands.[150] Further poly(N-isopropylacrylamide) (PNIPAM) surfactants produce temperature-responsive droplets for implementing droplet motility or a triggered demulsification.[12,158] Finally, surfactants with the ability to capture biomolecules, fabricate microcapsules and monitor single-cell gene expression are used, too.[159]

1.6 Synthetic cell modifications

GUVs are used as a template for implementing several cell functionalities towards a synthetic cell.[160] Therefore, different cell modules based on proteins or DNA were developed for mimicking these cell functions. The following list contains selected examples, which are in particular interest for the construction of artificial tissues.

ATP is the fuel for many cellular processes like metabolic reactions or actin polymerisation.[68,168] Therefore, the ability of ATP self-production means independence and increased lifetime for artificial tissues. Ishmukhametov *et al.* showed the reconstitution

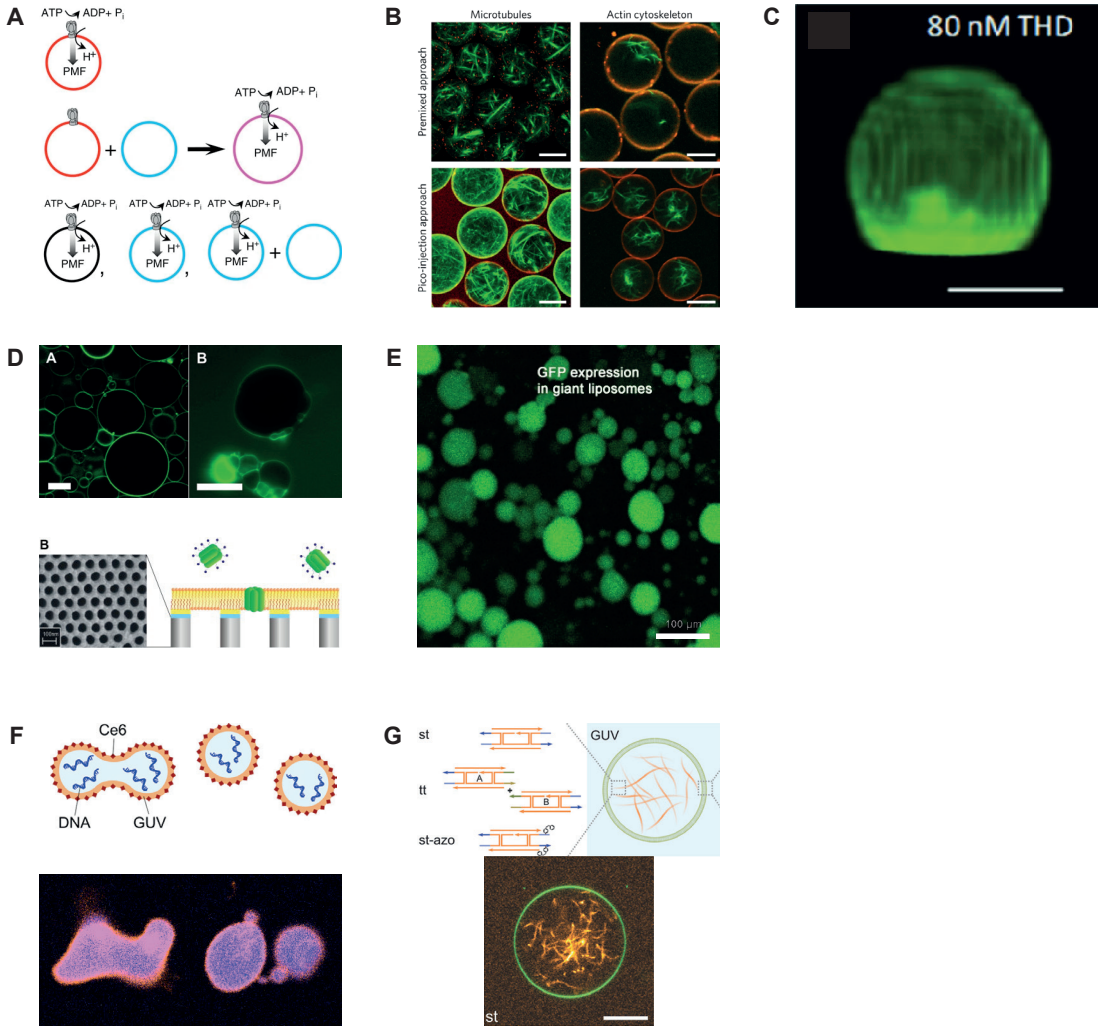


Figure 1.10: Examples for established reconstituted cell modules into synthetic cells using proteins or DNA mimics. Shown are the reconstitution of ATP synthase (A, adapted and modified from Ishmukhametov *et al*)[161], microtubules and actin cytoskeleton (B, adapted and modified from Weiss *et al*)[11], integrin $\alpha_{\mathrm{IIb}}\beta_3$ (C, adapted and modified from Benk *et al*)[162], connexin (D, upper images adapted and modified from Carnarius *et al* and lower images adapted and modified from Gaßmann *et al*)[163,164], cell-free GFP expression (E, adapted and modified from Saito *et al*)[165], DNA-mediated cell division (F, adapted and modified from Dreher *et al*[166] and DNA-based cytoskeleton (G, adapted and modified from Jahnke *et al*)[167].

of F_1F_o ATP-synthase, which can either catalyse the synthesis of ATP or is a proton pump under consumption of ATP, dependent of the conditions (Figure 1.10A).

As already described, the actin cytoskelton contributes in the mechanical stability, cell mobility and many regulatory processes inside a cell.[68] In addition, microtubules are also part of the cytoskeleton and are important for mitosis during cell division. Different groups showed already the reconstitution of these filaments into a synthetic cells (Figure 1.10B).[11,169–172]

In cells, integrins mediate adhesion to ECM and thus, are crucial for cell mobility. For reconstitution in synthetic cells, especially integrin $\alpha_{IIb}\beta_3$ is used (Figure 1.10C).[11,162,173]

From the cell junction, gap junctions are established for reconstitution. For the implementation of direct cell-cell communication through transmembrane channels, connexin 43 was used by Carnarius *et al.* (Figure 1.10D).[163,164]

The expression of proteins is a key feature to be implemented in synthetic cells. Therefore, the protein synthesis using recombinant elements (PURE) system is established (Figure 1.10E).[165,174–176]

1.6.1 DNA based modules

Beside the use of recombinant or purified proteins for reconstitution into GUVs, DNA structures are equivalent synthetic alternatives for the implementation of cell modules due to their higher stability and programmability.

Thus, DNA-based systems can be used in cell division. In doing so, they support the cleavage of osmolarity-driven seperation of one into two GUVs (Figure 1.10F).[166]

Further, the actin cytoskeleton can be replaced by DNA structures. Jahnke *et al.* established a method to light-triggered assemble and disassemble the DNA-based cytoskeleton (Figure 1.10G).[167]

In this thesis, the generation of GUVs was improved in terms of surfactants and lipid composition. These synthetic cells provided the platform for the implementation of different protein-based biomimicking and DNA-based synthetic modules. With this, it was possible to construct a hybrid system consisting of synthetic and natural cekks, and went a step further towards an artificial tissue.

Chapter 2

Motivation

In order to understand biological systems, such as a cell, it is necessary either to disassemble the complete system into its individual parts (top-down) or to assemble the individual parts to a functional system (bottom-up). While the top-down approach has to deal with the complexity of a cell and interactions between individual processes in biological systems, the advantage of the bottom-up construction is the modularity and programmability to select specific features of interest for further investigation. In addition, the bottom-up approach gives the possibility to combine biomimetic approaches with synthetic elements and thus to influence individual processes by interrupting specific features of a natural cell. The bottom-up constructions of a cell, so-called synthetic cells, containing adhesion and interaction modules can be used as building blocks to create an artificial tissue. Such a tissue could be used to study communications and interactions inside a cell network and could be modulated to influence natural tissue as a drug delivery tool or to aid in natural processes like wound healing.

The ultimate goal of my research is to develop bioinspired synthetic cells for the artificial tissue assembly. The best candidates for cell-like compartment assembly are GUVs. In recent years a very good progress has been achieved with control generation of GUVs by means of charge-mediated approach within the water-in-oil microfluidic droplets. Nevertheless, considerable challenges still loom at many steps in this process of GUVs formation. As a chemist, to overcome the limitations of the current approach I aimed to optimize the block copolymer surfactant chemistry and lipid composition in order to achieve a better GUVs formation yield. To achieve that, I aimed to screen three different surfactants synthesis routes and analyze them in terms of purity of the block copolymer surfactant product and its physicochemical properties. Moreover, I planned to synthesize two novel functional surfactants that, for my opinion, can significantly improve the efficiency of the GUVs formation. In particular, I aimed to synthesize a positively charged surfactant that will allow for straight-forward attraction of negatively charged lipids omitting complex Krytox-mediated coordina-

tion interactions. Additionally, to improve the release process I aimed to synthesize a photoliable surfactant. The light-mediated control over the amphiphilic properties of the surfactant is an important feature towards destabilization of the droplets and the sequential release of the assembled GUVs into physiological conditions.

In addition to surfactant synthesis I aimed to design a novel strategies for GUVs assembly. Particularly, I planned to focus on the implementation of lipid composition that have the ability to change its charge by an external trigger. The rationale behind the strategy is to enable first a charge-mediated self-assembly of lipid bilayer by triggered attraction between the lipids and the surfactants and as a second step to trigger the repulsive interactions between lipids and surfactant layer to facilitate the release of GUVs. I planned to realize this approach by implementation of pH-sensitive lipid composition.

Following the improved formation of GUVs I aimed to design the biofunctionalization approaches towards formation of adherens junctions and adhesive modules between the GUVs and ECM, respectively. Particularly, the main goal was to mimic the E-cadherin-mediated epithelial cell interactions. To mimic integrin-mediated cell-ECM adhesion interactions I aimed to design the approaches for efficient and functional reconstitution of $\alpha_{\mathrm{IIb}}\beta_3$ integrin proteins and actin cytoskeleton into the GUV-based synthetic cells.

Finally, to achieve my ultimate goal of a hybrid system formation I aimed to co-culture synthetic and natural cells. Particularly, I focused on formation of E-cadherin-mediated cellular network between the synthetic and natural cells. To analyze the network formation in a qualitative and quantitative manner I plan to develop and advance image analysis methods.

Chapter 3

Materials and Methods

3.1 Instruments

For microfluidics setup a Axio Vert.A1 bright-field microscope (Carl Zeiss) equipped with EoSens Cl high speed camera (Mikroton). A OB1 MK3+ Microfluidic Flow Controller (Elveflow) was used to control microfluidics pressure.

Confocal microscopy measurements were performed on a Zeiss LSM 800 and Zeiss LSM 980 (Carl Zeiss) inverted microscope with a 20x air ojective. Fluorescent microscopy measurments were performed on a DMi8 (Leica).

Fourier transform infrared spectrophotometry measurements were performed on an IRTracer-100 (Shimadzu GmbH, Duisburg, Germany) equipped with a QATR modul (QATR-10 single bounce - extended range) and a MCT detector.

Pendent drop tensiometry measurements were performed on a Drop Shape Analyser DSA25 (Krüss).

For plasma treatment, a Plasma System 300 SA (TePla) equipped with pressured oxygen was used.

Mass spectrometry measurments were performed on maXis II ETD - HRMS (Bruker).

NMR spectroscopy measurments were performed on 400 MHz NMR Spektrometer (Bruker).

3.2 Software

3.3 Materials

3.3.1 Chemicals

The following chemicals were purchased from the corresponding suppliers and used without further purification unless otherwise specified:

Lipids

Name	Supplier	Product no.
18:0 SM (d18:1/18:0)	Sigma-Aldrich	860586P-10MG
18:1 (Δ9-Cis) PC (DOPC)	Sigma-Aldrich	850375C-1G
18:1 (Δ9-Cis) PE (DOPE)	Sigma-Aldrich	850725C-1G
18:1 (Δ9-Cis) PG (DOPG)	Sigma-Aldrich	840475C-500MG
18:1 DGS-NTA	Sigma-Aldrich	790528C-5MG
18:1 DGS-NTA(Ni)	Sigma-Aldrich	790404C-25MG
18:1 Liss Rhod PE	Sigma-Aldrich	810150C-10MG
18:1 PEG1000 PE	Sigma-Aldrich	880730C-25MG
18:1 PEG2000 PE	Sigma-Aldrich	880130C-25MG
18:1 PEG350 PE	Sigma-Aldrich	880430O-25MG
18:1 PEG750 PE	Sigma-Aldrich	880630O-25MG
18:1 PS (DOPS)	Sigma-Aldrich	840035C-200MG
18:1 TAP (DOTAP)	Sigma-Aldrich	890890C-500MG
Atto 488 DOPE	Sigma-Aldrich	67335-1MG
Cholesterol (ovine)	Sigma-Aldrich	700000P-5G
Cholesterol-d7	Sigma-Aldrich	700041P-10MG
DOBAQ	Sigma-Aldrich	850310C-25MG
Egg PC	Sigma-Aldrich	840051C-1G
Egg PG	Sigma-Aldrich	841138C-500MG
EquiSPLASH	Sigma-Aldrich	330731-1EA

Polymers and surfactants

Name	Supplier	Product no.
KRYTOX 157 FSH	Costenoble	ACM30305XXX3
Jeffamine 800	Sigma-Aldrich	14527-500ML-F
PEG 600	EMD Millipore	8074861000
PEG 1400	Sigma-Aldrich	202436-250G
PEG 1500	EMD Millipore	8074891000
1H,1H,2H,2H-Perfluoro-1-octanol	Sigma-Aldrich	370533-25G
SYLGARD 184 ELASTOMER KIT	VWR	634165S

Solvents

Name	Supplier	Product no.
Acetone		
1,1,1,2,3,4,4,5,5,5-Decafluoropentane	Sigma-Aldrich	94884-500ML
Dichlormethane		
Dichloromethane anhydrous	Sigma-Aldrich	270997
Diethyl ether		
N,N-Dimethylformamide	Roth	T921.1
Ethanol	Emsure	1.00983.1011
1,1,1,3,3,3-Hexafluoro-2-propanol	Sigma-Aldrich	105228-25G
Methanol	Emsure	1.06009.1011
Novec 7100	Iolitec	FL-0001-HP-5000
Novec 7500	Iolitec	FL-0004-HP-1000
Tetrahydrofuran	Emsure	1.09731.1000
Tetrahydrofuran, dry	Acros Organics	348451000

Proteins

Name	Supplier	Product no.
Human E-Cadherin Protein (His Tag)	Sino Biological	10204-H08H1
Recombinant Human E-Cadherin	R&D systems	8505-EC-050

DNA

The following ssDNA strands with the according sequence were synthesized biomers. The given sequence is written from 5'-end to 3'-end.

Name	Sequence	5' mod.	3' mod.
Block A	`TCG ACA CGG AAA`		
	`TGT TGA ATA CTA`		
Block A'	`TAG TAT TCA ACA`		
	`TTT CCG TGT CGA`		
Fusion A	`TCG ACA CGG AAA`	Cholesterol-TEG	
	`TGT TGA ATA CTA`		
Fusion A'	`TAG TAT TCA ACA`		Cholesterol-TEG
	`TTT CCG TGT CGA`		

Name	Sequence	5' mod.	3' mod.
Palind. DNA 1	TGA AGT TTA ATT AAA CTT CAG GCC ATC GTC GCT ATA TAT ATA TAT TAT T		CholTEG
Palind. DNA 2	TAT AAT ATA TAT ATA TAG CGA CGA TGG C	ATTO488	
SurfAd(short, chol.)	TTT GTA TAA ATG	Cholesterol Pro	BMN-Q620
SurfAd(short, thiol)	CAT TTA TAC TTT	Cyanine 3	Thiol C6
SurfAd(middle, chol.)	TTT GGG TTA ACA TCT AGA TTC TA	Cholesterol Pro	BMN-Q620
SurfAd(middle, thiol)	TAG AAT CTA GAT GTT AAC CCT TT	Cyanine 3	Thiol C6
SurfAd(long, chol.)	TTT CGC CGC GGG CCG GCG CGC GG	Cholesterol Pro	BMN-Q620
SurfAd(long, thiol)	CCG CGC GCC GGC CCG CGG CGT TT	Cyanine 3	Thiol C6

Other chemicals

Name	Supplier	Product no.
4-Bromomethyl-3-nitrobenzoic acid	Sigma-Aldrich	423564-5G
n-Butyllithium solution	Sigma-Aldrich	186171-4X25ML
Copper(II) sulfate pentahydrate	Grüssing	12079
4-(Dimethylamino)pyridine	Sigma-Aldrich	8204990005
Neocuproine	Sigma-Aldrich	N1501-5G
Oxalyl chloride	Merck Millipore	8070660100
Propargylamine	Sigma-Aldrich	P50900-1G
Propargyl bromide solution, 80 wt.% in toluene	Sigma-Aldrich	P51001-50G
(+)-Sodium L-ascorbate	Sigma-Aldrich	A7631-100G
Sodium azide	EMD Millipore	8223350100

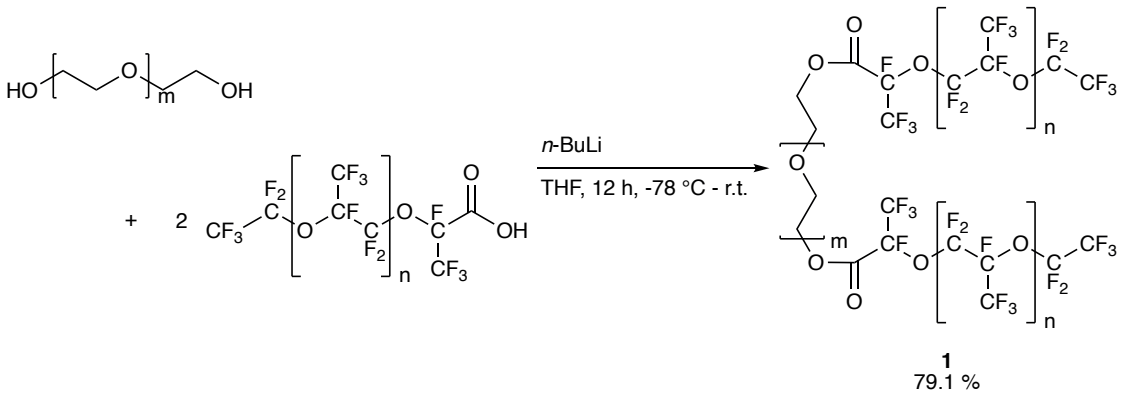
Name	Supplier	Product no.
Sodium hydroxide	Emsure	1.06498.1000
p-Toluenesulfonyl chloride	Sigma-Aldrich	T35955-250G
Triethylamine	Sigma-Aldrich	471283-100ML
Trimethylamine solution	Sigma-Aldrich	92260-250ML

Consumable materials

Name	Supplier	Product no.
BOLA Tubing, PTFE, 0.3 mm x 0.6 mm, t=0.15	BOLA	S 1810-04
Centrifugal filter, 0,45 µm	VWR	516-0235
Certified Vial Kit, Low Adsorption	Sigma-Aldrich	29653-U
Extruder Set	Sigma-Aldrich	610000-1EA
Hydrophobic-fluorophilic coating on coverslips	RAN Biotechnologies	022221-MaxPlanck
µ-Slide VI 0.5 Glass Bottom PFTE filters	ibidi	80607
Rapid-Core Disposable Microfluidic Punches, 0.5 mm	Darwin Microfluidics	PT-T983-05
Sephadex G-50	Sigma-Aldrich	G5080-50G
U PLATE ANGIOGENESIS 96 WELL	ibidi	89646

3.4 Synthesis

3.4.1 Esterified triblock surfactant PFPE 7000-PEG 1500-PFPE 7000 1



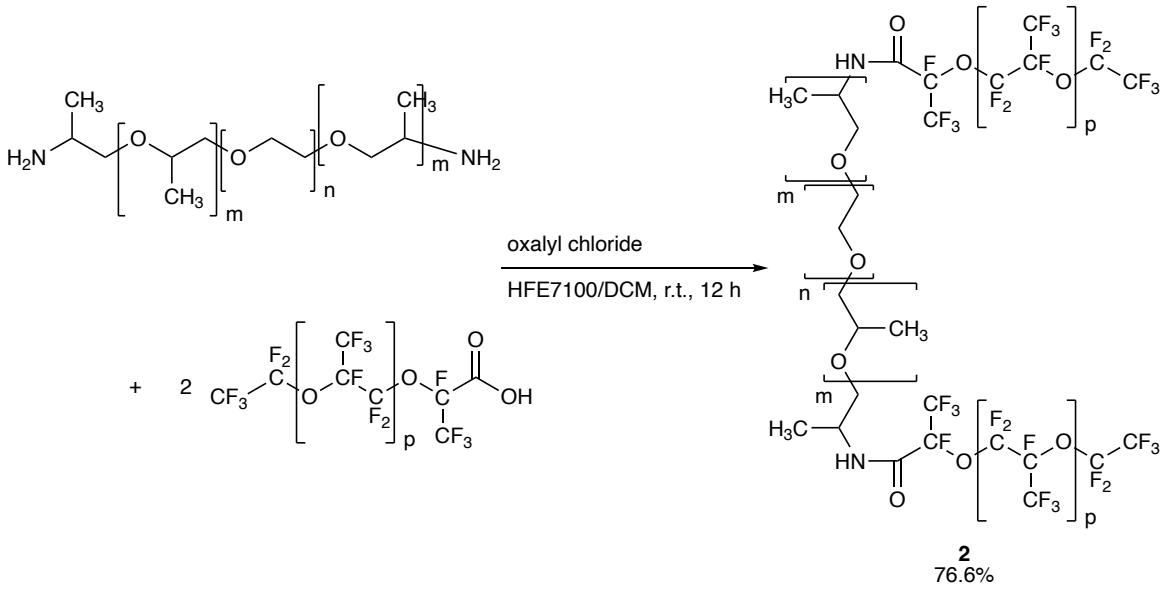
	M [g/mol]	n [mmol]	m [g]	c [M]	V [mL]	eq.
PEG 1400	1400	1.0	1.4			1.0
Krytox FSH	7000	2.0	14.0			2.0
***n*-BuLi**		2.0		1.6	1.25	2.0
THF					80	

The synthesis procedure was mainly predicted on the synthesis from I. Platzman *et al.*.[150]

PEG 1400 (1.4 g, 1.0 mmol, 1. eq.) was placed in a flame-dried 100 mL Schlenk flask and kept under reduced pressure over night. After drying, it was dissolved in tetrahydrofurane (THF, 80 mL), cooled down to -78 °C using an acetone/dry ice bath and *n*-butyllithium (*n*-BuLi, 1.25 mL, 2.0 mmol, 2.0 eq.) was added dropwise over one hour. The reaction mixture was stirred for 30 minutes at -78 °C and was then slowly warmed up to room temperature. PFPE 7000 acid (Krytox FSH, 14.0 g, 2.0 mmol, 2.0 eq.) was added and reaction mixture was stirred over night at room temperature.

Solvent was removed under reduced pressure. Milky crude product was re-suspended in methanol, transferred into a new flask and solvent was removed under reduced pressure. Ethanol was added and crude product was re-suspended using sonication. The precipitate was collected and dried under reduced pressure. The triblock surfactant was obtained as clear gel (12.2 g, 791 µmol, 79.1 %).

3.4.2 Amidated triblock surfactant PFPE 7000-JA 800-PFPE 7000 2



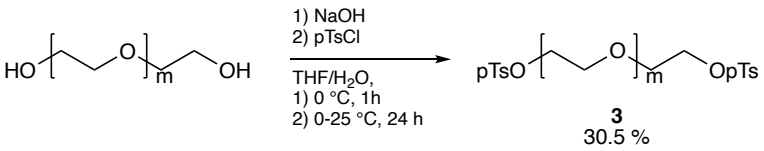
	M [g/mol]	n [mmol]	m [g]	ρ[g/mL]	V [mL]	eq.
JA 800	800	1.0	0.80			1.0
PFPE 7000	7000	2.0	14.0			2.0
Oxalyl chloride	126.93	20.0		1.479	1.72	20.0
DCM					4	
HFE 7100					14/10/2	

The synthesis procedure was mainly predicted on the synthesis from C. Holtze *et al.*.[139]

PFPE 7000 acid (Krytox FSH, 14.0 g, 2.0 mmol, 2.0 eq.) was placed in a flame-dried Schlenk flask and degassed under reduced pressure. It was then dissolved in HFE 7100 (Novec 7000, 14 mL) and oxalyl chloride (1.72 mL, 20.0 mmol, 20.0 eq.) was added dropwise. After stirring over night, solvent and excess of oxalyl chloride were removed under reduced pressure and collected in a liquid nitrogen cooling trap. Acid chloride was re-dissolved in HFE 7100 (10 mL) and jeffamine 800 (JA 800, 800 µg, 1.0 mmol, 1.0 eq.) solution, dissolved in dichlormethane (DCM, 4 mL) and HFE 7100 (2 mL), was added. Reaction mixture was stirred at room temperature over night.

Afterwards, solvents were removed under reduced pressure. The crude product was suspended in ethanol (80 mL) and stored at 4 °C. The precipitate was collected and dried under reduced pressure. The triblock surfactant was obtained as clear, highly viscous liquid (11.3 g, 766 µmol, 76.6 %).

3.4.3 PEG 1500 ditosylate 3



	M [g/mol]	n [mmol]	m [g]	V [mL]	eq.
PEG 1500	1500	83.3	125		1.0
NaOH	40.00	333	13.3		4.0
***p*TsCl**	190.65	191	36.4		2.3
THF				200/220	
H_2O				103	

The synthesis procedure was mainly predicted on the synthesis from R. Scanga *et al.* and published with F. Lussier *et al.*.[102,154]

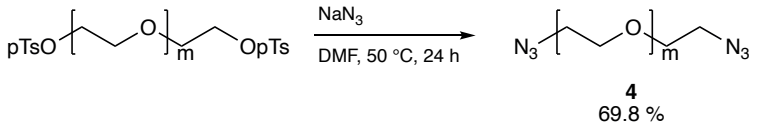
Water (103 mL) was cooled with ice bath and sodium hydroxide (NaOH, 13.3 g, 333 mmol, 4.0 eq.) was added. After complete dissolving, tetrahydrofuran (THF, 200 mL) was added and the mixture was cooled down to 0 °C. Polyethylene glycol 1500 (PEG 1500, 125 g, 83.3 mmol, 1.0 eq.) was added portionwise. During this process, it was ensured that the temperature never rose above 5 °C.

Afterwards, ice bath was removed and reaction mixture was stirred until it reached room temperature. After one hour of additional stirring, the mixture was cooled down to 0 °C again. *p*-Toluenesulfonyl chloride (*p*TsCl, 36.4 g, 191 mmol, 2.3 eq.) was dissolved in THF (200 mL) and added dropwise again with ensuring that the temperature never rose above 5 °C. After final addition, the reaction mixture was allowed to heat up to room temperautre and stirred for 18 hours.

The reaction mixture was separated and organic layer was collected, followed by removing solvent under reduced pressure. The crude product was redissolved in ethyl acetate (750 mL) and washed with 90 vol% brine (100 mL). Solution was dried over magnesium sulfate, filtered and solvent was removed under reduced pressure. The ditosylated PEG derivative was received as a white solid (46.0 g, 25.4 mmol, 30.5 %).

^{1}H-NMR (400 MHz, $CDCl_3$): δ = 2.385 (s, 6H, H6), 3.578 (m, H3, H2), 4.090 (t, J = 4.4 Hz, 4H, H1), 7.283 (d, J = 4.0 Hz, 4H, H5), 7.729 (d, J = 4.0 Hz, 4H, H4).

3.4.4 PEG 1500 diazide 4



4
69.8 %

	M [g/mol]	n [mmol]	m [g]	V [mL]	eq.
3	1810	11.1	20.0		1.0
NaN_3	65.01	24.3	1.58		2.2
DMF				30	

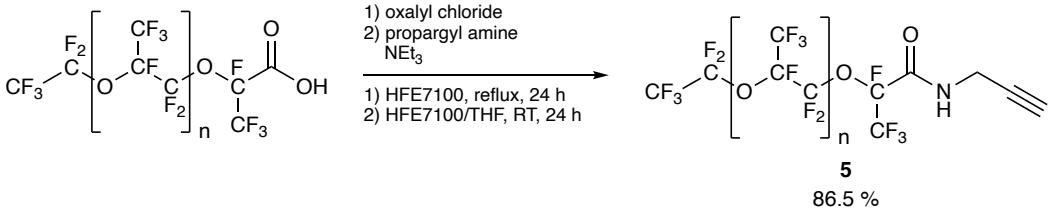
The synthesis procedure was mainly predicted on the synthesis from R. Scanga *et al.* and published with F. Lussier *et al.*.[102,154]

Sodium azide (1.58 g, 24.3 mmol, 2.2 eq.) was added to a solution of PEG derivative **3** (20.0 g, 11.1 mmol, 1.0 eq.) in dimethylformamide (DMF, 30 mL). After stirring for 90 minutes at room temperature, reaction mixture was heated up to 50 °C for 18 hours. During this reaction time, mixture became more and more cloudy.

After cooling down to room temperature, mixture was filtered and solvent was removed by co-evaporation with toluene under reduced pressure. The obtained solid was suspended in ethyl acetate (200 mL). After filtering and washing with 90 vol% brine (50 mL), the solution was dried over magnesium sulfate. Drying agent was removed by filtering and solvent was removed under reduced pressure. The diazide derivative of PEG 1500 was received as white solid (11.9 g, 7.71 mmol, 69.8 %).

^{1}H-NMR (400 MHz, $CDCl_3$): δ = 3.379 (t, J = 5.2 Hz, 4H, H1), 3.634 (m, H2, H3).

3.4.5 PFPE 7000 chloride and propargyl PFPE 7000 5



	M [g/mol]	n [mmol]	m [g]	ρ[g/mL]	V [mL]	eq.
Krytox FSH	6750	12.9	87.0			1.0
Oxalyl chloride	126.93	39.4	5.00	1.479	3.4	3.05
Novec 7100					150	
Propargylamine	55.08	13.5	0.744	0.860	0.87	1.05
NEt_3	101.19	19.3	1.96	0.726	2.7	1.5
THF					35	
Novec 7100					90	

The synthesis procedure was mainly predicted on the synthesis from R. Scanga *et al.* and published with F. Lussier *et al.*.[102,154]

PFPE 7000 acid (Krytox FSH, 87.0 g, 12.89 mmol, 1.0 eq.) was degassed under reduced pressure in a flame-dried Schlenk flask and dissolved in HFE 7100 (Novec 7100, 150 mL) under nitrogen atmosphere. Oxalyl chloride (3.4 mL, 39.4 mmol, 3.05 eq.) was added while stirring and afterwards, reaction mixture was refluxed at 61 °C for 18 hours. While reaction progressed, the solution became turbid.

Excess of oxalyl chloride and solvent were removed under reduced pressure, collecting removed material in a liquid nitrogen cooling trap. The acid chloride of PFPE 7000 was obtained as a slightly turbid, highly viscous liquid.

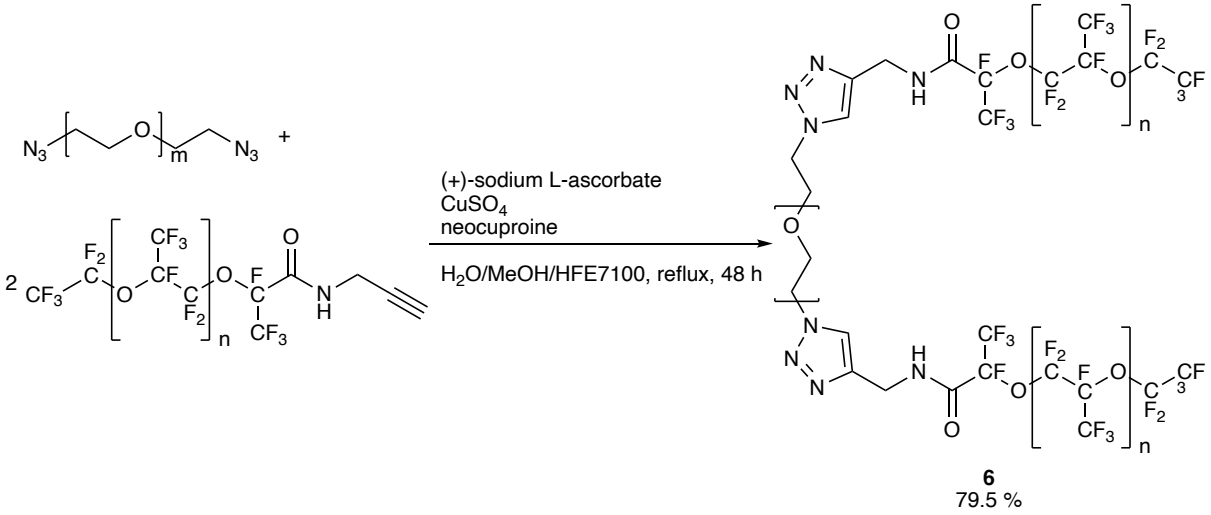
For the second reaction step, the acid chlorid was dissolved in HFE 7100 (90 mL). The Schlenk flask was equipped with a dropping funnel under nitrogen counter-flow. Propargylamine (870 µL, 13.5 mmol, 1.05 eq.) and triethylamine (2.7 mL, 19.3 mmol, 1.5 eq.) dissolved in dried tetrahydrofuran (THF, 35 mL) were loaded into the funnel and added dropwise to the acid chlorid solution. Afterwards, the reaction mixture was stirred for 18 hours.

Solvent and other volatile reagents were removed under reduced pressure. Crude product was redissolved in HFE 7100, filtered and solvent was again removed under reduced pressure. The propargyl derivative of PFPE was received as orange oil (75.7 g, 11.15 mmol, 86.5 %). The yield was calculated over both reactions.

As NMR solvent, a mixture of C_6F_6:C_6D_6 88:12 was used.

^{1}H-NMR (400 MHz, C_6D_6): δ = 2.186 (t, J = 2.8 Hz, 1H, H3), 4.135 (t, J = 2.8 Hz, 2H, H1), 6.602 (s, 1H, NH).

3.4.6 Clicked triblock surfactant PFPE7000-PEG1500-PFPE7000 6



	M [g/mol]	n [mmol]	m [g]	V [mL]	eq.
4	1550	1.49	2.31		1.05
5	6790	2.84	19.3		2.0
Na ascorbate	198.11	0.568	112 mg		0.4
$CuSO_4 \cdot 5\,H_2O$	249.69	0.284	70.9 mg		0.2
Neocuproine	208.26	0.455	94.8 mg		0.32
H_2O				15	
MeOH				15	
Novec 7100				30	

The synthesis procedure was mainly predicted on the synthesis from R. Scanga *et al.* and published with F. Lussier *et al.*.[102,154]

4 (2.31 g, 1.49 mmol, 1.05 eq.), sodium ascorbate (112 mg, 568 µmol, 40 mol%), copper(II) sulfate pentahydrate (70.9 mg, 284 µmol, 20 mol%) and neocuproine (94.8 mg, 455 µmol, 32 mol%) were dissolved in a mixture of water (15 mL) and methanol (15 mL). **5** (19.3 g, 2.84 mmol, 2.0 eq.) was dissolved in HFE 7100 (30 mL) and added to the aqueous solution. The reaction suspension was refluxed at 70 °C for 48 hours.

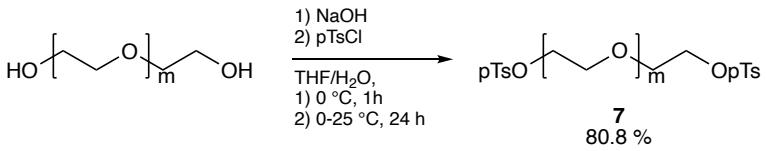
After reaction mixture cooled down to room temperature, it was transferred into a separation funnel. There, the suspension was carefully overlaid with methanol (15 mL). The two-phase system was swiveled without mixing. The methanol layer became orange and after saturation, it was replaced by fresh methanol. This procedure was repeated until the turbid suspension splited into two clear phases. If the volume of fluorinated oil phase decreased so much that the swiveling was not efficient anymore, HFE 7100

was added. The clear, fluorinated layer was collected and solvent was removed under reduced pressure. Crude product was redissolved in HFE 7100 and dried over magnesium sulfate over night. Dried solution was first filtered through Celite followed by PFTE syringe filter (0.45 µm). After removing solvent under reduced pressure, the clicked triblock surfactant was obtained as orange gel (17.1 g, 1.13 mmol, 79.5 %).

As NMR solvent, a mixture of C_6F_6:C_6D_6 88:12 was used.

^{1}H-NMR (400 MHz, C_6D_6): δ = 3.637 (m, H3), 3.970 (s, 4H, H2), 4.588 (s, 4H, H1), 4.678 (m, 4H, H6), 7.976 (s, 2H, H4), 8.433 (s, 2H, NH).

3.4.7 PEG 600 ditosylate 7



	M [g/mol]	n [mmol]	m [g]	V [mL]	eq.
PEG 600	600	83.3	50.0		1.0
NaOH	40.00	333	13.3		4.0
***p*TsCl**	190.65	192	36.5		2.3
THF				200/220	
H_2O				100	

The synthesis procedure was mainly predicted on the synthesis from R. Scanga *et al.*.[154]

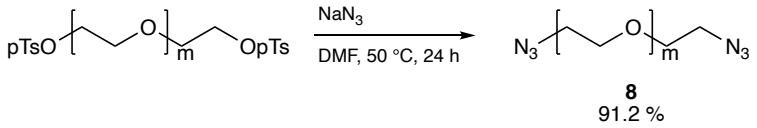
Sodium hydroxide (NaOH, 13.3 g, 333 mmol, 4.0 eq.) was dissolved in water (100 mL) and cooled to 0 °C. A solution of PEG 600 (50.0 g, 83.3 mmol, 1.0 eq.) in tetrahydrofuran (THF, 200 mL) was added slowly, so that the temperature did not rise above 5 °C. After complete addition, reaction mixture was allowed to warm up to room temperature and stirred for one hour at room temperature.

As next step, reaction mixture was cooled down again to 0 °C and a solution of *p*-toluenesulfonyl chloride (*p*TsCl, 36.5 g, 192 mmol, 2.3 eq.) in THF (220 mL) was added dropwise, so the temperature did not rise above 5 °C. Ice bath was removed and reaction mixture was stirred for 18 hours at room temperature.

For purification, the reaction mixture was separated and organic layer was collected, followed by removing solvent under reduced pressure. The crude product was redissolved in ethyl acetate (900 mL) and washed two times with water (100 mL) as well as once with brine (100 mL). Solution was dried over magnesium sulfate, filtered and solvent was removed under reduced pressure. The ditosylated PEG derivative was received as a clear oil (61.1 g, 67.3 mmol, 80.8 %).

^{1}H-NMR (400 MHz, $CDCl_3$): δ = 7.74 (d, J = 8.33 Hz, 4 H), 7.29 (d, J = 8.09 Hz, 4H), 4.10 (t, J = 4.83 Hz, 4H), 3.63 (t, J = 4.83 Hz, 4 H), 3.59-3.52 (m, 44 H), 2.39 (s, 6 H).

3.4.8 PEG 600 diazide 8



	M [g/mol]	n [mmol]	m [g]	V [mL]	eq.
7	910	91.1	82.9		1.0
NaN_3	65.01	200	13.0		2.2
DMF				230	

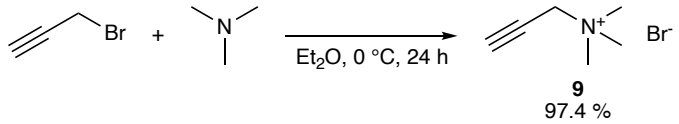
The synthesis procedure was mainly predicted on the synthesis from R. Scanga *et al.*.[154]

Sodium azide (NaN_3, 13.0 g, 200 mmol, 2.2 eq.) was added to a solution of PEG derivative **7** (82.9 g, 91.1 mmol, 1.0 eq.) in dimethylformamide (DMF, 30 mL). After stirring for 90 minutes at room temperature, reaction mixture was heated up to 50 °C for 18 hours. During this reaction time, mixture became more and more cloudy.

After cooling down to room temperature, mixture was filtered through Celite and solvent was removed by co-evaporation with toluene under reduced pressure. The obtained solid was suspended in ethyl acetate (800 mL) using a sonicator. After filtering and washing three times with brine (50 mL), the solution was dried over magnesium sulfate. Drying agent was removed by filtration and solvent under reduced pressure. The diazide derivative of PEG 600 was received as yellowish oil (53.98 g, 83.0 mmol, 91.2 %).

^{1}H-NMR (400 MHz, $CDCl_3$): δ = 3.69-3.65 (m, 50 H), 3.39 (t, J = 5.04 MHz, 4 H).

3.4.9 N,N,N-trimethylprop-2-yn-1-aminium bromide 9



	M [g/mol]	n [mmol]	m [g]	c [g/mL]	V [mL]	eq.
Propargyl bromide	118.96	116	13.8	1.335	116	1.0
TMA	59.11	129	7.61	4.2 M	30.7	1.11
Et_2O					30	

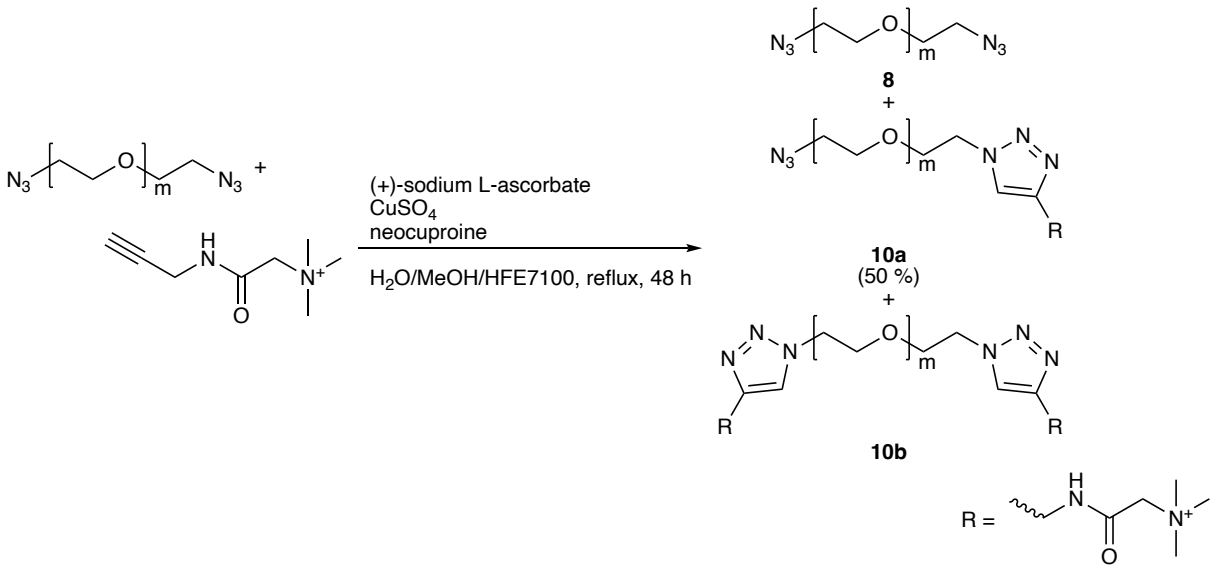
The synthesis procedure was mainly predicted on the synthesis from Z. Yao *et al.*.[177]

A mixture of trimethylamine (TMA, 4.20 M in ethanol, 30.7 mL, 129 mmol, 1.11 eq.) and diethyl ether (Et_2O, 30 mL) was cooled down to 0 °C. Propargyl bromide (80 w/w% in toluene, 10.0 mL, 116 mmol, 1.0 eq.) was added slowly and reaction mixture was stored for 24 hours at 4 °C.

Solvent and unreacted TMA were removed under reduced pressure. The assymetric ammonium bromide was received as white solid (17.1 g, 95.9 mmol, 82.7 %).

^{1}H-NMR (400 MHz, DMSO−d_6): δ = 4.47 (d, J = 2.52 Hz, 2 H), 4.08 (t, J = 2.53 Hz, 1 H), 3.16 (s, 9 H).

3.4.10 N3-PEG600-TAB 10a



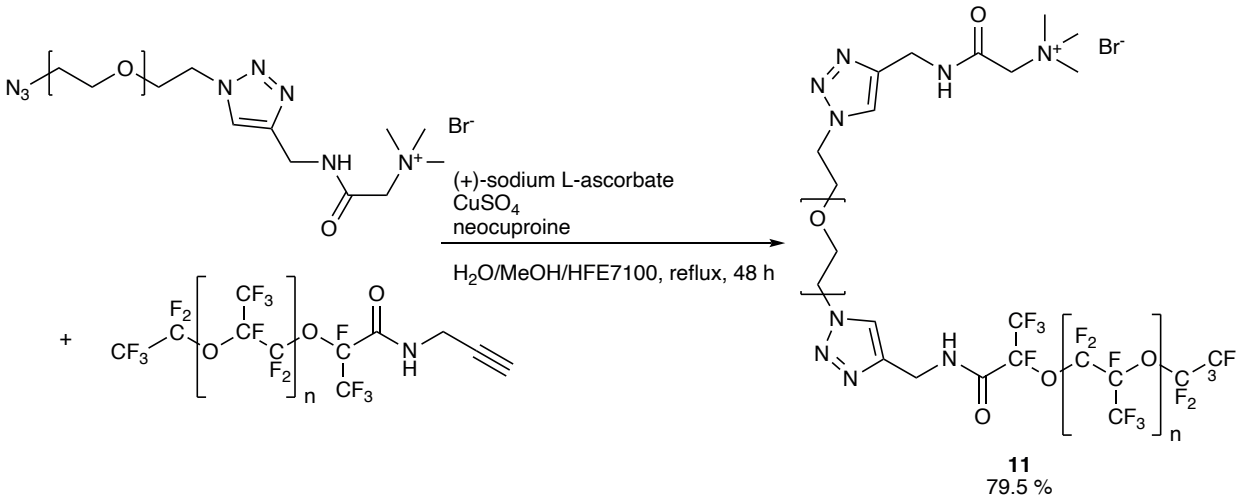
	M [g/mol]	n [mmol]	m [g]	V [mL]	eq.
8	650	15.4	10.0		1.0
9	178.07	15.4	2.74		1.0
Na ascorbate	198.11	30.8	6.10		2.0
$CuSO_4 \cdot 5\,H_2O$	249.69	15.4	3.84		1.0
H_2O				74.0	

A solution of **8** (10 g, 15.4 mmol, 1.0 eq.) and **9** (2.74 g, 15.4 mmol, 1.0 eq.) in water (74.0 mL) was sonicated until both substances were completly dissolved. Sodium ascorbate (6.10 g, 30.8 mmol, 2.0 eq.) was added and stirred for five minutes before copper(II) sulfate pentahydrate (3.84 g, 15.4 mmol, 1.0 eq.) was added. Reaction mixture was stirred at room temperature for 24 hours.

After filtering reaction mixture through Celite, the aqueous phase was washed three times with DCM (each 30 mL) and solvent was removed under reduced pressure. The green, amorph substance consisted of one-end funcionalized **10a**, both-end functionalized **10b** as well as starting materials salts, and was directly used for next synthesis step.

^{1}H-NMR (400 MHz, DMSO$-$d$_6$): δ = 8.40 (s, 1 H), 6.99-6.76 (m, 2 H), 4.64-3.48 (m, 49 H), 3.03 (s, 9 H).

3.4.11 Positively charged, clicked diblock surfactant PFPE7000-PEG600-TAB 11



	M [g/mol]	n [mmol]	m [g]	V [mL]	eq.
10a	830	(2.98)	(2.36)		1.05[1]
5	6790	2.84	20.0		1.0
Na ascorbate	198.11	0.568	112 mg		0.2
$CuSO_4 \cdot 5\,H_2O$	249.69	0.284	70.9 mg		0.1
Neocuproine	208.26	0.455	94.8 mg		0.16
H_2O				8	
MeOH				8	
Novec 7100				17	

5 (20.0 g, 2.84 g, 1.0 eq.) was dissolved in HFE 7100 (Novec 7100, 17 mL). **10a** (from last synthesis step), sodium ascorbat (112 mg, 568 µmol, 0.2 eq.), copper(II) sulfate pentahydrate (70.9 mg, 284 µmol, 0.1 eq.) and neocuproine (94.8 mg, 455 µmol, 0.16 eq.) were dissolved in methanol (8 mL) and water (8 mL). Both solutions were mixed and stirred under reflux for 48 hours.

Afterwards, reaction mixture was cooled down to room temperature, an aqueous EDTA solution (100 mM, 10 mL) was added and whole solution was transferred into a separation funnel. It was overlaid with methanol (20 mL) and carefully swivelled. The orange colored methanol phase was replaced by fresh methanol. This procedure was repeated until the methanol was not orange anymore. The fluorinated phase was dried of magnesium sulfate, filtered through Celite and again through PTFE syringe

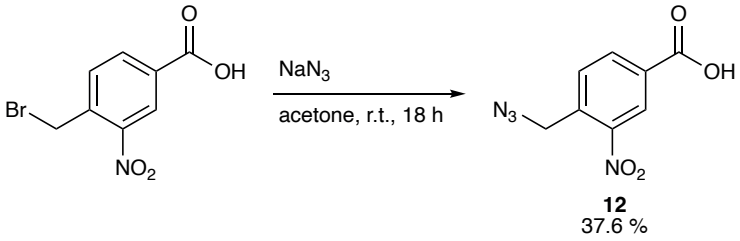
[1]Theoretical calculated amount of **10a** based on a qunatitative yield.

filter (0.45 µm). Solvent was removed under reduced pressure. The positively charged diblock surfactant was received as orange, viscous oil (17.6 g, 1.13 mmol, 79.58 %).

As NMR solvent, a mixture of C_6F_6:C_6D_6 88:12 was used.

^{1}H-NMR (400 MHz, $CDCl_3$): δ = 8.29 (br s, 1 H), 7.88 (br s, 1 H), 6.16-6.08 (m, 2 H), 5.72-5.64 (m, 2 H), 4.31 (br s, 2 H), 4.25 (br s, 4 H), 4.12-4.06 (m, 6 H), 3.88-3.87 (m, 69 H).

3.4.12 4-(Azidomethyl)-3-nitrobenzoic acid 12



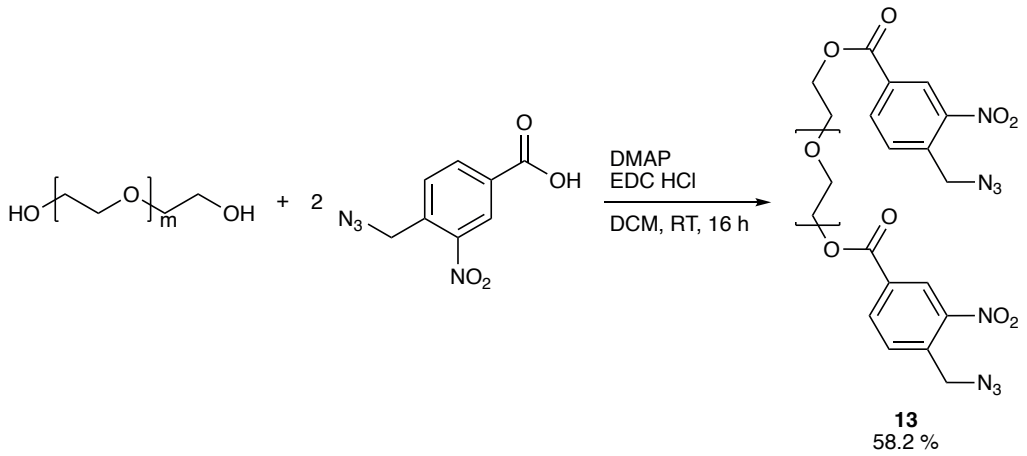
	M [g/mol]	n [mmol]	m [g]	V [mL]	eq.
BNBA	260.04	17.5	4.55		1.0
NaN_3	65.01	26.3	1.71		1.5
acetone				20.0	
water				5.00	

4-Bromomethyl-3-nitrobenzoic acid (BNBA, 4.55 g, 17.5 mmol, 1.0 eq.) was dissolved in acetone (20 mL) and cooled to 0 °C. A solution of sodium azide (NaN_3, 1.71 g, 26.3 mmol, 1.5 eq.) in water (5 mL) was0 added and reaction mixture was stirred at room temperature for 24 hours.

Afterwards, reaction mixture was stored at 4 °C for one week and during this time a white solid was precipitated. This was filtered off and dried under reduced pressure. The azide substituted product was obtained as a white solid (1.46 g, 6.58 mmol, 37.6 %).

^{1}H-NMR (400 MHz, DMSO$-d_6$): δ = 8.50 (d, J = 1.58 Hz, 1 H), 8.25 (dd, J = 7.90 Hz, J = 1.61 Hz, 1 H), 7.75 (d, J = 7.95 Hz, 1 H,), 4.90 (s, 2 H).

3.4.13 PEG 1500 bis(4-(azidomethyl)-3-nitrobenzoate) 13



13
58.2 %

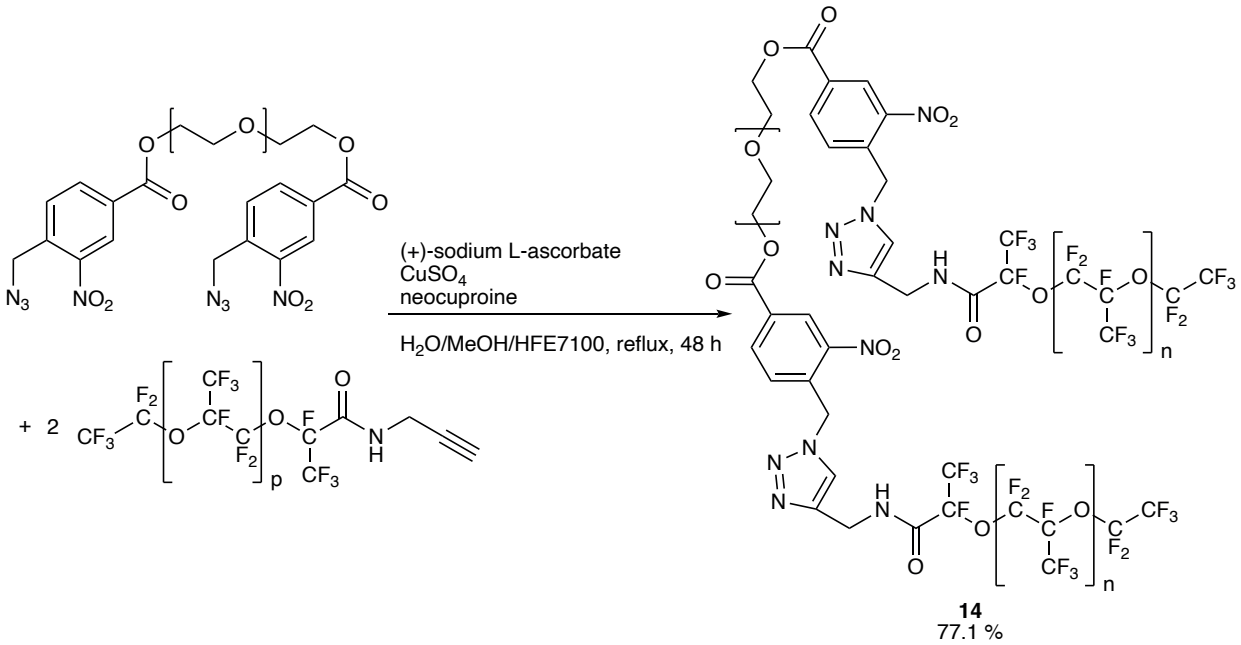
	M [g/mol]	n [mmol]	m [g]	V [mL]	eq.
PEG 1500	1500	2.48	3.71		1.0
12	222.16	5.45	1.21		1.0
DMAP	122.17	1.24	151 mg		0.5
EDC HCl	191.70	6.19	1.19		2.5
DCM				13/6/6	

PEG 1500 (3.71 g, 2.48 mmol, 1.0 eq.), **12** (1.21 g, 5.45 mmol, 1.0 eq.) and 4-(dimethylamino)pyridine (DMAP, 151 mg, 1.24 mmol, 0.5 eq.) were dissolved in dry dichlormethane (DCM, 13 mL) using a flame-dried Schlenk flask. In a further flame-dried Schlenk flask 1-ethyl-3-(3-dimethylaminopropyl)carbodiimide hydrochloride (EDC HCl, 1.19 g, 6.19 mmol, 2.5 ew.) was suspended in dry DCM (6 mL) and transferred to reaction mixture. After addding additional DCM (6 mL) reaction mixture was stirred at room temperature for 16 hours.

Afterwards, solvent was removed under reduced pressure and crude product was suspended in diethyl ether. Suspension was sonicated for 5 minutes and filtered. Precipitate was dissolved in DCM and washed three times with brine (each 10 mL). Aqueous phase was extracted two times with DCM (each 10 mL) and combined organic phase was dried over magnesium sulfate. After filtering through Celite, solvent was removed under reduced pressure. The functionalized PEG was obtained as brown solid (2.75 g, 1.44 mmol, 58.18 %).

^{1}H-NMR (400 MHz, DMSO−d_6): δ = 8.52 (s, 2 H), 8.32 (d, J = 7.31 Hz, 2 H), 7.90 (d, J = 8.03 Hz, 2 H), 4.98 (s, 4 H), 4.49-4.45 (m, 8 H), 3.79-3.77 (m, 10 H), 3.60-3.50 (m, 401 H).

3.4.14 Photoliable, clicked triblock surfactant PFPE7000-NB-PEG1500-NB-PFPE7000 14



	M [g/mol]	n [mmol]	m [g]	V [mL]	eq.
13	1940	1.44	2.79		1.05
5	6790	2.74	19.3		2.0
Na ascorbate	198.11	549 µmol	109 mg		0.4
$CuSO_4 \cdot 5\,H_2O$	249.69	274 µmol	68.4 mg		0.2
Neocuproine	208.26	439 µmol	91.4 mg		0.32
H_2O				8	
MeOH				8	
Novec 7100				16	

5 (19.3 g, 2.74 mmol, 1.0 eq.) was dissolved in HFE 7100 (Novec 7100, 16 mL). **13** (2.79 g, 1.44 mmol, 1.05 eq.), sodium ascorbat (109 mg, 549 µmol, 0.4 eq.), copper(II) sulfate pentahydrate (68.4 mg, 274 µmol, 0.2 eq.) and neocuproine (91.4 mg, 439 µmol, 0.32 eq.) were dissolved in methanol (8 mL) and water (8 mL). Both solutions were mixed and stirred under reflux for 48 hours.

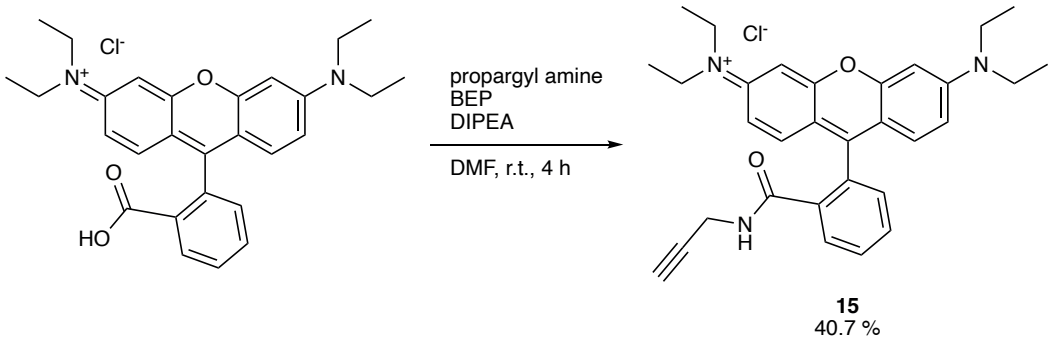
After finishing reaction mixture was cooled down to room temperature and EDTA solution (100 mM, 6 mL) was added. Reaction mixture was filtered through Celite and transferred into a speration funnel. It was carefully overlaid with methanol and swivelled without mixing. Methanol phase became orange and was replaced by fresh methanol. This procedure was repeated until the methanol phase was not orange

anymore. Fluorinated phase was dried over magnesium sulfate and filtered, first though Celite followed by through PFTE syringe filter (0.45 µm). Solvent was removed under reduced pressure. The photoliable surfactant was obtained as red-brown, viscous oil (17.75 g, 1.11 mmol, 77.14 %).

As NMR solvent, a mixture of C_6F_6:C_6D_6 88:12 was used.

^{1}H-NMR (400 MHz, C_6D_6): δ = 8.69 (br s, 2 H), 8.59 (d, J = 1.28 Hz, 2 H), 8.33 (br s, 2 H), 8.18 (dd, J = 1.34 Hz, J = 8.27 Hz, 2 H), 7.72 (s, 2 H), 6.19-6.05 (m, 2 H), 4.82-4.74 (m, 4 H), 4.55 (s, 4 H), 4.03-3.58 (m, 222 H).

3.4.15 Propargyl rhodamine B 15

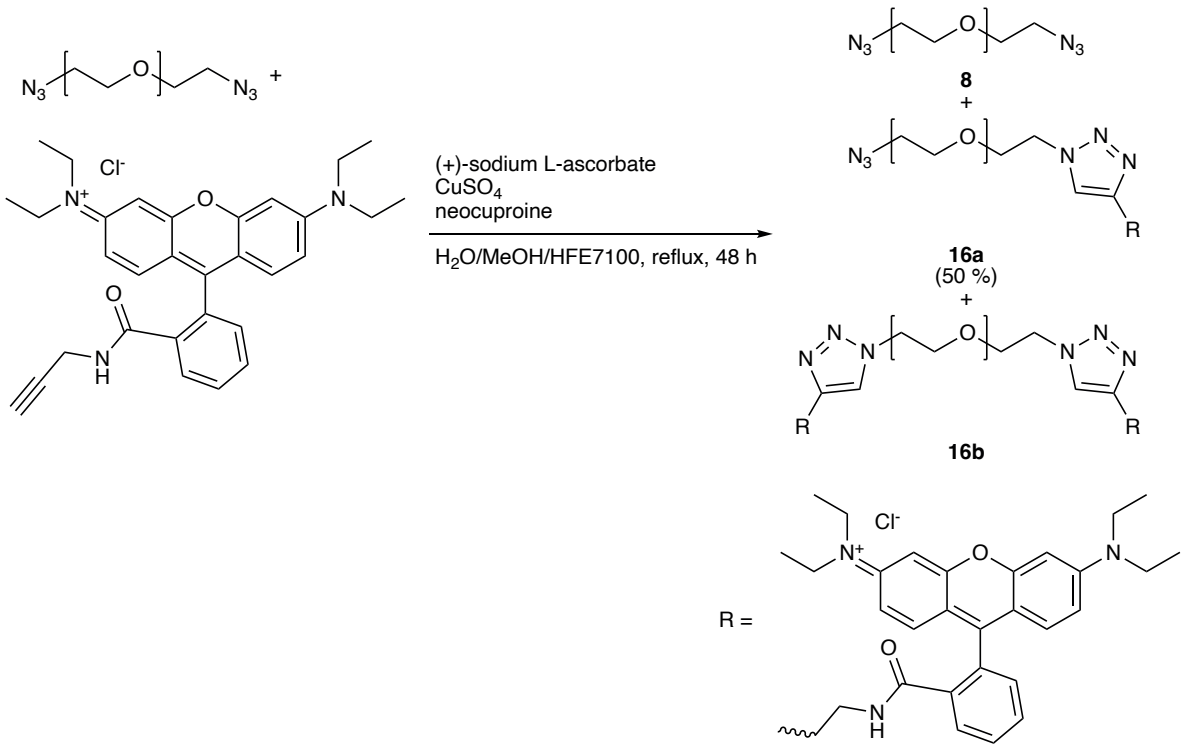


	M [g/mol]	n [mmol]	m [g]	ρ[g/mL]	V [μL]	eq.
rhodamine B	479.02	2.09	1.00			1.0
propargylamine	55.08	2.93	161 μg	0.860	138	1.4
BEP	273.86	4.18	1.14			2.0
DIPEA	129.24	4.18	540 μg	0.742	401	2.0
DMF					10 mL	2.0

Rhodamine (1.00 g, 2.09 mmol, 1.0 eq.) and propargylamine (138 μL, 2.93 mmol, 1.4 eq.) were dissolved in DMF (10 mL). 2-bromo-1-ethyl-pyridinium tetrafluoroborate (BEP) (1.14 g, 4.18 mmol, 2.0 eq.) and *N*,*N*-diisopropylethylamine (DIPEA) (401 μ, 4.18 mmol, 2.0 eq.) were added. The mixtur was stirred for 4 hours at room temperature.

Afterwards, the crude product was purified by flash column chromatography (1 % to 5 % methanol in DCM). The final product was received as pink solid (439 mg, 851 mmol, 40.7 %).

3.4.16 N3-PEG600-RhodB 16a

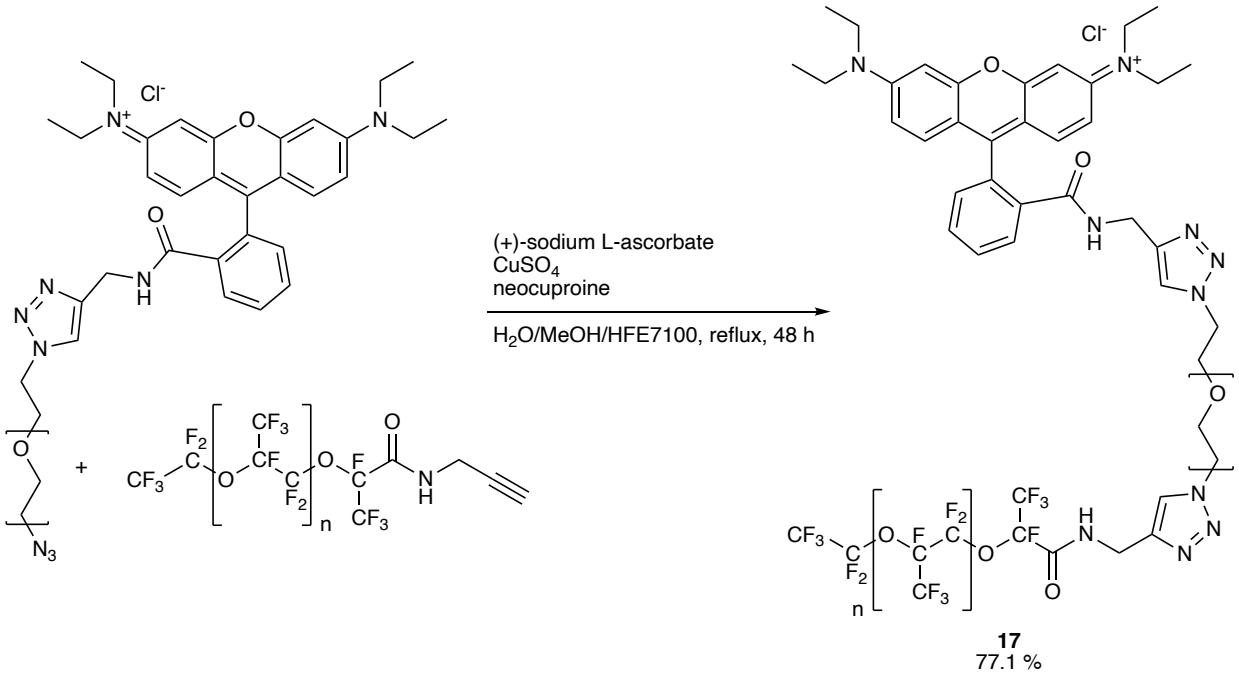


	M [g/mol]	n [mmol]	m [mg]	V [mL]	eq.
8	650	1.54	1.00 g		1.0
15	516.08	1.54	795		1.0
Na ascorbate	198.11	3.08	610		2.0
$CuSO_4 \cdot 5\,H_2O$	249.69	1.54	384		1.0
H_2O				7.40	

A solution of **8** (1 g, 1.54 mmol, 1.0 eq.) and **15** (795 mg, 1.54 mmol, 1.0 eq.) in water (7.4 mL) was sonicated until both substances were completely dissolved. Sodium ascorbate (610 mg, 3.08 mmol, 2.0 eq.) was added and stirred for five minutes before copper(II) sulfate pentahydrate (384 mg, 1.54 mmol, 1.0 eq.) was added. Reaction mixture was stirred at room temperature for 24 hours.

After filtering reaction mixture through Celite, the aqueous phase was washed three times with DCM (each 15 mL) and solvent was removed under reduced pressure. The pink substance consisted of one-end funcionalized **16a**, both-end functionalized **16b** as well as starting materials salts, and was directly used for next synthesis step.

3.4.17 Fluorescent, clicked diblock surfactant PFPE7000-PEG600-RhodB 17



	M [g/mol]	n [mmol]	m [mg]	V [mL]	eq.
16a	1165	(770)	(897)		1.05[2]
5	6790	733	4.98 g		1.0
Na ascorbate	198.11	147	29.1		0.2
$CuSO_4 \cdot 5\,H_2O$	249.69	73.3	5.2		0.1
Neocuproine	208.26	117	24.4		0.16
H_2O				2.5	
MeOH				2.5	
Novec 7100				5.0	

5 (4.98 g, 733 g, 1.0 eq.) was dissolved in HFE 7100 (Novec 7100, 5.0 mL). **16a** (from last synthesis step), sodium ascorbat (29.1 mg, 147 µmol, 0.2 eq.), copper(II) sulfate pentahydrate (5.2 mg, 73.3 µmol, 0.1 eq.) and neocuproine (24.4 mg, 117 µmol, 0.16 eq.) were dissolved in methanol (2.5 mL) and water (2.5 mL). Both solutions were mixed and stirred under reflux for 48 hours.

Afterwards, reaction mixture was cooled down to room temperature, an aqueous EDTA solution (100 mM, 1 mL) was added and whole solution was transferred into a separation funnel. It was overlaid with methanol (20 mL) and carefully swivelled.

[2]Theoretical calculated amount of **16a** based on a qunatitative yield.

The pinkish colored methanol phase was replaced by fresh methanol. This procedure was repeated until the methanol was not pink anymore. The fluorinated phase was dried of magnesium sulfate, filtered through Celite and again filtered PTFE syringe filter (0.45 µm). Solvent was removed under reduced pressure. The fluorescent diblock surfactant was received as pink, viscous oil (4.72 g, 593 µmol, 77.1 %).

3.4.18 Other synthesis instructions

Silica bead functionalization with amine group bearing silanes

The synthesis of silane functionaliced silica beades was adopted from Jochyms *et al.*[178] As silane (3-Aminopropyl)trimethoxysilane (APTMS) or N^1-(3-Trimethoxysilylpropyl)-diethylenetriamine (TRI-silane) was used.

Silica gel (pore size of 60 Å, 500 mL) was dried for two hours at 150 °C. Then, a mixture of dry toluene (450 mL) and silane (50 mL) was added to the cooled-down beads while shaking. The mixture was stirred for two hours. The functionalized silica gel was filtered and washed thoroughly with ethanol. After drying them over night at 80 °C, the amine functionalized silica gel was ready for use as flash column chromatography resign.

The successful functionalization could be proofed by ninhydrin assay.

3.5 Methods

3.5.1 Analytical methods

PFPE partition experiment

The method was adopted from Riechers *et al.* and Haller *et al.* and modified for more reproducible results.[96,179,180]

To create the calibration curve, a 10 mM stock solution of PFPE in HFE 7500 was diluted from 0.0 to 1.0 mM in 0.1 mM steps to receive 100 µL of each concentration and placed respectively in a 200 µL reaction tube. This was repeated two times to get triplicates of the calibration measurement. Each sample was overlayed with 100 µL of a aqueous 1 mM Rhodamine 6G solution and stored for 48 hours cooled and protected from light. After the incubation, 10 µL of each phase were diluted in 90 µL of the corresponding solvent in a 96 well plate. The absorbance was measured at 530 nm and the fluorescence at 565 nm with an excitation at 530 nm. The results of each solvent system (HFE 7500, water) and each type of measurement (absorbance, fluorescence) were plotted separately, a calibration curve was fitted and the coefficient of determination R^2 was calculated. The calibration curve with the highest R^2 value was used for further calculation.

For the determination of PFPE in the surfactants, 100 µL of a 2.5 mM surfactant solution in HFE 7500 were placed in a 200 µL reaction tube and overlayed with 100 µL of a aqueous 1 mM Rhodamine 6G solution. The samples were prepared in triplicates. They were incubated for 48 hours protected from light. Afterwards, 10 µL from each of the two phases were diluted in 90 µL the corresponding solvent and pipetted into a 96

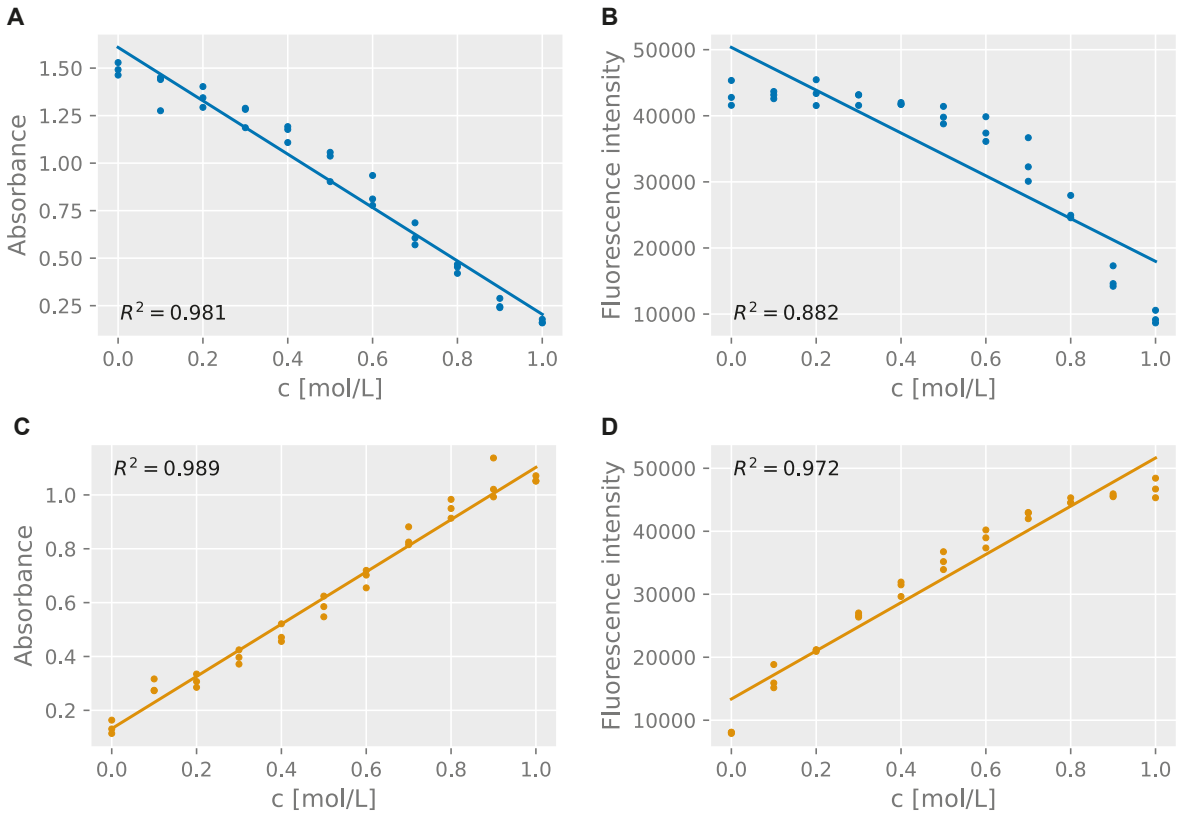


Figure 3.1: As part of an partition experiment to determine the concentration of PFPE in surfactants, calibration curves under different conditions where calculated. The amount of transferred Rhodamine 6G into the oil phase was determined ether in the water (A and B) or in the HFE 7500 phase (C and D) using ether absorbance (A and C) or fluorescence (B and D). The curve with the R^2 value closest to one, in this case absorbance in HFE 7500, was used for further calculations.

well plate. For each well, the absorbance was measured at 530 nm and the fluorescence at 565 nm with an excitation at 530 nm.

The concentration of PFPE c_{PFPE} was calculated using the measured absorbance or fluorescence intensity I and the intercept n and slope m of calibration curve:

$$c_{PFPE} = \frac{I - n}{m}$$

With the molecular mass of PFPE M_{PFPE} and the solvent volume V, the mass fraction of PFPE w_{PFPE} respectively the mole fraction x_{PFEP} in the balanced surfactant mass $m_{balanced}$ could be determined:

$$m_{PFPE} = c_{PFPE} * V * M_{PFPE}$$

$$w_{PFPE} = \frac{m_{PFPE}}{m_{balanced}}$$

$$x_{PFPE} = \frac{\frac{m_{PFPE}}{M_{PFPE}}}{\frac{m_{PFPE}}{M_{PFPE}} + \frac{m_{balanced} - m_{PFPE}}{M_{surfactant}}}$$

Quantitative mass spectrometry

For the analysis of lipid mixture consisting of 20.0 mol% cholesterol, 36.0 mol% DOPC, 20 mol% DOPG, 23 mol% 18:1 SM and 1 mol% Liss Rhod PE, two samples of lipids in low absorption vial (Certified Vial Kit, Low Adsorption) were prepared for creating a 500 μL of a 6.0 mM lipid solution. For both vials, the chloroform was removed for one hour under reduced pressure. Afterwards, one sample was dissolved in 500 μL HPLC-grad methanol. Together with the Standard (EquiSplash, Avanti Polar Lipids) the before extruder sample and thus the reference sample was created.

To the other sample, 500 μL HPLC-grad water was added, shaked for 30 minutes and extruded (Extruder Kit from Avanti Polar Lipids, 0.2 μm polycarbonate membrane). From this solution, the sample for after extrusion was created. 100 μL lipid solution and 200 μL HFE 7500 were shaken for 15 minutes and the separated aqueous phase used for creating the HFE sample.

The extruded lipids were used to produce GUVs as described in Chapter 3.5.2 (50) using either 2.5 mM cTS **6**, 5 mM posDS **11** or 1.4 w/v% CS. The respective samples were created by combining 20 μL GUV solution + 50 μL 1:100 Equi Splash + 930 μL HPLC-grad ACN.

The respective samples created following this pipetting scheme:

- Lipids (6000 μM to 1.2 μM):

  - 1:100: 990 µL HPLC-grad ACN + 10 µL lipids
  - (1:50: 980 µL HPLC-grad ACN + 20 µL 1:100 lipids)

- Equi Splash (100 µg/mL to 50 ng/mL):
  - 1:100: 990 µL HPLC-grad ACN + 10 µL Equi Splash
  - (1:20: 950 µL HPLC-grad ACN + 50 µL 1:100 Equi Splash)

- Sample: 20 µL 1:100 lipids + 50 µL 1:100 Equi Splash + 930 µL HPLC-grad ACN

Each sample was produced and measured in triplicates. The measurments were performed on µ-LC Eksigent 425 (Bruker).

3.5.2 Generation of synthetic cells

General microfluidic chip production

Silicon wafers with the corresponding negative of structure were produced by Dr. Christoph Frey and Dr. Sadaf Pashapour.

For PDMS imprint, monomer and current agent from PDMS kit (SYLGARD 184 ELASTOMER KIT) were properly mixed in a ratio 10:1. The silicon wafer with device structures was placed in a Petri dish and covered with monomer-current agent-mix. To remove air bubbles, which would disturb during usage of the device later, the Petri dish was placed in a desiccator under reduced pressure for 30 minutes. After some minutes, the mixture started to lather. As soon as the foam threatened to go over the edge of Petri dish, vacuum pumping was interrupted and after foam was reduced, started again. Degassed mixture was polymerised for at least four hours at 70 °C. Afterwards, the PDMS imprint was carefully cut out using a scalpel ([scalpel type must be added]). For connection with tubings, inlets and outlets of the device were punched using the 0.5 mm in diameter puncher (Rapid-Core Disposable Microfluidic Punches, 0.5 mm) and functional surface of the device was cleaned with sticky tape. For glass surface, cover slides from ??? ([cover slides must be added]) were used. To clean them, they were covered with ethanol, sonicated for 10 minutes and dried with an air gun. During this procedure, plasma machine ([which plasma machine]) was turned on using oxygen plsama with a pressure of 0.5 mbar and a power of 200 W for 10 minutes. Then, cleaned cover slide and PDMS device, with structure up, were placed on a sample holder and treated with oxygen plasma at a pressure of 0.5 mbar and a power of 200 W for 30 seconds. Directly afterwards, the PDMS device was pressed on the activated surface of the cover slide, ensuring to remove air bubbles between PDMS and glass. For the covalent binding, the microfluidic chip was stored over night at 70 °C. As a last step, the channels of the chips needed to be passivated to reduce the hydrophilicity of PDMS.

Therefore, [SigmaCoat oder Ombrello?] was carefully injected with a syringe connected with chip via PTFE tubing (BOLA Tubing, PTFE, 0.3 mm x 0.6 mm, t=0.15). After a incubation of five minutes, the device was ready to use.

Picoinjection chip production

The chips were produced as described in section before. In addition, the electrodes needed to be melted into the chip. Therefore, during the production process, the inlets for the electrodes were punched with a diameter of 0.75 mm instead. After the PDMS imprint and cover slide were connected and the channels were passivated, the device was heated up to 90 °C on a heating plate. Then, indium alloy wire, with a low melting temperature, was slightly pressed into the electrode channel. The wire started to melt and floated into the channel. With a little bit of pressure, channel and outlet were completely filled. In each, inlet and outlet, an electrical cable with stripped ends (approximately 5 mm) was plugged into. The same procedure was repeated for the other electrode channel. Afterwards, the chip was cooled down to room temperature. To stabilize the cables more, a drop of UV curing glue was placed on each connection and polymerized for 10 min using a UV lamp. The connectivity was tested by electrical resistance measurement.

GUV generation

For the generation of GUVs, the lipid solutions in chloroform or methanol were combined in a low absorption vial (Certified Vial Kit, Low Adsorption) according to aimed lipid composition and ratio, keeping the stock solutions at -20 °C. Afterwards, solvent was removed under reduced pressure in a desiccator for at least 30 minutes. Buffer was added and the lipid layer was allowed to swell, followed by shaking to generate multilamellar vesicles. To receive unilamellar vesicles with small size distribution, the vesicle solution was extruded (Extruder Set from Avanti Polar Lipids), and the size can be affected by the PC membrane used (Polycarbonate Membrane 0.2 μm). Size distribution and surface charge were determined by dynamic light scattering (DLS) measurment.

In a second step, dsGUVs were produced using droplet-based microfluidics or emulsification. For both methods, the SUV stock solution and additional components (proteins, salts and specific buffers) were used to prepare the aqueous inner phase. The oil phase consists unless otherwise specified of 2.5 mM **6** and 10 mM PFPE (KRYTOX 157 FSH) in HFE 7100 (Novec 7100).

For w/o droplet production with microfluidics, a droplet production microfluidic chip was used. It was connected to the pressure controller with PTFE tubing (BOLA

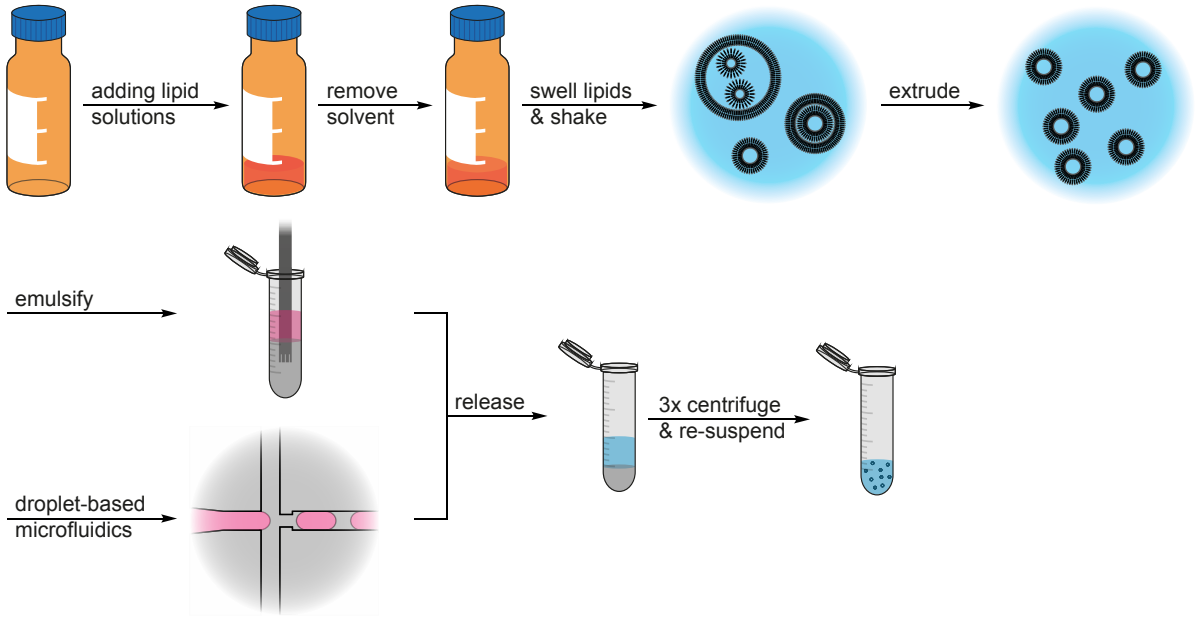


Figure 3.2: Stepwise description of the process of constructing GUVs. After mixing lipids in the wished ratio and solvent was removed under reduced pressure, the lipid layer was swelled and removed from glas bottle by mixing. The received multidisperse, multilamellar vesicles were extruded to obtain SUVs. Either emulsification or droplet-based microfluidics were used to produce dsGUVs. After realising them, only three further steps of purificaion were needed to receive the synthetic vesicles.

Tubing, PTFE, 0.3 mm x 0.6 mm, t=0.15). Before starting the procedure, both phases were filtered through a centrifugal filter (0.45 µm pore size). To start, first the oil channel was started and degassed applying 500 mbar. Instantly when oil was flowing into the device, the water channel was set to 500 mbar, too. As soon as both channels were degassed, the pressures were regulated that droplet of the aimed size were produced (approximately 1500 mbar for the oil channel and 1100 mbar for the water channel).

Another method used to produce w/o droplets is an emulsifier (IKA T10 basic Ultra-Turrax). Therefore, 1.0 mL of oil phase were presented, then 500 µL aqueous phase were added. Then, the mixture was emulsified for three minutes as level one. During this process, the vial with the mixture was moved up and down to ensure even dispersion.

Independent to the method, the emulsion was afterwards stored for 12 hours at 4 °C. The excess oil was removed and the same amount of release buffer was added as for the inner phase. And the same amount of destabilizing surfactant (1H,1H,2H,2H-perfluoro-1-octanol) was added, the vial closed and carefully rotated transversely about the horizontal axis. After most separation, vial was stored for at least 30 minutes at 4 °C. Then, 75–90 % of the aqueous solution was carefully pipetted into a new Eppendorf vial ensuring doing without transfering oil phase. To ensure that no oil droplets were transferred too, the vial was shortly centrifuged with a table centrifuge before removing

the aqueous phase. The vial was completely filled with release buffer and centrifuged for one hour at 21,000 xg (1,000 xg if glucose-sucrose gradient is used) until a dye dependent colored GUV pallet was visible. Afterwards, supernatant was replaced by fresh release buffer, pellet re-suspended and centrifuged under the same conditions. For the last step, the pellet was re-suspended in a smaller amount of release buffer to a concentration needed for the according experiment.

Laminin capsules formation

Implementing various droplet-based microfluidics devices allowed us to generate empty or cargo-filled protein droplets. The assembly of proteins at the periphery of droplets is purely based on electrostatic interactions. A single inlet microfluidic device is used to generate empty protein droplets. 5 mM of positively-charged diblock surfactant (posDS) **11** surfactant is diluted in HFE 7500 and used as the positively charged oil phase, while the aqueous phase consists of 0.77 μM laminin-111 with 10 % labelled laminin-111 and 10 mM calcium chlorid mixed in phosphate-buffered saline (PBS). By setting the oil flow rate to 600 μL/h and the aqueous inlet to 300 μL/h, we could produce droplets with 30 μm in diameter. To generate cell-laden droplets, a pico-injection device was implemented to reduce cell-protein interactions prior to their encapsulation. Hereby, the droplets were produced on chip with the previously described flow rates. The oil and aqueous conditions were also not altered. By integrating an electric field (900 V, 900 kHz) it was possible to inject single cells into already established droplets. To encapsulate *E. coli* into protein droplets we could make use of a more straightforward design, namely a double inlet production device. Here, two aqueous phases flow in parallel before being encapsulated by the oil phase. The oil phase was used as stated previously, the protein concentration, however, had to be increased to 1.17 μM laminin-111 with 20 mM calcium chloride. *E. coli* were diluted in LB media at an OD of 1.7 nm and encapsulated with the proteins.

Biotin-streptavidin-mediated GUV-GUV interactions

GUVs consisting of 49 % EggPG, 49 % EggPC, 1 % Biotinyl Cap PI, 1 % Liss Rhod PE were produced as described in Chapter 3.5.2 (page 50) using the microfluidic approach. Therefore, 500 μL of aqueous phase (0.8 mM lipids, 15 mM magnesium chlorid, 10 mM sucrose in PBS) and 1.0 mL of fluorinated phase (2.5 mM eTS **1**, 10 mM Krytox in HFE 7500) were prepared.

After incubation for 12 hours, GUVs were released into 500 μL of release buffer (15 mM magnesium chloride, 10 mM glucose in PBS) and purified to a final volume of 200 μL. This volume was equally split in two samples and in one, streptavidin (with

1 % ATTO 425-labeled streptavidin) was added to a final concentration of 0.1 mg/mL. Both samples were shaken over night at 4 °C and imaged with an inverted confocal microscope LSM800 (Zeiss).

GFP (His tag) functionalization of NTA- and PEG-containing GUVs

GUVs consisting of 30 % DOBAQ, 6 % DOPE, 20 % DOPS, 38.5 % DOPC, 1 % 18:1 DGS-NTA, 4 % 18:1 PEG PE and 0.5 % Liss Rhod PE with molecular PEG weight of 350, 750, 1000 and 2000 g/mol were produced as described in Chapter 3.5.2 (page 50) using the microfluidic approach. Therefore, 500 μL of aqueous phase (2.0 mM lipids, 30 mM Tris pH 7.4, 140 mM potassium chloride and 100 mM sucrose) for each PEG and 1.0 mL of fluorinated phase (2.5 mM cTS **6**, 10 mM Krytox in HFE 7500) were prepared.

After incubation for 12 hours, GUVs were released into 500 μL of release buffer (30 mM Tris pH 7.4, 140 mM potassium chloride and 100 mM glucose) and purified to a final volume of 200 μL for each PEG. Each volume was equally split in two samples and, to one, nickel(II) chloride was added to final concentration of 1.0 mM and incubated for 30 minutes. To the nickel(II) ion containing samples, 1.0 mL of release buffer was added and centrifuged for one hour at 1000 rmp, supernatent removed and re-suspended in 100 μL release buffer. To all samples, His tag GFP was added to a final concentration of 10 μg/mL and incubated over night at 4 °C. Afterwards, they were imaged with an inverted confocal microscope LSM800 (Zeiss).

E-cadherin-mediated GUV-GUV interactions

GUVs consisting of 30 % DOBAQ, 6 % DOPE, 20 % DOPS, 38.5 % DOPC, 1 % 18:1 DGS-NTA, 4 % 18:1 PEG2000 PE and 0.5 % Liss Rhod PE were produced as described in Chapter 3.5.2 (page 50) using the emulsification approach. Therefore, 8.0 mL of aqueous phase (2.0 mM lipids, 30 mM Tris pH 7.4, 140 mM potassium chloride and 100 mM sucrose) and 16 mL of fluorinated phase (2.5 mM cTS **6**, 10 mM Krytox in HFE 7500) were prepared. 2.0 mL of aqueous phase and 4.0 mL of fluorinated phase were placed into a 15 mL flacon and emulsified for three minutes at level 1. This procedure was repeated three times.

After incubation for 12 hours, GUVs were released into 2.0 mL of release buffer (30 mM Tris pH 7.4, 140 mM potassium chloride and 100 mM glucose) respectively. Before centrifugation, to half of the released GUVs, nickel(II) ions were added to a final concentration of 1 mM and incubated for 30 minutes. Afterwards, the GUVs were purified to a final volume of 1.2 mL of GUVs with nickel(II) ions and 1.2 mL of GUVs without nickel(II) ions. Each sample was equally split into two samples adding 100 μL

of 0.25 mg/mL reconstituted E-cadherin solution to one of them. The four samples were incubated for one hour at 4 °C.

In parallel, 24 wells of a 96-well microplate were passivated using a 1 mg/ml BSA solution and incubated for 30 minutes. Then, the protein solution was removed and the wells were dried with an air gun.

Each condition was divided into six wells, each containing 100 μL. To three of these six wells, calcium ions were added to a final concentration of 10 mM. The well plate was shaken with 300 rpm at 4 °C over night. Before imaging, the GUVs were let to settle down for one hour. Afterwards, the complete wells were imaged at the inverted fluorescent microscope DMi8 (Leica) and Z-stack images of representative areas were acquired on the inverted confocal microscope LSM800 (Zeiss).

The whole procedure was repeated with GUVs consisting of 30 % DOBAQ, 6 % DOPE, 20 % DOPS, 38.5 % DOPC, 1 % 18:1 DGS-NTA, 4 % 18:1 PEG2000 PE and 0.5 % ATTO 488 DOPE.

Integrin reconstitution

SUVs consisting of 30 % DOTAP, 70 % DOPC, if not mention differently, were produced as described in Chapter 3.5.2 (page 50). Using purified integrin $\alpha_{\mathrm{IIb}}\beta_3$ and the SUVs, 250 μL aqueous solution with a final concentration of 300 μM lipids, 3.0 μM integrin, 30 mM Tris pH 7.4, 140 mM sodium chloride, 1.0 mM calcium chloride, 0.1 v/v% Triton X-100. They were incubated for three hours at 37 °C shaking with 300 rpm.

Sephadex-G50 resin fine was swelled with 30 mM tris(hydroxymethyl)aminomethane (Tris) at pH 7.4, 50 mM sodium chloride, 90 mM potassium chloride and 0.5 mM calcium chloride for at least three hours. The resin was loaded in a 2 mL syringe with a glass wool-filter. Excess of swelling buffer was removed by centrifugation at 1000 xg for three minutes. The Triton X-100 containing proteoliposoms were carefully added and filtered through the resign by centrifuging 10 minutes at 50 xg. Then, the purified proteoliposoms were eluted by centrifugation at 1000 xg for three minutes.

The efficiency of the Triton X-100 removal was proofen by measuring the absorbance at 276 nm in a quartz 96 well microplate.[181]

GUVs consisting of 30 % DOBAQ, 6 % DOPE, 20 % DOPS, 38.5 % DOPC, 1 % 18:1 DGS-NTA, 4 % 18:1 PEG2000 PE and 0.5 % Liss Rhod PE were produced as described in Chapter 3.5.2 (page 50) using the emulsification approach. Therefore, 500 μL of aqueous phase (2.0 mM lipids, 30 mM Tris pH 7.4, 140 mM potassium chloride and 100 mM sucrose) and 1.0 mL of fluorinated phase (2.5 mM cTS **6**, 10 mM Krytox in HFE 7500) were used. After incubation for 12 hours, the GUVs were released into 500 μL of release buffer (30 mM Tris pH 7.4, 140 mM potassium chloride, 1.0 mM calcium chloride and 100 mM glucose) and purified to a final volume of 200 μL.

To fuse the proteoliposoms with the GUVs, 1.25 μL of 100 μM of fusion DNA A (5'-TCG ACA CGG AAA TGT TGA ATA CTA-3') was added to 50 μL of GUV solution, and 1.25 μL of 100 μM of fusion DNA A' (5'-TAG TAT TCA ACA TTT CCG TGT CGA-3') was added to 50 μL of proteoliposoms, incubating for 30 minutes at 37 °C. GUVs and proteoliposomes were combined and incubated over night at 37 °C shaking at 300 rpm.

To prepare the functionalized surface, a with ethanol re-cleaned glass coverslip was activated in a plasma machine to clean and charge the surface.[182] The coverslip was covered with 0.1 mg/mL fibrinogen (for the control experiments, 0.1 mg/mL poly-L-lysine (PLL)-PEG was used) for 60 minutes and unbound material washed away. The silicone chamber of the ibidi "12 Well Chamber, removable" chamber slide was glued with two-component glue on the functionalized glass coverslip. The integrin reconstituted GUVs mixed in ratio 4:1 with 30 mM Tris at pH 7.4, 100 mM glucose, 50 mM sodium chloride, 90 mM potassium chloride, 2.5 mM calcium chloride, 5.0 mM magnesium chloride and 5.0 mM manganese(II) chloride to receive the integrin activation buffer (30 mM Tris at pH 7.4, 100 mM glucose, 50 mM sodium chloride, 90 mM potassium chloride, 1.0 mM calcium chloride, 1.0 mM magnesium chloride and 1.0 mM manganese(II) chloride). The GUVs were let to settle down and adhere to the surface for two hours. Afterwards, they were imaged with an inverted confocal microscope LSM800 (Zeiss).

Integrin $\alpha_{\mathrm{IIb}}\beta_3$ were purified by Cornelia Weber and Raimund Jung.

Actin encapsulation

For the reconstitution of actin filaments, three solution were prepared: 100 μL actin mix (25 μM G-actin, 30 mM Tris pH 7.4, 140 mM sodium chloride, 1.0 mM calcium chloride, 6 w/v% OptiPrep), 100 μL polymerisation mix (3.0 mM lipids, 30 mM Tris pH 7.4, 40 mM sodium chloride, 100 mM potassium chloride, 1 mM calcium chloride, 4 mM magnesium chloride, 2 mM ATP) and 400 μL fluorinated oil phase (2.5 mM cTS **6**, 10 mM Krytox in HFE 7500).

For the microfluidic droplet production, the device shown in Figure 4.28 (106) is used. The left inlet was connected with the fluorinated oil phase, the middle one with polymerisation mix and the right one with actin mix. Droplets were produced using pressure controller (OB1 MK3+ microfluidic flow controller from Elveflow) regulating the flow (used pressures: 590 mbar for actin mix, 550 mbar for polymerisation mix and 640 mbar for fluorinated phase).

After incubation for 12 hours, GUVs were released into 200 μL of release buffer (30 mM Tris pH 7.4, 140 mM sodium chloride, 1 mM calcium chloride and 100 mM glucose) and iimaged with an inverted confocal microscope LSM800 (Zeiss).

DNA-mediated GUV-GUV interactions

GUVs consisting of 30 % DOBAQ, 6 % DOPE, 20 % DOPS, 39.5 % DOPC, 4 % 18:1 PEG2000 PE and 0.5 % Liss Rhod PE were produced as described in Chapter 3.5.2 (page 50) using the emulsification approach. Therefore, 2.0 mL of aqueous phase (2.0 mM lipids, 30 mM Tris pH 7.4, 140 mM potassium chloride and 100 mM sucrose) and 4.0 mL of fluorinated phase (2.5 mM cTS **6**, 10 mM Krytox in HFE 7500) were prepared. Aqueous phase and Fluorinated phase were placed into a 15 mL flacon and emulsified for three minutes at level 1.

In parallel, 6 wells of a 96-well microplate were passivated using a 1 mg/ml BSA solution and incubated for 30 minutes. Then, the protein solution was removed and the wells were dried with an air gun.

After incubation for 12 hours, GUVs were released into 2.0 mL of release buffer (30 mM Tris pH 7.4, 140 mM potassium chloride and 100 mM glucose) and purified to a final volume of 600 μL. The sample was equally split into two samples adding 10 μL of 100 μM palindromic DNA solution (sequence 1: `TGA AGT TTA ATT AAA CTT CAG GCC ATC GTC GCT ATA TAT ATA TAT TAT T` with 3'-CholTEG; sequence 2: `TAT AAT ATA TAT ATA TAG CGA CGA TGG C` with 5'-ATTO488) to one of them. Each sample was into three wells, each containing 100 μL. The well plate was shaken with 300 rpm at 4 °C over night. Before imaging, the GUVs were let to settle down for one hour. Afterwards, the complete wells were imaged at the inverted fluorescent microscope DMi8 (Leica) and Z-stack images of representative areas were acquired on the inverted confocal microscope LSM800 (Zeiss).

The whole procedure was repeated with GUVs consisting of 30 % DOBAQ, 6 % DOPE, 20 % DOPS, 39.5 % DOPC, 4 % 18:1 PEG2000 PE and 0.5 % ATTO 488 DOPE.

Experimental method of hybrid system

GUVs consisting of 30 % DOBAQ, 6 % DOPE, 20 % DOPS, 38.5 % DOPC, 1 % 18:1 DGS-NTA, 4 % 18:1 PEG2000 PE and 0.5 % Liss Rhod PE were produced as described in Chapter 3.5.2 (page 50) using the emulsification approach. Therefore, 8.0 mL of aqueous phase (2.0 mM lipids, 30 mM Tris pH 7.4, 140 mM potassium chloride and 100 mM sucrose) and 16 mL of fluorinated phase (2.5 mM cTS **6**, 10 mM Krytox in HFE 7500) were prepared. 2.0 mL of aqueous phase and 4.0 mL of fluorinated phase were placed into a 15 mL flacon and emulsified for three minutes at level 1. This procedure was repeated three times.

After incubation for 12 hours, GUVs were released into 2.0 mL of release buffer (30 mM Tris pH 7.4, 140 mM potassium chloride and 100 mM glucose) respectively. Before centrifugation, to half of the released GUVs, nickel(II) ions were added to a

final concentration of 1 mM and incubated for 30 minutes. Afterwards, the GUVs were purified to a final volume of 1.2 mL of GUVs with nickel(II) ions and 1.2 mL of GUVs without nickel(II) ions. Each sample was equally split into two samples adding 100 μL of 0.25 mg/mL reconstituted E-cadherin solution to one of them. The four samples were incubated for one hour at 4 °C.

These steps was repeated with GUVs consisting of 30 % DOBAQ, 6 % DOPE, 20 % DOPS, 38.5 % DOPC, 1 % 18:1 DGS-NTA, 4 % 18:1 PEG2000 PE and 0.5 % ATTO 488 DOPE and for GUVs consisting of 30 % DOBAQ, 6 % DOPE, 20 % DOPS, 38.5 % DOPC, 1 % 18:1 DGS-NTA and 4 % 18:1 PEG2000 PE and 10 μM Alexa 647 in the inner buffer.

Human embryonic kidney (HEK) 293T cells transfected to express E-cadherin-EGFP (HEK-E) cultured in Dulbecco's modified Eagle's medium (DMEM) with additional 10 % fetal bovine serum (FBS). For the experiment, HEK-E cells were suspended in: 1) DMEM with 1 % FBS, 2) DMEM with 10 % FBS, 3) DMEM with additional 10 mM calcium chloride and 1 % FBS and 4) DMEM with additional 10 mM calcium chloride and 1 % FBS in a concentration of 60,000 cells/mL.

In parallel, all wells of a 96-well microplate were coated using a 0.1 mg/ml fibronectin solution and incubated for 60 minutes. Then, the protein solution was removed.

For each condition in duplicates (GUVs: ± nickel(II) ions, ± E-cadherins, Liss Rhod/ ATTO488/ Alexa647; cells: 1 %/ 10 % FBS, ± calcium ions), 80 μL cell suspension and 20 μL GUV suspendion were combined in one well plate. The wells were imaged every 30 minutes for 24 hours using an inverted confocal microscope LSM980 (Zeiss). After 24 hours, the buffers were refreshed by the respective buffer and the wells were imaged every 30 minutes for 24 hours using an inverted confocal microscope LSM980 (Zeiss).

The HEK 293T cells were transfected by Drs. Jacqueline De Lora and Sadaf Pashapour.

3.5.3 Computational methods

Image analysis of hybrid system experiment

To measure the interaction of GUVs with cells, first cell area and GUV positions were processed and then for each GUV checked, if they are overlaying. For this processing, the scikit-image package for python was used.[183]

To detect cells, the images were first inverted (Figure 3.3B). To receive a binary image, an adaptive threshold was applied on the inverted one (Figure 3.3C).[184] Therefore, each $pixel(x, y)$ was compared with neighboured pixels. Those were defined by

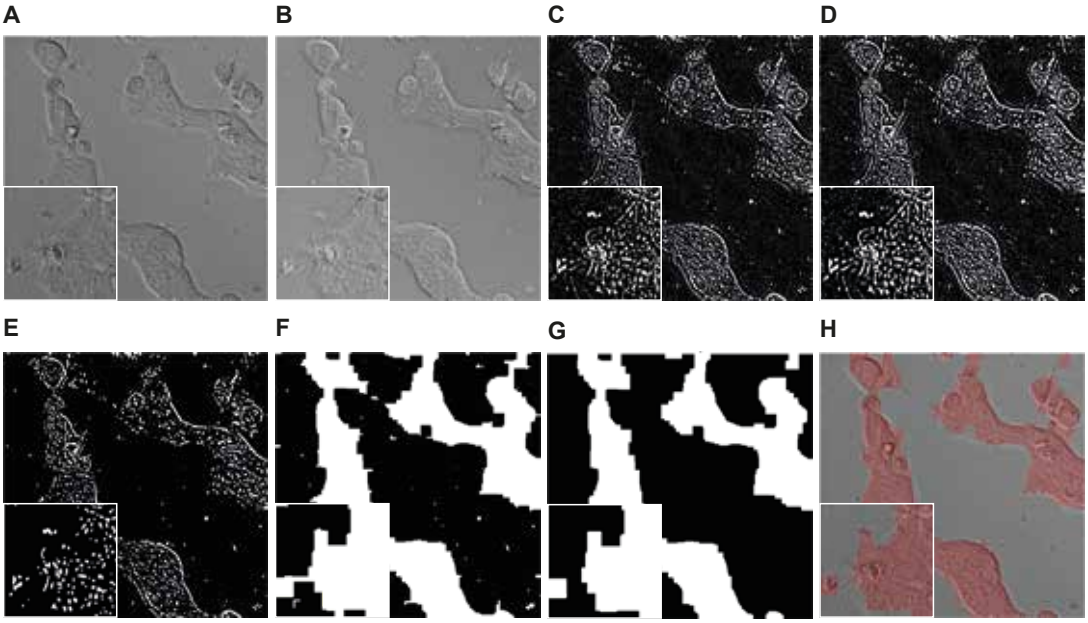


Figure 3.3: Stepwise illustration of cell detection. A: Original bright-field image captured with confocal microscope. B: In a first step, images were inverted. C: Binary images was received after local thresholding with a block size of 35. D: Areas with higher bright area concentration were connected using a dilution algorithm. E: Background signal were removed by opening algorithm. F: With a second closing, bright spots were connected to received the cell area spots. G: In a last step, wrong connections and last background noise was removed by a second opening step. H: Original cell images overplayed with a mask of the calculated area in red.

the block size, where the referred pixel was in the center of this block. The block size was set individual for each experiment and varied between 25 and 41. The threshold value $T(x, y)$ was default sigma calculated by a weighted sum (cross-correlation with a Gaussian window) of the intensity of neighboured pixels. The binary image was calculated by:

$$pixel(x, y) = \begin{cases} 1 & \text{for} \quad pixel(x, y) > T(x, y) \\ 0 & \text{for} \quad otherwise \end{cases}$$

.

Now, the noise from background was removed and the cell area combined. Therefore, closing and openinig algorithms where applied alternating. Closing algorithms first dilate the border of binary images using a specific matrix followed by an erosion using the same matrix. As a result, bright areas, which are close enough, are connected. Opening algorithms first erode and then dilate, so that too small bright areas are removed. During the dilation process, each pixel is checked to see if there is a bright area in its neighbourhood (defined by matrix around the specific pixel), and if so, the pixel is also classified as bright:

$$\begin{bmatrix} 0 & 0 & 0 & 0 & 0 \\ 0 & 0 & 0 & 0 & 0 \\ 0 & 0 & 1 & 0 & 0 \\ 0 & 0 & 0 & 0 & 0 \\ 0 & 0 & 0 & 0 & 0 \end{bmatrix} \xrightarrow[\text{3x3 square}]{\text{dilution}} \begin{bmatrix} 0 & 0 & 0 & 0 & 0 \\ 0 & 1 & 1 & 1 & 0 \\ 0 & 1 & 1 & 1 & 0 \\ 0 & 1 & 1 & 1 & 0 \\ 0 & 0 & 0 & 0 & 0 \end{bmatrix}.$$

During the erosion process, each pixel is checked to see if there is a dark area in its neighbourhood (defined by matrix around the specific pixel), and if so, the pixel is also classified as dark:

$$\begin{bmatrix} 0 & 0 & 0 & 0 & 0 \\ 0 & 1 & 1 & 1 & 0 \\ 0 & 1 & 1 & 1 & 0 \\ 0 & 1 & 1 & 1 & 0 \\ 0 & 0 & 0 & 0 & 0 \end{bmatrix} \xrightarrow[\text{3x3 square}]{\text{erosion}} \begin{bmatrix} 0 & 0 & 0 & 0 & 0 \\ 0 & 0 & 0 & 0 & 0 \\ 0 & 0 & 1 & 0 & 0 \\ 0 & 0 & 0 & 0 & 0 \\ 0 & 0 & 0 & 0 & 0 \end{bmatrix}.$$

To remove the noise, but not losing too much signals from the cell area, first a closing with a small matrix size (2-5) was applied to increase the bright areas (Figure 3.3D), followed by a opening with a small matrix size(2-4) to remove most of the background noise (Figure 3.3E). Now the cell area was closed using a closing with a bigger matrix (30-50, Figure 3.3F). And to remove some wrong connections, a second opening was applied (matrix size 10, Figure 3.3G). The size of each matrix had to be adjusted

individually for each experiment. A range of used matrix sizes were given in brackets in each case.

Next, the GUVs were detected. Here, in a first step the edges were detected using the Sobel transformation.[185] This operator was convolved with the orignal image, once with the horizontal operator and once with vertical operator. The edged images was then calculated by the square root of add squared.

$$\text{Horizontal Sobel operator: } \begin{bmatrix} 1 & 2 & 1 \\ 0 & 0 & 0 \\ -1 & -2 & -1 \end{bmatrix}, \text{ vertical Sobel operator: } \begin{bmatrix} -1 & 0 & 1 \\ -2 & 0 & 2 \\ -1 & 0 & 1 \end{bmatrix}.$$

This transformed images was then processed to a binary image by using the triangle algorithm.[186] It is normalizing height and dynamic range of pixel intensity histogram and calculates the intensity, which has maximum distance between frequency of this intensity and a line between maximum of the histogram and lowest intensity with no frequency. The threshold value is this intensity minus an offset of 0.2. Each region with an intensity higher then this value is defined as region of interest.

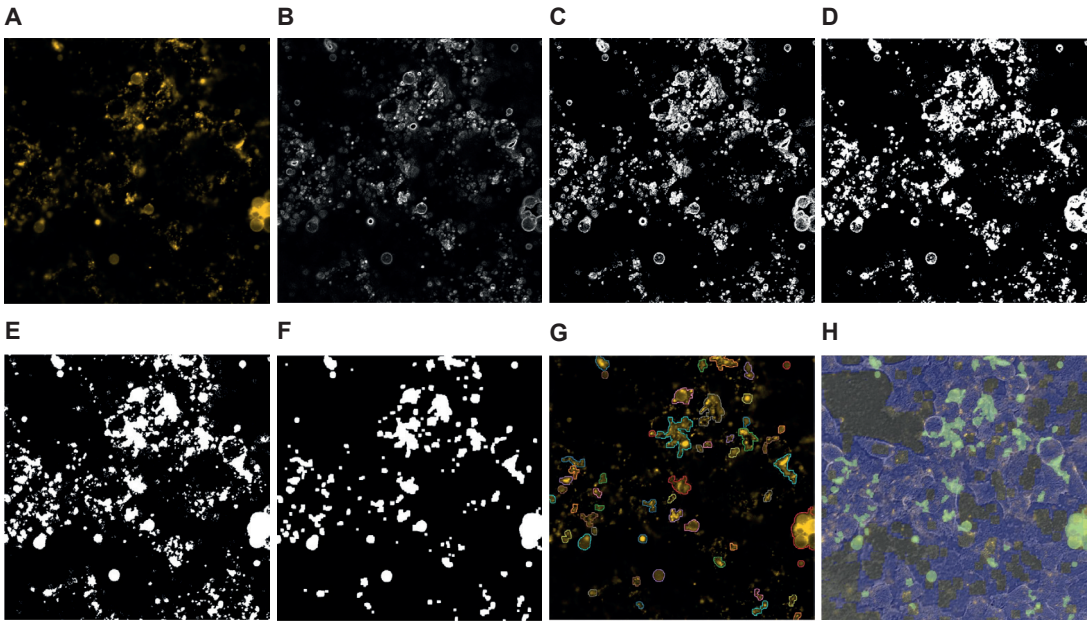


Figure 3.4: Stepwise illustration of GUV detection in hybrid system experiment from confocal fluorescent image (A). With the Sobel operator, the GUV borders are highlighted (B). Afterwards, the image was binarized (C). With a binary closing, the holes in detected GUV membrane are closed (D). The inside of GUVs is filles (E) and the background reduced by binary opening (F). The contour of each separated ROI was calculated (G). By overlapping with the detected cell area, for each contour it was decided, if the representing GUVs are adhesive or not.

To close the lipid membranes in the binarized images, the binary closing algorithm as previously described was applied. The areas enclosed from detected GUV membranes were filled and thus defined as ROIs. Because still some background signal existed, a binary closing algorithm was applied. The contour of separated ROIs was calculated and represents the lipid membrane of single GUVs or the outer lipid for contiguous GUVs.

Now, the detected GUVs were compared with the detected cell areas. If a GUV contour overlapped with the cell ares, this GUV counted as adhesive and labeled in green. The non-adhesive GUVs were labeled in red.

Chapter 4

Results

4.1 Synthesis of functional fluorinated block copolymer surfactants

In this chapter, different synthesis routes for perfluoro block copolymer surfactants consisting of polyethylene glycol (PEG) and perfluoropolyether (PFPE) will be compared and discussed. Particularly, I will emphasize the synthesis efficiency, purity and physicochemical properties. Moreover, purification of the surfactants using coated silica gel will be explained.

Finally, three different functionalized surfactants will be introduced: 1) A pH-independent positively charged surfactant. This surfactant can be implemented for efficient formation of dsGUVs; 2) A photoliable surfactant, consisting of PEG and PFPE blocks connected via a photoremovable linkage. This surfactant should enable a light-mediated control over the droplet's interfacial tension; 3) And a fluorescent surfactant that can be used for labeling the surfactant layer.

4.1.1 Comparison of different surfactant synthesis approaches

Perfluorinated block copolymers consisting of PEG and PFPE blocks are commonly used to stabilize water-in-oil (w/o) droplets in microfluidic systems.[139,187–190] The commercial resources are quite limited and there is a lack of information regarding the nature of the block copolymer (i.e., triblock or diblock) and molecular mass. In addition, the commercial surfactants may contain the starting material Krytox, a PFPE with a carboxylic acid at one end, which reduces the pH value of the inner phase in w/o droplets.[102] The reduction of pH will be strongly dependent on the concentration of this educt.[96,179] To have control over the polymeric composition, molecular mass, and purity, the synthesis of the surfactant was established and optimized.

PFPE(7000 g/mol)-PEG(1500 g/mol)-PFPE(7000 g/mol) is a very common surfactant in droplet-based microfluidics. Therefore, to synthesize this surfactant, I tested three different synthesis approaches: 1) esterification via PEG activation with *n*-butyllithium (*n*-BuLi) (Figure 4.1A); 2) amination of Jeffamine with PFPE acid chloride (Figure 4.1B) and; 3) copper click reaction of diazide PEG and propagyl PFPE (Figure 4.1C).

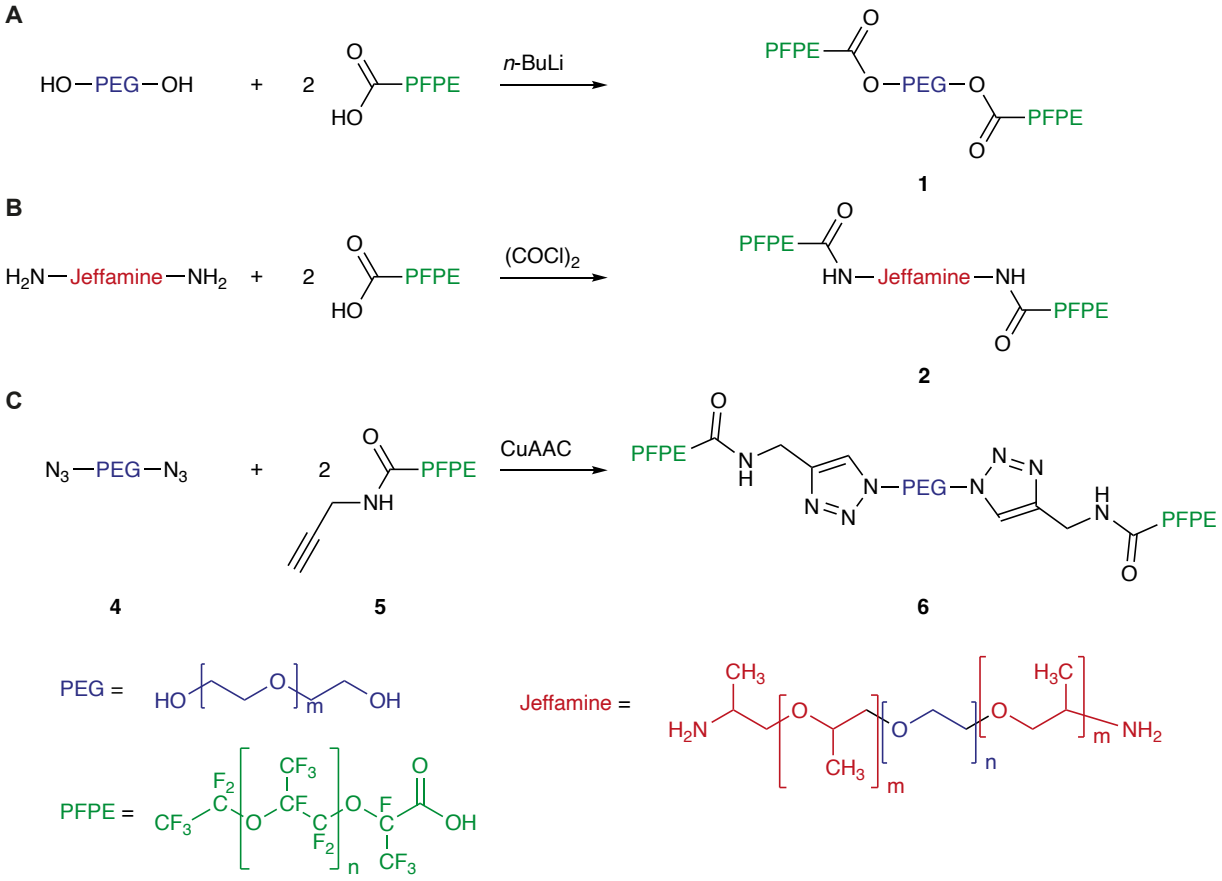


Figure 4.1: Three synthesis approaches to synthesize triblock copolymer surfactants consisting of PEG and PFPE blocks. A: The triblock was obtained by *n*-BuLi activation of PEG, followed by esterification with Krytox. B: As an alternative, the carboxylic acid of Krytox could be transformed into an acid chloride, which was used to react with two terminal amines of the PEG derivative Jeffamine. C: A third option is a coupling of diazide PEG with the propargyl derivative of PFPE using copper click chemistry.

For esterification of PEG I followed the Platzman *et al.*[150] protocol (Figure 4.1A). A solution of PEG in tetrahydrofurane (THF) was cooled down to -78 °C, followed by slowly addition of *n*-BuLi. After full addition, the reaction mixture was allowed to warm up to room temperature. During this process, both terminal hydroxyl groups of PEG were deprotonated and lithiated. The Krytox was added at -78 °C and the reaction mixture was slowly warmed up to room temperature. Under these strong

basic conditions, the lithiated PEG reacted with the carboxylic acid of PFPE and the esterified triblock surfactant (eTS) **1** was received.[191] The low mixability of eTS **1** with ethanol was used to purify it from side products and unreacted PEG. The synthesis is described in detail in Chapter 3.4.1 (page 24).

Alternative approach for PFPE(7000 g/mol)-PEG(1500 g/mol)-PFPE(7000 g/mol) synthesis is the amidation of Krytox with the PEG diamine (Figure 4.1B).[139] Instead of PEG diamine, the PEG derivative Jeffamine can be used as starting material. Jeffamine is the trade name of O,O'-bis(2-aminopropyl) polypropylene glycol-blockpolyethylene glycol-block-polypropylene glycol (structure is shown in Figure 4.1). It is important to mention that compared PEG diamine, Jeffamine has better accessibility and it remarkably cheaper. Moreover, in regards to amidation Jeffamine has similar reactivity as of PEG diamine. As a first step of reaction, PFPE acid was turned into acid chloride using oxalyl chloride to increase its reactivity. Afterwards, a Jeffamine solution in dichlormethane (DCM) was added and the final product, the amidated triblock surfactant (aTS) **2**, was obtained. For detailed description see Chapter 3.4.2 (page 25).

The third alternative approach for the PFPE(7000 g/mol)-PEG(1500 g/mol)-PFPE-(7000 g/mol) synthesis is to implement copper click chemistry, adopted from Scanga *et al.* (Figure 4.2).[154] For the click reaction, the precursors PEG diazide **4** and propargyl PFPE **5** were produced first. PEG was deprotonated with sodium hydroxide and used for substituting the chloride in *p*-toluenesulfonyl chloride (*p*TsCl) to obtain PEG ditosylate **3**. Compared with the purification procedure described by Scanga *et al.*, the crude product was washed only once with 90 vol% brine. In contrast to Scanga *et al.* the averaged molecular weight of PEG was 600 g/mol in-lieu-of 1500 g/mol PEG as it is in my case. Because of the increased size, the tosyl group has a lower influence on solubility of the product. When the washing step was performed like published (i.e., including additional water washing step), the yield decreased under 5 %. Therefore, brine was diluted in water from 0 vol% to 100 vol% in steps of 10 vol% and used to purify the crude product. Afterwards, yield was calculated and purity was determined with nuclear magnetic resonance spectroscopy (NMR) spectroscopy. 90 vol% brine showed the best results and was used for further synthesis. In the next step, to get PEG diazide **4**, the tosyl group was substituted by sodium azide in dimethylformamide (DMF) at 50°C. After cooling down to room temperature the reaction mixture was mixed with ethyl acetate and filtered through Celite. Sometimes, the filtration took several days due to the clogging of the filter. Then, the suspension was placed into 50 mL Falcon tubes and centrifuged for 5 min at 200 xg. The precipitate was washed with a small amount of DMF and centrifuged again under the same conditions. The combined supernatant, either from filtration or from centrifugation, was then further cleaned up

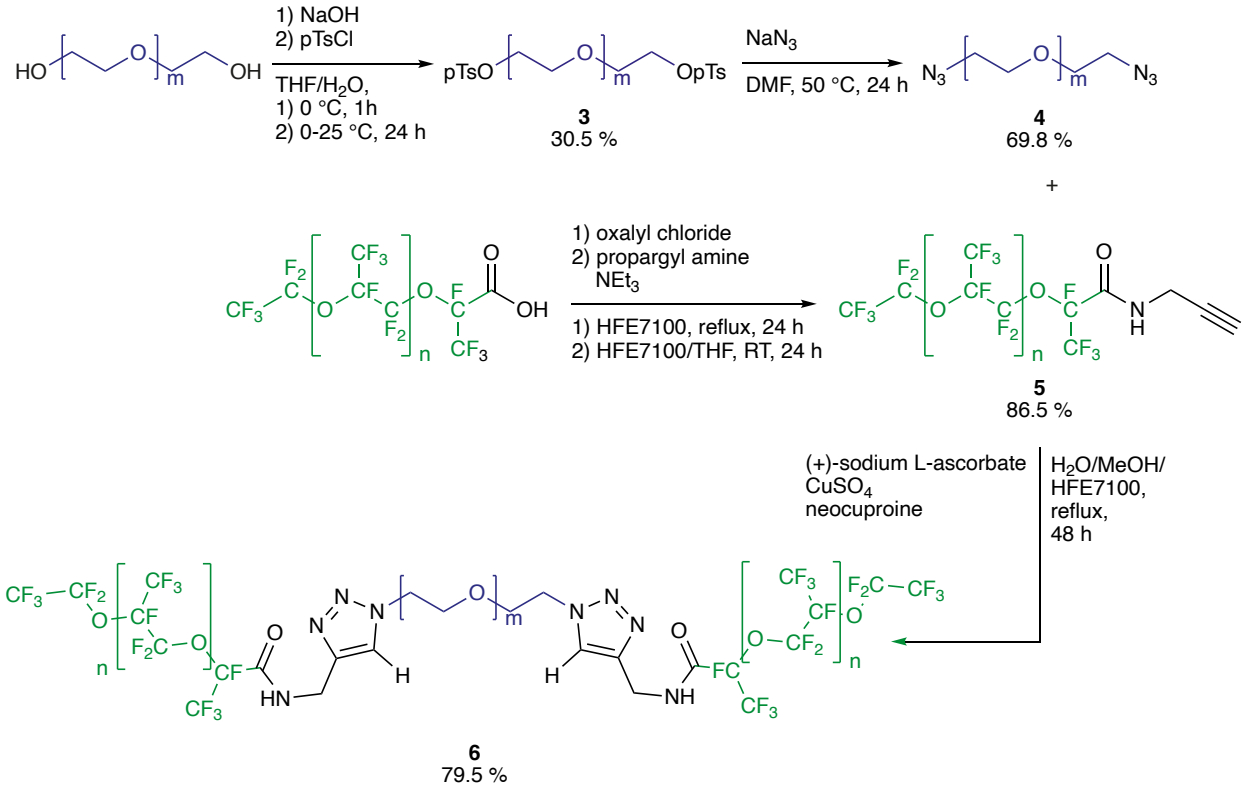


Figure 4.2: Synthesis route for producing clicked triblock surfactant **6**. First the two precursors PEG diazide **4** and propargyl PFPE **5** were produced. For the first one, PEG was first tosylated to obtain the PEG ditosylate **3**, followed by a substitution with sodium azide. For compound **5**, PFPE was activated with oxalyl chloride and instantly used for a reaction with propargyl amine. Then **4** and **5** were connected using a copper click reaction performed under reflux for 48 h.

like described for the filtrate. To remove the DMF efficiently, toluene was added because it forms a homogeneous minimum boiling azeotrope with DMF.[192] To synthesise the PFPE precursor, Krytox was activated with oxalyl chloride under reflux. The acid chloride was instantly converted to propargyl PFPE **5** by adding propargyl amine under basic conditions. The two precursors **4** and **5** were used for copper click reaction.[193] Neocuproine was used as additive to increase efficiency of the reaction.[194,195] The synthesis was done under reflux for 48 hours For purification, the reaction mixture was overlayed with methanol and swiveled carefully to avoid emulsion formation. With this procedure it was possible to remove catalyst, side products and unreacted PEG diazide **4**. All reaction steps are described in detail in Chapter 3.4.6 (pages 26 to 30).

The syntheses of eTS **1** and aTS **2** have a similar yield (79.2 % and 76.6 %) and a similar time requirement of two days exclusively for the purification steps. For eTS **6**, the yield for PFPE route is comparable (69 %) but the one for PEG route is much less (17 %). Also the time requirement is higher with around one to one and a half weeks.

Besides yield, the purity of the surfactant is even more important. Therefore, all three surfactants were analysed with the transfer method to determine the amount of PFPE in the final product (3.5.1 on page 46) as well as the more standard methods NMR, fourier transform infrared spectroscopy (FTIR) and pendant drop.

In the NMR spectra (Figure 4.3A), the peak at 7.16 ppm is the NMR solvent peak for deuterated benzene and all three spectra are calibrated for this peak. Krytox has only one peak in NMR and it was show that the shift of this peak is concentration dependent (Figure 6.16 in Appendix, page XVII). Therefore, the peak at 7.33 ppm for eTS **1** could correlate with Krytox contamination. The peaks around 8 ppm for cTS **6** can be assigned to the hydrogen on the amide group (8.38 ppm) and the CH_2 next to the amide group (7.96 ppm). For aTS **2** no peak in this area could be observed.

In the attenuated total reflection (ATR)-FTIR spectra (Figure 4.3B), characteristic peaks like C-O stretching at 1119 1/cm, C-F stretching at 1228 1/cm and a weak C-H bending at 1458 1/cm could be observed for all three surfactants and Krytox. The expected shift for C=O stretching from 1775 1/cm to 1718 1/cm before and after the fictionalization of the carboxylic acid group in Krytox could only be observed for cTS **6**.[150]

In pendent drop measurements the surfactants reduced the interfacial tension (IFT) between HFE 7500 and water in different amounts: for eTS **1** to 26.4 ± 0.1 mN/m, for aTS **2** to 24.0 ± 0.5 mN/m and for cTS **6** to 10.6 ± 0.2 mN/m. Due to the fact that lower interfacial tensions stabilizes the droplets more, the cTS **6** surfactant seems to perform better.

A transfer assay was applied to all three surfactants. In this assay the molecular ratio of Krytox in the surfactants were determined by the amount of transfer Rhodamine

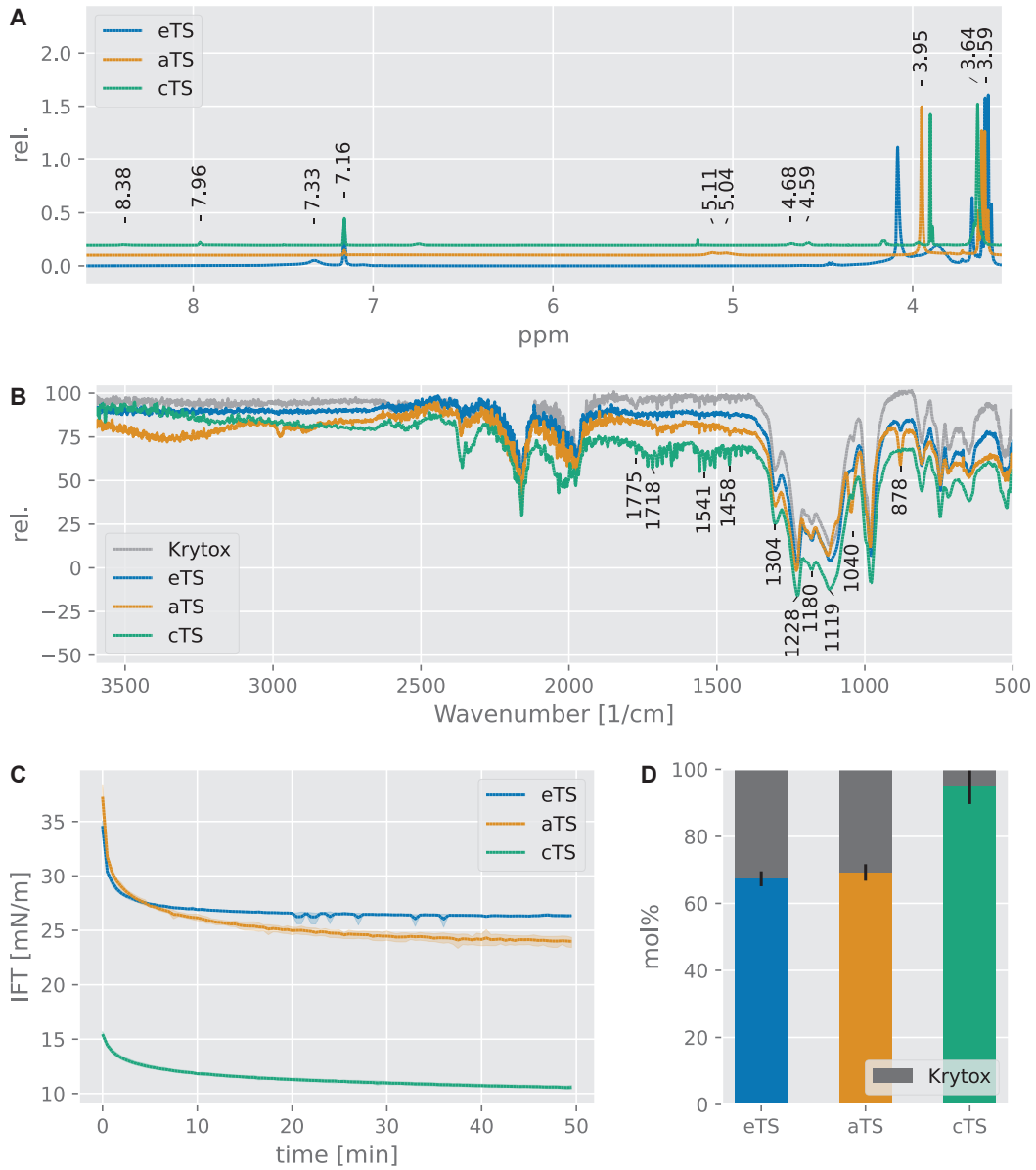


Figure 4.3: Analysis of the the surfactants eTS **1**, aTS **2** and cTS **6**. A: NMR spectra and B: ATR-FTIR spectra of the three synthesized surfactants. C: In the pendent drop measurements, a significantly lower IFT value was measured for cTS **6**, compared to eTS **1** and aTS **2**, indicating that it can stabilize w/o droplets better than the other two. D: The transfer assay showed that a large amount of Krytox was still present in eTS **1** and aTS **2**.

6G from the water into the fluorinated oil phase under the assumption that the surfactants do not interact with Rhodamine 6G. This measurements revealed that eTS **1** still contained 32.7 ± 2.3 mol%, aTS **2** 30.7 ± 2.5 mol% and cTS **6** was the cleanest with 4.78 ± 5.6 mol%.

The analysis of the purity and espacially the reduction of IFT showed that cTS **6** performs better as a surfactant than eTS **1** and aTS **2**. This could probably rely on the Krytox concentration, why I tried to further purify these two surfactants.

4.1.2 Surfactant purification

Krytox is an educt for most of the fluorosurfactants. Krytox itself can act as a surfactant at the water-oil interface. Because of the high electron withdrawing character of the perfluorinated polymer, the pKa value of the carboxylic acid should be in the range of a strong acid. Therefore, Krytox can decrease the pH value of the inner phase leading to side effects like denaturing the encapsulated proteins or, on kind of a positive side, pH-dependent reactions could be influenced.[180] Lussier *et al.* controlled the pH value of the inner phase of w/o droplets by changing the Krytox concentration.[102] In addition, presence of Krytox will affect the uncharged nature of surfactant stabilized water-oil interface and will enhance the electrostatic interactions between cells, proteins and other bio-molecules with the surfactant layer. Therefore, precise control over the Krytox concentration is essential for droplet-based microfluidic applications. Since eTS **1** and the aTS **2** contained Krytox in the product, it was necessary to purify them for further applications. Towards this end, different purification methods were tested.

The purification was performed via a flash column chromatography. To reduce the amount of synthesized surfactant needed to test different flash column chromatography conditions, the method was miniaturized using a glass pipette instead. The purification efficiency was analysed by separating the purified surfactants on a thin-layer chromatography (TLC) plate covered with silica gel C18. As eluent, a mixture of 1,1,1,2,3,4,4,5,5,5-decafluoropentane (Vertrel), acetonitril and methanol was used at a volume ratio of 80:10:10.[196] To visualize the surfactant (Rf = 0.0) and the Krytox spots (Rf = 1.0) visible, the separated spots were negatively stained with a 10 mM aqueous fluorescein solution.

In a first approach silica gel, silica gel C18, anion exchange, cation exchange and aluminium oxide (Alox) columns were tested. Silica gel is the most common column material for flash column chromatography of hydrophobic molecules, while silica gel C18 is used for hydrophilic molecules. Due to the amphiphilic property of the synthesized surfactants as well as Krytox, both column materials were potential options for the separation of both molecules. The anion exchange material can selectively bind anions due to its positively charged surface, e.g. the deprotonated Krytox. The

uncharged surfactants could instead be collected separately. The cation exchange material, in turn, has a negative surface charge and could repel the anionic Krytox and, on the other hand, interact with the hydrophilic block of surfactants, thus delaying elution and separating the two substances. Alox is like silica gel, used as a polar column material, but with a higher polarity. Therefore, it is particularly useful in the separation of unsaturated hydrocarbons, acids and bases and thus could be used for the separation of Krytox. Unfortunately, for the ion exchange columns, no separation could be observed, and for the other three column materials, neither the surfactant nor Krytox were possible to be eluted. Thus, the ion exchange materials are suitable for use in aqueous systems and the gradual change from first water to methanol and then to the running solvent mixture caused the material to collapse, which affected the functionality of the ion exchangers. The column materials silica gel, silica gel C18 and Alox showed too strong interactions of either the hydrophilic part with the polar column material (silica gel, Alox) or the hydrophobic part with the non-polar column material (silica gel C18). As a result, neither the surfactants nor Krytox could be eluted. Therefore, the silica gel should be modified to increase the specific interaction with Krytox.

In the doctoral thesis of Riechers, silica beads with an amine functional group were implanted to achieve an increased selectivity for removing Krytox.[179] The carboxylic acid group of Krytox can protonate the amine on the functionalized silica gel, thus increase the interaction between the column material and Krytox due to the charge. Krytox is thus prevented from eluting and separated from the surfactants. Therefore, two different silanes bearing an amine group were used: (3-Aminopropyl)trimethoxysilane (APTMS) and N^1-(3-Trimethoxysilylpropyl)diethylenetriamine (TRI-silane) (structures are shown in Figure 4.4). Dried silica beads were suspended in a mixture of toluene and the respective silane in a volume ratio of 90:10. The functionalized silica gels were filtered, washed with ethanol and dried (for more details see Chapter 3.4.18 on page 46).[178] Both amine-bearing silica gels were tested for their ability to remove PFPE carboxylic acid. In both cases, the TLC plate showed only the spot for the surfactant. For further purifications, the APTMS functionalized silica gel was used.

Using the APTMS functionalized silica gels the eTS **1** and the aTS **2** surfactants were both purified. Afterwards, the ratio of PFPE in the surfactants was measured by transfer method (3.5.1 on page 46, Figure 4.4 B) and a change in interfacial tension was determined by pendant drop (Figure 4.4 C). In case of the surfactant eTS **1** the additional purification step allowed for 68 % reduction of Krytox from 32.7 ± 2.2 mol% to 10.4 ± 1.8 mol%, which is a reduction of approximately 68 %. This reduction had a direct influence on the IFT of the eTS **1** stabilized water/oil interface. Following the purification step the IFT values decreased from 26.35 ± 0.09 mN/m to 22.45 ± 0.08 mN/m.

The purification had a similar effect on the surfactant aTS **2**. In that case, the molecular ratio of Krytox was reduced from 30.8 ± 2.5 mol% to 10.5 ± 1.6 mol%, corresponding to removal of around 66 % of Krytox. After purification the IFT values reduced from 24.00 ± 0.49 mN/m to 21.75 ± 0.03 mN/m.

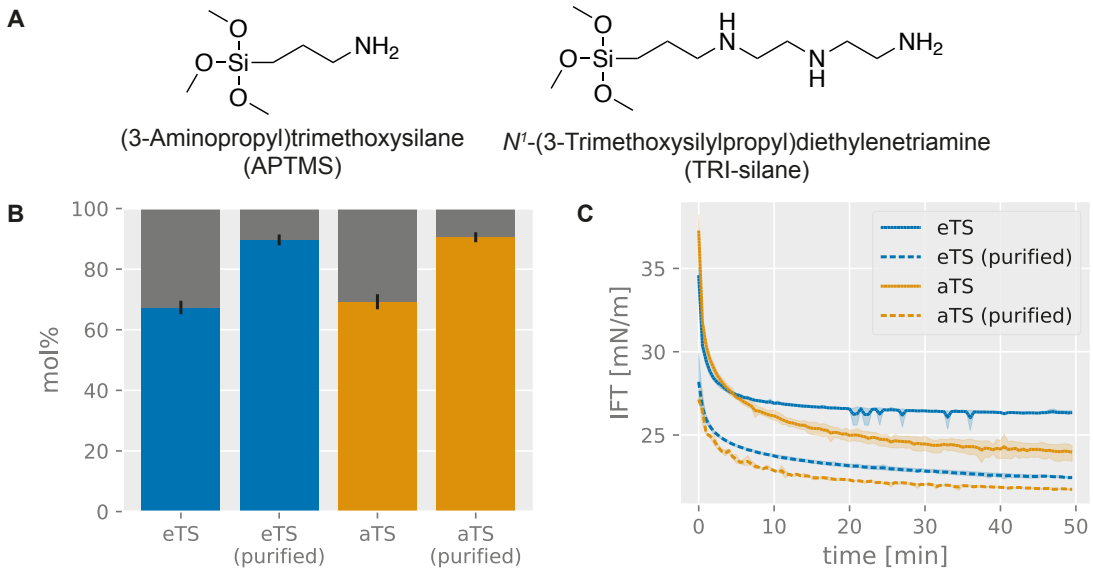


Figure 4.4: Analysis of eTS **1** and aTS **2** surfactants properties following their purification with amine functionalized silica gel. A: Chemical structures of the two silanes APTMS and TRI-silane, which were used for the functionalization of silica beads to introduce an primary amine functional group on the surface of the beads. B: Analysis of the molar ratio in the surfactants eTS **1** and aTS **2** before and after flash column chromatography using amine group bearing column resign. The molecular ratio of Krytox is shown in gray. With this purification step, it was possible to reduce the ratio of Krytox in eTS **1** from 32.7 ± 2.2 mol% to 10.4 ± 1.8 mol% and for aTS **2** from 30.8 ± 2.5 mol% to 10.5 ± 1.6 mol%. B: Pendant drop analysis of eTS **1** and aTS **2** to determine the IFT before and after further purification. So, it was possible to reduce the IFT of eTS **1** from 26.35 ± 0.09 mN/m to 22.45 ± 0.08 mN/m and for aTS **2** from 24.00 ± 0.49 mN/m to 21.75 ± 0.03 mN/m.

I was able to show that amine functionalized silica gel can be implemented to partially remove PFPE carboxylic acid from the synthesized eTS **1** and aTS **2** surfactants. The purification step had a positive impact on the IFT values of the respective surfactants. However, it is important to mention here that, the Krytox ratios and the IFT values were still not optimal and less optimal compared to the clicked triblock surfactant (cTS) **6** (see Chapter 4.1.1 on page 63). Therefore, the latter was used for further experiments.

4.1.3 Synthesis of functionalized surfactants

So far, inert, uncharged block copolymer surfactants have been discussed for stabilizing w/o droplets.[197–199] In synthetic biology and biomedical applications, a water-oil interface stabilized with surfactants containing the specific functional groups can be beneficial. Haller *et al.* showed the charge-mediated formation of droplet-stabilized giant unilamellar vesicles (dsGUV) is dependent on the concentration of Krytox surfactant, that creates negative charge on the water-oil interface.[96] The negatively charged interface attracts cations that, in turn, attract anionic small unilamellar vesicles (SUVs), forming a lipid bilayer by self-assembly. Functional water-oil interfaces were also produced by directly functionalizing the surfactants with gold nanoparticles,[150] or PNIPAM to generate temperature-responsive droplets.[12] Moreover, surfactants with different functionalities for capturing biomolecules, fabrication of microcapsules and monitoring of single-cell gene expression have been described before.[159]

In this section, three different functional surfactants and their synthesis routes will be discussed: 1) the positively-charged diblock surfactant (posDS) **11**; 2) the photoliable triblock surfactant (plTS) **14**; and 3) the Rhodamine B-labeled fluorescent diblock surfactant (fluoDS) **17** (Figure 4.5).

Positively-charged diblock copolymer surfactant

Recently droplet-based microfluidic technology and particularly w/o droplets have been used as a stabilizing 3D compartments for the charge-mediated formation of giant unilamellar vesicles (GUVs). In that approach, the SUVs consisting of lipids with total negative or positive charges (e.g., negatively charged 1,2-dioleoyl-sn-glycero-3-phosphoethanolamine (DOPE), 1,2-dioleoyl-sn-glycero-3-phospho-(1'-rac-glycerol) (DOPG) and 1,2-dioleoyl-sn-glycero-3-phospho-L-serine (DOPS) or positively charged lipids 1,2-dioleoyl-3-trimethylammonium-propane (DOTAP)) are encapsulated into w/o droplets. To form a supported lipid bilayer on the inner droplet interface, the charged SUVs adhere and rapture on the oppositely charged droplet interface. One established method is to add Krytox to the surfactant solution.[96,101] Krytox leading to a negative charge on the water/oil interface, so that cationic SUVs can directly interact with the surfactant layer. In case of anionic SUVs, magnesium ions can be implemented for the sequential attraction of the magnesium ions first and the following attraction of the negatively charged SUVs. Following the formation of the dsGUVs, the GUVs are released to physiological conditions by removing the oil phase and the polymer-stabilizing layer. It is important to mention here that the release process was more efficient in the case of positively charged dsGUVs in comparison to negatively charged. This observation can be attribute to the fact that the electrostatic interactions between the lipids and

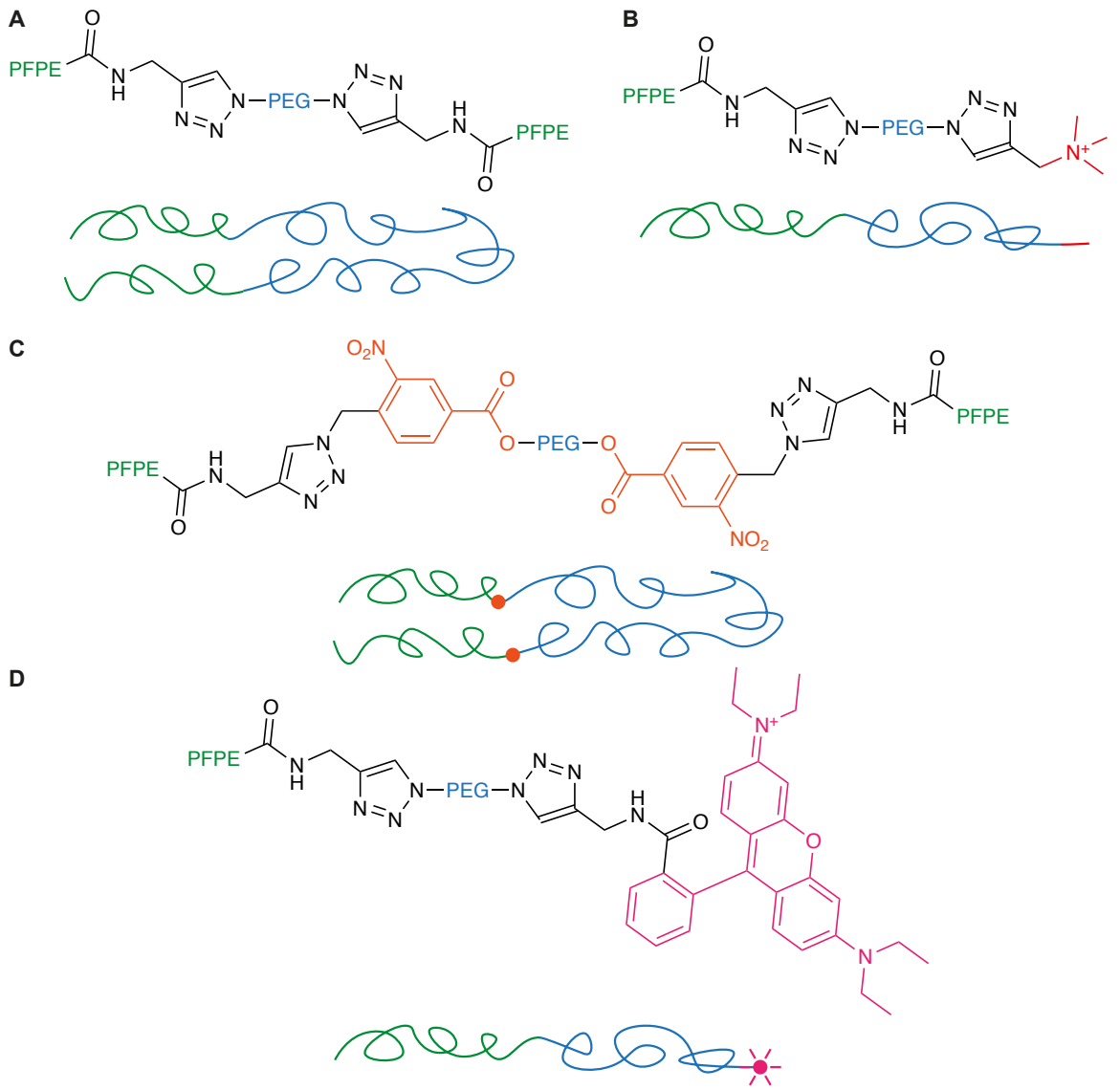


Figure 4.5: Overview of the chemical structures of the functionalized surfactants synthesized in this thesis. A: Chemical structure of the triblock copolymer surfactant synthetized via the click chemistry approach cTS **6**. B: Chemical structure of the positively-charged diblock copolymer surfactant (posDS) **11**, the PEG block is asymmetrically connected with the PFPE block on the one side and on the other side with a pH-independent positively charged quaternary ammonium. C: Chemical structure of the photoliable surfactant, the polymerblocks are linked via a nitrobenzoyl group. Irradiation with UV light cleaves the linker and the surfactant breaks down into its PEG and PFPE blocks. D: Chemical structure of the fluorescent diblock copolymer surfactant (fluoDS) **17**. The PEG is asymmetrically coupled on the one side with a PFPE block and on the other side with Rhodamine B.

the surfactant layer are not involving any intermediate ionic conditions. The binding energy of coordination complex are typically several times higher than electrostatic interactions. This strong interaction can cause rupturing of the lipid membrane during the release. However, the implementation of positively charged GUVs for synthetic biology and biomedical applications is quite limited due to their cytotoxic nature. Therefore, I considered to synthesize positively charged surfactants for direct charge-mediated assembly of negatively charged dsGUVs. The surfactant was designed in a way that the pH independent positive charge is introduced by a quaternary ammonium (Figure 4.5B).

To synthetize the surfactant, PEG with an average molecular weight of 600 g/mol was converted into a diazide derivative. In a first step, PEG was deprotonated with sodium hydroxide and used for a substitution reaction with *p*TsCl to obtain the ditosylate derivative **7** (Figure 4.6). In a second substitution, the tosyl group was replaced by an azide group using sodium azide and the PEG diazide **8** was isolated. In parallel, the quaternary ammonium containing molecule was produced by mixing propargyl bromide and trimethylamine (TMA) in diethyl ether. Following 24hoursat 0 °C, the reaction mixture was just placed under reduced pressure. Because starting material, solvent and side products were volatile, pure N,N,N-trimethylprop-2-yn-1-aminium bromide (TAB) **9** was obtained and no further purification steps were needed. Diazide PEG **8** and TAB **9** were equimolarly converted in a click reaction to a mix of starting material PEG **8**, one end-functionalized PEG **10a**, and both end-functionalized PEG **10b**. This mixture was then extracted with DCM. Because of the charge of the quaternary ammonium, both TAB-functionalized surfactants **10a** and **10b** were not soluble in DCM. Therefore, it was possible to separate the unreacted starting material with DCM. In the next synthesis step, the doubly functionalized PEG **10b** could not react or affect the reaction, so no further purification was necessary. In the second click reaction, propargyl PFPE was coupled to the remaining azide of **10a**. The ligand Neocuproine was added to increase the efficiency of the reaction.[194,195] Catalyst, starting material and side products were separated from the positively-charged diblock surfactant (posDS) **11** by swiveling with methanol. All reaction steps are described in detail in Chapter 3.4.6 (pages 32 to 36).

Pendant drop measurements have been performed to analyze the ability of the posDS **11** to stabilize w/o droplets (Figure 4.7B). An IFT value of 13.91 ± 0.56 mN/m was obtained. Importantly, this IFT value is similar or slightly higher to the values obtained from the commercially available surfactant (CS). Moreover, transfer method assay was used to evaluate the Krytox content within the posDS **11** (Figure 4.7A). Krytox content of 14.2 ± 1.9 mol% was measured. Surprisingly, the obtained amount of Krytox is higher in comparison to the analysis with cTS **6** that has been synthesized

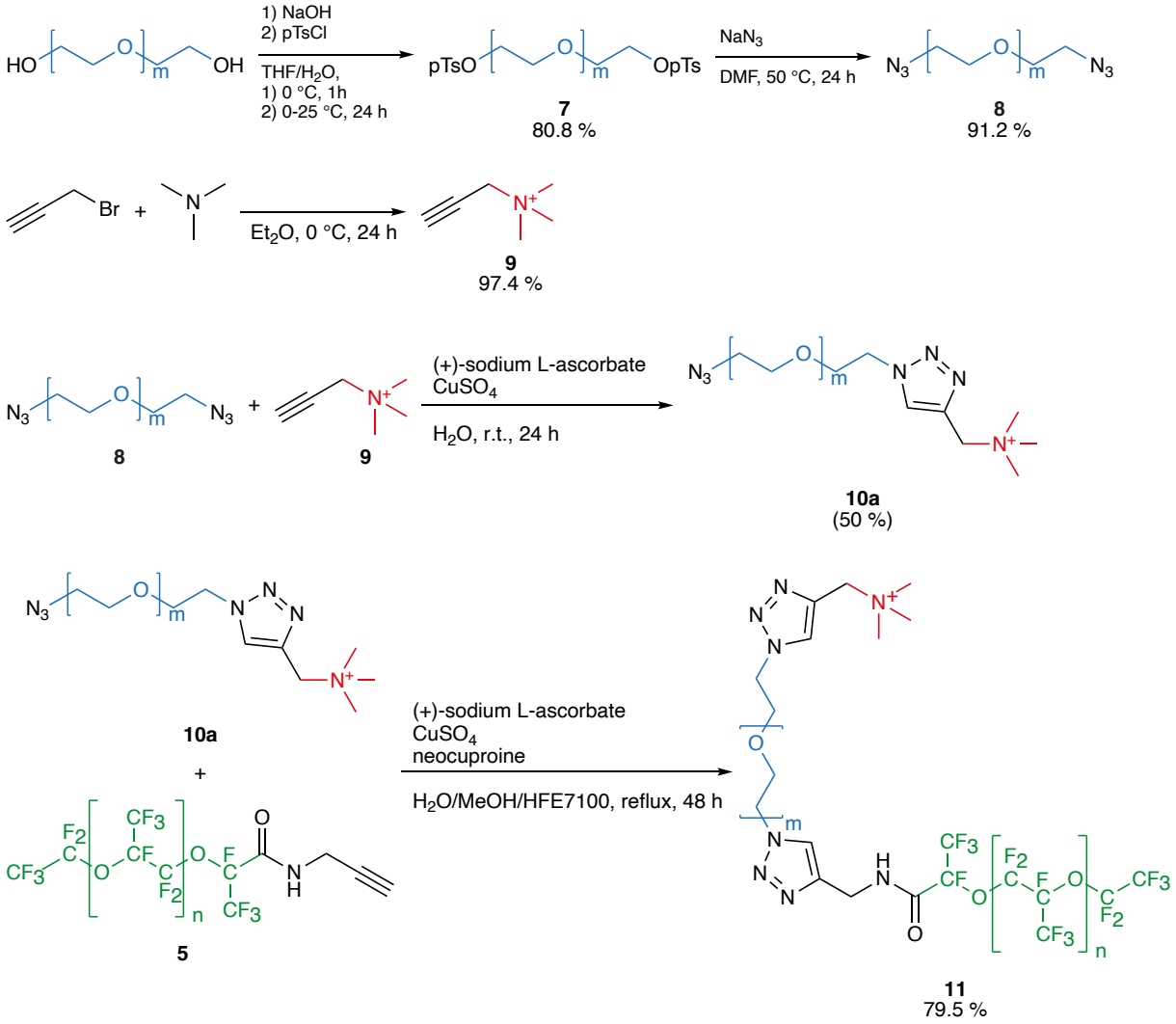


Figure 4.6: Synthesis of positively charged diblock surfactant posDS **11**. In the first step, the terminal hydroxyl groups of PEG600 performed a substitution with *p*TsCl to receive the ditosylate derivative **7**. In a next substitution reaction, the tosyl group is replaced by an azide group to get the diazide **8**. In parallel, TMA was used to substitute the bromine atom in propargyl bromide and TAB **9** was obtained. In a first click reaction, the diazide PEG **8** and the alkyne **9** were converted in same equivalents and at the end a mixture of starting material **8**, one side-functionalized **10a** and both sides-functionalized **10b** was obtained. The diazide PEG was removed by extraction with DCM and the mixture of **10a** and **10b** was directly used to do a second click reaction with propargyl PFPE **5** to obtain the positively charged surfactant posDS **11**.

using the similar approach. Moreover, NMR measurements of posDS **11** did not show any peaks attributed to Krytox or propargyl PFPE **5** (Figure 6.12 on page XIII). The high Krytox content as obtained in the transfer method assay can be attributed to possible interaction between the positive charge surfactant and Rhodamine B leading to a transfer of the dye into the oil phase. NMR measurement can be used to estimate a percentage of Krytox in posDS **11** lower than 5 %.

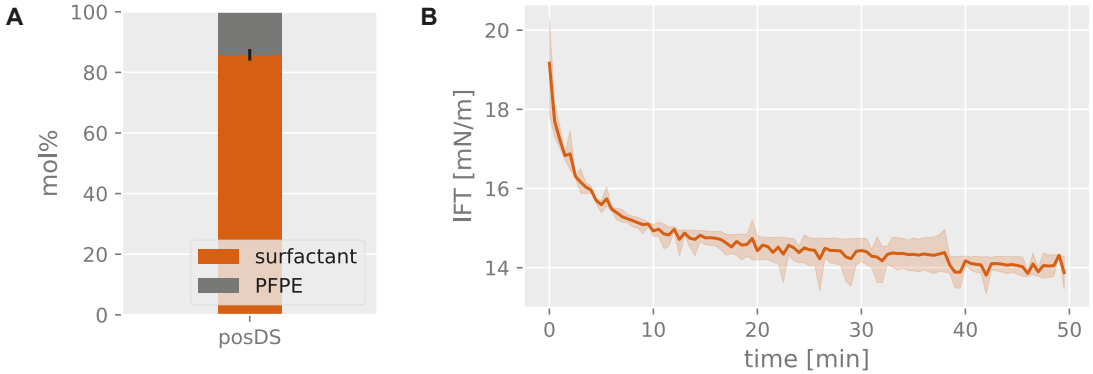


Figure 4.7: Transfer assay (A) and pendant drop measurements (B) of posDS **11**.

The positively charged surfactants were used to generate GUVs by the charge-mediated approach. The method is discussed in Chapter 4.2.1 (page 87) and described in detail in Chapter 3.5.2 (page 50). The working surfactant concentration of 20 mM in HFE 7500 was chosen for these experiments. As water phase, a tris(hydroxymethyl)-aminomethane (Tris) buffer with different sodium chloride concentrations were used (Figure 4.8). Surprisingly, without addition of sodium chloride, no dsGUV formation was observed. Therefore, the ionic strength was step-wise increased to improve the lipid bilayer self-assembly, and with already 20 mM of sodium chloride, it was possible to form dsGUVs and to release them. By increasing the ionic strength, more SUVs were recruited to the water-oil interface and at the sodium chloride concentration of 150 mM, complete colocalization of lipids at the droplet inner interface was observed. Moreover, higher ion concentration leaded to better release efficiency. The stability, and thus the ability to self-assemble a lipid double membrane, of lipid vesicles is dependent on the ionic strength of the buffer.[200–202] Addition of sodium chloride increased the ionic strength and thus facilitated the formation of dsGUVs. In contrast to magnesium ions, sodium ions are less able to allow the formation of dsGUVs from negatively charged SUVs to a Krytox-containing surfactant layer, so formation of dsGUVs via this mechanism can be ruled out.

For these experiments, a lipid composition of 20.0 mol% cholesterol, 36.0 mol% 1,2-dioleoyl-sn-glycero-3-phosphocholine (DOPC), 20 mol% DOPG, 23.0 mol% 18:1 sphingomyelin (SM), 1.0 mol% Liss Rhod PE was chosen. The lipid composition was determined by means of electrospray ionization (ESI) mass spectrometry (MS) at different

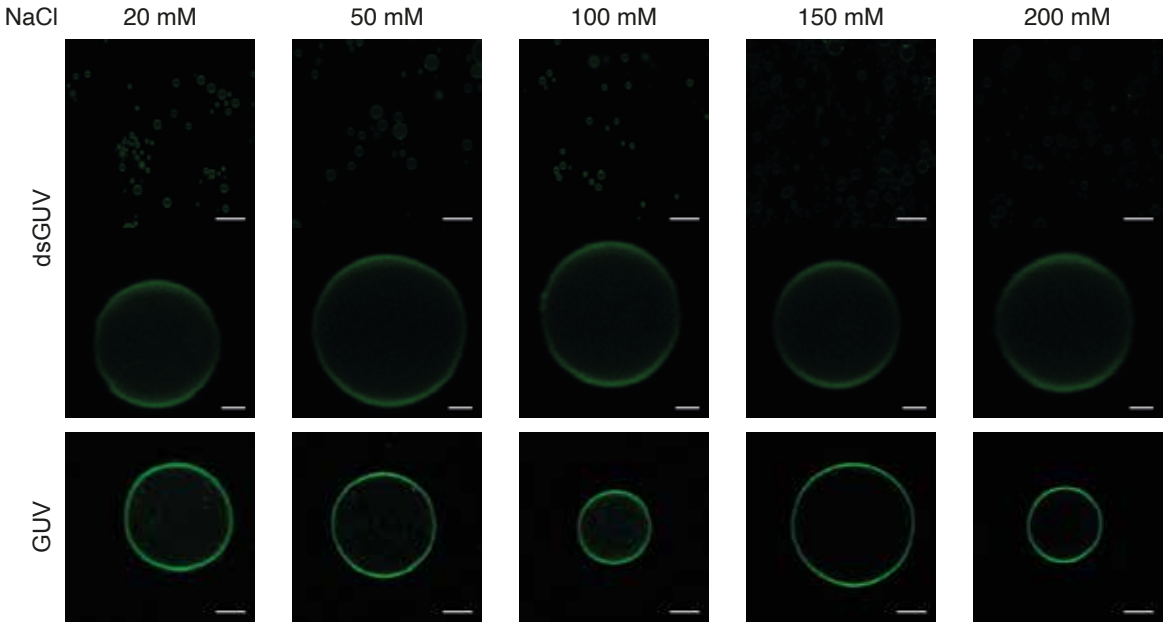
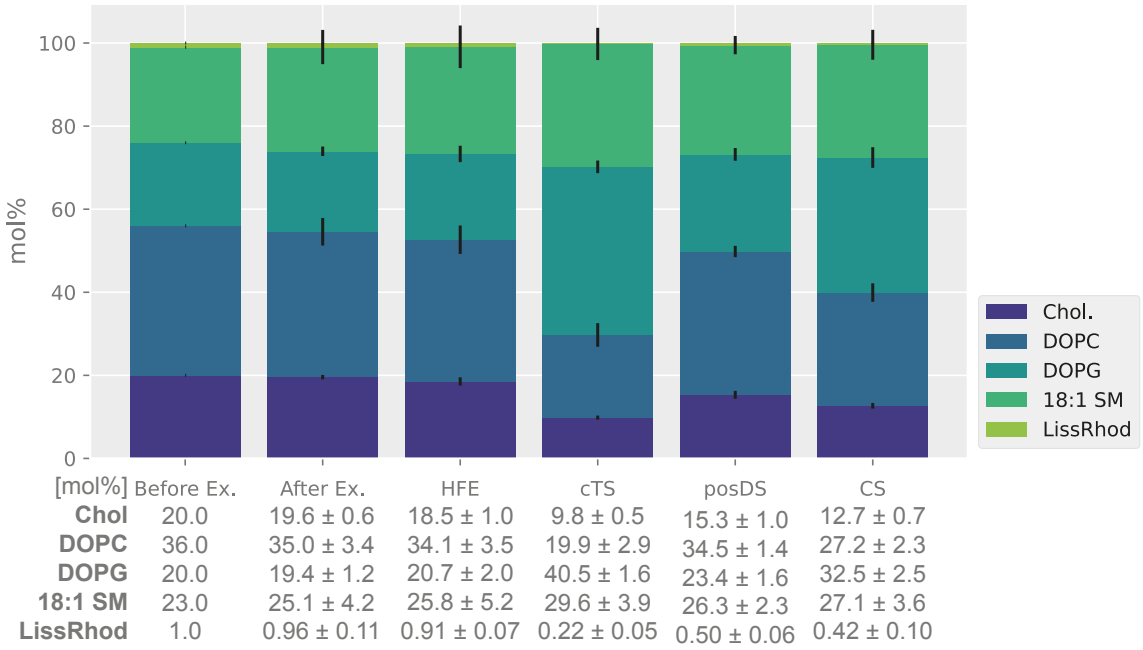


Figure 4.8: Representative confocal images of dsGUVs (top row) obtained with different sodium chloride concentration (indicated on top) and the released GUVs (bottom row). The droplets for these experiments were stabilized by using the posDS **11**. Scale bar: 50 μm for overview image, 5 μm for single dsGUV and GUV image.

steps during the GUV formation. For cholesterol, DOPC, DOPG and 18:1 SM an internal standard was added to the measurements. The whole experimental procedure and analysis is explained in detail in Chapter 3.5.1 (page 48).

The lipid composition was measured first immediately after their mixture and removal of the chloroform solvent. The relation of the area under the curve for the respective lipids was set for the expected lipid composition and the rest of the measurements were proportionally correlated to the initial conditions (i.e before extrusion). As can be observed in Figure 4.9 no significant changes in lipid composition were observed following their extrusion. To exclude the effect that HFE 7500 can have on the lipid composition, the extruded vesicles solution was dispersed within HFE 7500 and the lipid composition in the water phase was analyzed by MS. As expected, the lipid composition of the lipids did not differ from the expected ratio. For the charge-mediated GUVs formation three different surfactants were implemented: 1) cTS **6** and 10 mM Krytox; 2) posDS **11** and 3) CS and 10 mM Krytox. The final lipid compositions were measured from the released appropriate GUVs. As can be observed in Figure 4.9, the lipid composition changed the most when cTS **6** was implemented. In that conditions, 51 % of cholesterol, 45 % of DOPC and 78 % of Liss Rhod PE were lost during the production process. In comparison, the portion of DOPG increased by 103 %. The lipid composition of the GUVs produced with posDS **11** changed slightly. Beside for cholesterol (decreased by 24 %) and Liss Rhod PE (decreased by 50 %), the



[mol%]	Before Ex.	After Ex.	HFE	cTS	posDS	CS
Chol	20.0	19.6 ± 0.6	18.5 ± 1.0	9.8 ± 0.5	15.3 ± 1.0	12.7 ± 0.7
DOPC	36.0	35.0 ± 3.4	34.1 ± 3.5	19.9 ± 2.9	34.5 ± 1.4	27.2 ± 2.3
DOPG	20.0	19.4 ± 1.2	20.7 ± 2.0	40.5 ± 1.6	23.4 ± 1.6	32.5 ± 2.5
18:1 SM	23.0	25.1 ± 4.2	25.8 ± 5.2	29.6 ± 3.9	26.3 ± 2.3	27.1 ± 3.6
LissRhod	1.0	0.96 ± 0.11	0.91 ± 0.07	0.22 ± 0.05	0.50 ± 0.06	0.42 ± 0.10

Figure 4.9: :Quantitative MS analysis of the lipid composition in process of GUV formation (i.e., first measurement of the lipid composition is before lipids extrusion and the last measurement after GUVs release). For the charge-mediated GUV formation three different surfactants were implemented (cTS, posDS and CS). The presented results were calculated in comparison to the measurements of lipid composition prior to extrusion.

ratio between the lipids did not change within the error limits. The lipid composition of GUVs produced using the CS changed in the similar direction as for cTS **6** conditions, but to a lesser extent. The portion of cholesterol, DOPC and Liss Rhod PE decresead by 37, 24 and 58 %, respectively and DOPG and 18:1 SM increased by 63 and 18 %, respectively.

In summary, posDS **11** affects lipid composition in GUVs less than cTS **6** and CS. The additional Krytox is probably responsible for the difference. Krytox has a stronger interaction with the negatively charged lipids via magnesium ions than in comparison the electrostatic interactions of the positively charged surfactant.

The positively charged surfactant posDS **11** was also suitable for encapsulating cells in w/o droplets because it did not contain Krytox. For example, Dr. Sadaf Pashapour demonstrated that the positively charged surfactant is able to electrostatically attract the extracellular matrix protein laminin to the water-oil interface to form protein capsules (Figure 4.10A).[203] Furthermore, she was able to encapsulate and culture different cell types (Figure 4.10B: HaCaT, C: Jurkat, D: *E. Coli*) in these protein capsules. A description of this method can be found in Chapter 3.5.2 (page 52).

In this section I showed that it is possible to synthesize a positively charged surfactant and that this surfactant can be implemented for charge-mediated GUVs and

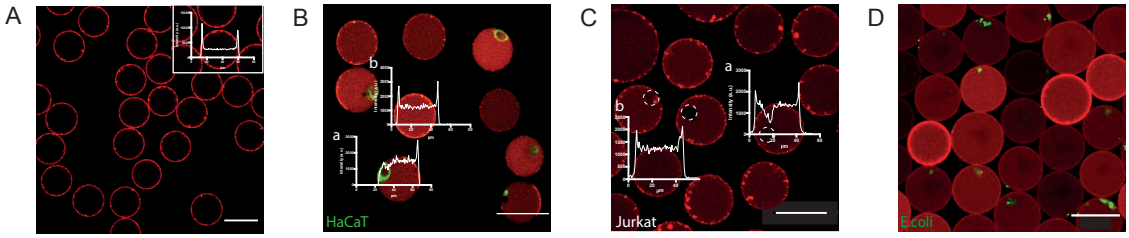


Figure 4.10: Laminin-111 assembly at the periphery of positively charged w/o droplets prepared via droplet-based microfluidics. A) Strong electrostatic attraction of negatively charged protein molecules to the positively charged water/oil interphase using posDS **11**. Inset shows the elevated fluorescence intensity at the periphery of a single droplet. B) Adherent HaCaT cells (green) encapsulated in laminin-111 droplets. Fluorescence intensity graphs highlight the attraction of protein on the opposing side of the cell. C) Non-adherent Jurkat cells (dotted circle) encapsulated in laminin-111 droplets. Fluorescence intensity plots reveal the attraction of laminin-111 to the periphery in empty and cell-laden droplets. D) Bacteria cells (green) encapsulation in laminin-111 droplets. Scale bar: 50 μm.

protein capsules formation. Depside the surfactant charge, still ions had to be added for dsGUVs formation and the ionic strength strongly affected the release efficiency. importantly, by implementation of posDS **11** I was able to produce GUVs with the controlled lipid composition.

Photoliable triblock copolymer surfactant

The water-in-oil emulsion stability is strongly dependent on the physicochemical properties of the surfactants. To date, in order to affect the stability of the emulsion demulsifiers are mainly implemented. For example, *1H,1H,2H,2H*-perfluoro-1-octanol (PFO) surfactant is used in our case to destabilize the emulsion for GUVs release. Due to their high concentration these short surfactants are replacing the stabilizing surfactants and allows fusion of the emulsion. High concentration of the demulsifier can potentially affect the stability of the droplets bio-content and particularly affect the release efficiency. To overcome these drawbacks I aimed to design a photoliable surfactant by light-mediated breaking of the bond between PEG and PFPE blocks.

To design the photoliable surfactant a nitrobenzoyl group was selected as a linker. This group and its photo mechanism are well explored and are already used in different bio-related systems.[204,205] By irradiating with light in the range of 200 to 320 nm, the π bond in the nitro group breaks and creates a diradical.[206,207] After activation, the linker undergoes several intermolecular rearrangements and the rest on the ester bond is released (Figure 4.12B).[208]

For the synthesis, the bromine atom in 4-bromomethyl-3-nitrobenzoic acid (BNBA) was substituted by an azide group to obtain 4-azidomethyl-3-nitrobenzoic acid (ANBA)

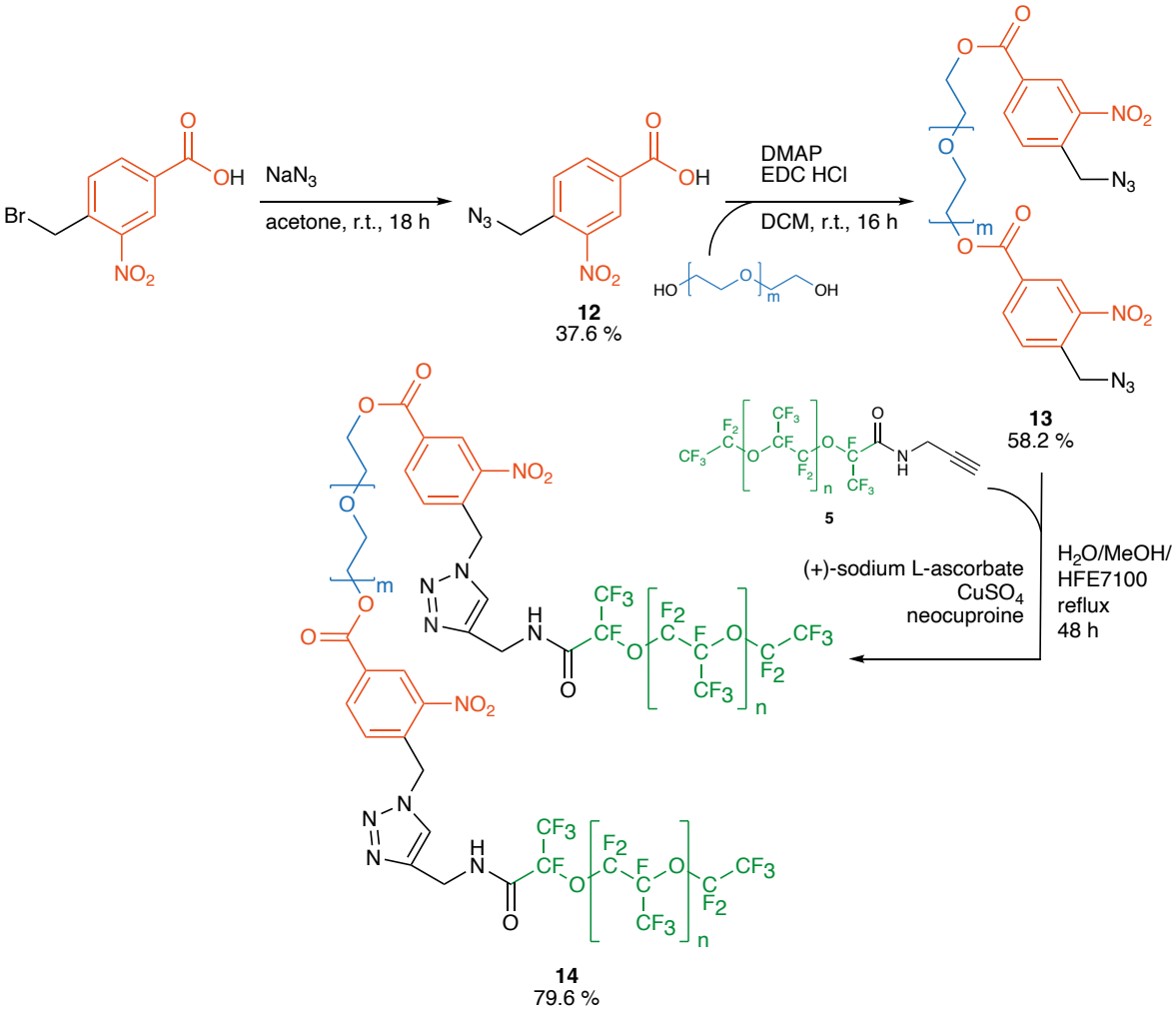


Figure 4.11: Synthesis of the photoliable triblock surfactant plTS **14**. In the first step, the bromine atom in BNBA was substituted with sodium azide to receive ANBA **12**. In a Steglich esterification, ANBA **12** was coupled with PEG1500 to obtain the functionalized PEG **13**. In a click reaction the PEG derivative **13** with propargyl PFPE **5** leads to the triblock surfactant plTS **14**.

12 (Figure 4.11). Using a Steglich esterification, ANBA **12** was esterified with PEG 1500 and the and the bilaterally functionalized PEG **13** was obtained. It is important to do the substitution before the esterification. If the synthesis steps are carried out in reverse order, a substitution of the ester can occur as a side reaction and to reduce the yield significantly. In a last step the photoliable surfactant photoliable triblock surfactant (plTS) **14** was created by performing a click reaction with PFPE **5** and the PEG derivative **13**. To this reaction, neocuproine was added to stabilize the reaction and increase its efficiency.[194,195] During the purification, ethylenediaminetetraacetic acid (EDTA) was added to bind the copper ions. Otherwise it is possible that they stay as an impurity in the surfactant, what changes the color of the product from orange to green or brown. The reaction procedure is described in detail in Chapter 3.4.12 (page 38 to 40).

To assess the successful synthesis of the plTS **14** and the effect of the photo-sensitive linkage a pendant drop measurements were performed. Towards this end, a oil-in-water droplet was created and left hanging until the interfacial tension stabilized. Following the stabilization, the droplet was illuminated with UV light for 30 min (Figure 4.12C and D). During this process, the formation of particles within the droplet could be observed. These particles can be potentially attributed to the split-off PEG residues that are not soluble in the HFE 7500. During this process, the IFT value increased from 22.60 ± 0.02 to 24.23 ± 0.03 mN/m. This increase in IFT values can indicate a successful light-mediated brakeage of the PFPE-PEG linkage. Together with the particle formation, it indicates that the surfactant has the expected functionality. Unfortunately, the resulting PFPE derivative appears to have sufficient amphiphilic nature enough to reduce IFT compared to pure HFE 7500.

The ability to destabilize droplets was tested using a confocal microscopy experiment. The water-containing droplets were produced via the emulsification method by using 2.5 mM of plTS **14** in HFE 7500 and immediately after production transferred to the observation chamber. An area, where two droplets were close in contact, was irradiated with full laser power (405 nm wavelength) for up to one minute. Unfortunately, even after this long illumination time, it was not possible to cause a fusion of these droplets. One possible explanation is that the photolabile nitrobenzoyl linker has a low quantum yield and HFE 7500 absorbs in the UV region.[209–211] Therefore, the cleavage of the surfactant is very inefficient. In addition, there was an excess of photoliable surfactant in the fluorinated oil phase, which could replace the cleaved surfactant fast enough to prevent the fusion of the droplets.

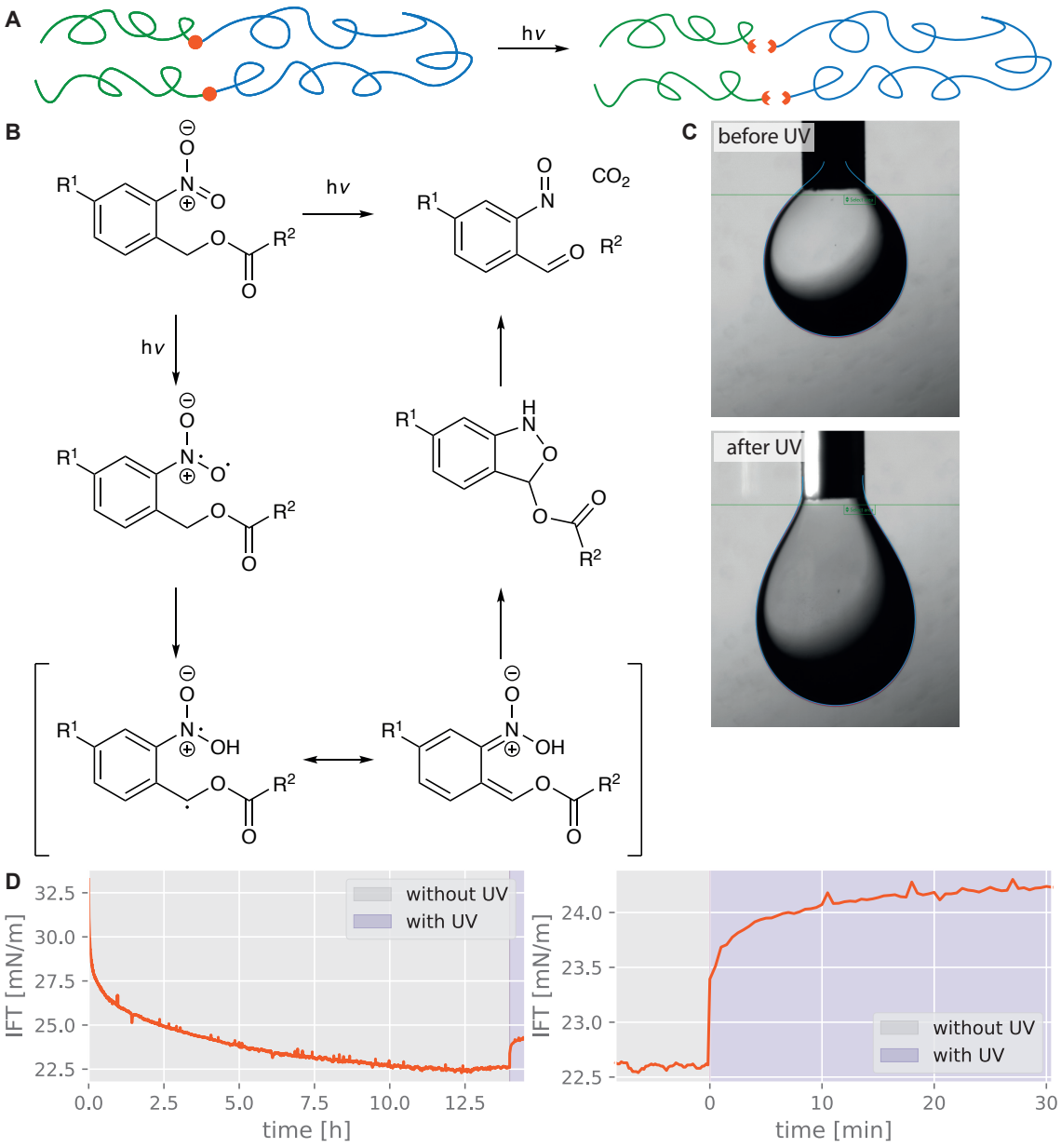


Figure 4.12: Light-induce cleavage mechanism of the PFPE-PEG bond in the photoliable triblock surfactant (plTS) **14** and IFT measurements. A: Schematic illustration and B: molecular mechanism of the light-triggered splitting of plTS **14**. By breaking the linkage between PEG block and PFPE blocks, the surfactant loses its amphiphilic property. C: Representative bright field images of the oil-in-water droplet stabilized by plTS **14**. The images were obtained during the pendant drop measurement before and after radiating the droplet with UV light. During illumination, clearly discernible particles formed, presumably consisting of the split-off PEG insoluble in fluorinated oil. D: Evaluation of the IFT values before and after light application.

Fluorescent diblock copolymer surfactant

Potential interactions between the block copolymer surfactants and the bio-content in many conditions are of particular importance. Therefore, designing a fluorescently labeled surfactant can help to analyze the diffusion coefficient of the polymers at droplet membrane and will shine a light on the nature of the surfactant interactions with the encapsulated bio-content or on their interactions with the other droplets or coverslips. Weiss *et al.* measured a diffusion coefficient of $0.13 \pm 0.03\,\mu m^2/s$ for labeled integrin bound to a gold linked surfactant. It is important to mention that due to the size of integrin and gold nanoparticle the measured diffusion coefficient does not directly represent the diffusion of surfactants and their interaction with the system.[11] Additionally, in case of charge-mediated formation of GUVs the labeled surfactants can be used to analyze whether residual surfactants subsequently adhere to the lipid bilayer of the releasedGUVs. Due to these reasons, I decided to synthesize a fluorescent PFPE-PEG-Rhodamin B surfactant (Figure 4.5D).

In a first step, propargyl amine was used to amidate rhodamine B. Towards this end, 2-bromo-1-ethyl-pyridinium tetrafluoroborate (BEP) and *N*,*N*-diisopropylethylamine (DIPEA) were used (Figure 4.13). Both chemicals are commonly used to perform amidation reaction during peptide synthesis.[212] At the end of the reaction, the rhodamine B derivative **15** was purified by flash column chromatography. In a click reaction with PEG600 diazide **8**, compound 16 was turned over to a mix of starting material **8**, one-end functionalized **16a** and both-end functionalized **16b**. The asymmetric and symmetric functionalized PEG **16a** and **16b** were isolated by extracting the starting material with DCM. Without further purification, the mix was used for a click reaction with propargyl PFPE **5** to receive the rhodamine B labeled surfactant fluorescent diblock surfactant (fluoDS) **17**. To this reaction, neocuproine was added to stabilize the catalyst and increase the efficiency.[194,195] While the purification, EDTA was added to the reaction mixture for binding the copper ions, what simplified their removal. All synthesis procedures are described in detail in Chapter 3.4.15 (page 42 to 44).

A solution of 2.5 mM cTS **6** with 5 mol% fluoDS **17** was used to produce w/o emulsion by emulsification method. The resulting droplets were placed in an observation chamber and analyzed using a confocal microscopy. Because of the high background caused by unbound fluoDS **17** in an oil phase, it was not possible to determine an accumulation of the surfactant on the water-oil interface. The excess of oil phase was removed and replaced by HFE 7500. With the reduced background, it was possible to observe the fluorescence on the droplets interfaces (Figure 4.14A). These droplets were used to determine the surfactants diffusion coefficient by the fluorescence recovery after photobleaching (FRAP) measurements. To achieve that, an area on the bottom

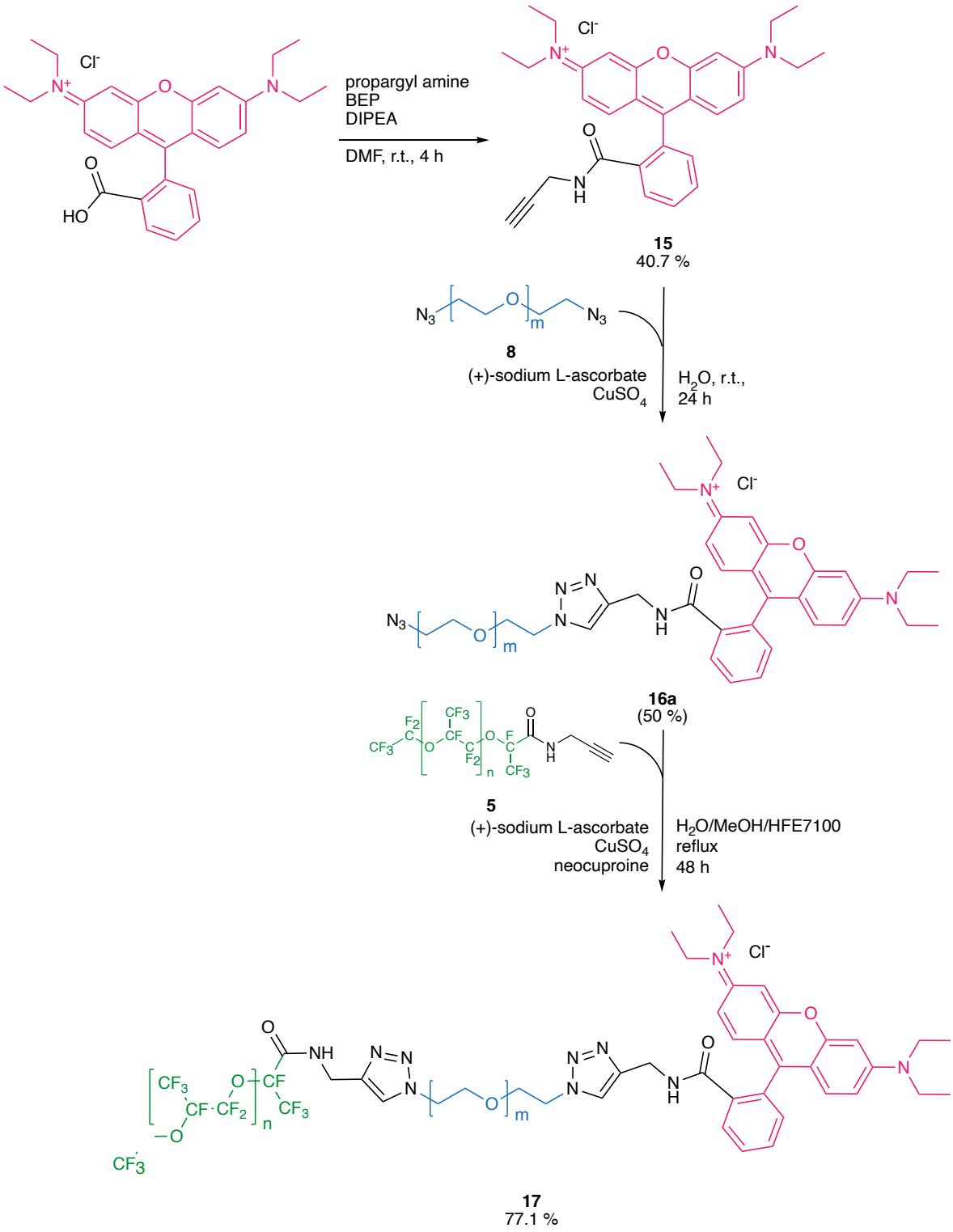


Figure 4.13: Synthesis of the rhodamine B labeled fluorescent surfactant fluoDS **17**. First, rhodamine B was amidated with propargyl amine using BEP and DIPEA. In a click reaction, the rhodamine B derivative **15** was coupled to obtain the asymmetric functionalized PEG **16a**. Propargyl PFPE **5** was connected to the other azide group in a second click reaction and the rhodamine B labeled surfactant fluoDS **17** was received.

of a droplet was bleached and the fluorescence recovery was analyzed (Figure 4.14B). This procedure was repeated on five different droplets. Average diffusion coefficient of $4.6 \pm 0.2\,\mu m^2/s$ was obtained. As expected the diffusion coefficient of the surfactants as obtained in this thesis is order of magnitude higher in comparison to the value obtained by Weiss *et al.* for labeled integrin bound to a gold linked surfactant.[11] Remarkably, the diffusion coefficient of $4.6 \pm 0.2\,\mu m^2/s$ is similar to the diffusion coefficients measured for different GUV lipid membranes. It is a bit surprising due to higher molecular weight of the block copolymer surfactants compared to lipids. However, the lower viscosity of HFE 7500 (0.77 cSt) compared to water (1.00 cSt) can be a potential explanation to similar values according to the Stokes-Einstein relation.[213–215]

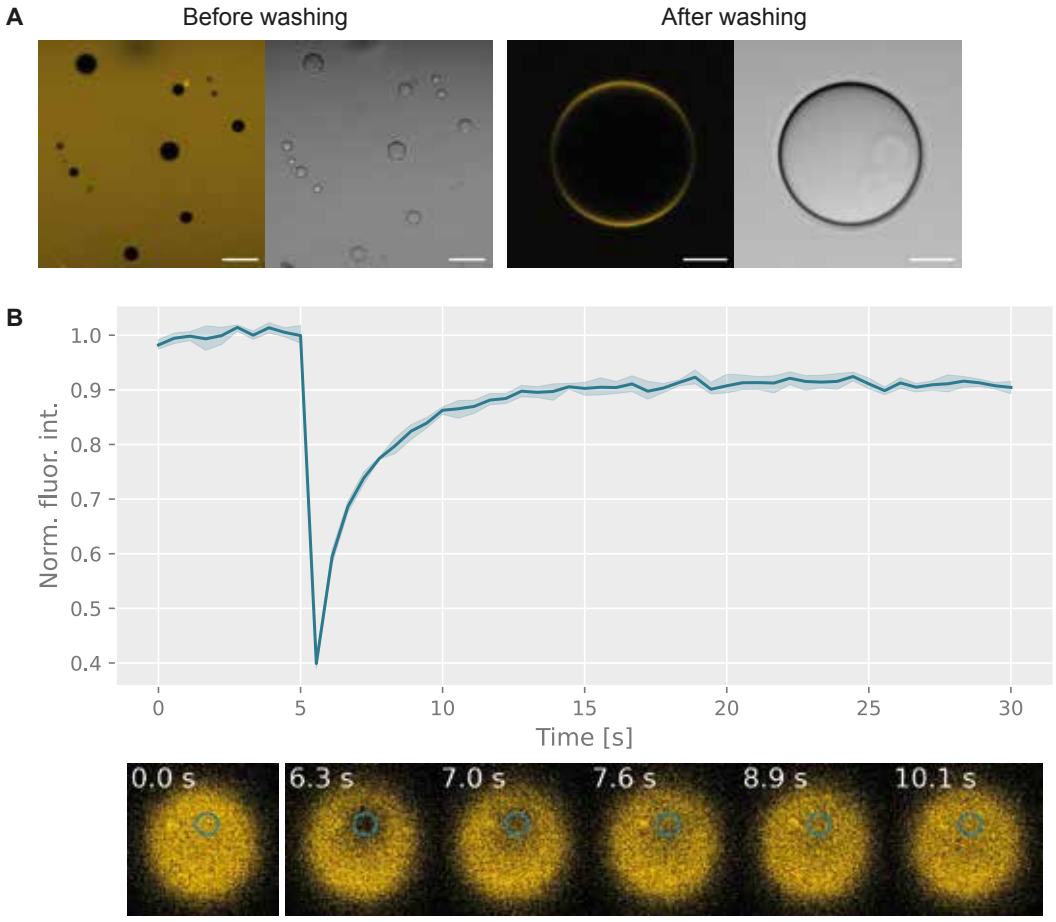


Figure 4.14: Representative confocal images and FRAP analysis of droplets stabilized by 2.5 mM cTS **6** with 5 mol% fluoDS **17**. A: Representative confocal fluorescence and bright field images of w/o droplets in HFE 7500. Scale bar: 50 μm for before washing, 10 μm for after washing. B: The diffusion coefficient of fluoDS **17** surfactant was determined by FRAP measurement.

In this section, I was able to show the synthesis of three functionalized surfactant: 1) the positively charged diblock copolymer surfactant posDS **11**. This surfactant could be used to improve the production of GUVs quantitatively (increased release

rate) and qualitatively (reliable lipid composition). It also enables the production of protein capsules for the encapsulation of bacteria and cells. 2) the photoliable triblock copolymer surfactant. Photolability could be achieved by inserting a nitrobenzoyl group between the PEG and PFPE blocks. I could show that irradiation by light increased the surface tension and separated the blocks from each other. However, this destabilization was not sufficient to fuse the droplets together. 3) the fluorescent diblock copolymer surfactant. With this surfactant it was possible to visualize the surfactant layer and to measure the diffusion coefficient of fluorinated block copolymers directly for the first time.

4.2 Synthetic cells adhesion interactions

In the previous section, I described different methods of surfactants synthesis that might be beneficial for the charge-mediated assembly of GUVs. In this section I will describe first how lipid composition can be implemented to design properly the GUV-based synthetic cells. Then, I will focus on introduction of different modules towards an artificial tissue assembly. Particularly, GUV-GUV interactions established by biotin-streptavidin connections or epithelial cell mimicking E-cadherin will be discussed. Additionally, integrin and actin cytoskeleton reconstitution and integrin-mediated interactions of synthetic cells with substrates will be described.

As an alternative to the protein-based GUV interaction and adhesion, a fully synthetic system using modified deoxyribonucleic acid (DNA) was established. For the interaction between synthetic cells a DNA with a palindromic sequence at the sticky ends was integrated. The complex reconstitution of integrin was able to be substituted by cholesterol-tagged DNA functionalization on the GUV and complementary, thiol-tagged DNA fixed on a block copolymer micelle nanolithography (BCML) gold nanoparticles functionalized surface. Finally, I will discuss the assembly of hybrid system in which the E-cadherin functionalized synthetic cells will be combined with natural cells.

4.2.1 pH-mediated construction of negatively charged GUVs

The production efficiency of GUVs by charge-mediated approach is mostly limited by the release efficiency. As discussed previously, the mechanism how the lipid membrane is assembled has a high influence on this step. For example, formation via simple electrostatic interactions like in the case of positively charged SUVs and negatively charged surfactant layer leading for more gentle release conditions with lower stress on lipid bilayer. In contrast, coordination complex mechanism that involves magnesium-mediated self-assembly of anionic SUVs on the negatively charged surfactant layer possesses higher stresses during the release and, therefore less efficient. Because of the cytotoxicity of cationic lipids,[96,216,217] especially with regard to experiments with cells, this type of charged vesicles was excluded from this study. To achieve the efficient release of negatively charged GUVs, a novel pH-dependent lipid composition that changes its charge based on the pH was designed in collaboration with Dr. Felix Lussier (Figure 4.15A).[102]

Walsh *et al.* studied several zwitterionic lipids, whose charge can be changed from neutral to positive by increasing the acidity of the environment. For example, DOBAQ lipids showed the biggest change in surface charge at a pH values lower then 5. Therefore, DOBAQ lipids were chosen for designing pH- mediated GUVs formation.

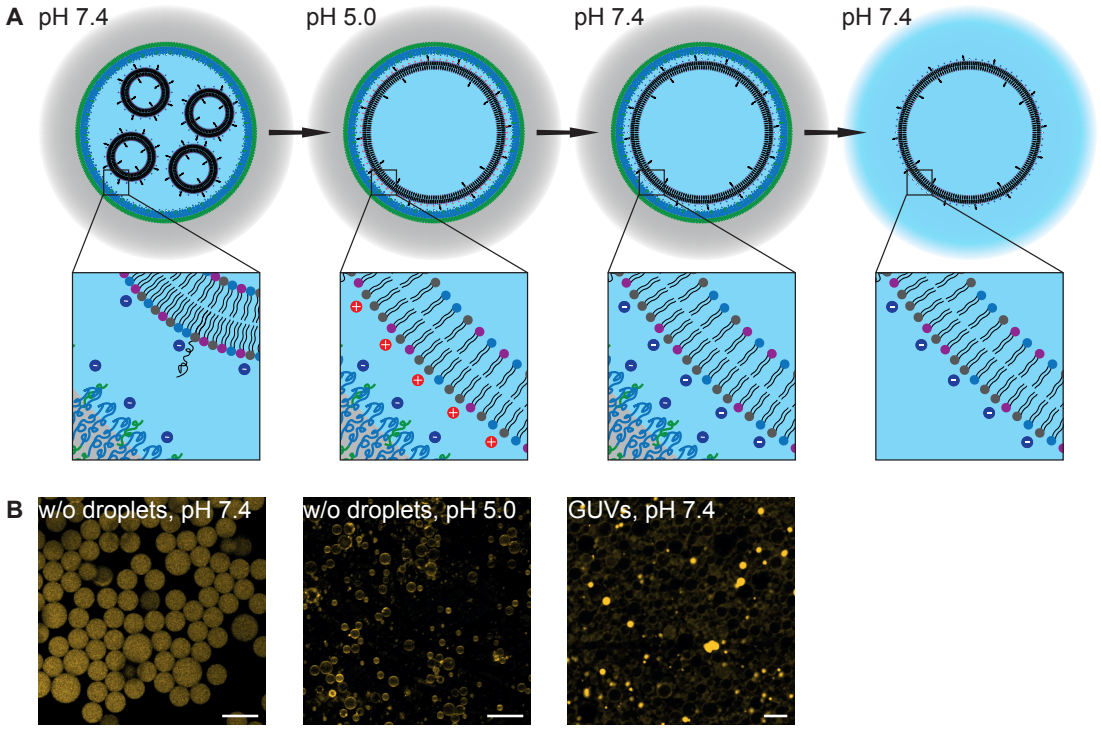


Figure 4.15: A: Schematic illustration of the pH-mediated GUVs formation. At a pH of 7.4, the SUVs containing the pH-sensitive lipid N-(4-carboxybenzyl)-N,N-dimethyl-2,3-bis(oleoyloxy)propan-1-aminium (DOBAQ) are negatively charged. Because both the surfactant layer (caused by Krytox) and the vesicle surface are negatively charged, they repulse each other. The Krytox reduces the pH value to around 5.0. Under this condition, the carboxylic acid of DOBAQ is protonated and the ratio between zwitterionic and positively charged DOBAQ shifts towards the cationic state, leading to more positive surface charge and enables a self-assembly of the lipid membrane on the water-oil interface. During the release step, the addition of the release buffer leading to increase in pH inside the GUVs and consequent DOBAQ deprotonation. The reduced interaction between the lipid membrane and the surfactant layer makes the release process more efficient. B: Representative confocal images of lipid containing droplets and the release GUVs. At pH 7.4, the fluorescence of the Liss Rhod PE containing SUVs is distributed equally. When the pH dropped to around 5.0, the vesicles accumulated on the water-oil interface and formed a lipid bilayer. For the release, excess of oil was removed and additional buffer as well as PFO were added while rotating the vessel. The release process resulted in a much improved amount of GUVs. Scale bar: 50 μm for w/o droplets, 25 μm for GUVs.

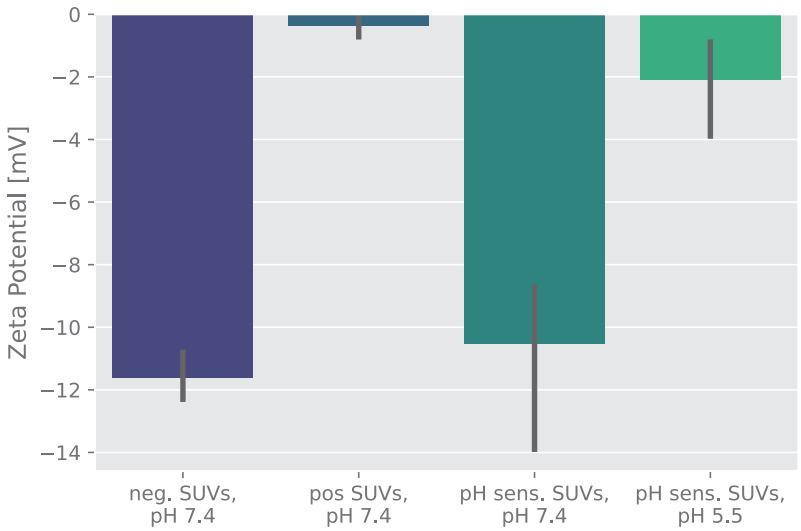


Figure 4.16: Zeta potential measurements of vesicles consisting of different lipid composition. The negatively charged SUVs consisted of 30 % DOPG, 69.5 % DOPC and 0.5 % Liss Rhod PE, the positively charged SUVs consisted of 30 % DOTAP, 69.5 % DOPC and 0.5 % Liss Rhod PE, and the pH-sensitive SUVs consisted of 30 % DOBAQ, 10 % DOPE, 20 % DOPG, 39 % DOPC and 0.5 % Liss Rhod PE). The measurements were performed in 140 mM potassium chloride and 30 mM Tris buffer were measured at pH 7.4 and the pH-sensitive lipids at pH 5.5 as well. The potential of pH-sensitive SUVs (ζ = -10.5 $\pm$ 3.0 mV) at pH 7.4 is comparable to the negatively charged lipids (ζ = -11.6 $\pm$ 0.8 mV). By decreasing the pH to 5.5 the zeta potential of the pH-sensitive SUVs is increasing too (ζ = -2.1 $\pm$ 1.6 mV).

For the pH-mediated formation of GUVs, SUVs consisting of 30 % DOBAQ, 10 % DOPE, 20 % DOPG, 39.5 % DOPC and 0.5 % Liss Rhod PE were implemented. At a physiological pH, most DOBAQ molecules exists as a zwitterion, therefore DOPG creates a net negative charge on the vesicle (Figure 4.15A). By decreasing the pH value, the ratio between zwitterionic and positively charged DOBAQ is shifting to the cationic side. At pH values close to 5, the amount of positively charged lipid molecules enables strong-enough interaction with the surfactant layer to self-assemble a lipid membrane. To verify the change in surface charge, the zeta potential of pH-sensitive SUVs was measured at a pH 7.4 and 5.0, and compared with negatively charged SUVs (30 % DOPG, 69.5 % DOPC, 0.5 % Liss Rhod PE) and positively charged SUVs (30 % DOTAP, 69.5 % DOPC, 0.5 % Liss Rhod PE). The measurements were performed in 140 mM potassium chloride and 30 mM Tris buffer at pH 7.4 (Figure 4.16). At a pH value of 7.4, the pH-sensitive SUVs have a zeta potential of -10.5 $\pm$ 3.0 mV, which is similar to the zeta potential of the negatively charged SUVs (-11.6 $\pm$ 0.8 mV). By decreasing the pH value to 5.0, the zeta potential of the pH-sensitive SUVs increased up to -2.1 $\pm$ 1.6 mV. It would be expected that positively charged SUVs would also measure a positively charged zeta potential. However, the high salt concentration in the buffer shielded the charge enough that a nearly neutral zeta potential of -0.4 $\pm$ 0.3 mV was measured.[218]

For the pH mediated dsGUV formation, it is necessary to control the pH value inside the GUV. To generate acidic conditions within the droplets, Krytox was added to the surfactant solution. To measure Krytox concentration dependent change, first a calibration curve using the pH dependent fluorescein was created (Figure 4.17A).[219] Towards this end, w/o droplets containing 1 μM fluorescein, 140 mM potassium chloride and 10 mM potassium phosphate buffer with different pH values in the range of 4.5 to 8.0 in the water phase and stabilized with 2.5 mM cTS **6** in HFE 7500 were produced. These droplets were imaged with a confocal microscope close to the equatorial plane and the mean fluorescence with an excitation at 488 nm was measured (Figure 4.17B). Subsequently, droplets with a potassium phosphate buffer at pH 7.4 and an oil phase composed of 2.5 mM cTS **6** and Krytox at the concentration range between 2.5 to 10 mM were generated. From the fluorescent intensity measured in the equatorial plane, the pH values inside the droplets were calculated using the previously created calibration curve. The images were taken by Dr. Félix Lussier. As can be observed in Figure 4.17C, Krytox at the concentrations of 2.5, 5.0, 7.5 and 10 mM resulted in pH values of 6.2, 5.9, 5.5 and 5.1, respectively. Due to these results, 10 mM Krytox was chosen for further experiments.

For pH-mediated assembly of GUVs, the aqueous phase consisted of 30 mM Tris buffer (pH 7.4) containing 140 mM potasium chloride, 100 mM sucrose and 2.0 mM

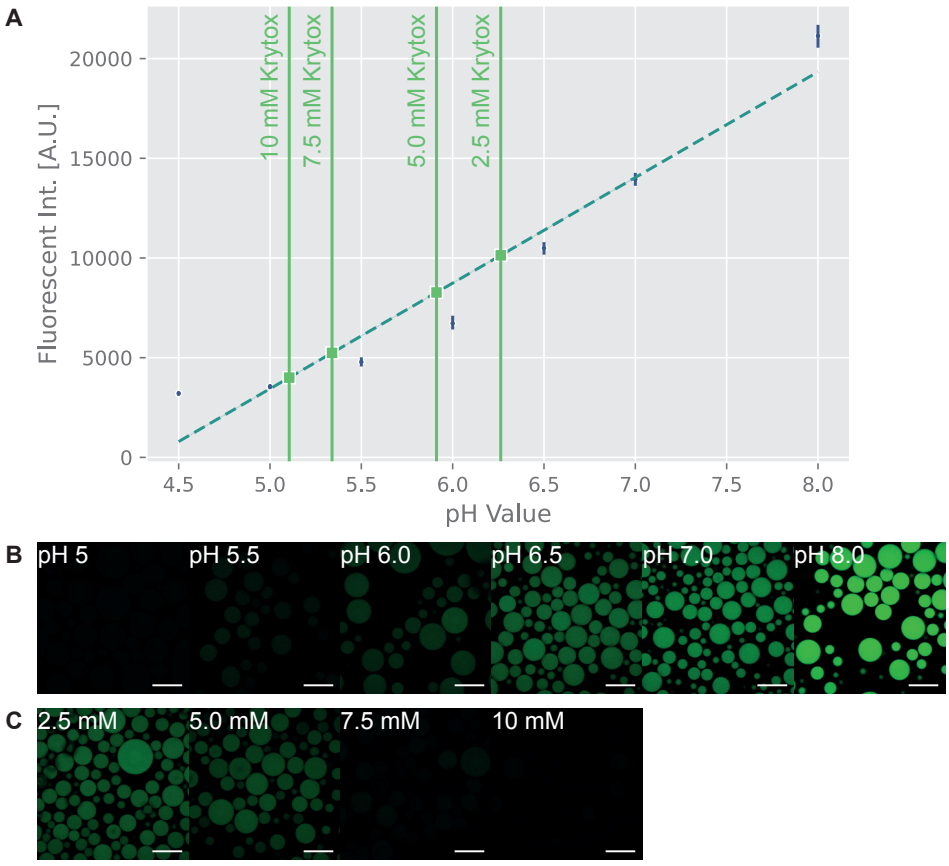


Figure 4.17: Effect of Krytox addition on the pH values within the droplets and the pH-mediated dsGUVs formation. A: W/o droplets containing 1 μM fluorescein, 140 mM and 10 mM potassium phosphate buffer at different pH values between pH 4.5 and pH 8.0 were generated with 2.5 mM cTS **6**. The droplets were imaged with a confocal microscope and the mean intensity was plotted against the respective pH value. A calibration curve was fitted to the measured data (dashed line). W/o droplets with pH 7.4 were produced using 2.5 mM cTS **6** dissolved in HFE 7500 with additional Krytox concentration between 2.5 and 10 mM. The pH values were calculated with the calibration curve. B: Representative confocal images of w/o droplets with adjusted pH values for the inner water phase. All images have the same intensity scale. Scale bar: 125 μm. C: Representative confocal images of w/o droplets with additional Krytox in the oil phase. All images have the same intensity scale. Scale bar: 125 μm. The images shown were taken by Dr. Felix Lussier.[102]

pH-sensitive SUVs (30 % DOBAQ, 10 % DOPE, 20 % DOPS, 39.5 % DOPC and 0.5 % Liss Rhod PE). Note, sucrose was added to increase the density within the assembled GUVs and the released buffer contained 100 mM glucose to match the osmolarity. Due to the density gradient, it is easier to pelletize the GUVs during the purification procedures and it is easier to image them at the bottom of the observation chamber. The oil phase composed of 2.5 mM cTS **6** and 10 mM Krytox in HFE 7500. The droplets were generated by emulsification or by microfluidics. At pH 7.4 DOPS determines the anionic surface charge since the DOBAQ is a zwitterion. Therefore, at neutral pH the surfactant layer and the SUVs are negatively charged leading to the repulsion from each other (Figure 4.15). By Krytox-mediated acidic conditions, DOBAQ lipids are protonated and the surface charge increases. At a pH values around 5.0, the surface charge of the SUVs increased enough to enable a recruitment of the vesicles on the water-oil interface for dsGUVs formation. Following incubation of the dsGUVs for several hours, the GUVs have been released. Towards this end, excess of the oil was removed and a buffer consisting of 30 mM Tris at pH 7.4, 140 mM potassium chloride and 100 mM glucose was added. Note, the addition of buffer probably increases the pH inside the droplets, leading deprotonation of DOBAQ and as a consequence the interaction of the surfactant layer and lipid membrane decreases. Therefore, following the addition PFO demulsifier, the GUVs were released into the release buffer. Compared to the release efficiency of the magnesium ion-mediated and the positively charged surfactant-mediated methods, the amount of released GUVs increased dramatically. The general procedures how to generate GUVs are described in Chapter 3.5.2 (page 50).

4.2.2 GUV-GUV interaction

Adherens junctions are one type of cell-cell interaction, that regulates trans-membrane proteins the actin cytoskeleton and play an important role in different cellular signaling pathways.[15,220] These junctions are mediated by transmembrane protein E-cadherin in a calcium ion-dependent manner.[15,221] Because of the key function of E-cadherins in adherens junction, I aimed to reconstitute these proteins into the GUVs membranes for the formation of GUV-GUV interactions. It is important to mention here that the isolation of full-length E-cadherin is very difficult. Maker *et al.* published a protocol for full-length E-cadherin purification for the first time in 2022.[222] Therefore, in this thesis only the extracellular domains (Asp155 to Ala709 human E-cadherin) were used for the adherens junctions formation. Additionally, I tested different approaches for the controlled interactions between GUV-based synthetic cells.

As a first approach, the interaction between GUVs was created using the biotin-streptavidin interaction. This bond is one of the strongest non-covalent bindings in biological systems.[223] Therefore, GUVs consisting of 1 % 18:1-12:0 Biotin PE, 30 %

DOPG, 1 % Liss Rhod PE and 68 % DOPC in a 1x phosphate-buffered saline (PBS) were generated with the microfluidic method (Figure 4.18). Streptavidin, labeled with ATTO 425, was added to a concentration of 50 μg/mL. In order for the GUVs to come into contact and thus enable GUV-GUV adhesion, the GUVs were shaken overnight at 300 rpm. As control, GUVs without streptavidin were prepared in a similar way. The experimental procedure is described in detail in Chapter 3.5.2 (page 52). In case of streptavidin-functionalized GUVs, it could be observed that the GUVs interacted with each other leading to the deformation of the vesicles. Furthermore, the fluorescence signal for labeled streptavidin accumulated on the adhesion surface. In the control experiment, only single GUVs were spotted. Because this experiment was done before optimizing surfactants and lipid composition, the release rate was low and just small clusters compared with later experiments were formed. Nevertheless, the result gives an expectation, how GUV-GUV adherens junction should look like.

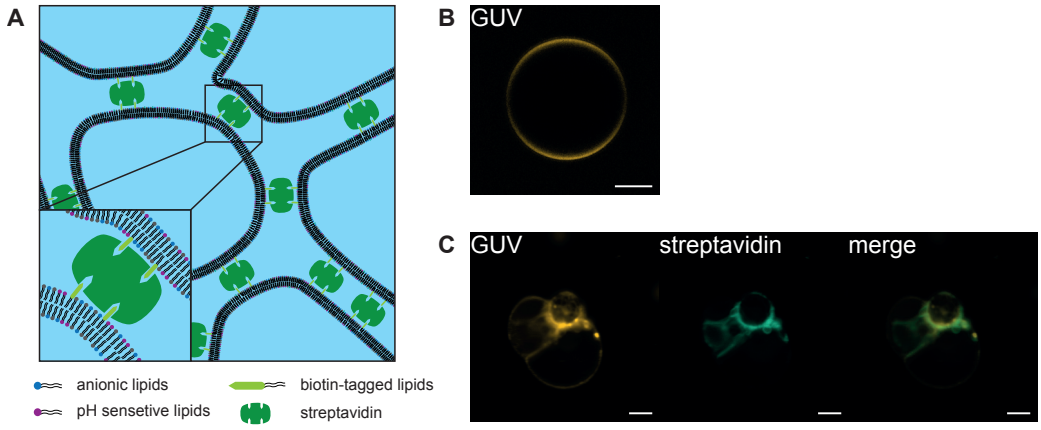


Figure 4.18: Biotin/streptavidin-mediated adherens junction of GUVs. A: Schematic illustration of the biotin/streptavidin-mediated interaction. B: Representative fluorescence confocal image of the control experiment in which no streptavidin was not added. No GUV clusters were observed. C: Representative confocal image of biotin-labeled GUVs. The addition of streptavidin mediated the adherens junction between vesicles. An accumulation of ATTO 425-labeled streptavidin was observed on the adhesion surfaces.

For the E-cadherin-mediated formation of the adherens junctions the extracellular domains of E-cadherin was linked to the GUVs via the nickel(II)-nitrilotriacetic acid (NTA)-polyhistidine tag (His tag) coordination complex. The recombinant E-cadherin domains were expressed with a His Tag at the C-terminus and bought from commercial source. The pH-sensitive lipid composition of the vesicles was slightly modified to add 1 % of 18:1 1,2-dioleoyl-sn-glycero-3-succinate (DGS)-NTA. However, addition of 1 % 18:1 DGS-NTA(Ni) affected the GUV release efficiency dramatically. The reduced release efficiency can be attributed to stronger interactions between NTA, nickel(II) ions and the carboxylic acid group of PFPE. Therefore, 18:1 DGS-NTA without coordinated

nickel(II) was used and the central ion was added directly to the GUVs after the release (Figure 4.20).

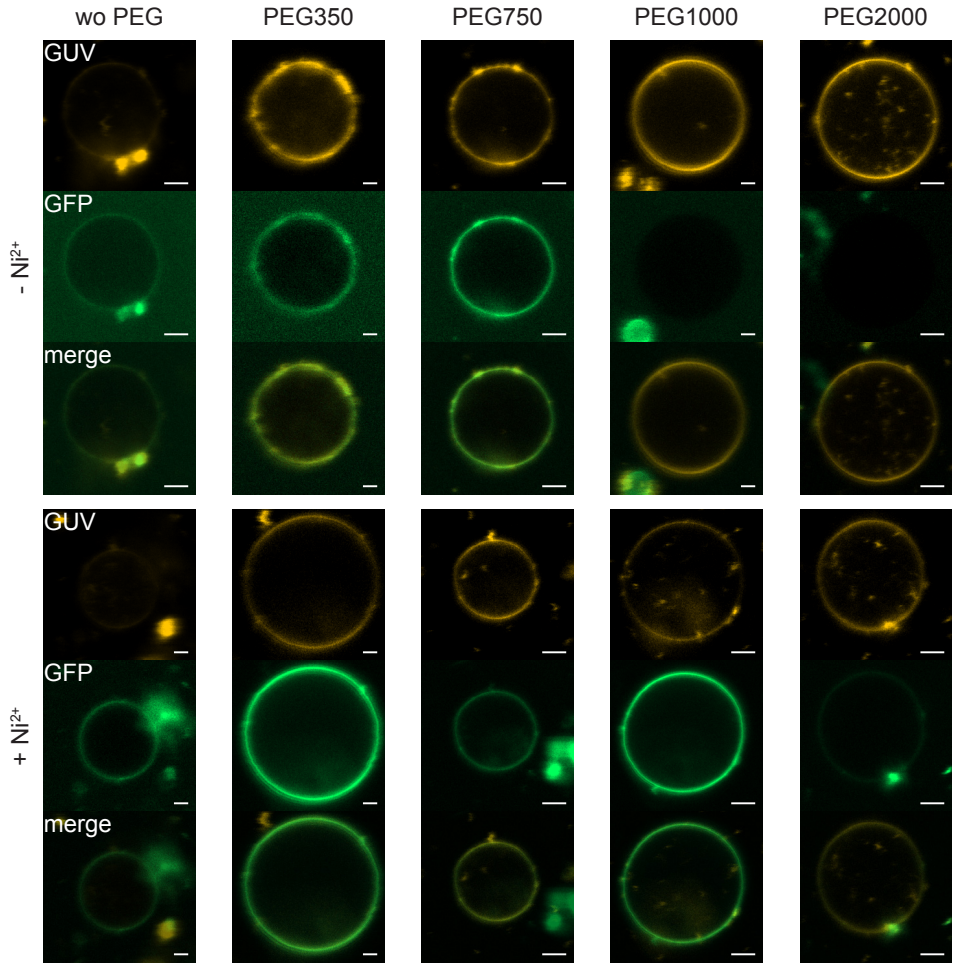


Figure 4.19: Representative fluorescence confocal images of His-tagged GFP interactions with PEGylated and not PEGylated GUVs and in presence and absence of nickel(II) ions. Scale bar: 2 μm.

Because both GUVs and E-cadherin are charged, a potential charge-mediated unspecific interaction between the protein and the vesicle can happen. To prevent this unspecific interaction PEGylation of the membrane can help. The shielding effect of different PEG length was analyzed by modifying the lipid composition to 30 % DOBAQ, 6 % DOPE, 20 % DOPS, 38.5 % DOPC, 1 % 18:1 DGS-NTA, 4 % 18:1 PEG PE and 0.5 % Liss Rhod PE with average molecular mass of PEG of 350, 750, 1000, and 2000 g/mol. Following the release, part of the GUVs were functionalized with nickel(II) ions, and the control GUVs were not exposed to nickel(II) ions. The GUVs were incubated with His tag green fluorescent protein (GFP) for one hour. The analysis of confocal images for the not PEGylated GUVs revealed unspecific accumulation of GFP on the lipid membrane even without presence of nickel(II) ions. The GUVs with PEG350 and PEG750 showed similar results. Above an average molecular mass

of 1000 g/mol of PEG, shielding was efficient and no colocalization of GFP with the vesicle membrane was observed. For all samples in which nickel(II) ions have been presented, the GFP signal was colocalized on the lipid membrane. Therefore, PEGylation of GUV membrane does not block the specific binding of His Tag proteins with the NTA functionalized lipids. For further experiments, 18:1 PEG2000 PE was used because it better shields the non-specific interactions due to its higher molecular mass and still allows specific NTA-His Tag binding. The experimental procedure of this experiment is described in detail in Chapter 3.5.2 (page 53).

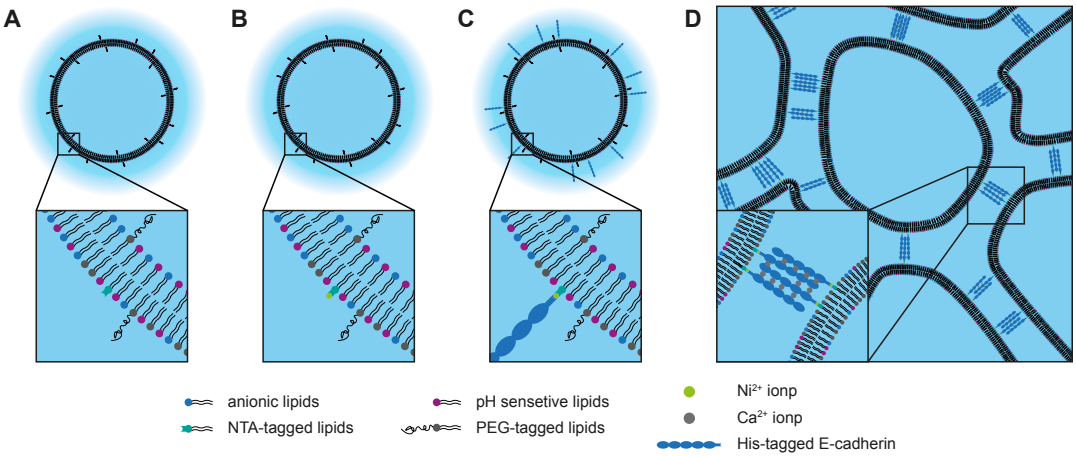


Figure 4.20: Schematic step-wise representation of GUV functionalization with E-cadherin. A: Released GUV with 18:1 DGS-NTA lipids. B: Complexing Nickel(II) ions with the NTA lipids. C: Interaction of recombinant E-cadherin via His-tag with the Nickel(II) NTA lipids on the membrane of the GUV. D: E-Cadherin mediated adherens junction between GUVs.

For the construction of E-cadherin-functionalized GUVs, 2.0 mM of pH-sensitive SUVs (30 % DOBAQ, 6 % DOPE, 20 % DOPS, 38.5 % DOPC, 1 % 18:1 DGS-NTA, 4 % 18:1 PEG2000 PE and 0.5 % Liss Rhod PE) in 30 mM Tris buffer at pH 7.4 containing 100 mM sucrose and 140 mM potassium chloride were used. For GUVs production either microfluidic or the emulsification methods were implemented. Both methods are described in detail in Chapter 3.5.2 (page 50). For the droplet production, the HFE 7500 oil phase contained 2.5 mM cTS **6** and 10 mM Krytox. After the release and purification, outer buffer with additional 2.0 mM nickel(II) chloride was mix 1:1 with GUVs to complex the nickel(II) ion with the NTA group. In a control group, this step was skipped. Following additional GUVs purification His tag E-cadherin solution, 25 μL of 250 μg/mL was added and incubated at 4 °C for 5 h. For the assembly of adherens junctions In a 96 well plate, the wells were passivated with bovine serum albumin (BSA). GUVs were mixed with outer buffer containing 50 mM calcium chloride in addition in a ratio 4:1 and shaken over night at 4 °C. After settling down, the whole wells were imaged with a fluorescent microscope and representative areas with

a confocal microscope. The results are partly shown in Figure 4.21 and a summary for each condition are described in the appendix (see pages XVIII to XXXIII). To exclude an interaction with rhodamine B, the experiment was repeated for the same lipid composition and theLiss Rhod PE was replaced by ATTO 488 DOPE (see Appendix pages XXXIV to XLI). Following the optimization steps I was able to generate an exceptionally large amount of GUVs. The procedure for assembly E-cadherin-mediated adherens junctions is described in detail in Chapter 3.5.2 (page 53).

To analyze the E-cadherin-mediated adherens junctions, a Z stack was recorded on a confocal microscope and the ZX projection, as well as the ZY projection, were calculated for each condition (Figure 4.21). In the conditions, where E-cadherin was not added some interactions between single GUVs could be observed. These interactions can be attributed to the centrifugation during the purification steps. Considering the ZX and ZY projections, the GUVs laying all flat on the surface. By adding E-cadherin, the interaction between the GUVs significantly increased. More interactions were observed also in the conditions, where neither nickel(II) nor calcium ions were added. However, analysis of ZX and ZY projections showed that the created clusters are very flat (20 to 30 μm). This can be explained by weak unspecific interaction between the unspecific bound E-cadherins on the different GUVs. These interactions can be supported by potassium ions, which have low complex stability constant with NTA of 0.6, which does not give stability enabling big networks.[224] By adding calcium ions instead of nickel(II) ions, there is already a wide network created up to a height of around 100 μm. Calcium ion can on the one hand initiate the E-cadherin-mediated adherens junction, and on the other hand, it can produce stable complexes with NTA and the His Tag of E-cadherin. Its complex stability constant of 6.45 is still smaller than the one for nickel(II) ions (11.54), but high enough to stabilize the formed GUV network. With E-cadherin and nickel(II) ions as well as calcium ions, the interaction increased furthermore. So, the height of the GUV networked observed in the ZX and ZY projection increased up to 200 μm. And by deflation, they tried to increase the adhesion surface in a way that they became more compact and the fluorescent signal intensity increased. Note, the fluorescence images of the well show that the effect of the single conditions as discussed for a representative area appears in the whole sample. Similar observations can be described for the samples with the ATTO 488 PE instead of Liss Rhod PE, from which a dye dependence of the experiment can be excluded.

I was able to show a first GUV-GUV adhesion cluster mediated by biotin-streptavidin. Afterwards, I optimized the E-cadherin functionalization of GUVs to increase the selectivity of GUV-GUV interactions by PEGylating the GUVs. Finally, the dependency of E-cadherin, nickel(II) ions and calcium ions for the construction of a GUV network was analysed.

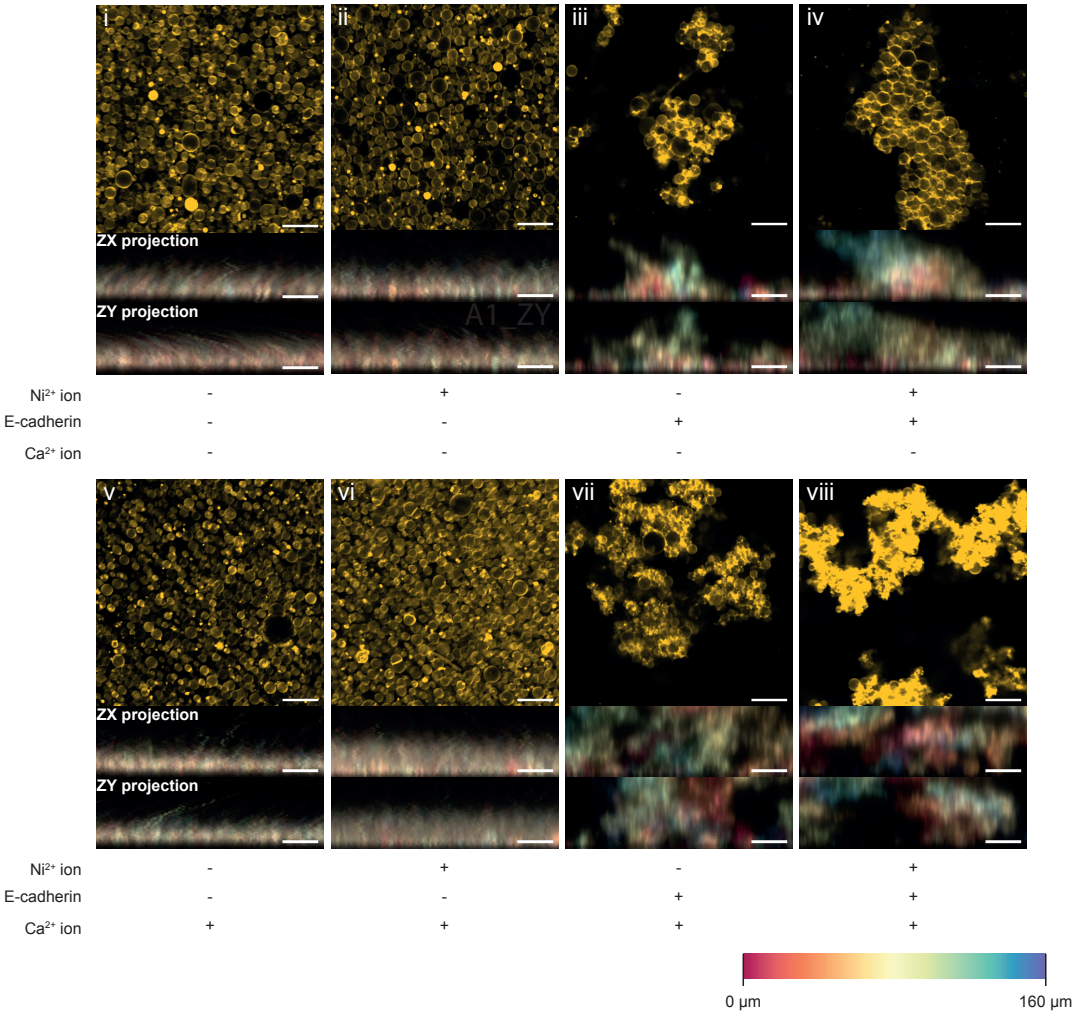


Figure 4.21: Representative fluorescence confocal images of the assembly of E-cadherin-mediated adherens junctions as achieved at different experimental conditions. In the samples without E-cadherin (i, ii, v, vi), there is no interaction between the GUVs beside some sporadic adhesion between single GUVs. By adding E-cadherin, even without any additional metal ions, the GUVs start to cluster (iii). These interactions are stabilized by unspecific interactions, therefore only small clusters are observed at the bottom of the well. By adding nickel(II) ions (iv), E-cadherin is bound to the NTA-tagged lipids, but still there is no specific interaction between the E-cadherins, the formed clusters are just formed on the bottom of the well. In the presence of calcium ions instead of nickel(II) (vii), a GUV network was formed which was up to 100 μm in height. Calcium ions are important for the E-cadherin self-interactions and can coordinate as central ion NTA and the His tag of E-cadherin, but not as strong as nickel(II) ions. By adding both metal ions, calcium and nickel(II), the adherens junctions increased so much that the GUVs were deflated to increase the adhesion surface (viii). This increased the fluorescent signal in the respective areas. Scale bar: 25 μm.

4.2.3 GUV-substrate adhesion

Achievement of adhesion of synthetic cells to the extracellular matrix (ECM) is a necessary step towards assembly of an artificial tissue. In this regard, integrin proteins play a major role in transmembrane signaling by providing the linkage between the ECM and the cellular cytoskeleton.[13,57] In this thesis I will concentrate on integrin $\alpha_{\mathrm{IIb}}\beta_3$, which has been purified inn our department and has been previously tested for reconstitution in synthetic cells.[11,173] To overcome the limitations related to electroformation or dsGUV methodes my ultimate aim was to introduce functional integrin into GUVs (Figure 4.22) in reproducible and efficient manner using an alternative complementary DNA-mediated approach. Therefore, pH-sensitive GUVs were generated as described in Chapter 4.2.1 (page 87) and prepared for the fusion with the proteoliposomes by adding cholesterol-tagged fusion DNA A. In parallel, the proteoliposomes (i.e., integrin-reconstituted liposomes) were prepared. The proteoliposomes were functionalized with a complementary fusion DNA A' and the selectivity of this process was analyzed and will be discussed. To trigger the adhesion, the integrin proteins were activated with manganese(II) ions and their adhesion on a fibrinogen coated surfaced was analyzed.

The surface charge of SUVs for the integrin $\alpha_{\mathrm{IIb}}\beta_3$ reconstitution has a high influence on reconstitution efficiency. Galkin *et al.* could show that it is possible to achieve detergent-free reconstitution of membrane proteins into oppositely charged SUVs.[225] according to their protocol I tried to reconstitute the negatively charged integrin $\alpha_{\mathrm{IIb}}\beta_3$ into cationic SUVs. However, I was not able to reproduce the results from Galik *et al.* Therefore, I used a slightly modified protocol from Erb *et al.*[226] The protocol was optimized regarding Triton X-100 removal and lipid composition (see Chapter 3.5.2). Towards this end, in collaboration with Dr. Felix Lussier, a size-exclusion chromatography (SEC) method was developed to rapidly remove Triton X-100 (Figure 4.23). To proof the efficiency of this method, the ultraviolet (UV)/Vis spectrum of 250 μM SUVs (30 % DOPG, 70 % DOPC), 0.1w/v % Triton X-100 and 250 μM Triton X-100 containing proteoliposomes (30 % DOPG, 70 % DOPC before and after SEC was recorded in the range from 200 to 300 nm. Triton X-100 has its maximum absorbance at 276nm.[181] To reduce the background caused by the plate, the samples were measured in a quartz 96 well microplate. In case of the samples with only Triton X-100, it was possible to remove around 89 % of the detergent. In proteoliposome sample, 93 % of Triton X-100 was removed. The remaining peak at around 230 nm is attributable to the absorbance of integrin.[227] The removal percentage was calculated from the background-corrected absorbance at 276 nm. The experimental procedure for purifying proteoliposomes with SEC is described in detail in Chapter 3.5.2 (page 54).

Following detergent removal, the influence of SUV surface charge on the reconstitution of integrin was explored. Therefore, negatively charged (30 % DOPG, 70 %

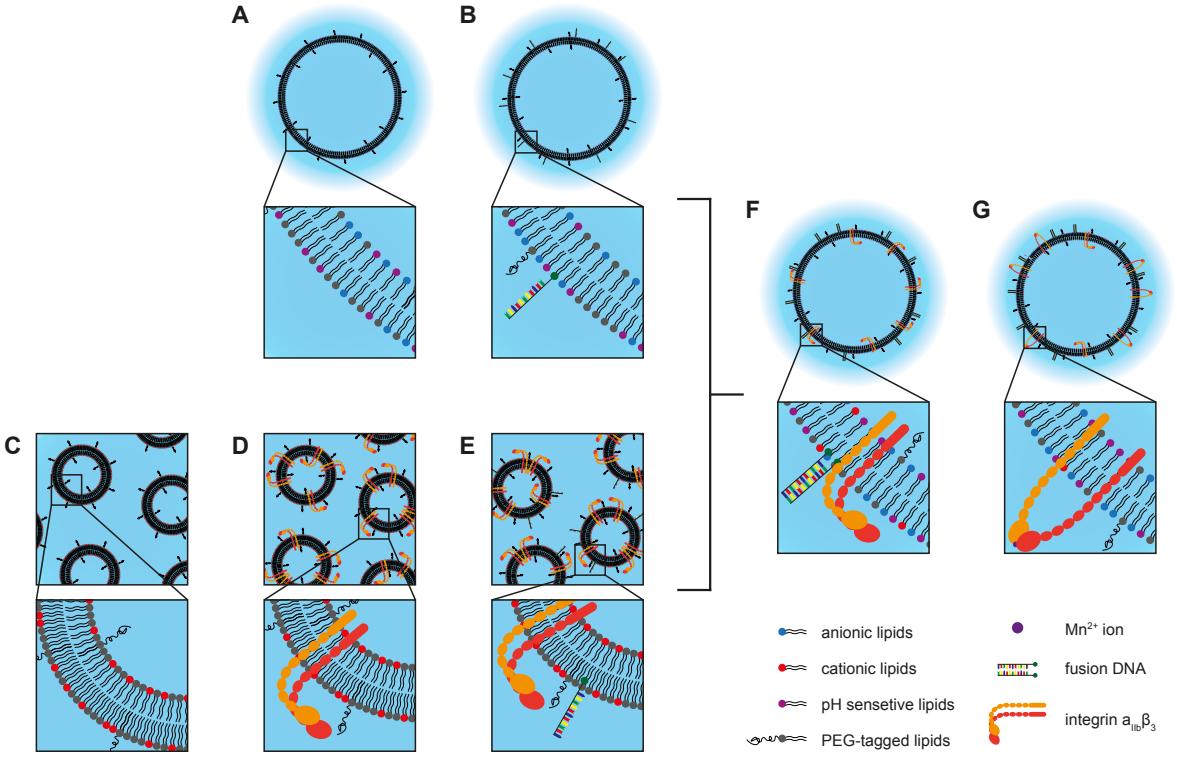


Figure 4.22: Schematic illustration of the complimentary DNA-mediated fusion of GUVs with integrin reconstituted proteoliposomes. (A) pH-sensitive GUVs were prepared and (B) functionalized with cholesterol tagged fusion DNA A. (C and D) Integrin $\alpha_{\mathrm{IIb}}\beta_3$ is reconstituted into positively charged SUVs. (E) Functionalization with fusion DNA A'. (F) the proteoliposomes are mixed and fused with the complementary DNA functionalized GUVs. (G) The reconstituted integrin proteins are activated outside with manganese(II) ions.

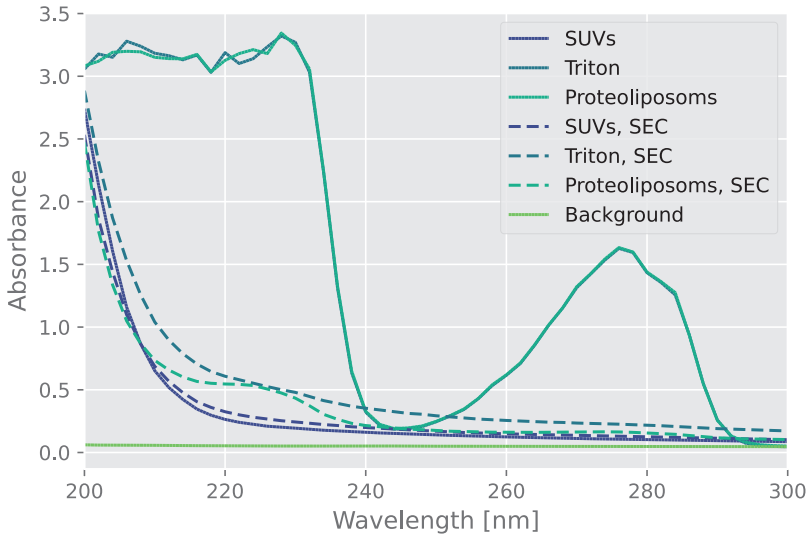


Figure 4.23: Comparative UV/Vis spectra of SUVs, Triton X-100, and integrin reconstituted proteoliposomes before and after SEC purification.

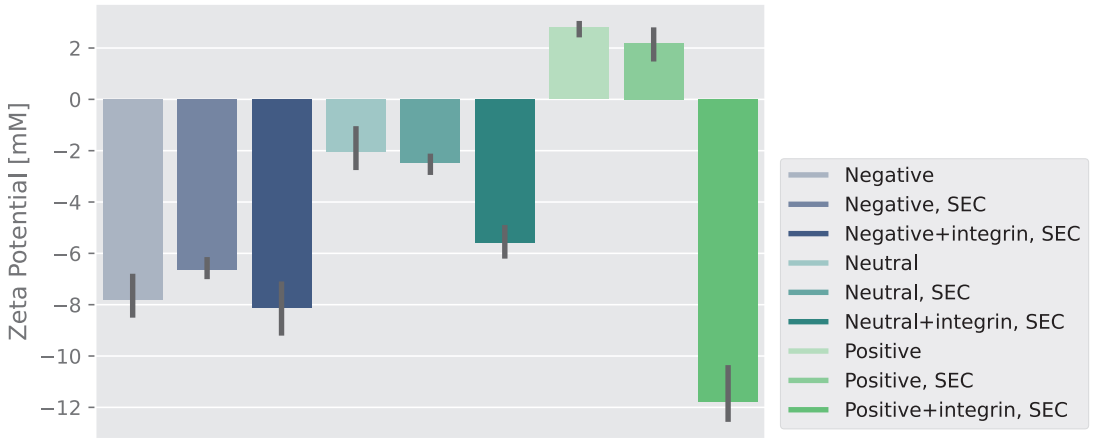


Figure 4.24: Zeta potential measurements of differently charged SUVs before and after integrin reconstitution.

DOPC), neutral (100 % DOPC) and positively charged (30 % DOTAP, 70 % DOPC) SUVs were produced and integrin $\alpha_{\mathrm{IIb}}\beta_3$ was reconstituted as described above. The zeta potential of the SUVs was measured before and after reconstitution (Figure 4.24). To exclude that the change in zeta potential was caused by SEC, the zeta potential of the SUVs was measured after SEC. The SUVs and proteoliposomes were diluted to a concentration of 50 μM in 30 mM Tris at pH 7.4, 50 mM sodium chloride, 90 mM potassium chloride and 0.5 mM calcium chloride. For the negatively charged SUVs, a zeta potential of -7.8 $\pm$ 0.8 mV was determined. After SEC, the zeta potential increased slightly to -6.6 $\pm$ 0.4 mV, and in the purified proteoliposomes decreased again to -8.1 $\pm$ 1.0 mV. For the neutral SUVs, zeta potentials of -2.1 $\pm$ 0.8 and -2.5 $\pm$ 0.4 mV were determined before and after SEC, respectively. After reconstituting integrin, the zeta potential dropped to -5.6 $\pm$ 0.6 mV. For the positively charged SUVs, zeta potentials of 2.8 $\pm$ 0.3, 2.2 $\pm$ 0.6 mV and -11.8 $\pm$ 1.2 mV were measured before, after the SEC filtration and for the proteoliposomes, respectively. Based on these results one can conclude that SEC has no influence on the zeta potential of the vesicles. Using the negatively charged SUVs for proteoliposome formation, the zeta potential did not change significantly, indicating that reconstitution of integrin proteins was not efficient or did not occur. In case of neutral SUVs, the reconstitution was more efficient due to a bigger decrease in zeta potential. The best reconstitution occurred for the positively charged SUVs. Therefore, the positively charged SUVs were used for further integrin reconstitution.

The activity of the proteoliposomes was tested with an adhesion assay using surface plasmon resonance (SPR) (Figure 4.25). Therefore, a gold-sputtered SPR prism was functionalized with fibrinogen. To achieve that, the prism was first functionalized with 3-mercaptopropionic acid overnight. After starting the measurement, the carboxylic acid groups on the prism surface reacted with 1 mM *N*-hydroxysuccinimide

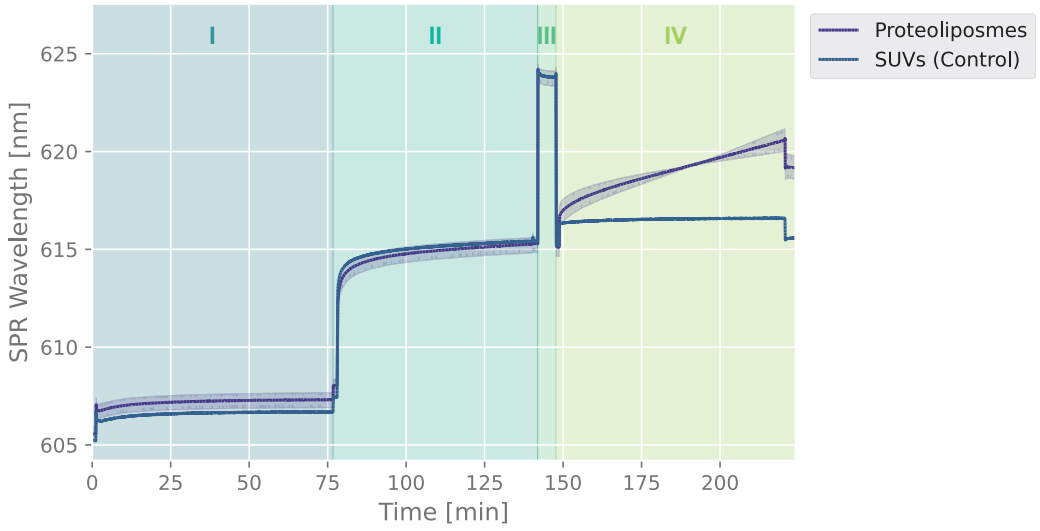


Figure 4.25: SPR measurements of the adhesion of integrin-reconstituted proteoliposomes. The SPR prism with free carboxylic acid groups on the surface was prepared. I: The carboxylic acid was converted into a NHS ester by adding NHS and EDC HCl. II: Fibrinogen was added and it was bound to the surface by primary amines reacting with the NHS ester. III: Unreacted NHS ester was deactivated with ethanolamine. IV: Proteolipsomes and SUVs in integrin activation buffer were allowed to interact with the fibrinogen surface. Following washing steps, higher SPR wavelength shift can be observed in case of proteoliposomes.

(NHS) and 2 mM 1-ethyl-3-(3-dimethylaminopropyl)carbodiimide hydrochloride (EDC HCl) for 75 minutes to obtain NHS esters (step I in Figure 4.25). Afterwards, the prism was washed with 4-(2-hydroxyethyl)-1-piperazineethanesulfonic acid (HEPES) buffer (30mM HEPES at pH 7.4, 140 mM potassium chloride). Following the washing step, 250 nM fibrinogen in HEPES buffer wasadded. The primary amines of fibrinogen reacted with the NHS ester leading to immobilization of the fibrinogen on the surface (step II in Figure 4.25). After 60 minutes, the prism was washed with HEPES buffer. The remaining NHS esters on the surface were blocked with ethanolamine, which was washed away after five minutes with integrin-activation buffer (30 mM Tris at pH 7.4, 50 mM sodium chloride, 90 mM potassium chloride, 1.0 mM calcium chloride, 1.0 mM magnesium chloride and 1.0 mM manganese(II) chloride) (step III in Figure 4.25). Proteoliposomes or positively charged SUVs (1 μM each) were seeded in integrin-activation buffer to interact with the fibrinogen. Higher shift in the SPR wavelength was achieved in the case of proteoliposome sample, indicating better interactions with fibrinogen. After 80 minutes, the prism was washed with integrin activation buffer (step IV in Figure 4.25). The increased SPR wavelength shift reveals an adhesion of the proteoliposomes on the functionalized prism and shows that the integrins in the proteoliposomes are active.

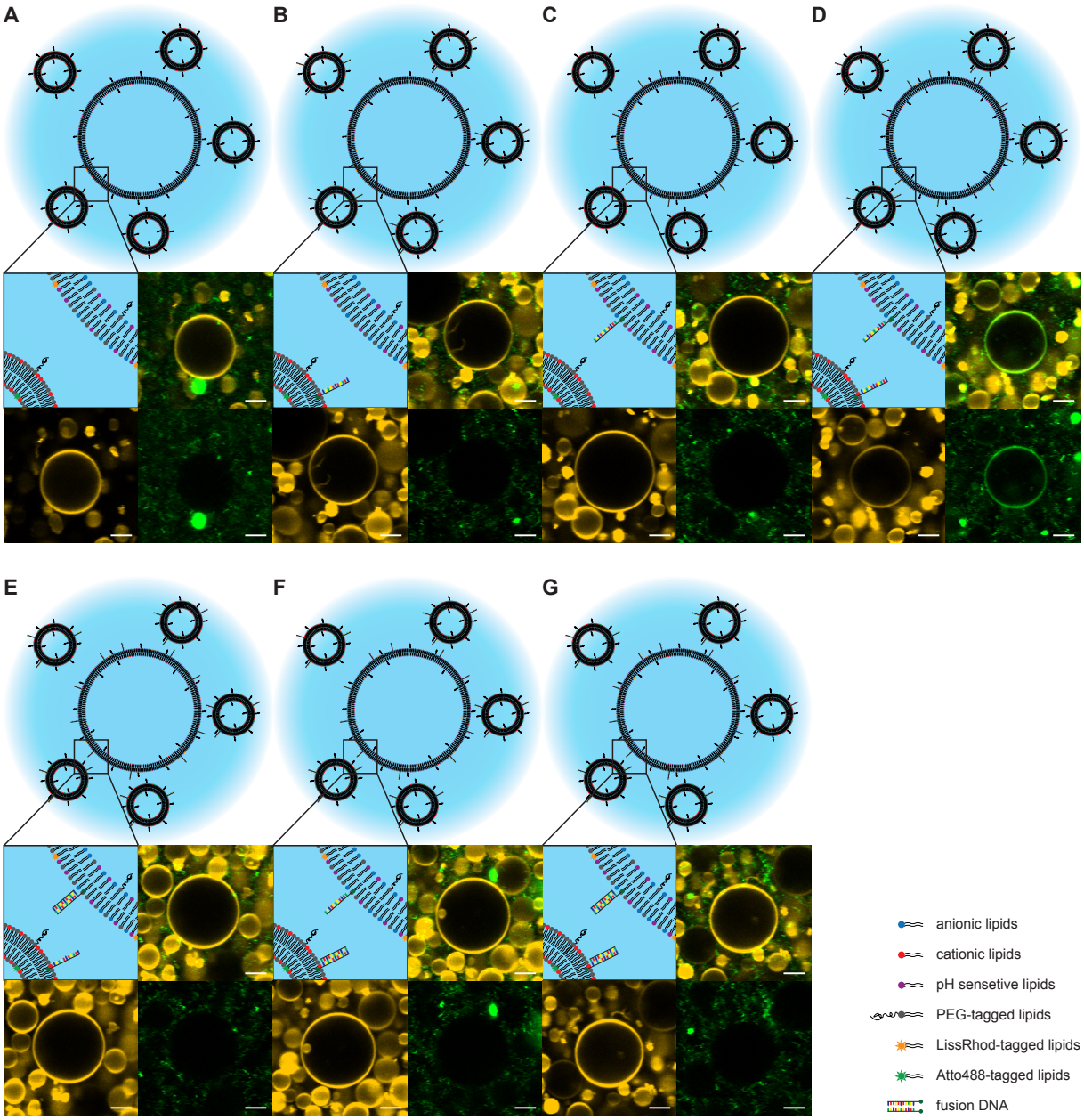


Figure 4.26: Schematic representation and representative fluorescence confocal images of the DNA-mediated vesicle fusion. In addition to non-functionalized SUVs and GUVs (A), the following vesicles were used: SUVs or GUVs functionalized with DNA A (B), DNA A' (C) and DNA A and A' (D) before mixing them. For the first three conditions, no fusion of the vesicles could be observed. Only when both vesicles were functionalized with the respective fusion DNA, a colocalization of both lipid membranes could be observed. In an additional experiment, blocking DNA, with the same sequence like the particular fusion DNA but without cholesterol tag, was added to prevent the fusion. For this purpose, blocking DNA A' was added to GUVs with fusion DNA A (E), blocking DNA A to SUVs with fusion DNA A' (F), or both blocking DNAs with the respective vesicle (G) before incubating them together. All three condition were sufficient enough to block the vesicle fusion.

Following SEC purification and SPR-based adhesion assays, for the reconstitution of integrin proteins into GUVs the proteoliposomes were fused with GUVs using a DNA-based complimentary approach (Figure 4.22).[228–231] Towards this end, DNA A (5'-TCG ACA CGG AAA TGT TGA ATA CTA-3') with a cholesterol tag on the 5' end and the complementary fusion DNA A' (5'-TAG TAT TCA ACA TTT CCG TGT CGA-3') with a cholesterol tag on the 3' end, were designed. In a first experiment, the selectivity of this fusion was verified. Therefore, pH-sensitive GUVs composed of 30 % DOBAQ, 6 % DOPE, 20 % DOPS, 39.5 % DOPC, 4 % 18:1 PEG2000 PE and 0.5 % Liss Rhod PE were generated in Tris buffer (30 mM Tris at pH 7.4, 140 mM potassium chloride) and, if indicated, decorated with fusion DNA A. Furthermore, positively charged SUVs composed of 30 % DOTAP, 69.5 % DOPC and 0.5 % ATTO 488 DOPE were produced in Tris buffer and, if indicated, decorated with fusion DNA A'. The pH-sensitive GUVs, without and with fusion DNA A, were mixed with the positively charged SUVs, without and with fusion DNA A', and all four combinations were incubated for two hours at 4 °C. Afterwards, they were placed into observation chambers and imaged with confocal microscope (Figure 4.26A-D). For the conditions where no fusion DNA, only fusion DNA A or A' were added, no interactions between the SUVs and the GUVs could be observed. Only by adding both fusion DNAs to the respective vesicles, a colocalisation of SUVs and GUVs was visible. Note, it could be observed, that in case of traces were observed, the SUVs agglomerated due to the charge interaction with the Krytox (Figure 4.26A, below the GUV). The experimental procedure of this experiment is described in detail in Chapter 3.5.2 (page 54).

As an additional control, blocking DNA with the same sequence as fusion DNA A and A', but without the cholesterol tag, were designed. So, either blocking DNA A', blocking DNA A or both DNAs strands were added to the respective vesicles (blocking DNA A' to GUVs with fusion DNA A, and blocking DNA A to SUVs with fusion DNA A') before mixing them (Figure 4.26E-G). Already one blocking DNA, negligible which one, was already enough to hinder the fusion.

Adhesion of integrin $\alpha_{\mathrm{IIb}}\beta_3$ reconstituted GUVs was tested on a fibrinogen coated surfaces. To prepare the fibrinogen coated surfaces, a pre-cleaned glass coverslip was activated in a plasma machine.[182] The coverslip was covered with 0.1 mg/mL fibrinogen (for the control experiments, 0.1 mg/mL poly-L-lysine (PLL)-PEG was used) for 60 minutes and unbound material washed away. The silicone chamber of the ibidi "12 Well Chamber, removable" chamber slide was glued with two-component glue on the functionalized glass coverslip. The integrin reconstituted GUVs were generated as described above. For the control experiments, the vesicle suspension was directly used. To let the GUVs settle down and interact with the fibrinogen surface, 100 μL of the suspension was placed inside the prepared wells and incubated over night at 4 °C. The

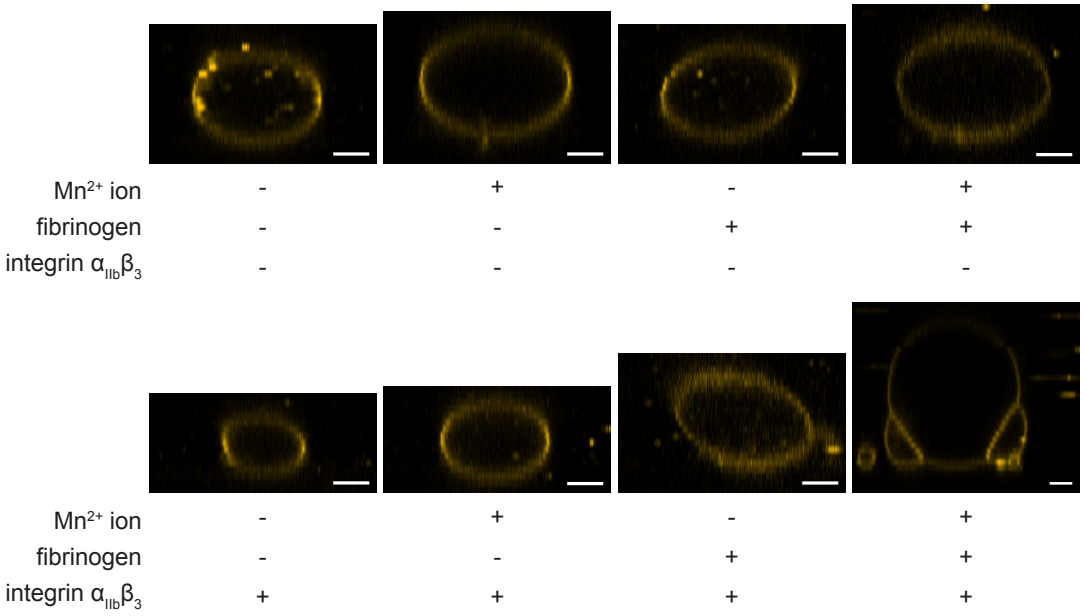


Figure 4.27: Representative fluorescence confocal images of XZ plane of the integrin $\alpha_{\mathrm{IIb}}\beta_3$ reconstituted GUV adhesion on a fibrinogen coated surface and respective control experiments. The oval shape of the GUV, even if they are not attached to the surface, is caused by the higher density because of sucrose in the inside buffer. A substrate adhesion, indicated by a flat contact area of the GUV with the substrate, could only be observed in case manganese(II) ions activated integrin reconstituted GUVs on a fibrinogen surface. Scale bar: 2 μm.

integrin-mediated adhesion was verified by doing control experiments with and without manganese(II) ions, with and without fibrinogen, and with and without integrin $\alpha_{\mathrm{IIb}}\beta_3$ (Figure 4.27). The experimental procedure of this experiment is described in detail in Chapter 3.5.2 (page 54).

The shape of the GUVs in contact with the surfaces is oval due to the density gradient between the inner GUV buffer that contains 100 mM sucrose and the outside buffer that contains 100 mM glucose. For an adhesive GUV, it is expected to have a flat surface in the adhesion area. This was observed only for the condition, where integrin $\alpha_{\mathrm{IIb}}\beta_3$ was reconstituted into GUVs on a fibrinogen surface and activated with manganese(II) ions. Additionally, some GUV-GUV interactions were observed for these conditions. The hypothesis is that the fibrinogen was only attached to the surface because of electrostatic interaction, and could detach. The dissolved fibrinogen could the cause an interaction between the GUVs. After fusing the proteoliposomes with the GUVs, the amount of observed GUVs decreased by estimated 70 % to 90 % and the proportion of small GUVs increased. One reason could be, that the proteoliposomes still contained Triton X-100, which can destabilize GUVs. This reason could be determined by repeating the SEC purification step a second time. Another possibility is that the reconstituted integrins were too heavy and the GUV membrane too fragile to hold

together and thus the lipid bilayer ruptured. To prevent this, either less integrin could be reconstituted or the rigidity of the GUVs could be increased, for example by a cytoskeleton or increased viscosity, for example by adding methyl cellulose or OptiPrep.

4.2.4 Reconstitution of actin cytoskeleton

Actin cytoskeleton is involved in many processes such as regulation of transcription, cell division and cell migration.[68] In particular, its involvement in cell mobility and mechano-signaling makes it a key player in the construction of an artificial tissue. Different methods to reconstitute actin into GUVs have been explored previously.[232–234] In this chapter, an improved method for the construction of GUVs with an actin cytoskeleton using droplet-based microfluidics will be introduced. One major drawback in microfluidic-based charge-mediated assembly of GUVs is to co-encapsulate F-actin or actin monomers due their negatively charged surface that leads to the disturbance of the system.[235] There is a possibility to deliver actin into the dsGUVs subsequently by picoinjection.[11] However, during the process of injection, the droplets can fuse because of the pressure and the method is susceptible, in particular, to the clogging of the injection channel, which makes it difficult to achieve a stable and uniform process. Moreover, application of electric field may destabilize and destroy the preassembled droplet supported lipid bilayer.

Therefore, in this thesis a new microfluidic device was designed with three inlets: one for the surfactant-containing oil phase, one for low viscous aqueous actin actin polymerization buffer (APB) containing SUVs, and one for high viscous globular actin (G-actin) in adenosine triphosphate (ATP)-free buffer (Figure 4.28).

For the droplet production, solutions of 2.5 mM cTS **6** and 10 mM Krytox dissolved in HFE 7500, 3.0 mM pH-sensitive SUVs in APB (20 mM Tris, 140 mM KCl, 4 mM $MgCl_2$, 2 mM ATP), and 20 μM actin in actin buffer (AB) (20 mM Tris, 140 mM KCl) with 10 v/v% OptiPrep were prepared. The oil phase was connected with the outer inlet, the SUV phase in the middle inlet, and the actin phase in the inner outlet, as described in Figure 4.28. With a pressure controller, the solutions are flushed into the device and the droplets were collected from the outlet. Afterwards the droplets were incubated over night at 4 °C and release into 20 mM Tris, 140 mM KCl, 100 mM glucose and 2 mM $MgCl_2$. The procedure is described in detail in Chapter 3.5.2 (page 55).

In the previously described dsGUVs approaches in which actin was co-encapsulated the actin destirbd the bilayer formation due to charge-mediated interaction with the Krytox. Moreover, actin starts to polymerize instantly in the polymerization buffer, therefore if that happened before the droplets were formed, filamentous actin (F-actin) could clog the microfluidic channels. Therefore, in the new device, actin is encapsulated in a high-viscous solution with OptiPrep inside the SUVs in APB. This allows the SUVs

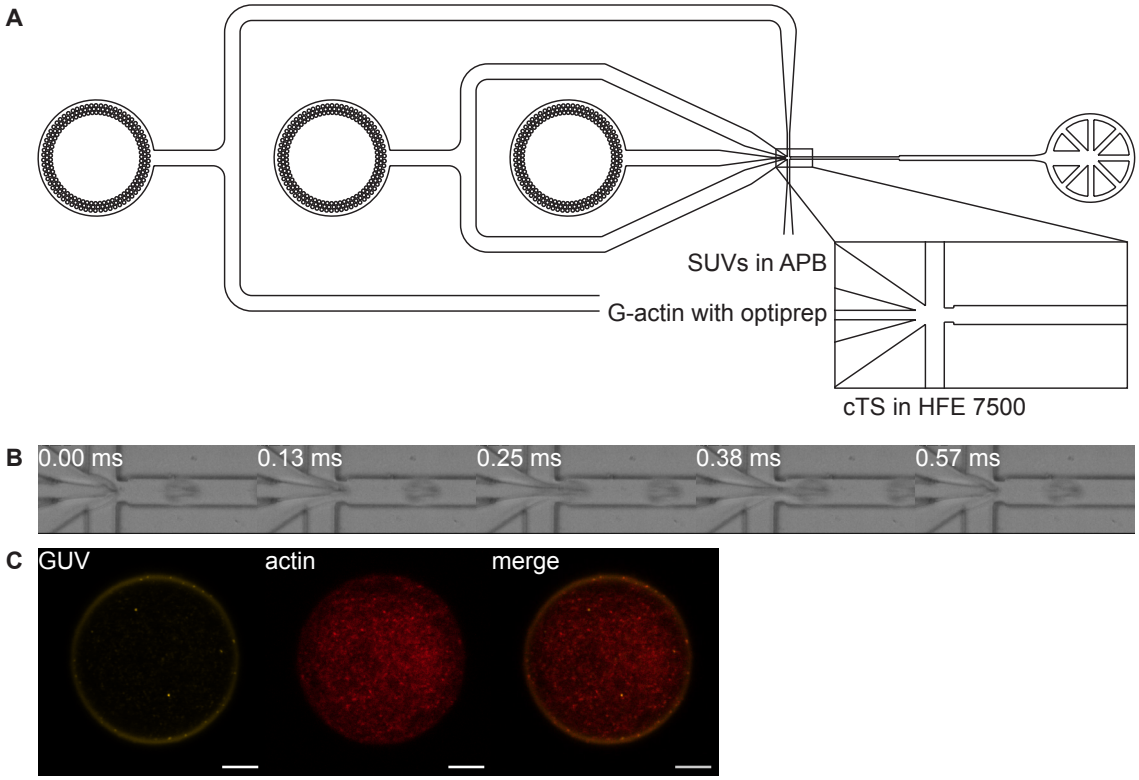


Figure 4.28: Actin cytoskeleton reconstitution within GUV-based synthetic cells. A: Design of a microfluidic device, which was used to produce an OptiPrep drop in w/o droplets. B: Time series of bright field images recorded with a high speed camera of the droplet production process. The OptiPrep drop inside the droplet stands out well against the other water buffer because of its difference in refractive index. The drop stayed assembled during the production process. C: Representative confocal images of released actin cytoskeleton loaded GUV. Scale bar: 2 μm.

to first self-assemble at the water-oil interface to form a lipid bilayer. Afterwards the OptiPrep drop dissolves in the inner buffer and enables the polymerization of G-actin inside the dsGUV. Then, it was possible to receive after the release process GUVs with an intact actin cytoskeleton inside (Figure 4.28C).

4.2.5 DNA-mediated adhesion in GUV-based synthetic cells

In bottom-up synthetic biology natural proteins are key players in reconstitution of certain cellular functions such as adhesion, sensing and many other. However, the implementation of natural proteins often comes with some complications. Starting with production and purification, through storage and handling there are always protein-dependent conditions that have to be considered for their proper implementation.[236,237] To overcome these complications is to use more stable molecules to replace the activity of proteins. In bottom-up synthetic biology DNA is one of the candidates to replace the functions of the natural proteins because of its flexibility and ease of handling. Compared to proteins, DNAs have improvements concerning programmability, tunability and handleability. For example, Jahnke *et al.* replaced the actin cytoskeleton with DNA and Thomsen *et al.* used DNA nanopores as membrane channels.[167,238]

In this chapter, I will describe the DNA-based synthetic alternatives to integrin and E-cadherin proteins for the formation of GUV-based adherens junctions and ECM adhesion. For the GUV-GUV adherens junction, a DNA sequence was designed with a palindromic sticky end, tagged with ATTO 488 and with cholesterol (Figure 4.29A). A palindromic sequence has the same sequence like the complementary DNA in the same reading direction. This type of sequence enables a self-interaction of the DNA strands. DNA-based substrate adhesion could be induced with two differently functionalized DNA strands. One DNA strand was functionalized with a thiol group, which was used to immobilize the DNA onto a BCML surface on gold nanoparticles.[239] The complementary DNA strand was incorporated into the GUV membrane with a cholesterol tag. The sticky ends are such that application of force causes the DNA duplex to unzip.[240,241] Of this type of DNA pair, three with different long sticky ends (short, middle, long) were used to vary the binding strength. Furthermore, the thiol DNA strand was labeled with a fluorophore (Cy3) and the cholesterol DNA strand with a suitable Förster resonance energy transfer (FRET) acceptor (BMN-Q620).[242] Thus, it should be possible to identify the areas of specific DNA-based adhesion by quenching the DNA-bound fluorophores at the substrate surface.

For the GUV-GUV adhesion experiment, pH-sensitive GUVs where generated as described in Chapter 4.2.1 (page 87) in 30 mM Tris, 140 mM potassium chloride, 100 mM glucose. To the GUV suspension, pre-assembled, palindromic DNA duplex (sequence 1: `TGA AGT TTA ATT AAA CTT CAG GCC ATC GTC GCT ATA TAT ATA TAT TAT`

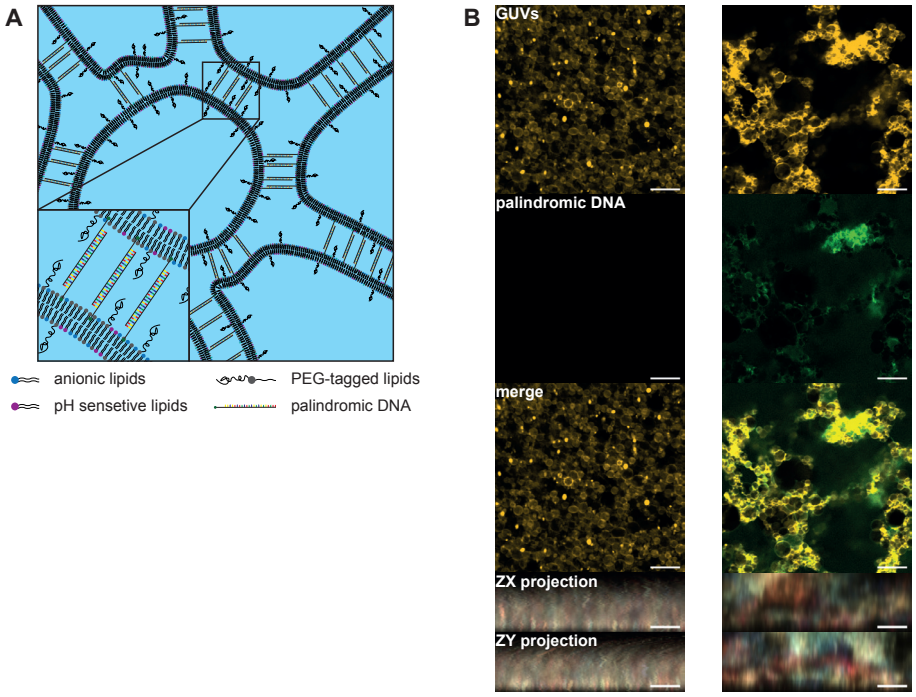


Figure 4.29: A: Schematic representation of the DNA-mediated assembly of adherens junctions between the GUV-based synthetic cells. B: Representative fluorescence confocal images of pure GUVs and functionalized with DNA. The XY-level confocal fluorescence images show the interaction of GUVs in one Z plane. Scale bar: 25 μm.

T with 3'-CholTEG; sequence 2: TAT AAT ATA TAT ATA TAG CGA CGA TGG C with 5'-ATTO 488) was added, placed in a well of a 96 well plate and shacked over night at 300 rpm. As control pH-sensitive GUVs without adding DNA were shaken over night as well. After letting them settle down for one hour, the GUVs were imaged with a fluorescent and confocal microscopes (Figure 4.29, and Appendix from page XLII to XLIV). The experimental procedures are described in Chapter 3.5.2 (page 56). For the control experiment without DNA, no adhesion could be observed. By adding the palindromic DNA, the GUVs formed a network comparable to the network achieved by implementation of E-cadherin proteins. The colocalization of GUVs and DNA appears especially in the areas of strong interaction. The ZX- respectively ZY-projection show the GUV arrangement in 3D. Without DNA, the GUVs just lay on the bottom of the well, whereby with self-interacting DNA they build a network in 3D up to 150 μm height. Without the addition of DNA, no interaction between the GUVs could be observed (Figure 4.29B).

For the DNA-mediated interactions of GUVs with the functionalized surfaces the GUVs where generated as described in Chapter 4.2.1 (page 87). They GUVs were incubated together with cholesterol tagged surface adhesion DNA for one hour; one sample for each sticky end length (short, middle and long). A gold-nanostructured surfaces generated by BCML (provided by Dr. Ilia Platzman) were cleaned and activated in

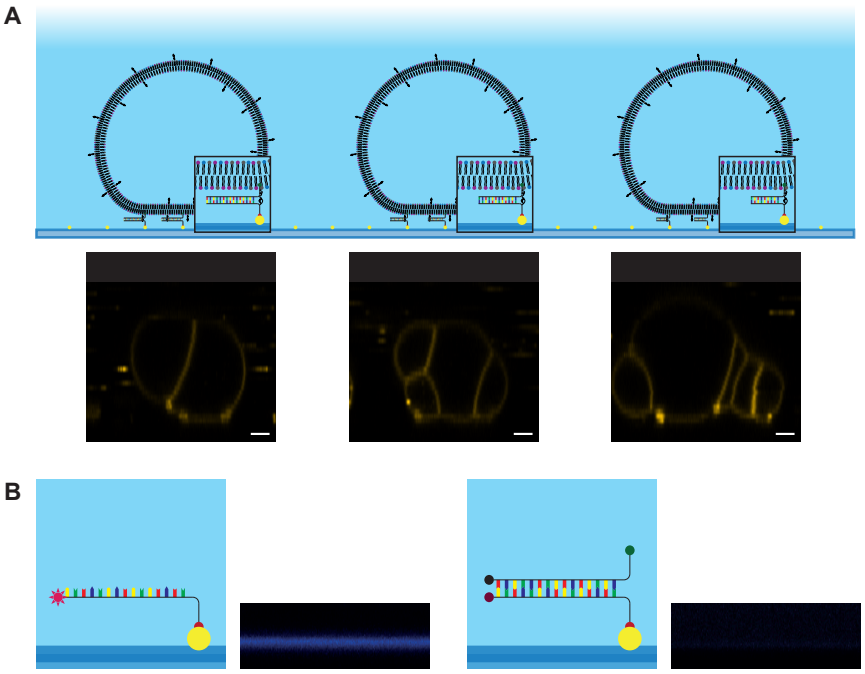


Figure 4.30: Schemes and representative confocal images of DNA-mediated surface adhesion. A: For this, DNA with a thiol group was immobilized on a BCML functionalized surface. A complementary DNA strand with a cholesterol tag was incorporated into the GUV membrane. Three different DNA pairs were used for varying the interaction strength between the sticky end sequence to program the adhesion force. B: A FRET resonance pair was added to the DNA to enable a specific bleaching of adhesion area.

a plasma machine. Subsequently, the glass surfaces were passivated with PLL-PEG and the DNA was immobilized on the gold nanoparticles via thiol-based chemistry; one glass slide per different DNA length. The prepared glass surfaces were attached under a silicone chamber of the ibidi "12 Well Chamber, removable" chamber slide. The GUVs were seeded into these chambers, settled down for one hour and imaged with confocal fluorescence microscopy (Figure 4.30A). Adhesion to the glass surface was observed for all three DNA strands. In addition, GUV-GUV interactions were observed as well. These interactions can be attributed to the unspecifically bound thiol-tagged DNA on the GUV's membranes. These DNA molecules can potentially interact with the complementary cholesterol-tagged DNA in lipid membrane, led to adhesion between the GUVs. Unfortunately, no difference in adhesion to the surface, for example due to a stronger curvature at the adhesion side, could be observed for the three DNA strands. This can probably be attributed to the very low rigidity of GUVs. By increasing the rigidity, for example by increasing the viscosity inside by e.g. methylcellulose or with an actin cytoskeleton, it can be assumed that the three DNA strands show a clearly different behavior. In flow experiments or by increasing the temperature, differences due to the different binding strengths of the DNA duplexes should be observed.

In a separate experiment, the surface was prepared as described above using thiol functionalized surface adhesion DNA labeled with Cy3. In solution, the complementary, cholesterol tagged surface adhesion DNA containing the quencher BMN-Q620 was added. The XZ plane through the glass surface was imaged using a confocal microscope (Figure 4.30B), before and after the addition of quencher DNA. Because of the Cy3 tag, the glass plane was clearly visible. After adding the quencher DNA, the fluorescent intensity on the glass plan decreased. The same experiment was repeated using GUVs containing quencher DNA. Unfortunately, it was not possible to obtain the same results as with solubilized DNA. This observation can be explained by the fact that probably the density of quencher DNA in GUVs is lower than in solubilized DNA. Thus, significantly fewer Cy3-containing DNA strands were quenched at the surface and this is lost in the background noise of the non-quenched fluorophores.

I was able to show that the functionality of the adhesion proteins E-cadherin and integrin $\alpha_{\mathrm{IIb}}\beta_3$ can be mimicked by functionalized DNA strands. In these experiments, DNA was shown to be much easier to handle compared to proteins and assays were noticeably simplified.

4.2.6 Hybrid system

Synthetic lipid vesicles can have a high impact on natural cells research. For example, Staufer *et al.* were able to establish a method to use the interactions between GUVs and

cells for drug delivery or synthetic extracellular vesicles have demonstrated biomedical applications in wound healing processes.[98,100,243,244] These examples already show the potential of how synthetic cells can have an impact on cells as well as intercellular and intracellular processes. Therefore, a first approach towards a hybrid tissue consisting of natural cells and GUVs is shown in Figure 4.31A.

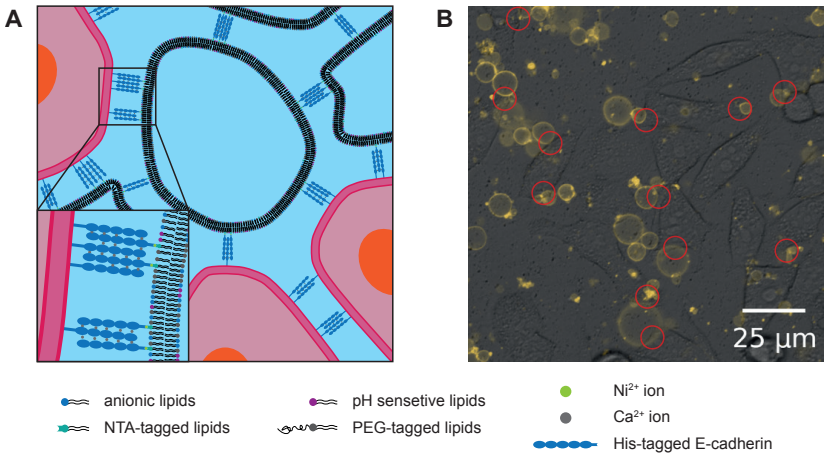


Figure 4.31: A: Schematic illustration showing the E-cadherin-mediated interaction between GUVs and cells (pink), and B: representative confocal image of the hybrid system experiment. The image shows the HEK-E cells in brightfield co-seeded with E-cadherin-containing GUVs in yellow (LissRhod) in DMEM with 1 % FBS and additional 10 mM calcium chloride after incubating for 4 hours at 37 °C and 5 % carbon dioxide. The HEK-E cells are already attached to the fibronectin-functionalized surface and first adherens junctions between GUVs and GUVs, as well as between GUVs and HEK-E cells could be observed (red circles).

For the GUV aspect of the hybrid experiment, pH-sensitive GUVs containing 1 mol% DGS-NTA were generated as described in Chapter 4.2.1 (page 87) in 30 mM Tris, 140 mM potassium chloride, 100 mM glucose and further functionalized with His-tag E-cadherin as described in Chapter 4.2.2 (92). To rule out that the interactions with the cells occurred through nonspecific interactions with LissRhod PE-(fluorophore functionalized lipid), in control experiments the lipid is: replaced with ATTO 488 PE; or omitted completely and instead the inner buffer was labeled with Alexa 647. These were chosen accordingly, since LissRhod is a negatively charged fluorophore and ATTO 488 is positively charged; and Alexa 647 is known not to diffuse from vesicles. To coat the vesicles with E-cadherin, human recombinant E-cadherins with a His tag were complexed to lipids functionalized with NTA(Ni). To achieve the protein coating, the GUVs were first incubated in a buffer containing nickel(II) ions for one hour. The GUVs were then centrifuged and the buffer was replaced with a nickel(II)-free formulation. His-tag E-cadherin was then added and incubated overnight. Human embryonic kidney (HEK) 293T cells transfected to express E-cadherin-EGFP (HEK293T-E-cadherin-EGFP, from now on referred to as HEK-E) were used for the hybrid experiment.

HEK-E cells were first cultured in Dulbecco's modified Eagle's medium (DMEM) with additional 10 % fetal bovine serum (FBS).

For the cell aspect of the hybrid experiment, HEK-E cells were suspended in DMEM cell culture media with the following formulations: either 1 or 10 % FBS and with or without additional 10 mM calcium chloride. Then, in an ibidi "µ-Plate Angiogenesis 96 Well" functionalized with fibronectin, 70 μL of HEK-E cell suspension (60,000 cells/mL) together with 10 μL of GUV suspension were transferred into one well to establish the hybrid coculture. Each condition was produced in duplicates. The cocultured HEK-E cells and GUVs were incubated for 24 h at 37 °C and 5 % carbon dioxide. The culture media in the wells was then replaced with fresh cell culture media formulations, washing away any non-adherent GUVs, and incubated again for an additional 24 h. During the incubation time, the wells were timelapse imaged every 30 min using a confocal microscope (Figure 4.31B). The experimental procedure of this experiment is described in detail in Chapter 3.5.2 (page 56). The experiments were designed and conducted in collaboration with Dr. Jacqueline De Lora. The HEK 293T cells were transfected by Drs. Jacqueline De Lora and Sadaf Pashapour.

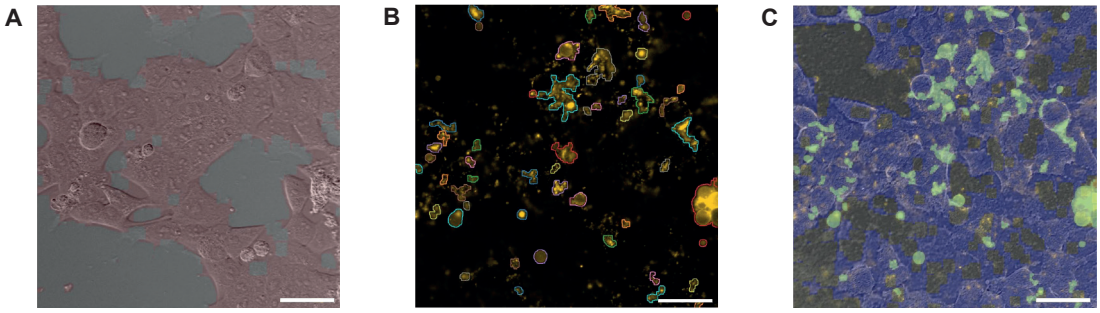


Figure 4.32: Representative confocal images of hybrid system experiment after detecting cell area and GUVs. The image shows the HEK-E cells with E-cadherin-containing GUVs in a DMEM buffer with additional calcium ions directly after the washing process. A: The bright field image was used to detect the cell area and B: the corresponding channel of the fluorophore used (in this example LissRhod) to detect the GUVs. The GUVs that occupied a common area with the cells (blue) were classified as adherent (green), and the others were classified as non-adherent (red). Scale bar: 25 μm.

Image analysis was performed using a self-programmed Python-based algorithm for step-wise detection of cell area and individual GUVs. The bright-field channel was used to detect the cell area. In a first step, the bright-field image was inverted. This image was then converted to binary, where the regions of interest (ROIs) were white, using a local thresholding. Here, the threshold for each pixel is calculated by the intensity of the pixels surrounding it in a given block size. The resulting image still contained many background areas and the entire cell area was not yet completely filled. To first reduce the background, the ROIs were dilated by a small number of pixels and then eroded by

the same number of pixels. This process is called binary closing, which merged nearby ROIs. This was especially the case inside the cells and prevented too many relevant ROIs from disappearing in the next step, binary opening. Here, the ROIs were first eroded by a small number of pixels and then dilated by the same number of pixels. This allowed the majority of the small ROIs to be removed from the background. Now, to connect the ROIs in the cell area, the binary closing was done with a larger distance. In a final step, the binary opening was performed with a higher number of pixels. The subsequent ROIs were defined as cell area and could be used to label these areas in the bright-field image (Figure 4.32A). Single steps are visualised in Figure 3.3 (page 58) in the Material and Methods Chapter. This approach to detecting cell areas reaches its limits especially when the cells occupy a large area in the acquired image. Then, the complete image is erroneously recognized as a cell area, leading to a false positive (adhesive) categorization in the subsequent differentiation between adhesive and non-adhesive GUVs.

To detect the GUVs, the appropriate channel was used depending on the contained fluorophore (LissRhod, ATTO 488, Alexa 647). In a first step, the fluorescent signals at the edges of GUVs were increased by applying the Sobel operator.[185] This operator calculates the intensity for each pixel depending on the pixels surrounding it, emphasizing edges in particular; in this case the membrane of the GUVs. By thresholding using the triangular algorithm, the image was binarized.[186] Smaller holes between ROIs representing lipid membranes were closed by applying binary closing. Subsequently, the inner surfaces in the ROIs were filled. After applying a binary opening, each separate ROI was recognized as a GUV (Figure 4.32B). Single steps are visualised in Figure 3.4 (page 60) in the Material and Methods Chapter. A problem with this method is that contiguous GUVs were only recognized as one, and thus the number of GUVs was estimated to be significantly less than actually existed.

The detailed operation of the mentioned algorithms is described in Chapter 3.5.3 (page 57). All parameters necessary for the application of this algorithm (e.g. block size and offset for local thresholding, sizes for binary opening and binary closing) were optimized for each Time Series and then applied to each of its frames. To determine the number of GUVs in a frame, the number of detected GUVs was summed. A detected GUV was declared adherent if it overlapped with the labeled cell area and then added together for each frame (Figure 4.32C).

These algorithms for detection of cell area and GUVs and subsequent analysis of the number of GUVs, adhesive GUVs, and cell confluency were applied to all conditions and time lapse images. These results were analyzed as a function of the use of E-cadherin and the use of additional calcium ions in the cell culture medium, and summarized in two violin plots (Figure 4.33). The first violin plot shows the distributed

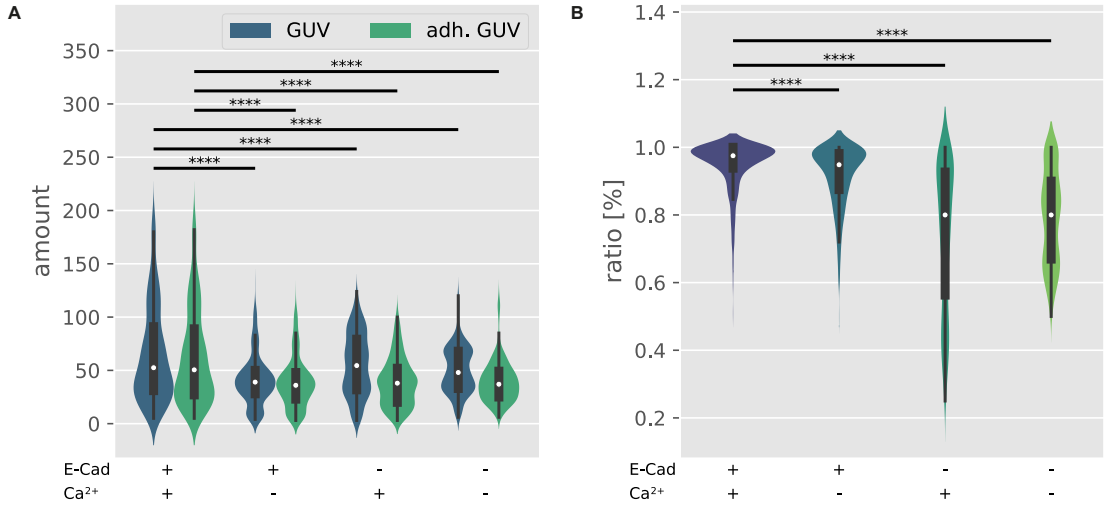


Figure 4.33: Violin plots showing the number and ratio of GUVs and adhesive GUVs depending on the experimental conditions in the hybrid experiment. A: This violin plot shows the distribution of the number of detected GUVs and adherent GUVs. It shows that when using E-cadherin-containing GUVs, a significantly higher number of GUVs were detected in one image on the confocal microscope compared to the control experiments. B: This plot shows the fraction of adherent GUVs from the detected GUVs. It indicated that the proportion of adherent GUVs was significantly higher when E-cadherin-containing GUVs were used than without E-cadherin; regardless of whether additional calcium ions were added or not. (n = 576 per condition)

amount of detected GUVs and adhesive GUVs depending on the use of E-cadherin and the addition of calcium ions (Figure 4.33A). It can be seen that a significantly higher amount of both GUVs and adhesive GUVs could be detected in the experiment with E-cadherin and additional calcium ions compared to the control experiments. Furthermore, the distribution of GUVs and adhesive GUVs are similar for the experiments with E-cadherin, both with and without additional calcium ions. In comparison, the distribution for GUVs and adhesive GUVs differs significantly for the experiments without E-cadherin. This shows that in the experiments with E-cadherin, a large proportion of the GUVs detected were also adhesive, whereas in the controls the proportion of non-adhesive ones was larger. To better illustrate this, a second violin plot was created showing the proportion of adherent GUVs among the detected GUVs for each experimental condition (Figure 4.33B), is presented. Here, the distribution of the proportion of adherent GUVs is even more evident. When E-cadherin was used, the proportion of adherent GUVs increased significantly. These observations are consistent with the expectation that GUVs can form specific adherens junction using E-cadherins. The fact that E-cadherin-containing GUVs can already interact with HEK-E cells or other GUVs without the use of additional calcium ions can be explained by the calcium ions already present in DMEM (200 mg/L or 1.8 mM). This concentration was not sufficient to completely form E-cadherin self-binding, which also resulted in more GUVs being

removed during the washing step compared to the experiment with additional calcium ions.

Principal component analysis (PCA) was used to further interpret the data in detail. The advantage of this analysis is that the extensive data set is restructured to simplify multidimensional relationships to fewer dimensions. In this case, the influence of the use of E-cadherin, additional calcium ions, the type of fluorophore used, and the amount of added FBS on the number of detected GUVs, adherent GUVs, and cell area (from now on called features) will be investigated (Figure 4.34). The calculated principal components, in this case pca_0 and pca_1, represent the most meaningful linear combinations of the variables. Each point in the diagrams represents the data obtained from one confocal microscope image. To further simplify interpretation, data were split with respect to fluorophore used (A, B: LissRhod PE; C, D: ATTO 488 DOPE; E, F: Alexa 647 core) as well as the percentage of FBS added (A, C, E: 1 % FBS; B, D, F: 10 % FBS). It is to be expected that the data points of a condition are close to each other and thus show a similar correlation between features and conditions. The more the data point clouds of different conditions separate from each other, the more different their correlation is and the more distinct are the observed features. First, it can be seen that when 10 % FBS is used, there is significantly more cloud overlap than when 1 % FBS is used. This could indicate that the additional proteins promote non-specific interactions between GUVs and cells and that the passivation of the GUV surface by using PEGylated lipids is no longer sufficient under these conditions. With respect to fluorophores, all three show a separation of data points for the use of E-cadherin-containing GUVs and additional calcium ions from the other three conditions (with E-cadherin-containing GUVs, but without additional calcium ions; without E-Cadherin with and without additional calcium ions). There are partial overlaps, which are understandable considering that this is a biological system.

So, I was able to create a hybrid system consisting of GUVs and HEK-E cells. This system was observed for 48 hours, with the buffer replaced and the non-adherent GUVs removed after 24 hours. This experiment was analyzed using a self-programmed Python-based algorithm to determine the amount of GUVs, adherent GUVs, and cell area. These data showed a significant difference between the experiments using E-cadherin-containing GUVs in calcium ion-enriched buffer and the control experiments. PCA analysis of the calculated data showed that the use of 10 % FBS resulted in nonspecific interactions between GUVs and HEK-E cells, even when the GUVs were PEGylated. The use of 1 % FBS allowed differentiation of the correlation between the use of E-cadherin-containing GUVs and the addition of calcium ions, regardless of the fluorophore used.

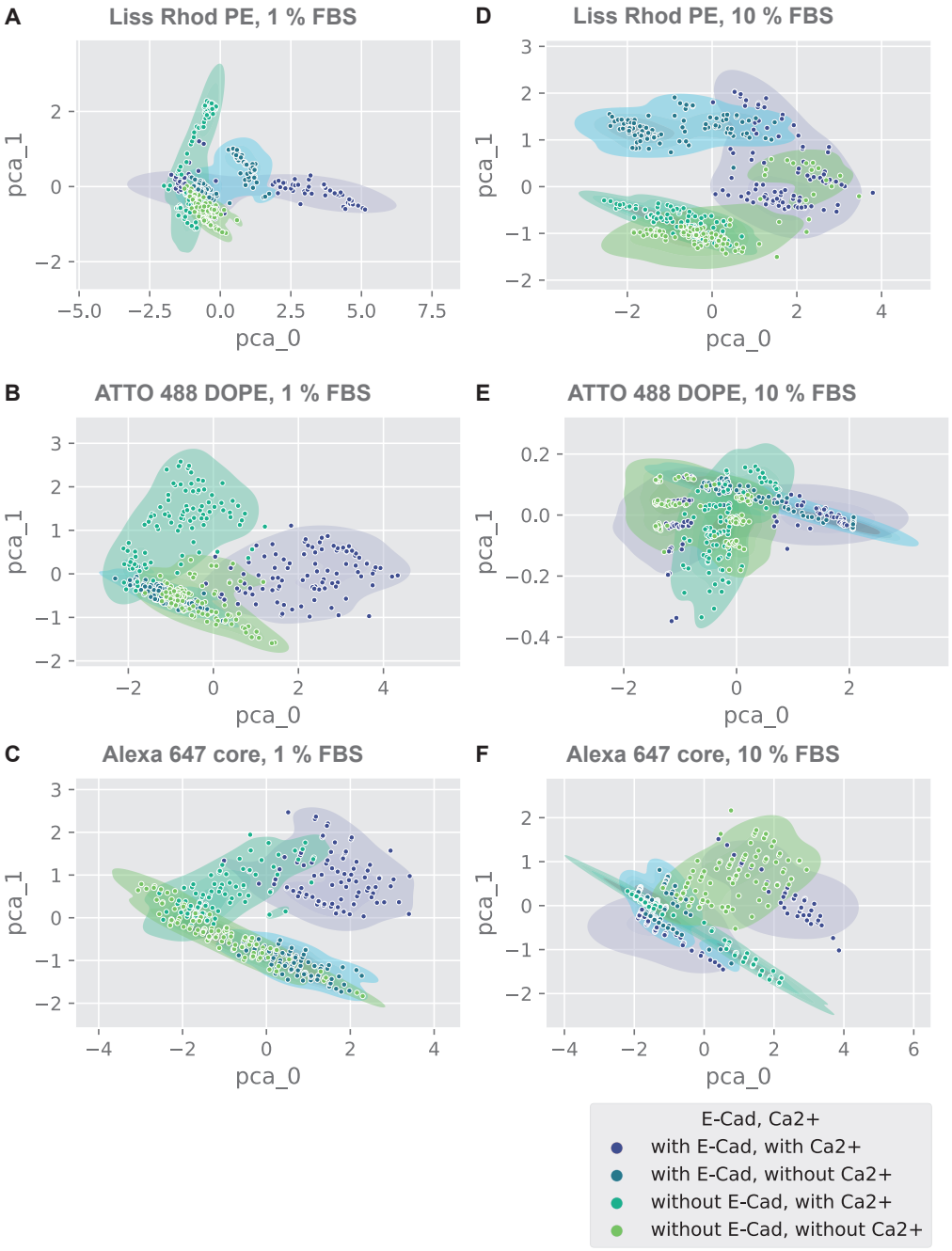


Figure 4.34: PCA of the hybrid system with respect to the dependence of detected GUVs, adhesive GUVs and cell area on different parameters. A: There is a clear distinction between the purple data points (E-cadherin-containing GUVs with calcium-enriched buffer) in comparison to other conditions in blue (E-cadherin-containing GUVs with normal buffer), dark green (GUVs with calcium-enriched buffer) or light green (GUVs with normal buffer), indicating that there is a dependence on the presence of E-cadherin and calcium ions for GUVs to adhere to cells. B: When using ATTO 488-labeled lipids, the purple data points are still separated from the rest of the data point clouds. Only a small part overlaps with the light green data cloud. C: In the experiments in which only the inner buffer of the GUV was labeled with Alexa 647, seperation of the violet data points can again be observed. This time, however, the dark green ones partially overlap. D-F: By increasing the FBS concentration, all observations became nonspecific as all data point clouds are superimposed for all three fluorophores.

Chapter 5

Summary and Outlook

5.1 Summary and Conclusions

Giant unilamellar vesicles (GUVs) are ideal compartments for the bottom-up assembly of synthetic cells and are in the focus of this thesis. For the charge-mediated generation of GUVs, the use of droplet-based microfluidics is a well-established method. However, despite the progress made in recent years, considerable challenges still loom at many steps in the process of GUVs production in a high yield. Towards an artificial tissue, a large number of GUVs is required, therefore it is necessary to improve the current process of charge-mediated GUV production. Accordingly, in this thesis a range of functional block copolymer surfactants was synthesized to improve the yield of GUV formation. Subsequently, efficient approaches to reconstitute adhesion and interaction modules into GUVs were developed and described. Finally, the development of hybrid system consisting of functional GUV-based synthetic cells and natural cells network is demonstrated for the first time.

5.1.1 Synthesis of functional fluorinated block copolymer surfactants

In the first part of the thesis, I focused on improving the established method for charge-mediated GUV generation by means of droplet-based microfluidics. Therefore, I synthesized novel functional block copolymer surfactants and tested their effect on the GUV production yield. Towards this end, I first compared different routes to synthesize triblock copolymer surfactants composed of polyethylene glycol (PEG) and perfluoropolyether (PFPE). In one of the studied routes, the hydroxyl groups of PEG were activated and allowed for higher reaction efficiency with PFPE to give the esterified triblock surfactant (eTS) **1**. In another synthesis route, the carboxylic acid group of Krytox was converted into an acid chloride, followed by reaction with PEG-diamine to

produce amidated triblock surfactant (aTS) **2**. In a final route, PEG was converted into diazide-PEG1500 **4** and Krytox into propargyl-PFPE7000 **5** over several reaction steps. A copper click reaction was performed with these two precursors to obtain clicked triblock surfactant (cTS) **6**. Subsequently, all three surfactants were analyzed by NMR, FTIR and interfacial tension (IFT) values were determined by pendant drop measurements and the proportion of Krytox in the final product was measured by a partition experiment. The analysis revealed that the cTS **6** surfactant was the purest and had the most promising results in terms of its physicochemical properties.

To reduce the amount of Krytox to minimum and possibly to improve the properties of the surfactants eTS **1** and aTS **2**, I used flash column chromatography with different column materials to purify them further. To determine the amount of leftover Krytox, a method was developed to visualize Krytox and surfactants on a TLC plate coated with C18 silica gel by negative staining with a fluorescein solution. In a first attempt, the standard column materials silica gel, silica gel C18, aluminium oxide (Alox), anion exchange and cation exchange were tried. With silica gel, silica gel C18 and Alox neither one of the surfactants nor Krytox could be eluted. This can be explained, because either the hydrophilic or the hydrophobic block interacted too strongly with the column material due to the amphiphilic properties of these molecules. The ion exchangers first had to be transferred from an aqueous system via methanol to the fluorinated running medium. In the process, the column material collapsed further over time, losing its ion-exchange property, and surfactants were eluted with Krytox. To increase the specific interactions of Krytox with the column material, silica gel was now functionalized with an amine group. For this purpose, the two chemicals (3-Aminopropyl)trimethoxysilane (APTMS) and N^1-(3-Trimethoxysilylpropyl)diethylene-triamine (TRI-silane) were tested. Since the standard column materials (silica gel, silica gel C18, aluminum oxide, anion exchange and cation exchange) failed in separating the surfactants and Krytox, silica gel was functionalized with an amine groupe using APTMS or TRI-silane. Purification of the surfactants using the amine functionalized silica gel resulted in Krytox separation. In subsequent pendent drop measurements or partition experiments, it was shown that further purification reduced the IFT values and the amount of Krytox in the surfactant. Nevertheless, these values were still not as optimal when compared to those of cTS **6**. Therefore, the click chemistry approach was continued for the following surfactant syntheses and, unless otherwise stated, the cTS **6** was used for further experiments.

To further improve the charge-mediated GUV formation, I synthesized three different functionalized surfactants: 1) a pH-independent positively charged diblock copolymer surfactant; 2) a photoliable triblock copolymer surfactant; and 3) a fluorescent diblock copolymer surfactant.

The positively charged diblock copolymer surfactant enables the charge-mediated self-assembly of the negatively charged lipid bilayer membrane at the water-oil interface due to electrostatic interactions. In the previously developed approach to generate droplet-stabilized giant unilamellar vesicless (dsGUVs), Krytox was added to the surfactant solution in order to achieve negatively charged water-oil interface due to carboxylic acid. Subsequently, magnesium ions were added to the inner buffer to generate a positive charge on the surfactant interface in order to attract the negatively charged lipid vesicles. Due to the Krytox-mediated strong interaction, the efficiency of the GUV release process is reduced, leading to a total low yield of GUV production. Moreover, implementation of Krytox has several undesirable side effects on proteins and lipids due to a reduction of pH. Therefore, the synthesis of the positively charged surfactants can generate a straight forward method for charge mediated assembly of negatively charged vesicles. For the synthesis, PEG600 **8** was first coupled with a quaternary ammonium-containing TAB **9** on one side and propargyl PFPE **5** on the other side by click reactions. The obtained positively-charged diblock surfactant (posDS) **11** was then analyzed for its physicochemical properties. In the process of charge-mediated GUVs assembly I revealed that the ionic strength of the inner buffer had to be increased (20-150 mM sodium ions) in order to sufficiently destabilize the small unilamellar vesicles (SUVs). Using quantitative MS, the lipid composition of the released vesicles was studied. The results revealed only minor changes in lipid composition. In contrast to positively charged surfactants, the use of surfactants like CS and cTS **6** that required addition of Krytox for GUVs production, mass spectrometry revealed a notable change in lipid composition in comparison to initial lipid mixture used for SUVs formation. Additionally, the biocompatibility of the positively charged surfactant was demonstrated by Dr. Sadaf Pashapour, who used the surfactant to encapsulate different cell types of cells and proteins.

The photoliable triblock copolymer surfactant was designed to allow light-mediated breakage of the bond between the PEG and PFPE blocks, causing the surfactant to lose its amphiphilic property leading to fusion and efficient release of the droplet content without the addition of destabilizing surfactant. Therefore, PEG1500 was first esterified with 4-azidomethyl-3-nitrobenzoic acid (ANBA) **12**, followed by coupling with propargyl PFPE **5** by a click reaction. The light-triggering properties of the obtained photoliable triblock surfactant (plTS) **14** were determined in pendent drop measurements. During the illumination process, the oil drop became turbid, probably because of the cleaved PEG, which is not soluble in HFE 7500, and the IFT values slightly increased. However, using confocal microscopy and 404 nm laser irradiation I was not able to destabilize the droplets sufficiently in order to achieve their fusion. I assume that due to the low quantum yield of the nitrobenzoyl group and the absorption

of the fluorinated oil in the irradiated wavelength, the cleavage process was not efficient enough. Moreover, more analysis has to be done to evaluate the efficiency of the light-triggered breakage of the bone in the oil phase as well as at the water/oil interface.

The fluorescent diblock copolymer surfactant was designed to allow for direct surfactant detection. A direct label is desirable because it allows physical properties such as the diffusion coefficient to be measured directly and residues of surfactants to be visualized after the release process. For the synthesis, diazide PEG600 **8** was first coupled with a propargyl rhodamine B **15** on one side and propargyl PFPE **5** on the other side by click reactions. The obtained fluorescent diblock surfactant (fluoDS) **17** was then used to determine the diffusion coefficient ($4.6 \pm 0.2\,\mu m^2/s$) by FRAP measurements.

5.1.2 Synthetic cells adhesion interactions

In the second part of this thesis, I described the improved production of GUVs with regards of lipid composition and efficiency. In collaboration with Dr. Félix Lussier, a lipid system containing the pH-sensitive N-(4-carboxybenzyl)-N,N-dimethyl-2,3-bis-(oleoyloxy)propan-1-aminium (DOBAQ) lipid for the production of GUVs was investigated. Through the controlled implementation of Krytox, the pH value inside the GUVs was lowered to allow pH-mediated conversion of negatively charged SUVs into the positively charged ones. This enables the self-assembly of the lipid bilayer at the negatively charged surfactant layer through electrostatic interactions. The pH was then increased again by adding release buffer, leading back to negative charge of the lipids and as a consequence reducing the interaction between the surfactant and the lipid layers. These pH mediated processes allowed for enhanced GUVs release efficiency. To achieve these goals I first investigated the effect of pH on the surface charge of SUVs by measuring the zeta potential. The result revealed that the reduction pH values from 7.4 to 5.5 reduced the negative zeta potential of lipids from -11.6 ± 0.8 to -2.1 ± 1.6 mV. Subsequently, I determined the minimum Krytox concentration required to lower the pH to approximately 5. For this purpose, a calibration curve was established using fluorescein-containing droplets with different pH-adjusted buffers. The results revealed that at a concentration of 10 mM Krytox in the oil phase and a water to oil ratio of 1:2, a pH value of 5.1 could be set inside the droplets. When GUVs were prepared under these conditions, a significantly higher release rate was obtained. The developed pH-mediated method allowed for high yield GUV production. Therefore I used this method for the assembly of biofunctional GUV-based synthetic cells for further synthetic biology applications.

After the optimization of GUV generation, the adherens junctions between GUVs were reconstituted. In a first approach, synthetic ways for GUV-GUV interactions based on biotin-streptavidin chemistry have been successfully explored. In case of the

biomimetic approach, the interactions between GUVs were mediated by E-cadherins. Towards this interaction, the specificity of functionalizing nitrilotriacetic acid (NTA)-containing GUVs with His-tagged proteins was tested. To minimize the use of the expensive E-cadherin His-tagged proteins the optimization was done with His-tagged green fluorescent protein (GFP). Moreover, to reduce unspecific interactions between proteins with the GUVs, PEGylated lipids with different PEG sizes were added to the GUV membrane. In the experiments without addition of nickel(II) ions, which are important for the formation of the NTA-His tag complex, no nonspecific adhesion of GFP to the pegylated GUV membrane could be observed above a PEG size of 1000 g/mol. When nickel(II) ions were used, GUVs with PEG1000 and PEG2000 showed colocalization of GFP and GUV membrane, so PEG2000 was added for passivation of GUV membrane for all further experiments. To investigate E-cadherin-mediated adhesion between GUVs, the influence of calcium and nickel(II) ions on this interaction was tested. The results revealed that without the addition of E-cadherin, no interactions between GUVs were observed. Stable E-cadherin-mediated GUVs network was possible to achieve only if calcium ions were used.

Following the establishment of the adherens junctions I set out to reconstitute transmembrane $\alpha_{\mathrm{IIb}}\beta_3$ integrin proteins for the assembly of GUV-extracellular matrix (ECM) module. For this purpose, I first established optimized detergent-mediated method for integrin reconstitution into SUVs. Moreover, I designed an efficient size-exclusion chromatography (SEC) method for the detergent removal. To enable the most successful reconstitution of integrin proteins, negatively, neutral, and positively charged SUVs were tested and the efficiency was related to the change in zeta potential due to biofunctionalization. The results revealed that the integrin reconstitution was the most efficient into the positively charged SUVs. These results were expected taking into account the negative charge of integrin $\alpha_{\mathrm{IIb}}\beta_3$. The functionality of integrin after reconstitution and purification by SEC was confirmed by adhesion of proteoliposomes to a fibrinogen surface.

As an alternative approach to charge-mediated reconstitution of proteoliposomes into GUVs a SNARE protein-mimicking deoxyribonucleic acid (DNA) was developed. This DNA pair, hereafter referred to as fusion DNA A and A', was first examined for selectivity. For this purpose, the fusion DNA was used to fuse ATTO 488-labeled SUVs with LissRhodamine-labeled GUVs, and successful incorporation was observed only when both, fusion DNA A on the SUVs and fusion DNA A' on the GUVs, were used. Using this method, it was possible to incorporate integrin $\alpha_{\mathrm{IIb}}\beta_3$ into GUVs by fusion with proteoliposomes and adhere them to a fibrinogen surface. This result showed that it was possible to reconstitute membrane proteins into the GUV membrane in a simplified procedure compared to the picoinjection method.

To reconstitute actin cytoskeleton into a GUV, globular actin (G-actin) was incorporated into GUVs where it was polymerized to filamentous actin (F-actin) using adenosine triphosphate (ATP). To reduce the electrostatic interactions of actin with the Krytox in the surfactant layer, a special design of a microfluidic chip was developed in which three channels meet at the droplet-generating junction. In that microfluidic device, a droplet containing G-actin in OptiPrep was generated in SUVs and ATP congaing droplets. Due to the high viscosity of OptiPrep, the G-actin initially remained trapped in the middle of the droplet lumen leading to nonperturbed formation of ds-GUVs. Over time, the OptiPrep dispersed in the droplet and the G-actin was able to polymerize. In this way, it was possible to subsequently release GUVs with an assembled F-actin cytoskeleton. It is important to mention here that so far without using the designed method in this thesis, the release of actin-loaded GUVs was not possible to achieve.

Importantly, to reduce the implementation of natural proteins for adhesion and interaction modules assembly, I was able to show how comparable observations could be obtained by using DNA-based alternatives to the E-cadherin and integrin $\alpha_{\mathrm{IIb}}\beta_3$ proteins. For the DNA-mediated GUV-GUV interactions, a DNA sequence with a palindromic sticky end was designed. This enabled a self-interaction comparable to E-cadherin. The palindromic DNA contained a cholesterol tag that was used to bind the DNA to the GUV membrane. Thus, the interaction between GUVs could be achieved by the addition of the palindromic DNA, and the resulting GUV networks were comparable to those of E-cadherin-containing GUVs. For the DNA-mediated surface adhesion of GUVs, a complementary DNA pair was design that the sticky ends are such that application of force causes the DNA duplex to unzip. One strand of the DNA pair was tagged with a thiol group to be immobilized on a block copolymer micelle nanolithography (BCML) surface. The other DNA strand contained a cholesterol tag and was bound via this tag to the GUV membrane. When the GUVs were now placed on the prepared surface, they began to adhere directly to the surface. In addition, the thiol-containing DNA strand was functionalized with Cy3 and the cholesterol-containing DNA strand was functionalized with the compatible FRET quencher BMN-Q620. This allowed the glass surface to be fluorescently labeled with Cy3. When the solubilized quencher DNA was added, the fluorescent signal was quenched. This mechanism should be used to indicate the selective adhesion area by quenching the fluorescent signal. Unfortunately, this effect was not observable in experiments with GUVs.

Following the successful assembly of E-cadherin-functionalized GUVs, in collaboration Dr. Jacqueline De Lora I set out to establish a hybrid system consisting of natural HEK cells and GUV-based synthetic cells. The influence of E-cadherins, calcium ion

enriched buffer, fluorophore used (LissRhod PE, ATTO 488 DOPE or inner buffer labeled with Alexa 647) and concentration of fetal bovine serum (FBS) on the hybrid system was investigated. The time-lapse images obtained by confocal microscopy were analyzed with respect to the number of GUVs, adherent GUVs and cell area using a python-based self-written algorithm. In a comprehensive experimental summary, it was shown that by using E-cadherin-functionalized GUVs in a calcium ion-enriched cell medium, more GUV-HEK cell interactions were detected. When normal cell medium with E-cadherin-containing GUVs was used, the number of GUVs detected was significantly lower, but they were proportionately similar in adherence to those detected when calcium ion-enriched cell medium was used. When GUVs without E-cadherin were used, both the number of GUVs and the proportion of adherent GUVs were significantly lower. For more detailed analysis of GUV-cell interactions the principal component analysis (PCA) was implemented. The analysis allowed to investigate separately the influence of the experimental conditions such as the type of used fluorophore, the concentration of FBS and the correlation between the use of E-cadherin and calcium ion-enriched buffer. The resuts revealed that when 1 % FBS was used, the data points for E-cadherin-containing GUVs in calcium-enriched buffer were well separated compared to those with no E-cadherins, regardless of additional calcium ions or fluorophore. While further studies along with an improved experimental design are needed to corroborate this result, this distinction indicates that E-cadherin mediated interactions were the underlying cause of GUV-cell adhesions. When 10 % FBS was used, a majority of the data points overlapped, indicating nonspecific interactions between GUVs and human embryonic kidney (HEK) cells triggered by the increased protein concentration.

Taking the three independent parts of my thesis together, I show that by improving surfactant synthesis and by optimizing lipid composition, the generation of GUVs could be made much more efficient. The increased number of GUVs allowed for the investigation of wide-ranging effects in the construction of GUV-GUV adherens junction and the formation of a first hybrid system within a cell coculture. This bottom-up approach enables a simplified and modular construction of GUVs containing different adhesion modules and is a further step towards an artificial tissue.

5.2 Outlook

5.2.1 Surfactant modifications

In the presented research, the influence of the synthesis route and purity on the physicochemical properties of block copolymer surfactants has been described. However, what was not investigated so far is the influence the PEG and PFPE blocks sizes have on physicochemical properties of the block copolymer surfactants. In addition to the construction of GUVs, the dimensions of the surfactant blocks can have potential effects on the stability of cell and protein-containing droplets. Therefore, in collaboration with Ms. Anastassiya Schramm, PFPE-PEG-PFPE triblock surfactants were synthesized using PEG with molecular masses of 300, 600 and 1500 g/mol and PFPE with molecular masses of 2000, 4000 and 7000 g/mol. Initial pendent drop measurements showed that the used polymer sizes had a large effect on both the IFT value and the adsorption kinetics of the surfactant on the water-oil interface (Figure 5.1). The range of optimized properties can be further extended by using PFPE-PEG diblock copolymer surfactants. In addition, mixtures of surfactants containing polymers of different sizes or of diblock and triblock copolymer surfactants can extend the repertoire and allow fine-tuning of the properties required for a specific application.

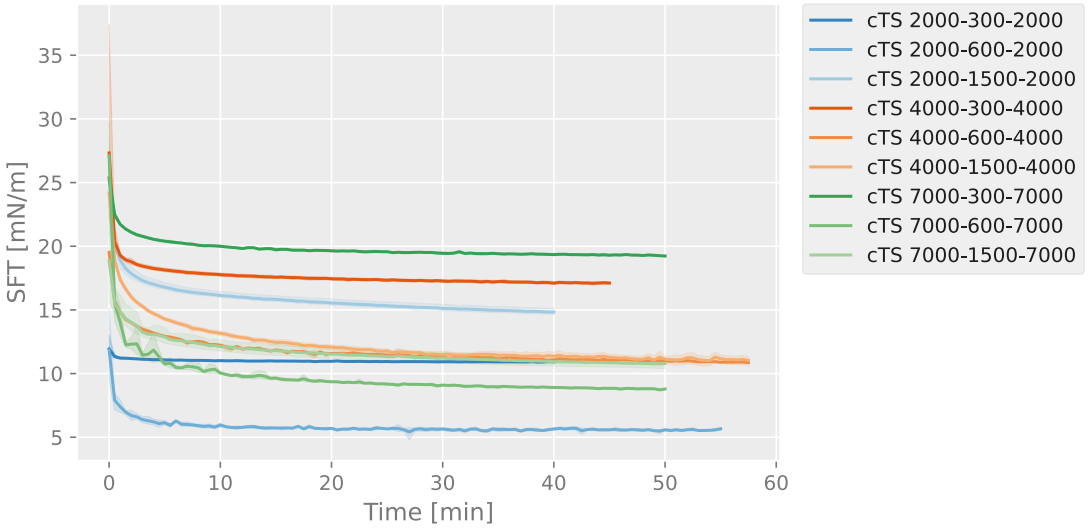


Figure 5.1: Pendent drop measurements of triblock copolymer surfactant containing PEG and PFPE of different molecular masses.

As discussed previously, using the synthesized photoliable surfactant that contains a nitrobenzoyl linkage I was unable to trigger fusion of w/o droplets upon irradiation with light. One possible explanation is that the quantum yield for the cleavage of nitrobenzoyl groups is very low and, in addition, the fluorinated oil HFE 7500 absorbs in the UV range. Furthermore, UV light is cytotoxic and damages a large proportion of biomolecules. These problems could be overcome by changing the photolabile linker.

On one hand, by using derivatives of nitrobenzoyl substituted on the benzene ring, both the quantum yield could be increased and the activation wavelength redshifted. Alternatively, another photolabile group, for example derivatives of coumarin, could be used.[245] Moreover, instead of a photoliable linker, a photoswitchable linker, such as azobenzene, could also be incorporated between the polymer blocks. This approach could reversibly disable the droplet stabilizing property of surfactants (by time or by irradiation with a different wavelength of light), instead of cleaving the surfactant.[246]

In addition to already synthesized block copolymer functional surfactants, the introduction of other functional groups may be of interest. For example, a surfactant with a terminal NTA group could allow specific immobilization of His tagged proteins on the surfactant layer. Functionalization of surfactants with proteins will generate an adhesive layer for the encapsulated cells. Moreover, oil-in-water droplets coated with adhesion proteins, could be implemented as stable synthetic cells in hybrid systems. Additionally, a pH-dependent charged surfactant, comparable to the pH-dependent lipid DOBAQ, could enable pH-mediated formation of dsGUVs using negatively charged lipids. This would increase the flexibility in applicable lipid compositions.

5.2.2 Towards artificial tissue

As described previously, only the extracellular domains of E-cadherin proteins were used in the experiments to construct GUV-GUV interactions. However, transmembrane mechano-signal transduction is essential for proper signalling of biomimetic adherens junctions. This could be achieved by using either the full-length E-cadherin or, as an alternative, a transmembrane DNA construct with its ends functionalized with NTA.[97,222] This would allow an extracellular binding of His-tagged E-cadherin and an intracellular connection with the actin cytoskeleton, for example via His-tagged actin or His-tagged α-catenin. This would require the DNA to be incorporated into the GUV membrane by internal functionalization of the DNA strands with lipophilic groups, for example with cholesterol, palmitate or porphyrin.[97,247,248]

In addition to adherens junctions, gap and tight junctions between GUVs are also of interest in the construction of an artificial tissue. The natural gap junction is formed by a collection of cell-cell channels that connects the cytoplasm of cells, enabling communication between the connected cells by diffusion of ions and small molecules.[23] This can be achieved in a synthetic environment by reconstitution of connexin into the GUV membrane, where a protein complex of six connexins would self-assemble.[249] These so called connexones could link GUVs to form a synthetic gap junction. In contrast, the tight junction is formed by epithelial cells to control the flow of molecules across the epithelium. This is due to a strong connection between the epithelial cells through the transmembrane proteins occludin or claudins and a larger intracellular

protein complex.[250,251] Therefore, tight junctions between GUVs could be achieved by reconstitution of occludin or a memeber of the claudin protein family.

By combining GUV-GUV adherens junction, GUV-substrate adhesion, and the cytoskeleton, it is possible to construct a minimal artificial tissue. To implement these modules in synthetic cells a biomimetic approach using proteins, or a DNA-mediated approaches can be used, as shown in this thesis. For the latter approach, a DNA-mediated actin alternative was not discussed in this work because it has already been established by Jahnke *et al.*[167] By combining different modules of the biomimetic and DNA-based approach, minimal synthetic tissues could be assembled in a modular manner and specifically programmed for their application.

It has already been shown that, in principle, it was possible to build a hybrid system consisting of GUVs and natural cells. The interactions between the synthetic and natural cells were based on calcium ion-mediated E-cadherin homotypic interactions. During the experiment, it was often observed that shortly after cells started to interact with GUVs, the GUVs moved out of the focal plane of the microscope, probably because they were moved by the cells. This effect could be prevented by adhering the GUVs to the substrate, either by integrin or the corresponding DNA alternative. For the hybrid system experiment HEK 293T cells were ectopically transfected to express E-cadherin-EGFP (HEK-E). Unfortunately, only low amounts of E-cadherin-EGFP were expressed and therefore only weak signals were measured. To improve the observations, with integrative transfection (e.g. possibly CRISPR) the E-cadherin-EGFP expression could be improved. In case of increased E-cadherin-EGFP synthesis, it will be possible to highlight the adhesion surfaces between HEK-E cells and GUVs by accumulation of the fluorescently labeled E-cadherin.

The presented hybrid system consisting of synthetic and natural cells represents only the simplest hybrid system. The next logical designs to consider would be to exploit the interactions between synthetic cells and natural cells for drug delivery applications. This could be realized, for example, by the incorporation of pores into the GUV membrane and the subsequent diffusion into the ECM, where the drugs are taken up by the cells. Alternatively, gap junctions could be incorporated to allow small molecule drugs to enter cells through the connexone channels. In a technical application, a minimal artificial tissue could be used as a polarizing biomimetic surface whereby natural cells would be seeded on the engineered artificial tissue instead of glass, cell plastic or other polymers. This would be closer to recapitulating the natural cell-cell adhesion surface of cells in a tissue, where one could flexibly adjust the stiffness and control communication with natural cells. In conclusion, the artificial tissue has a high flexibility due to its modular structure and thus a wide range of possible applications.

Chapter 6

Appendix

6.1 Spectra

6.1.1 Mass spectrometry

N,N,N-trimethylprop-2-yn-1-aminium bromide 9

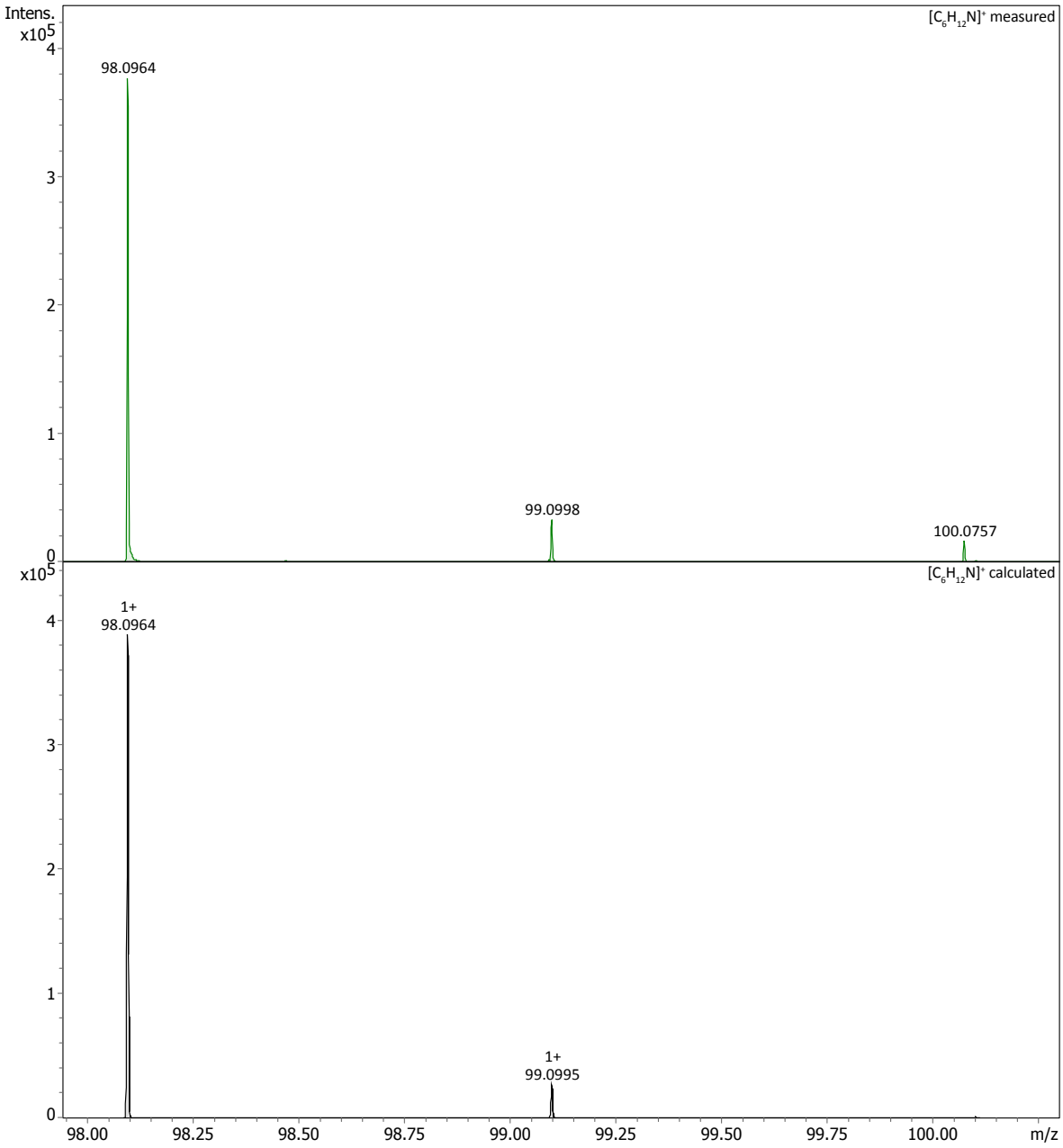


Figure 6.1: ESI-MS spectrum of N,N,N-trimethylprop-2-yn-1-aminium bromide **9**.

4-(Azidomethyl)-3-nitrobenzoic acid 12

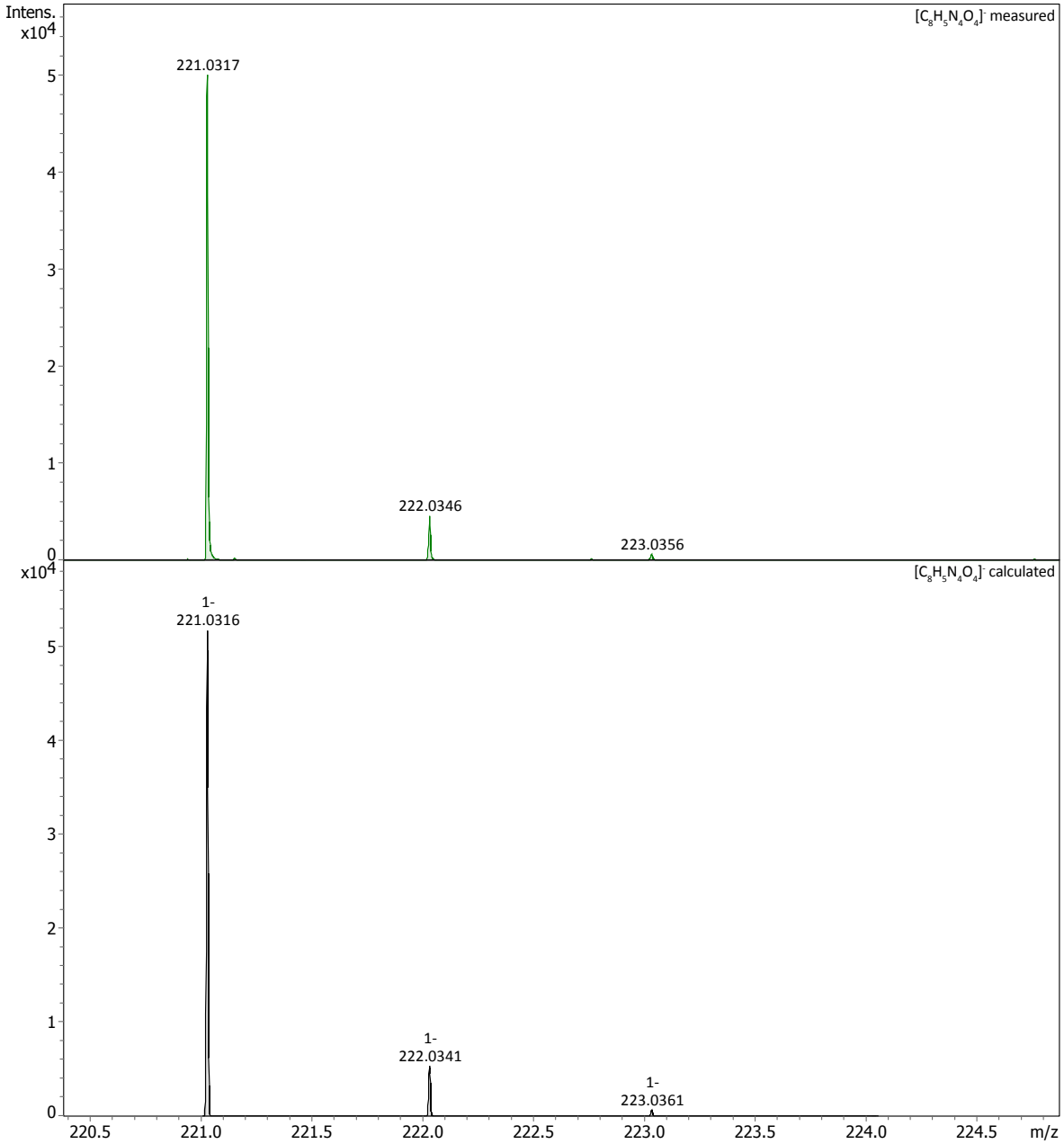


Figure 6.2: ESI-MS spectrum of 4-(azidomethyl)-3-nitrobenzoic acid **12**.

6.1.2 NMR spectroscopy

Esterified triblock surfactant PFPE 7000-PEG 1500-PFPE 7000 1

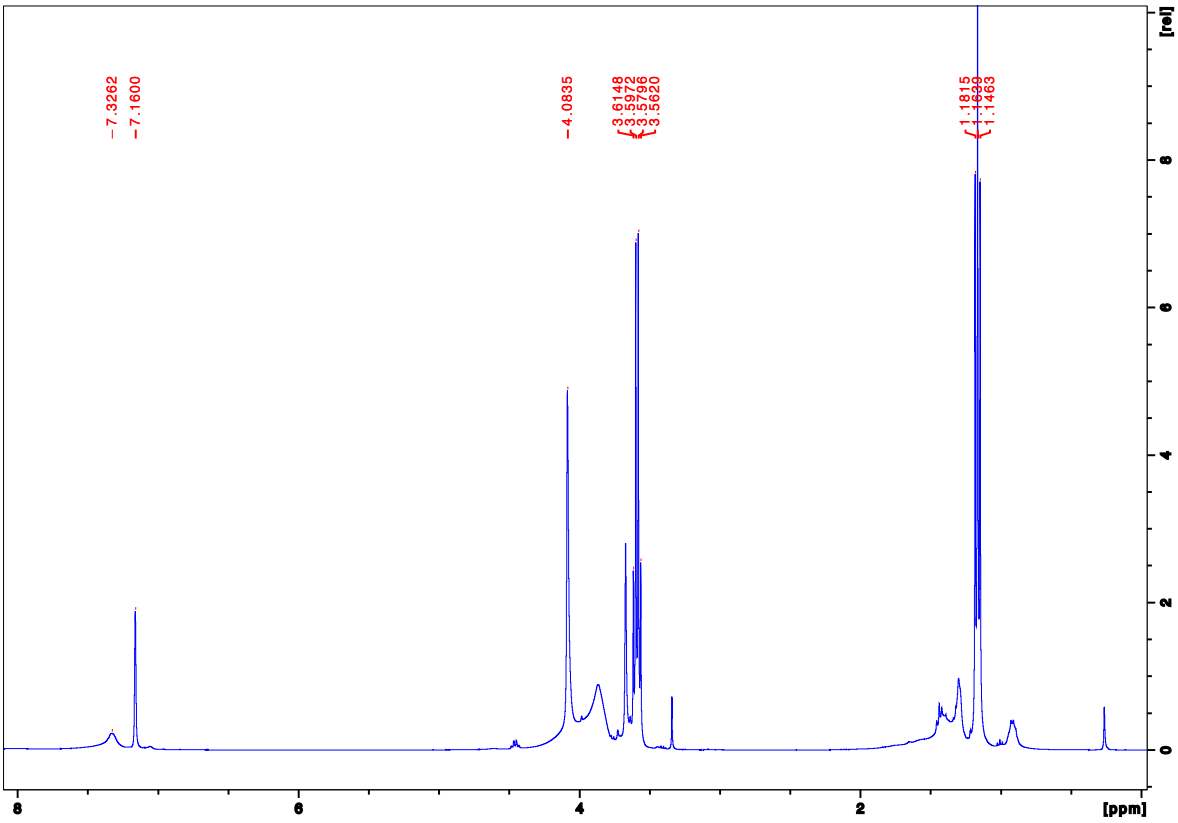


Figure 6.3: ^{1}H-NMR of esterified triblock surfactant PFPE 7000-PEG 1500-PFPE 7000 **1**.

Amidated triblock surfactant PFPE 7000-JA 800-PFPE 7000 2

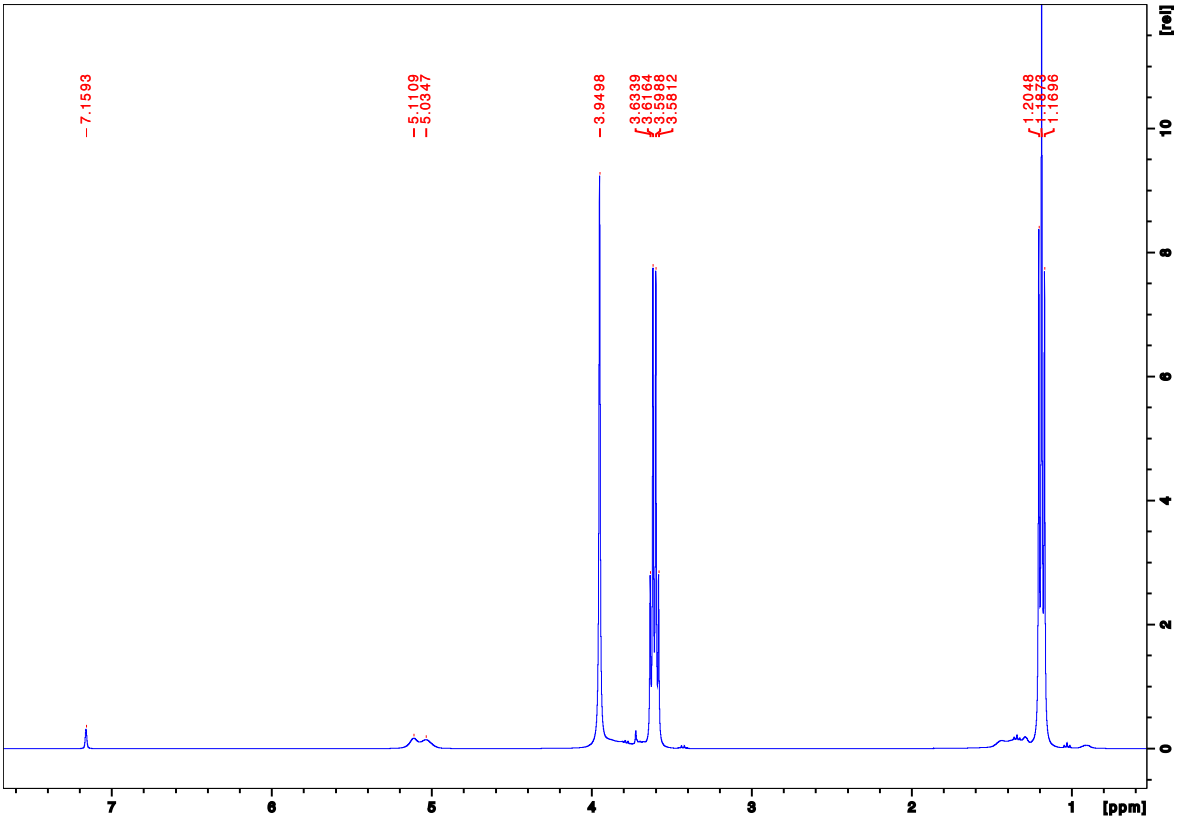


Figure 6.4: ^{1}H-NMR of amidated triblock surfactant PFPE 7000-JA 800-PFPE 7000 **2**.

PEG 1500 ditosylate 3

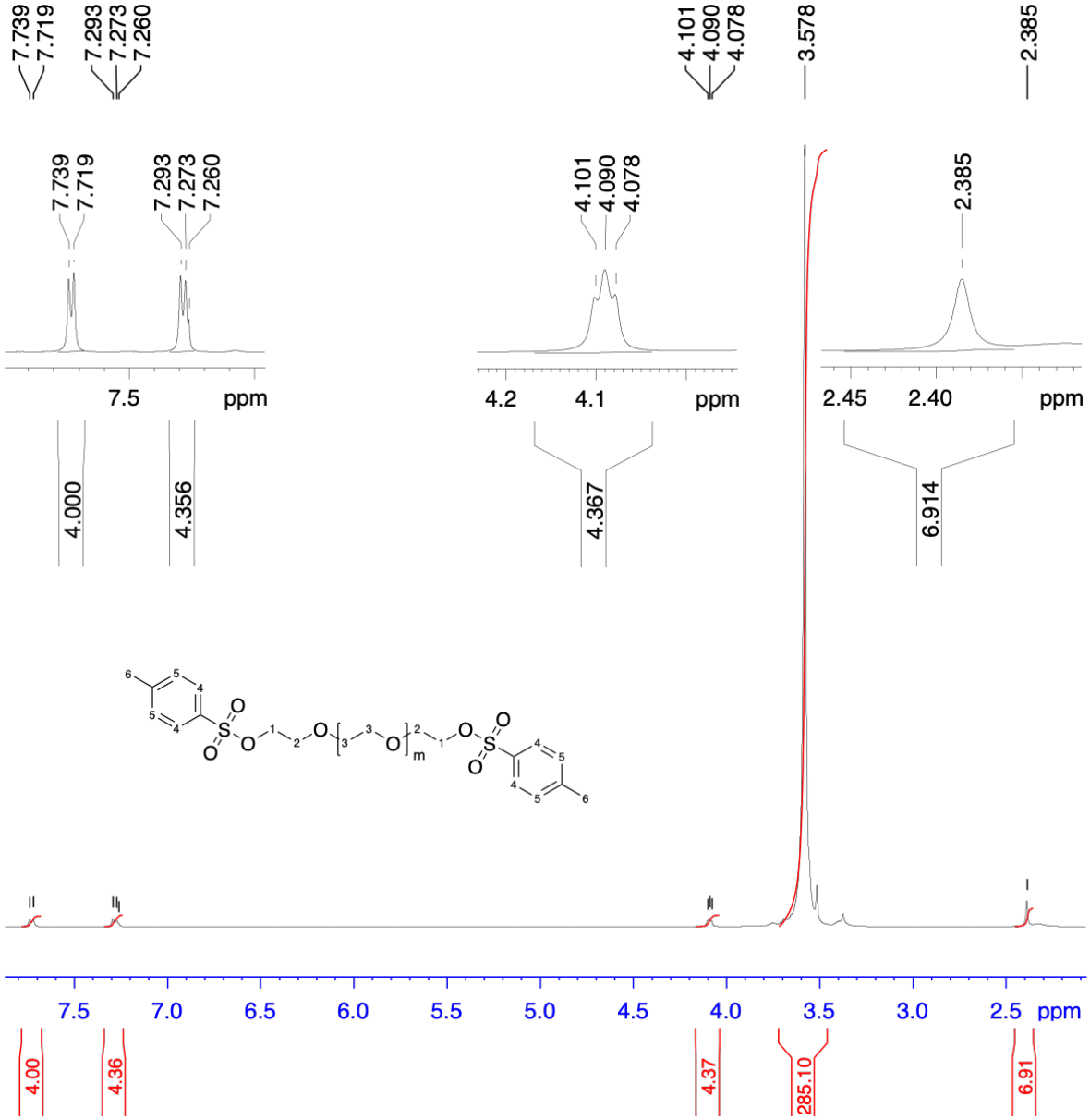


Figure 6.5: ^{1}H-NMR of PEG 1500 ditosylate **3**.

PEG 1500 diazide 4

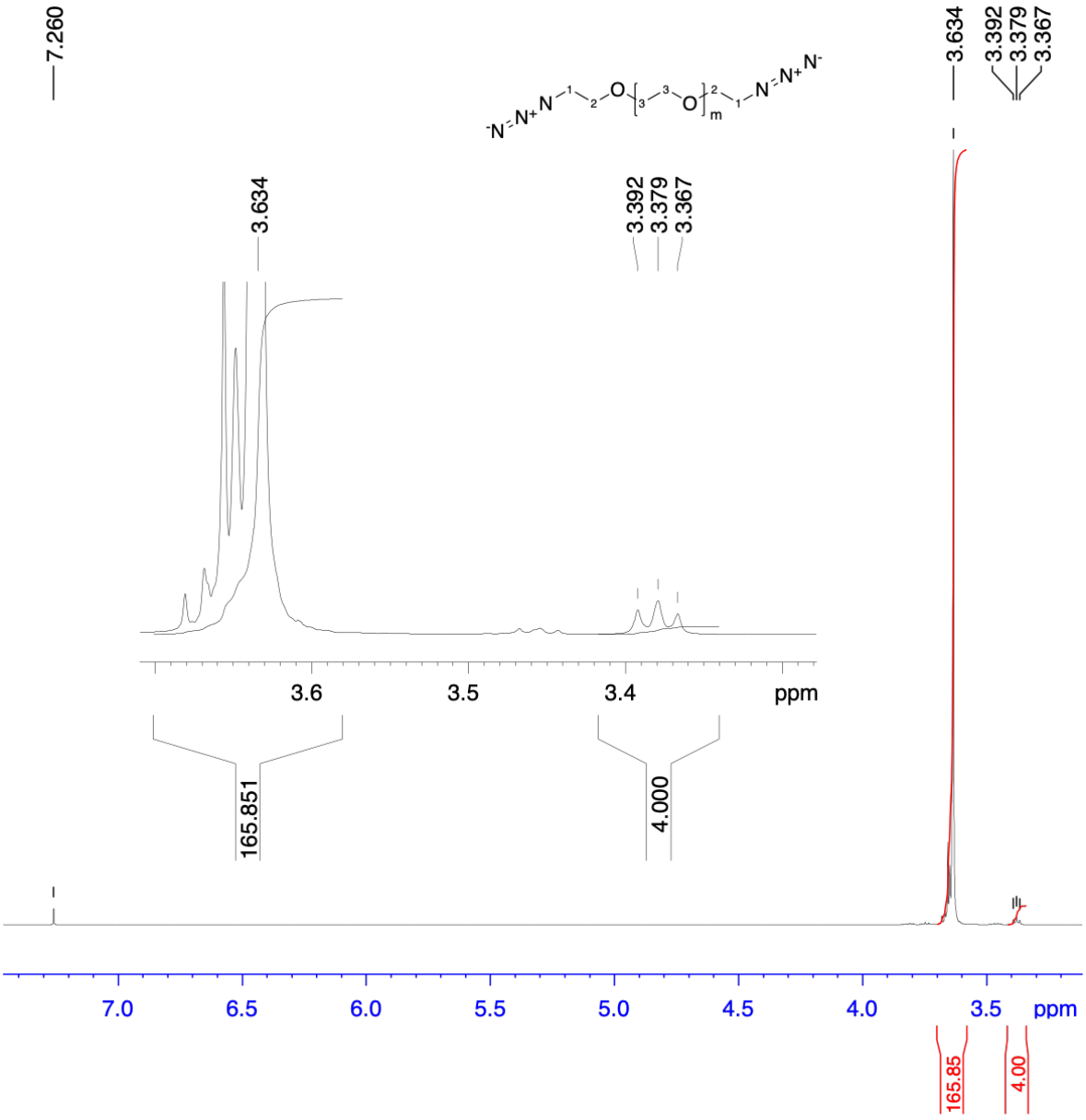


Figure 6.6: ^{1}H-NMR of PEG 1500 diazide **4**.

Propargyl PFPE 7000 1

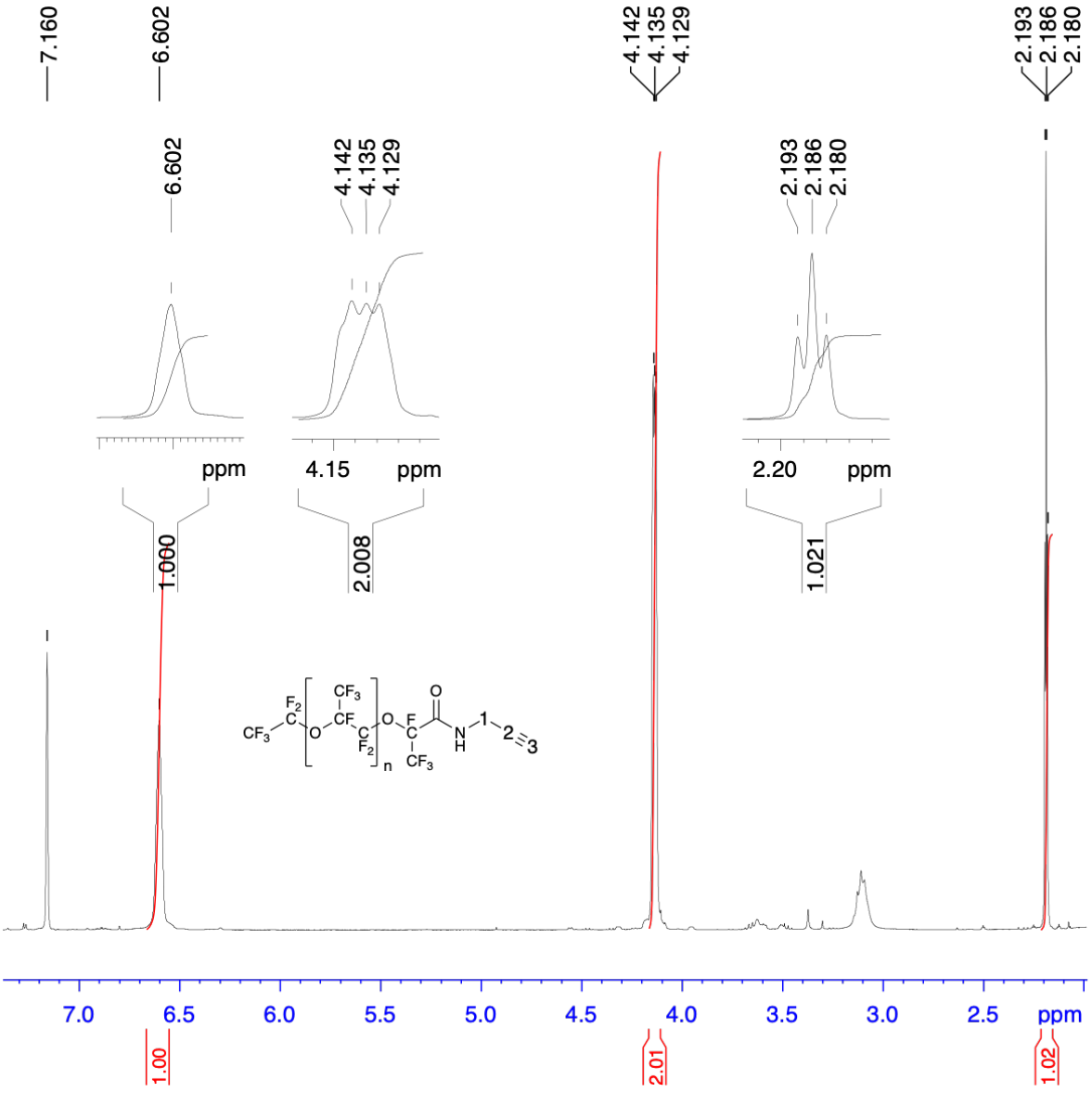


Figure 6.7: ^{1}H-NMR of propargyl PFPE 7000 **1**.

Clicked triblock surfactant PFPE7000-PEG1500-PFPE7000 6

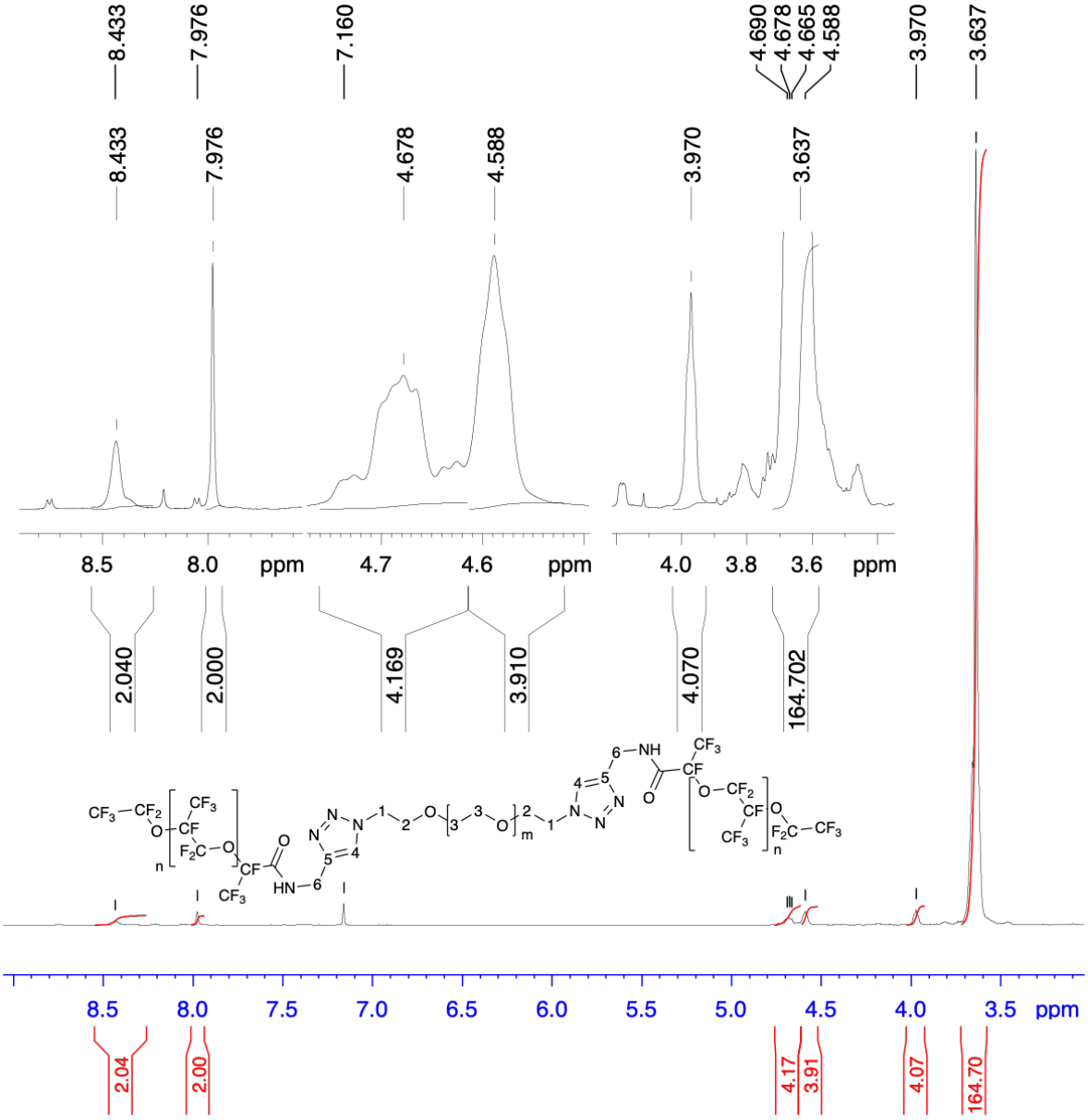


Figure 6.8: ^{1}H-NMR of licked triblock surfactant PFPE7000-PEG1500-PFPE7000 **6**.

PEG 600 ditosylate 7

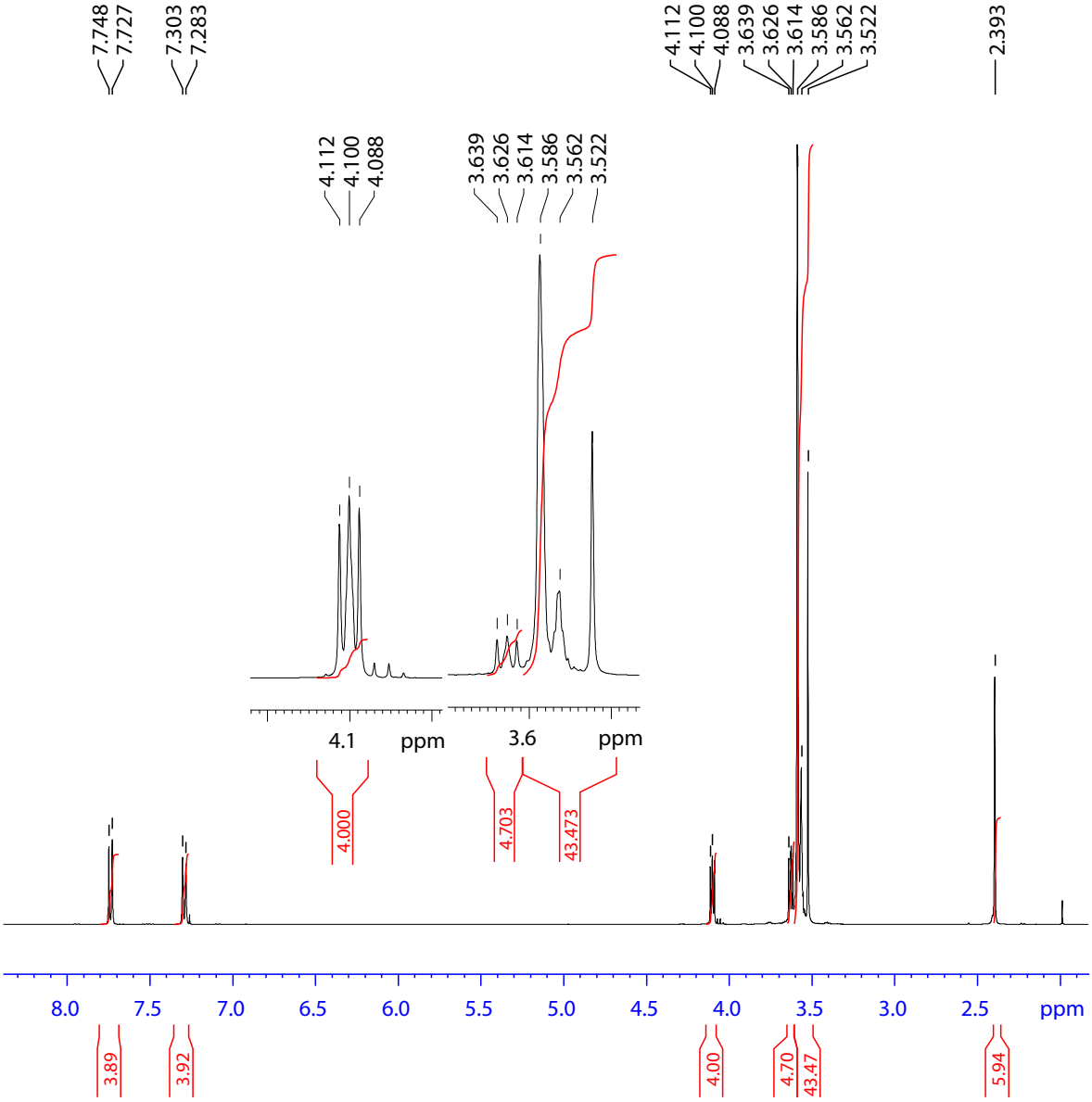


Figure 6.9: ^{1}H-NMR of PEG 600 ditosylate **7**.

PEG 600 diazide 8

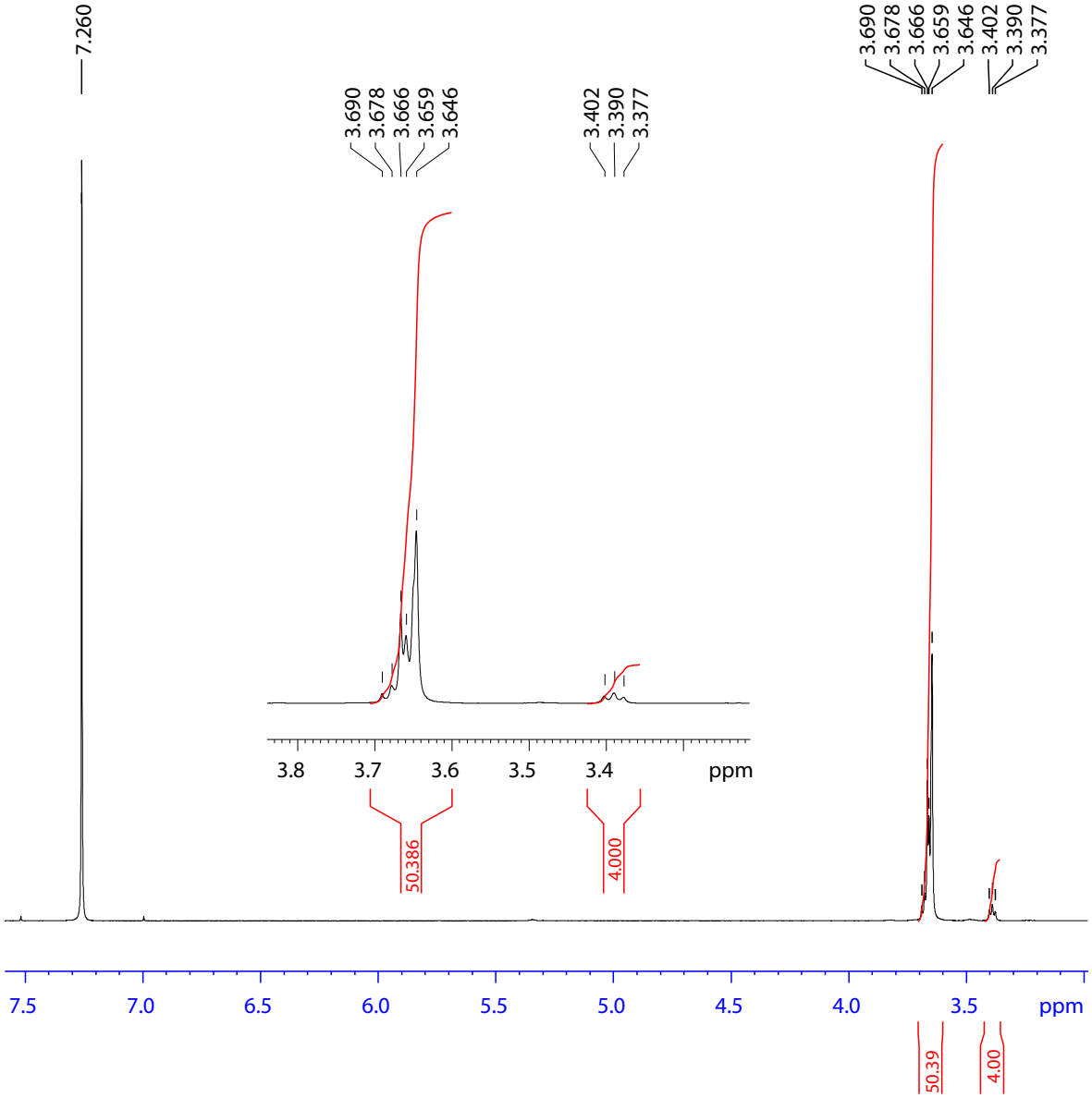


Figure 6.10: ^{1}H-NMR of PEG 600 diazide **8**.

N3-PEG600-TAB 10

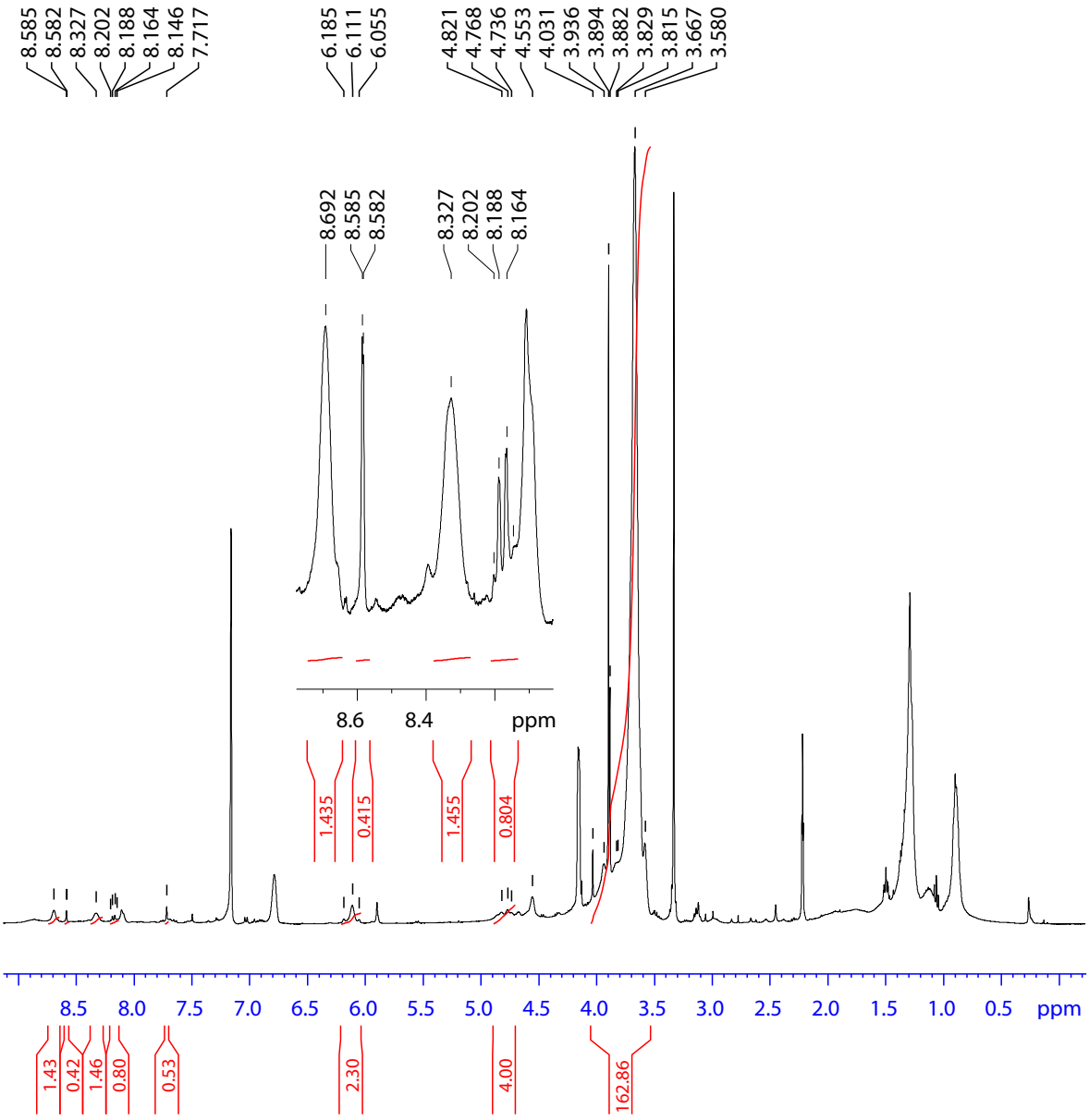


Figure 6.11: ^{1}H-NMR of N3-PEG600-TAB **10**.

Positively charged, clicked diblock surfactant PFPE7000-PEG600-TAB 11

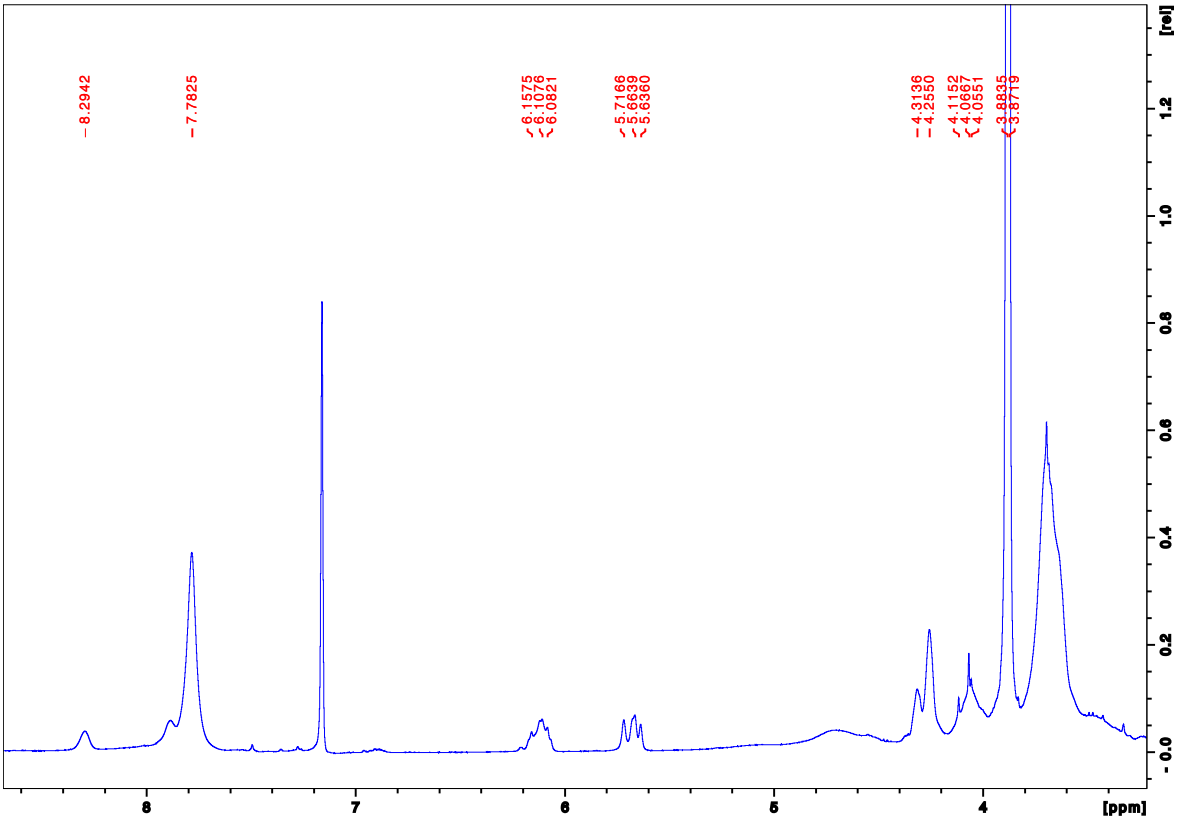


Figure 6.12: ^{1}H-NMR of Positively charged, clicked diblock surfactant PFPE7000-PEG600-TAB **11**.

4-(Azidomethyl)-3-nitrobenzoic acid 12

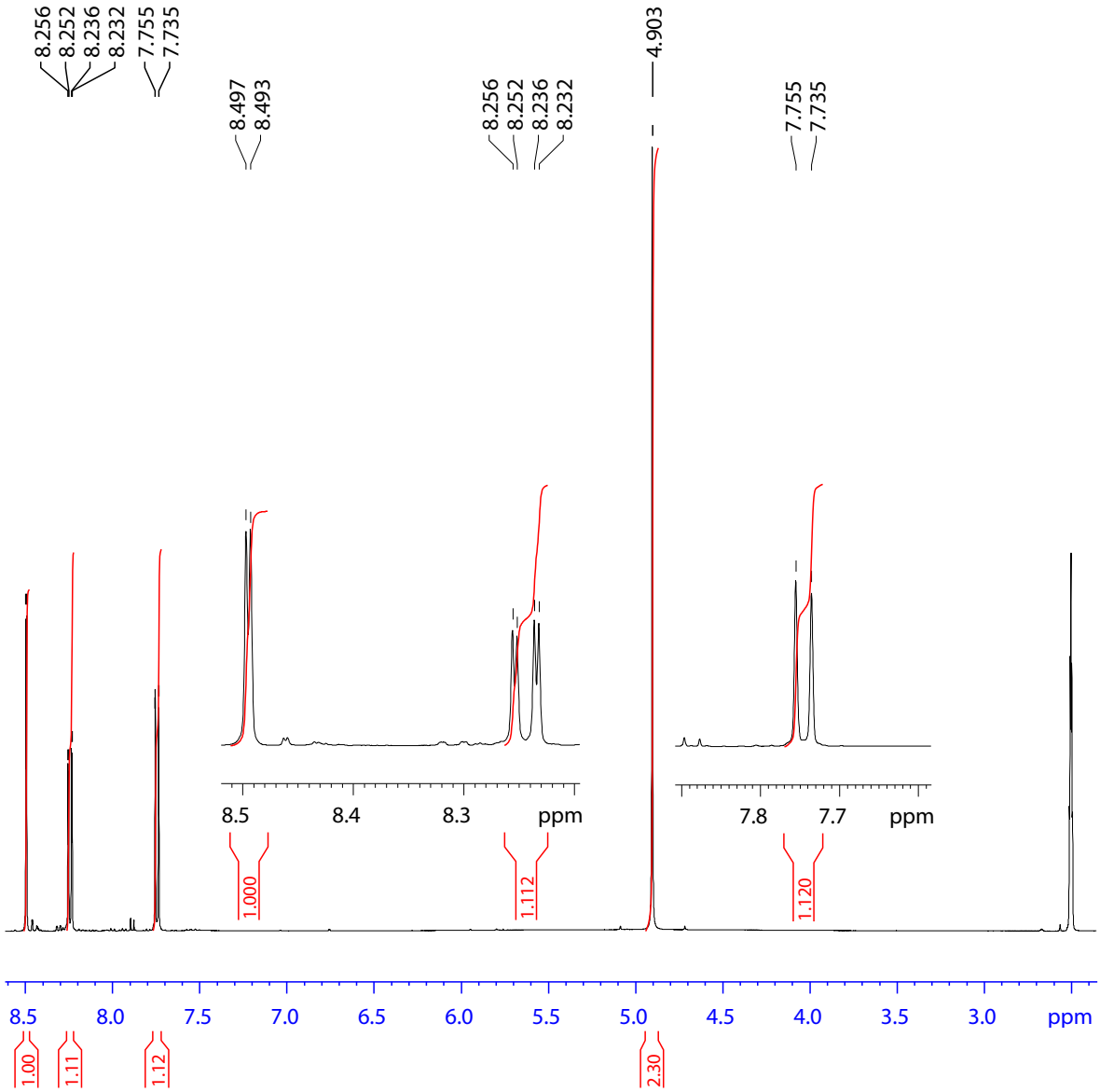


Figure 6.13: ^{1}H-NMR of 4-(azidomethyl)-3-nitrobenzoic acid **12**.

PEG 1500 bis(4-(azidomethyl)-3-nitrobenzoate) 13

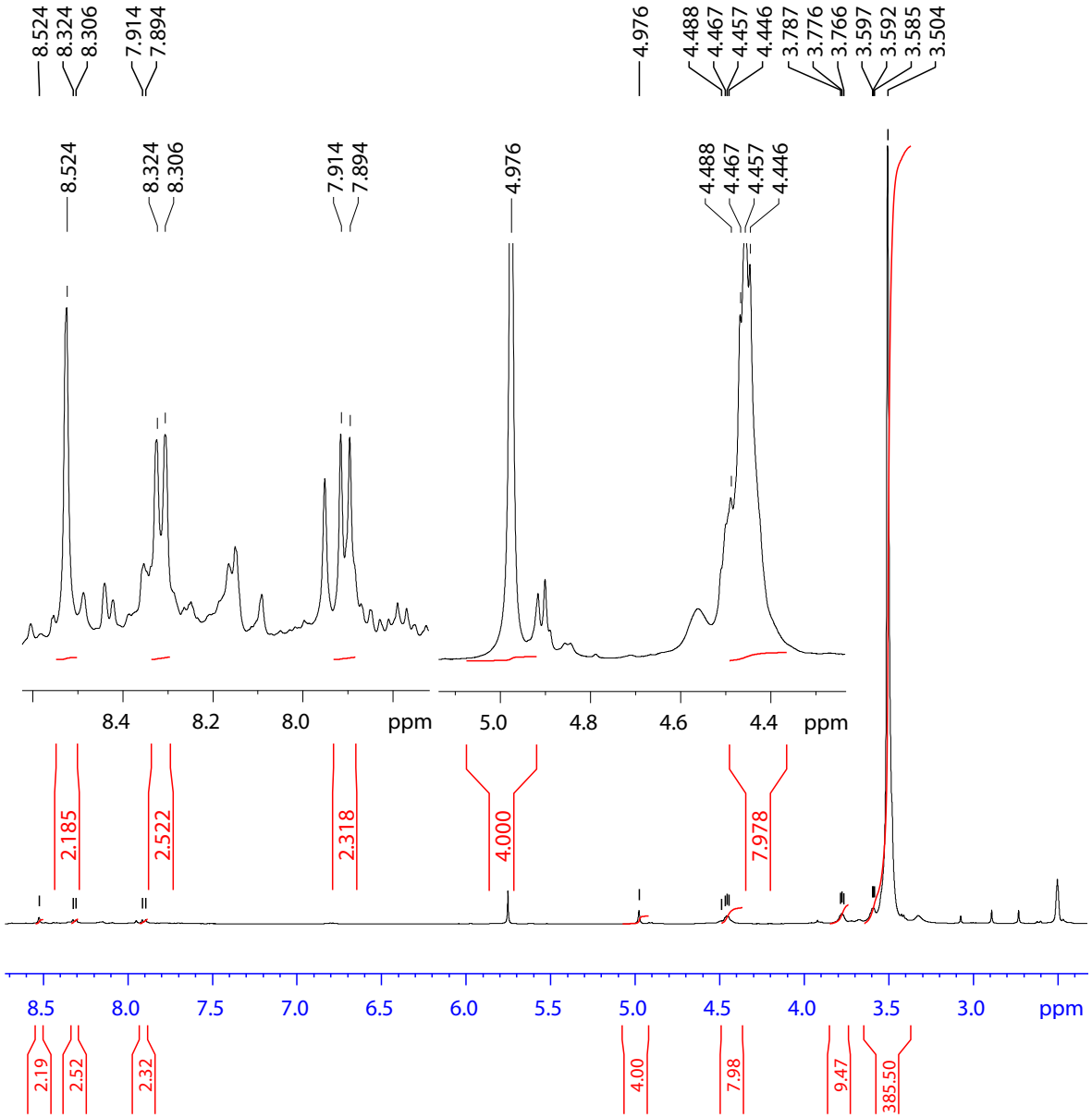


Figure 6.14: ^{1}H-NMR of PEG 1500 bis(4-(azidomethyl)-3-nitrobenzoate) **13**.

Photoliable, clicked triblock surfactant PFPE7000-NB-PEG1500-NB-PFPE7000 2

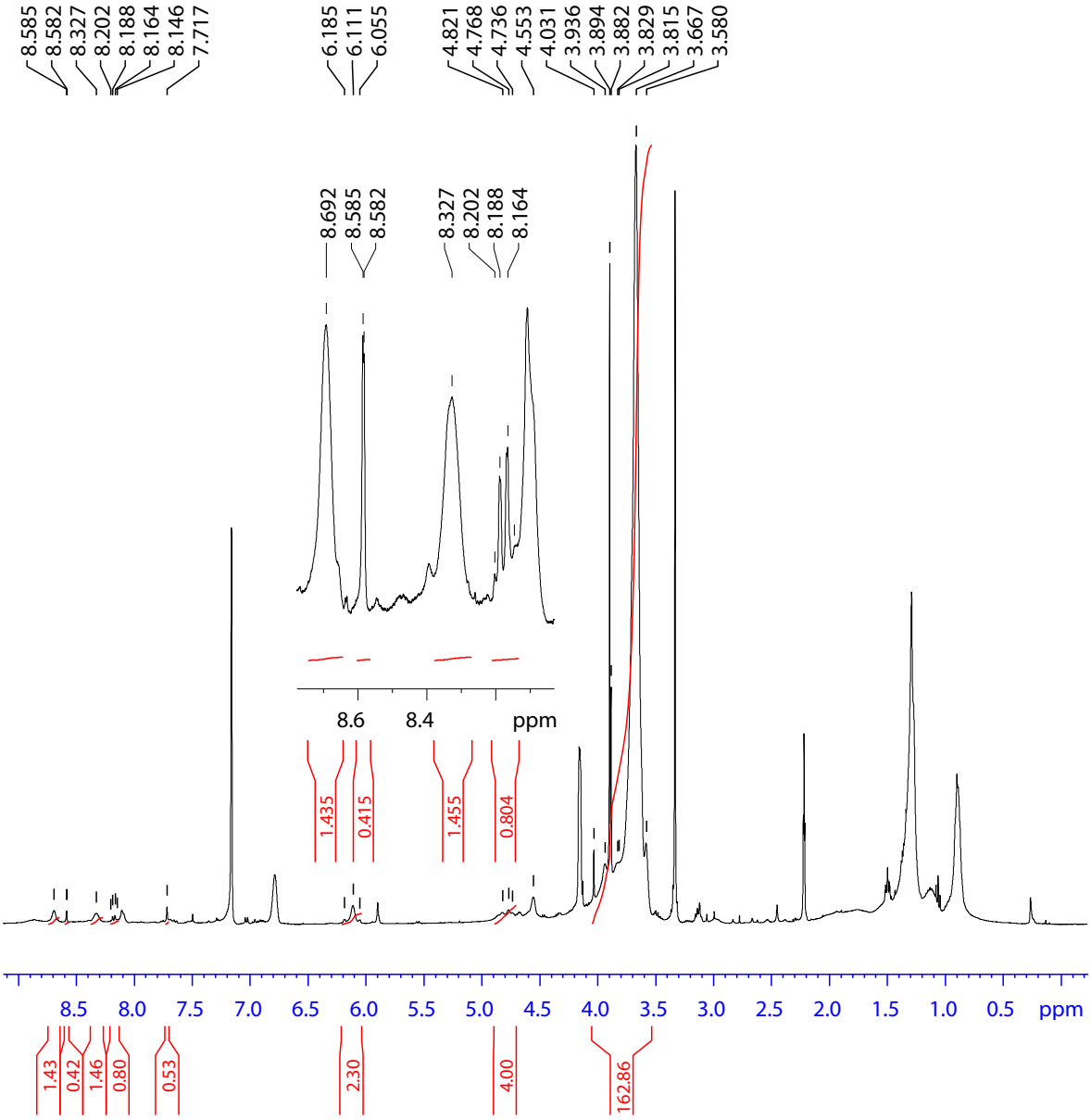


Figure 6.15: ^{1}H-NMR of photoliable, clicked triblock surfactant PFPE7000-NB-PEG1500-NB-PFPE7000 **2**.

Krytox, different concentrations

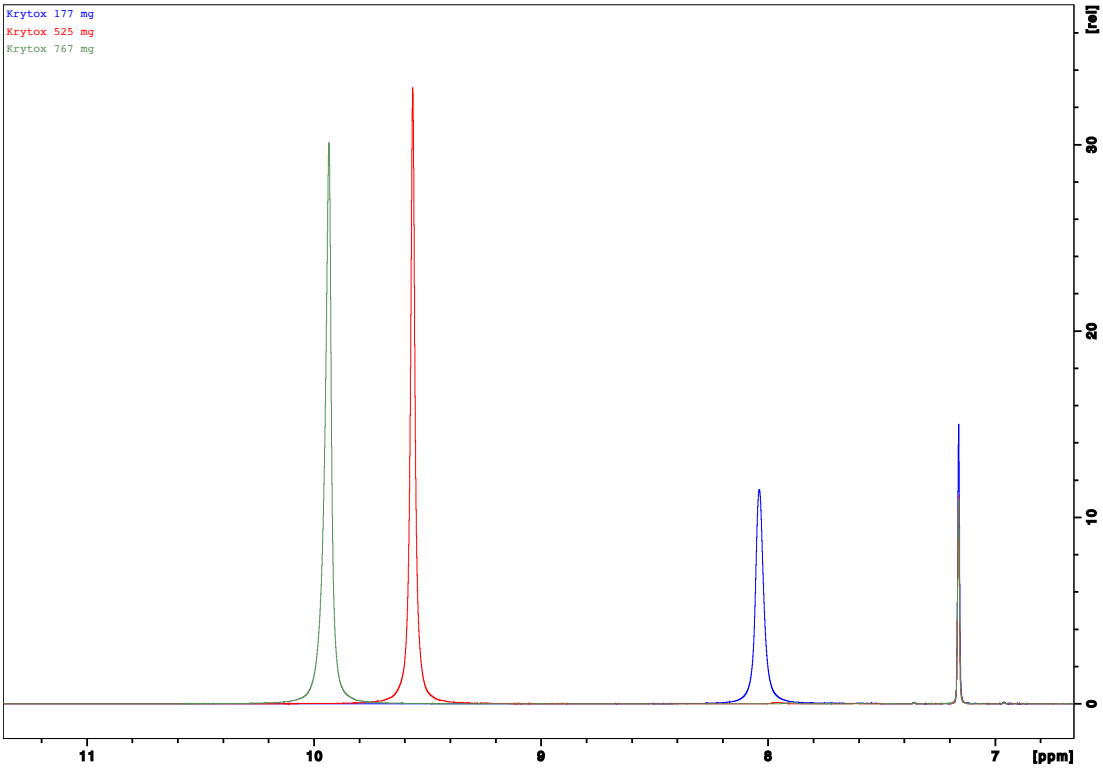


Figure 6.16: ^{1}H-NMR of Krytox with different concentrations. Different masses of Krytox where dissolved in 500 μL of a mixture of C_6F_6:C_6D_6 88:12.

6.1.3 Microscopy

GUV-GUV interactions using E-cadherins (without Ni(II) ion, without Ca(II) ion, without E-cadherin, Rhodamine)

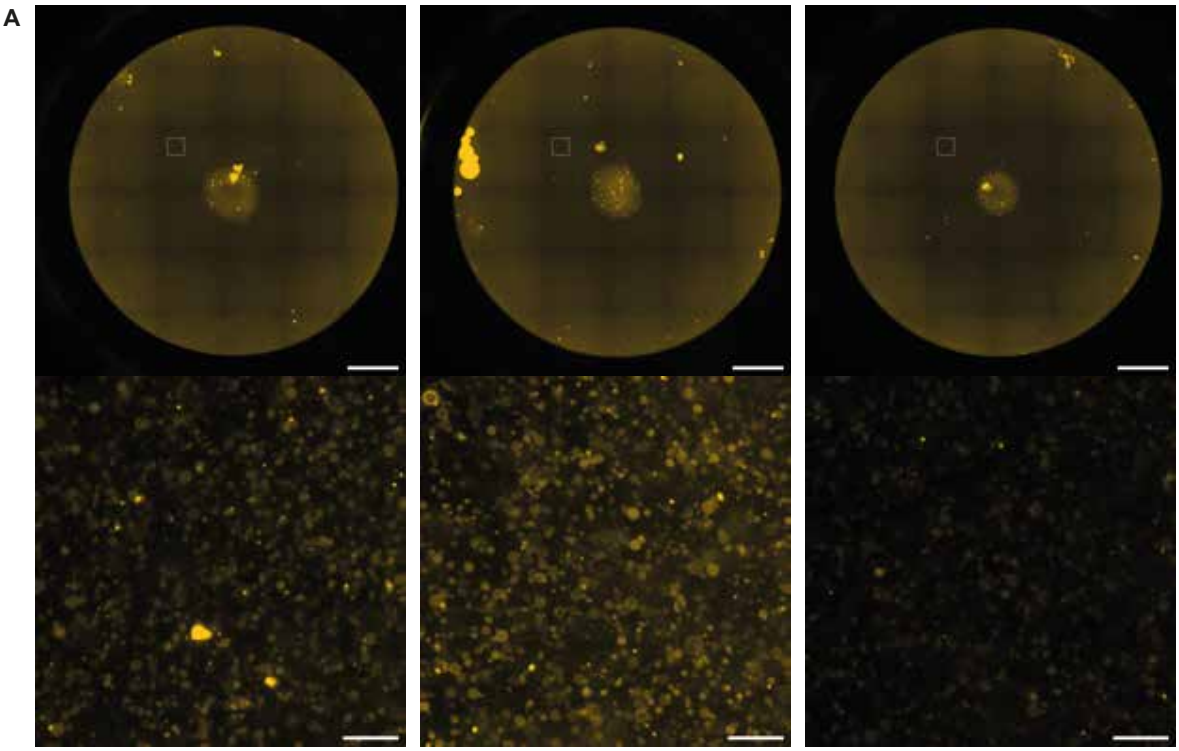


Figure 6.17: Fluorescent microscope images of Liss Rhodamine-labeled GUVs.

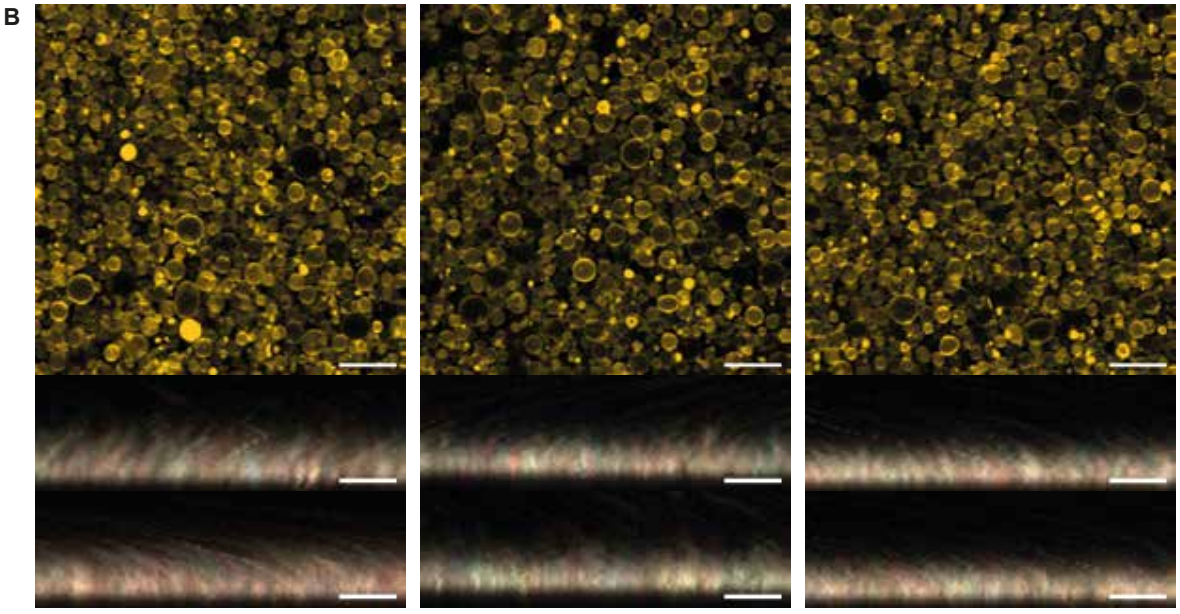


Figure 6.18: Confocal Z-stack (XZ- and YZ-projection) images of Liss Rhodamine-labeled GUVs.

GUV-GUV interactions using E-cadherins (with Ni(II) ion, without Ca(II) ion, without E-cadherin, Rhodamine)

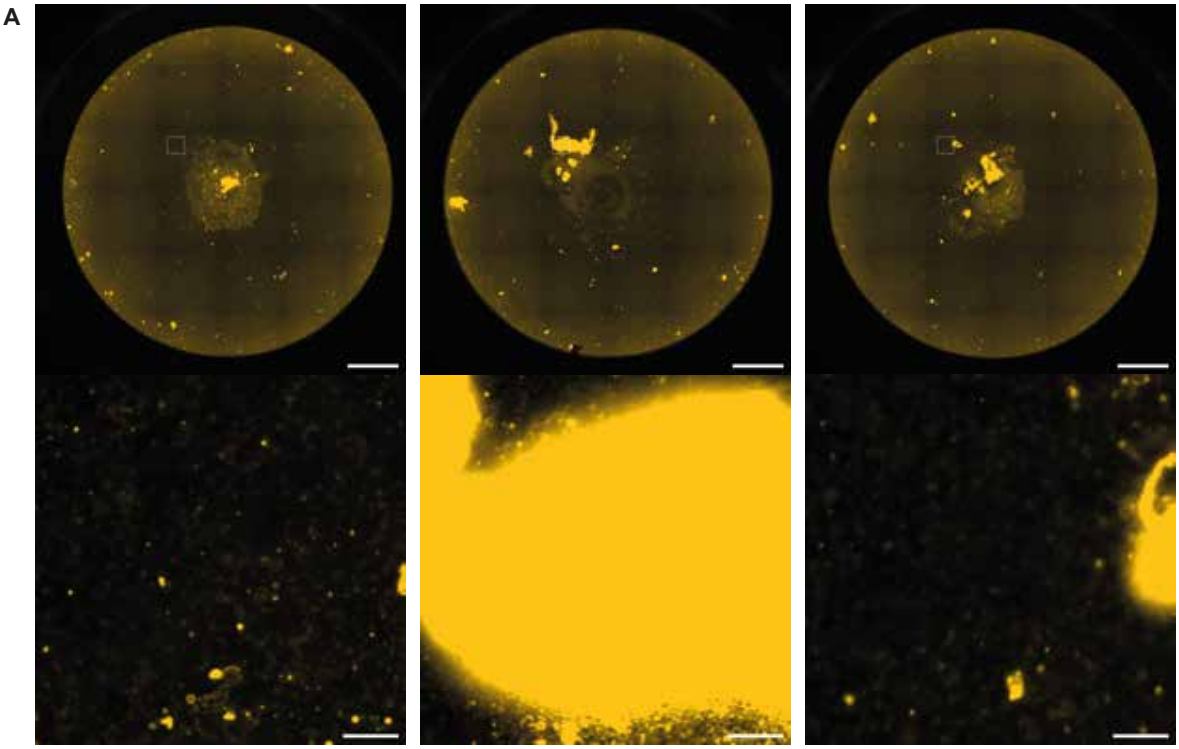


Figure 6.19: Fluorescent microscope images of Liss Rhodamine-labeled GUVs with nickel(II) ions.

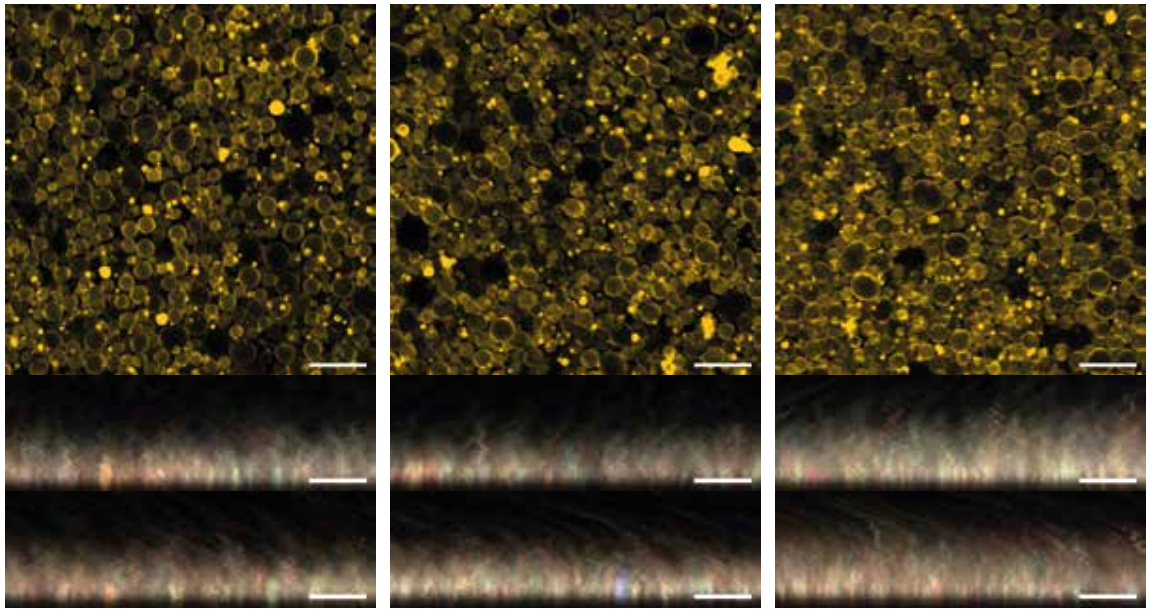


Figure 6.20: Confocal Z-stack (XZ- and YZ-projection) images of Liss Rhodamine-labeled GUVs with nickel(II) ions.

GUV-GUV interactions using E-cadherins (without Ni(II) ion, with Ca(II) ion, without E-cadherin, Rhodamine)

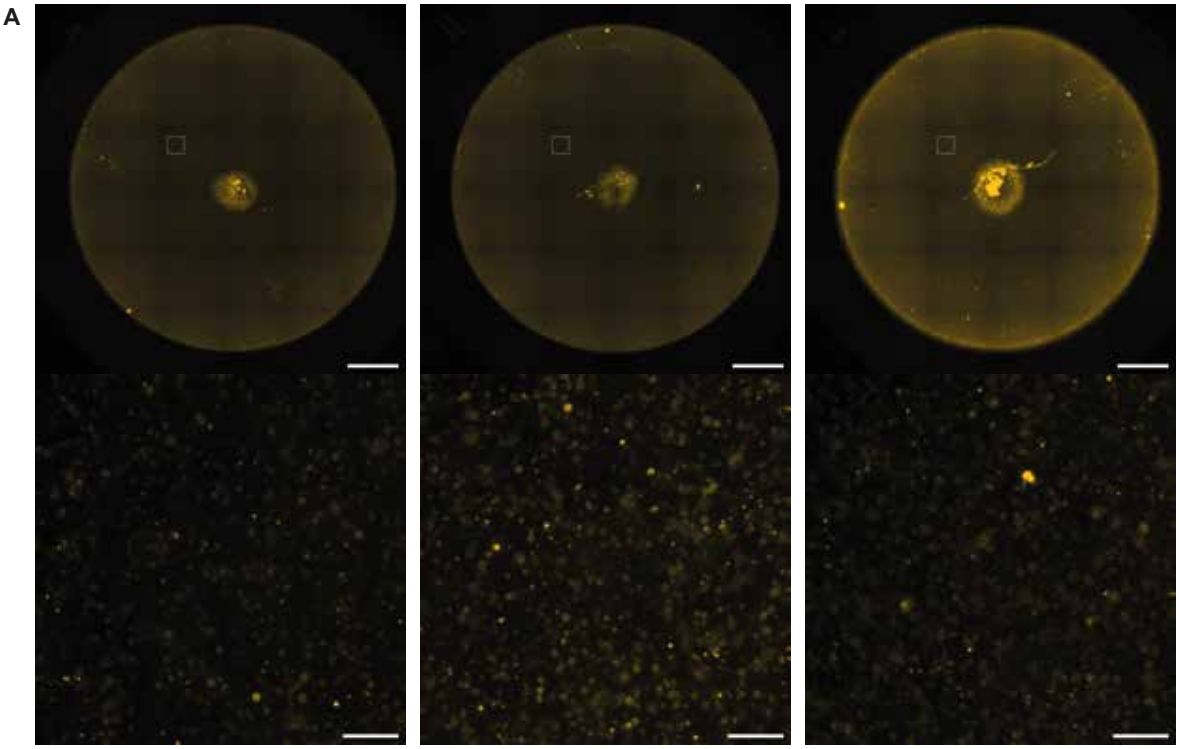


Figure 6.21: Fluorescent microscope images of Liss Rhodamine-labeled GUVs with calcium ions.

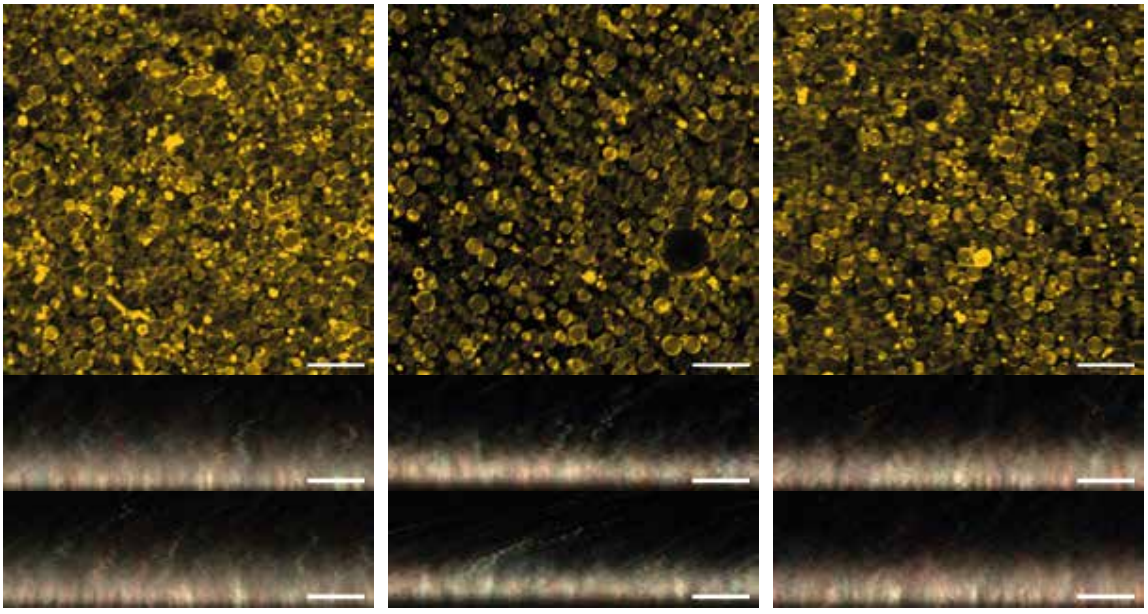


Figure 6.22: Confocal Z-stack (XZ- and YZ-projection) images of Liss Rhodamine-labeled GUVs with calcium ions.

GUV-GUV interactions using E-cadherins (with Ni(II) ion, with Ca(II) ion, without E-cadherin, Rhodamine)

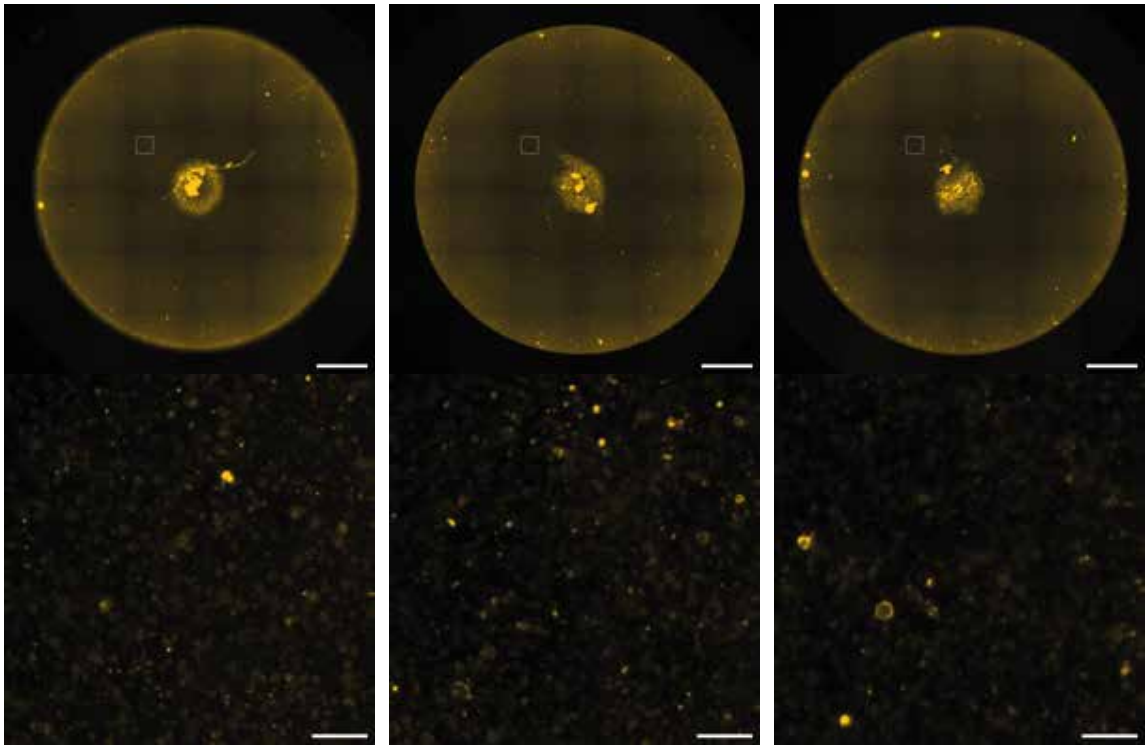


Figure 6.23: Fluorescent microscope images of Liss Rhodamine-labeled GUVs with nickel(II) and calcium ions.

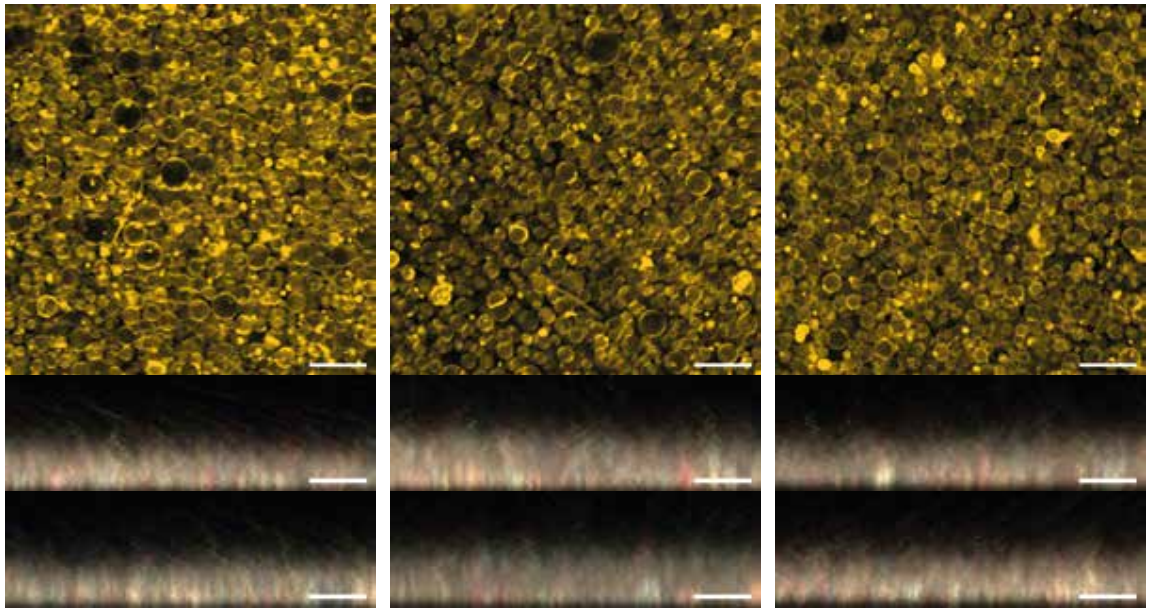


Figure 6.24: Confocal Z-stack (XZ- and YZ-projection) images of Liss Rhodamine-labeled GUVs with nickel(II) and calcium ions.

GUV-GUV interactions using E-cadherins (without Ni(II) ion, without Ca(II) ion, with E-cadherin, Rhodamine)

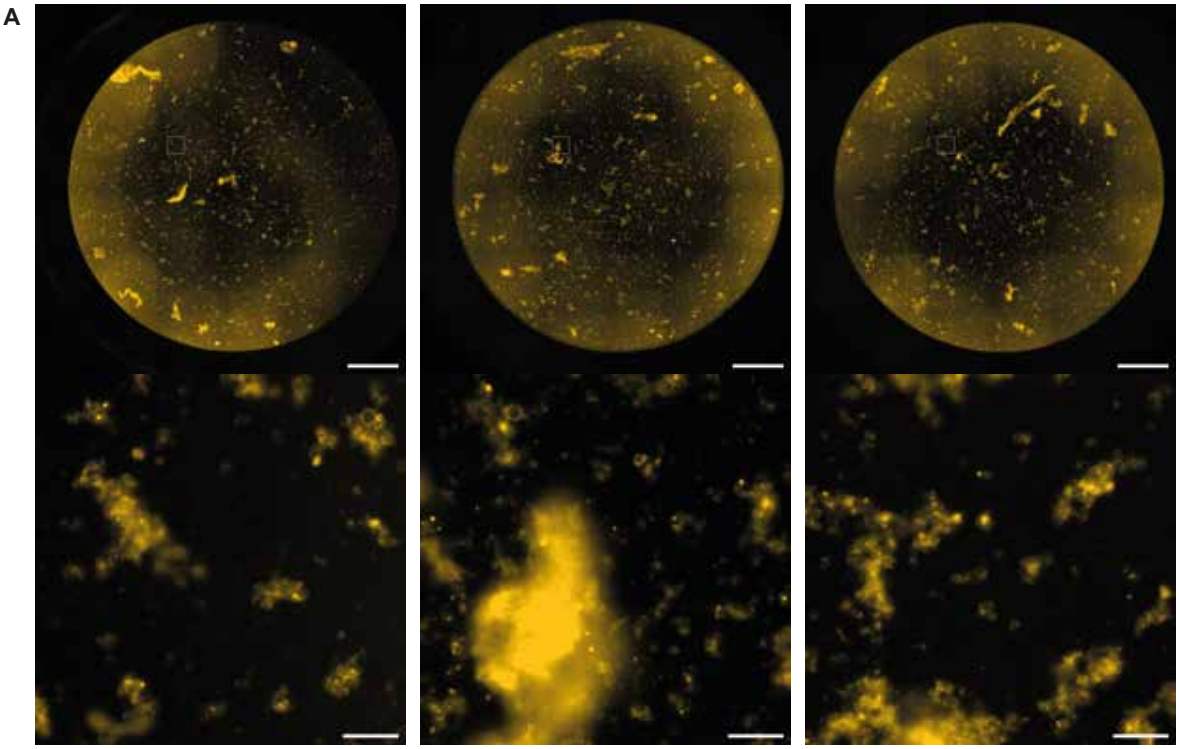


Figure 6.25: Fluorescent microscope images of Liss Rhodamine-labeled GUVs with E-cadherin.

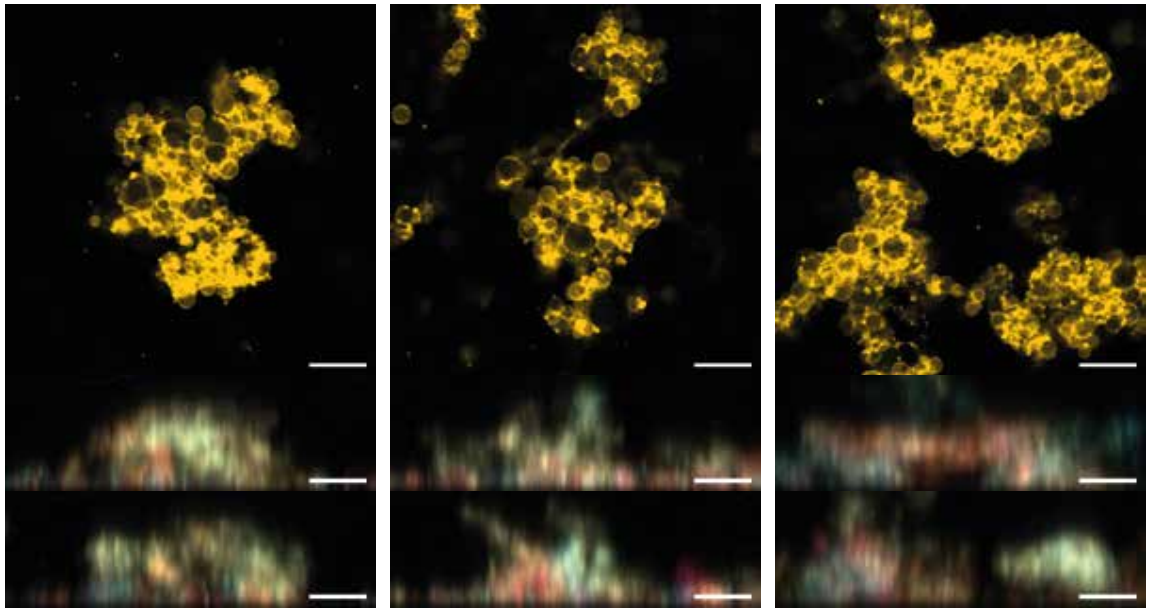


Figure 6.26: Confocal Z-stack (XZ- and YZ-projection) images of Liss Rhodamine-labeled GUVs with E-cadherin.

GUV-GUV interactions using E-cadherins (with Ni(II) ion, without Ca(II) ion, with E-cadherin, Rhodamine)

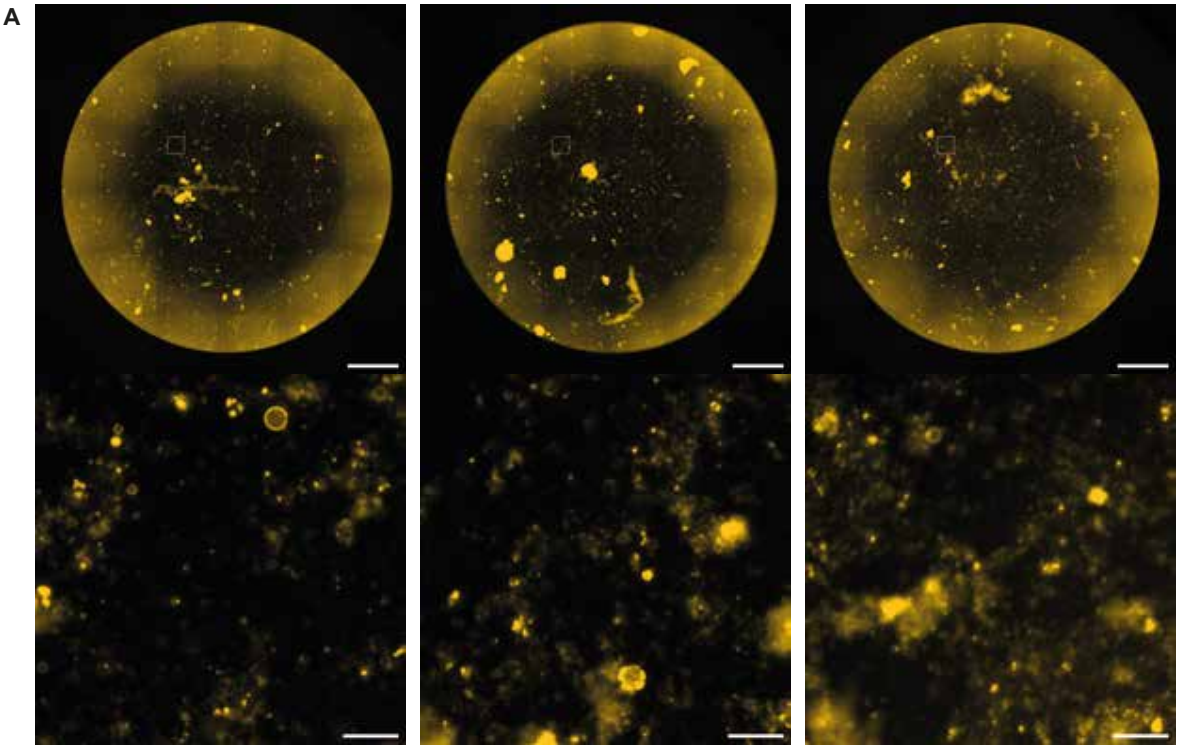


Figure 6.27: Fluorescent microscope images of Liss Rhodamine-labeled GUVs with E-cadherin and nickel(II) ions.

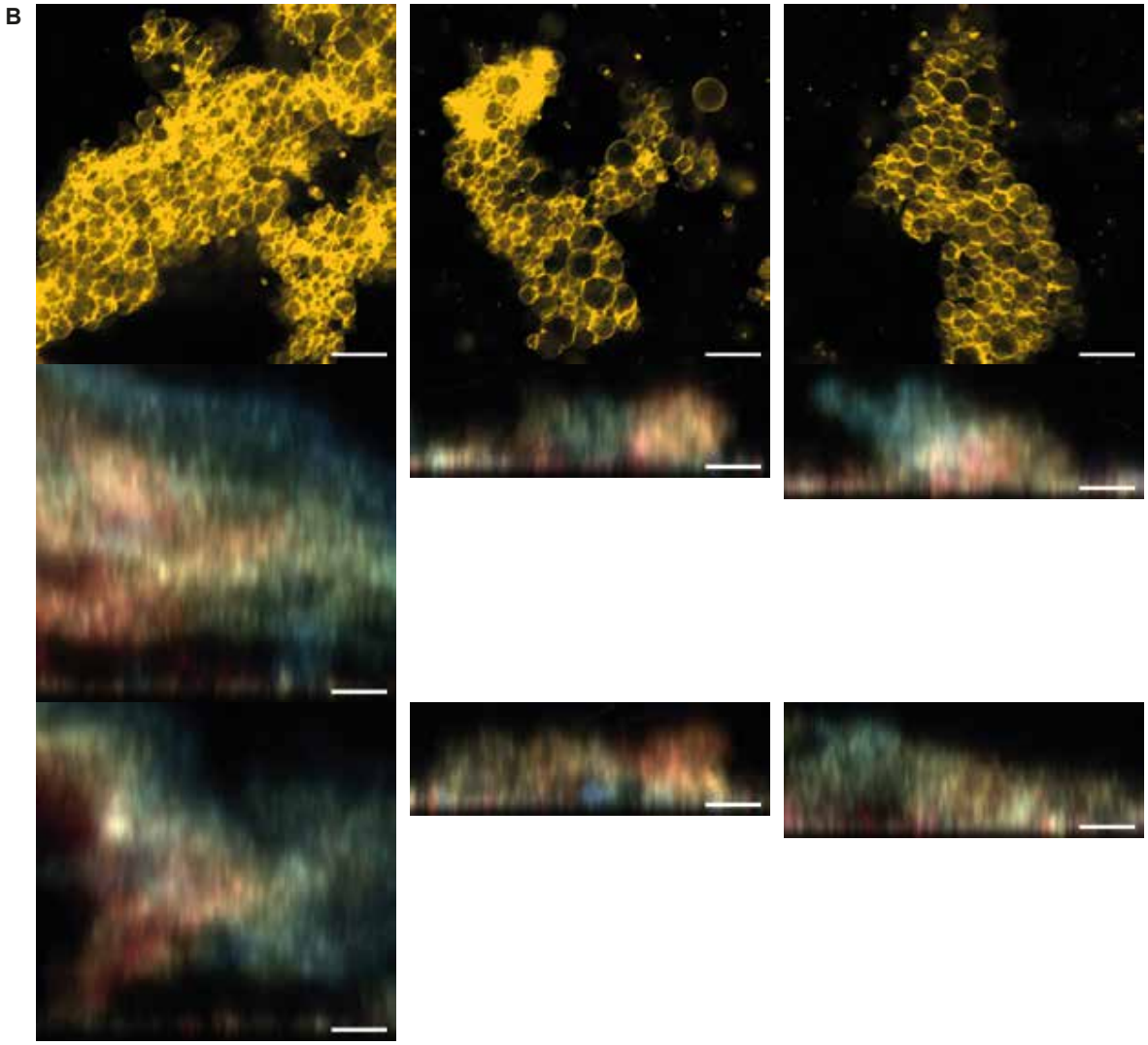


Figure 6.28: Confocal Z-stack (XZ- and YZ-projection) images of Liss Rhodamine-labeled GUVs with E-cadherin and nickel(II) ions.

GUV-GUV interactions using E-cadherins (without Ni(II) ion, with Ca(II) ion, with E-cadherin, Rhodamine)

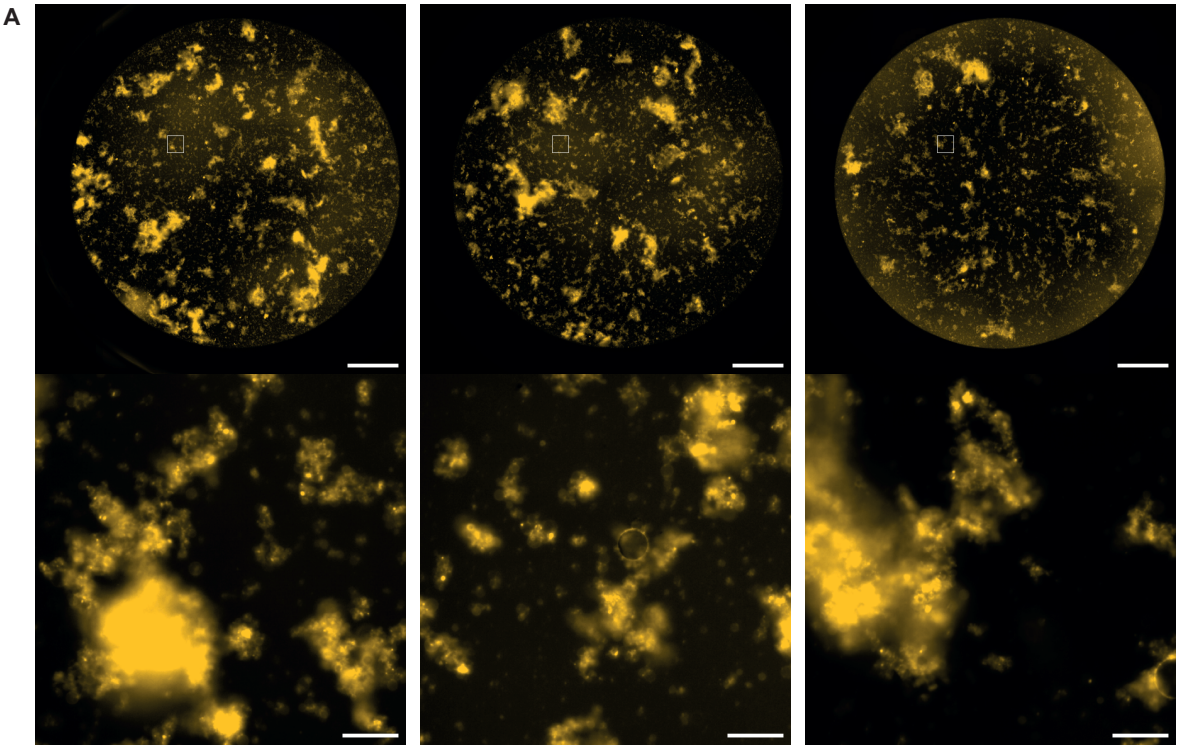


Figure 6.29: Fluorescent microscope images of Liss Rhodamine-labeled GUVs with E-cadherin and calcium ions.

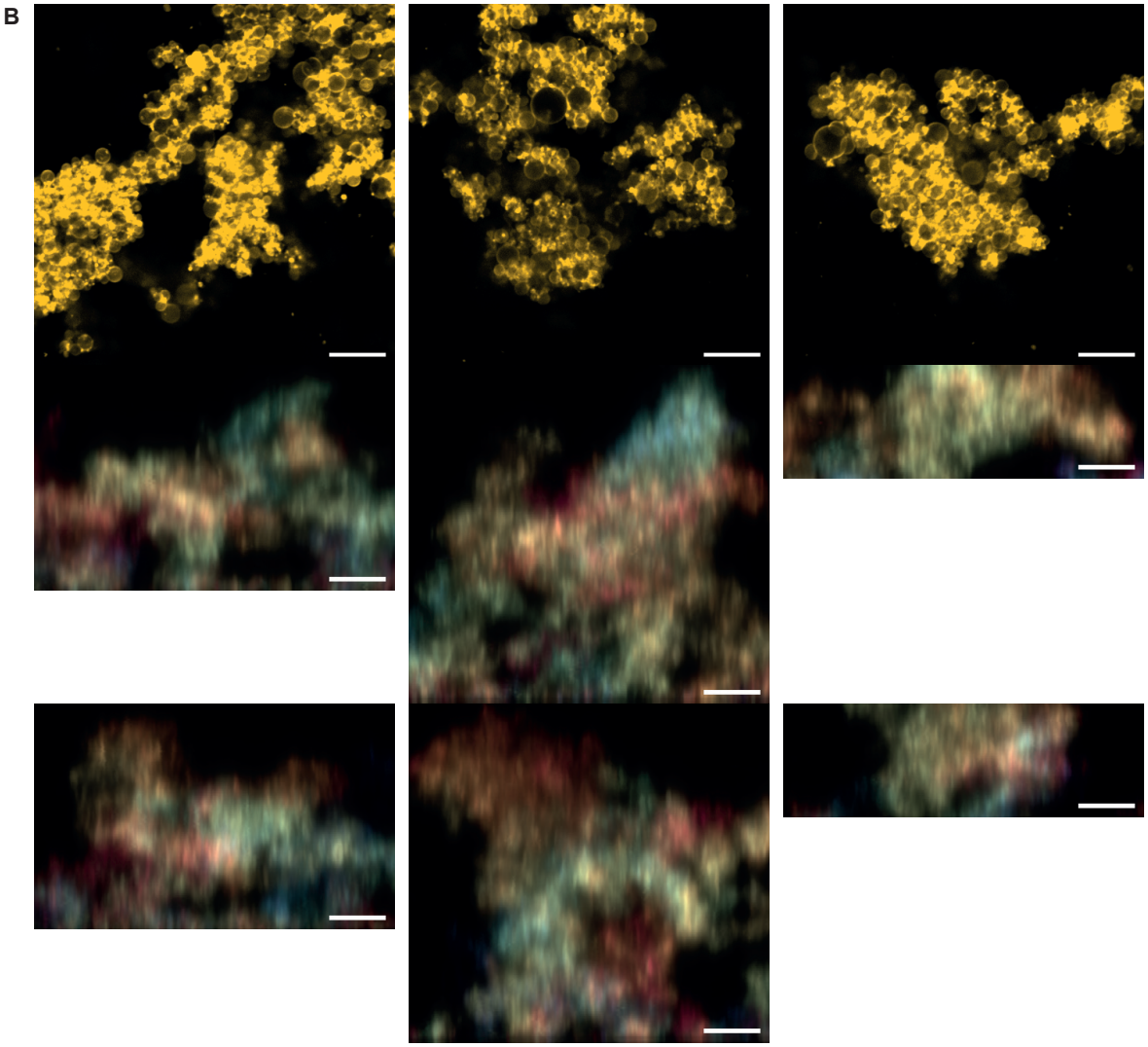


Figure 6.30: Confocal Z-stack (XZ- and YZ-projection) images of Liss Rhodamine-labeled GUVs with E-cadherin and calcium ions.

GUV-GUV interactions using E-cadherins (with Ni(II) ion, with Ca(II) ion, with E-cadherin, Rhodamine)

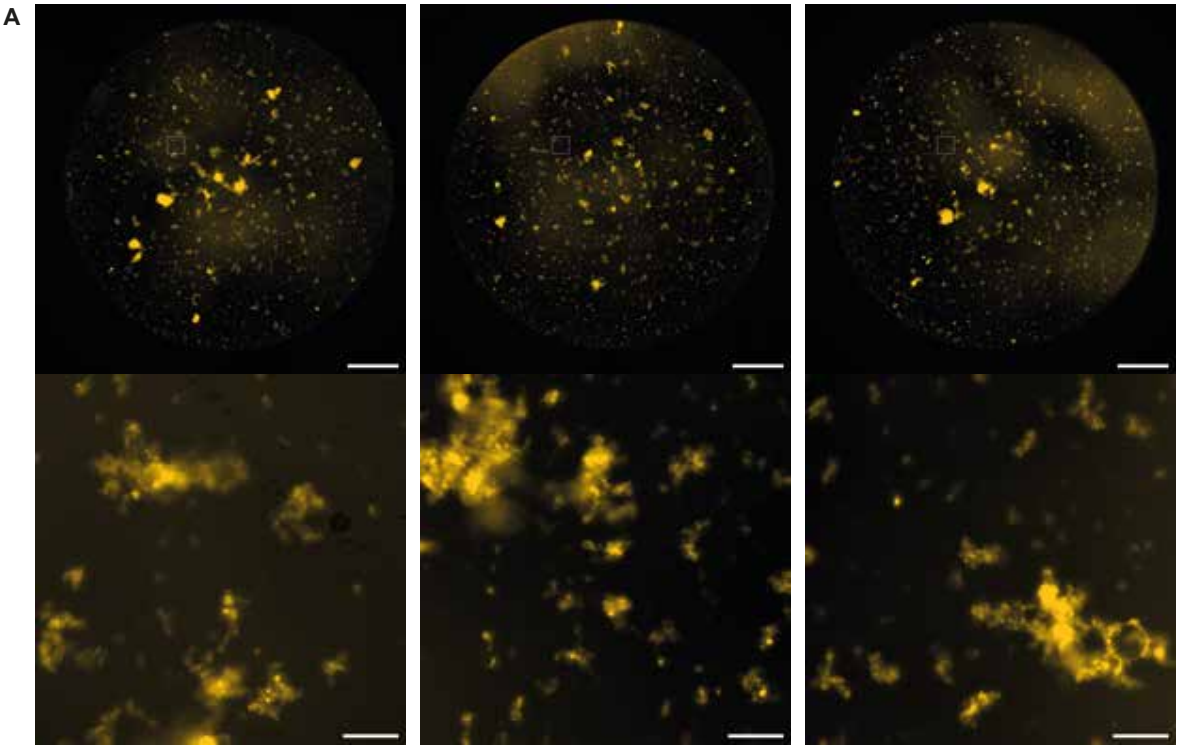


Figure 6.31: Fluorescent microscope images of Liss Rhodamine-labeled GUVs with E-cadherin, nickel(II) ions and calcium ions.

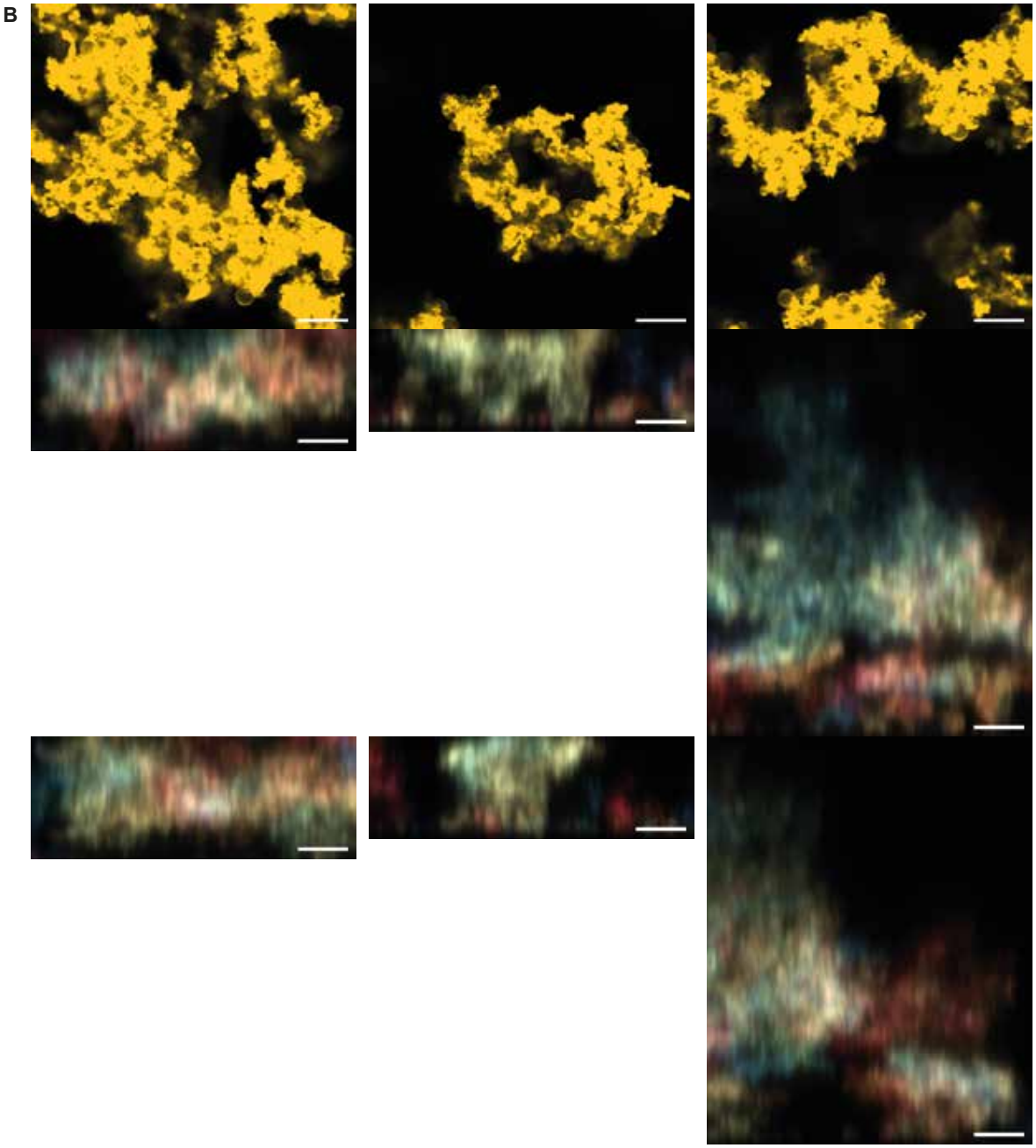


Figure 6.32: Confocal Z-stack (XZ- and YZ-projection) images of Liss Rhodamine-labeled GUVs with E-cadherin, nickel(II) ions and calcium ions.

GUV-GUV interactions using E-cadherins (without Ni(II) ion, without Ca(II) ion, without E-cadherin, Atto488)

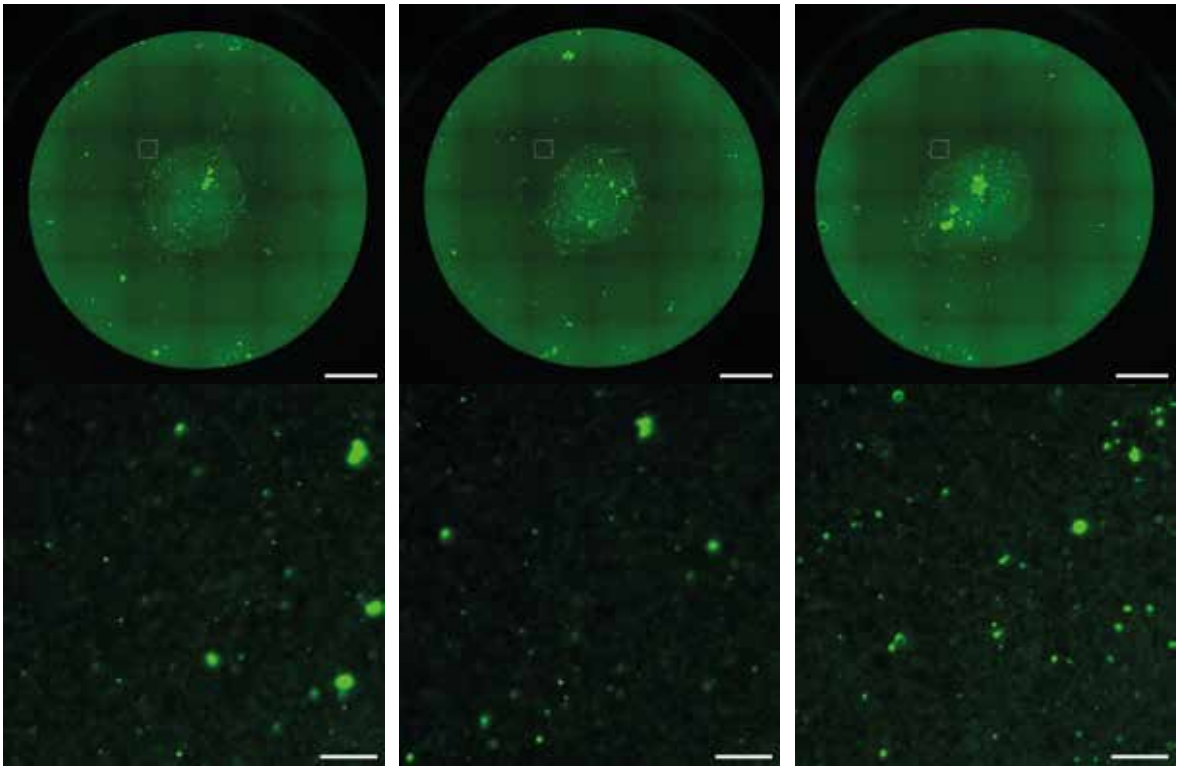


Figure 6.33: Fluorescent microscope images of ATTO 488-labeled GUVs.

GUV-GUV interactions using E-cadherins (with Ni(II) ion, without Ca(II) ion, without E-cadherin, Atto488)

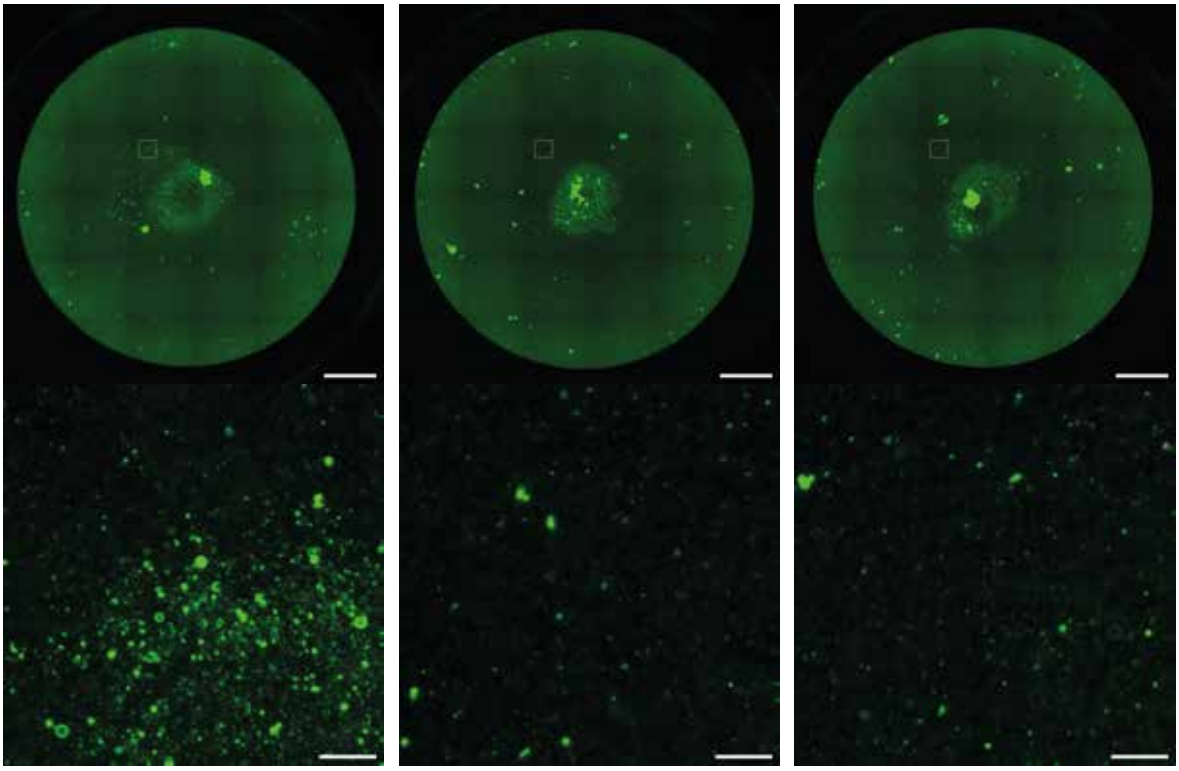


Figure 6.34: Fluorescent microscope images of ATTO 488-labeled GUVs with nickel(II) ions.

GUV-GUV interactions using E-cadherins (without Ni(II) ion, with Ca(II) ion, without E-cadherin, Atto488)

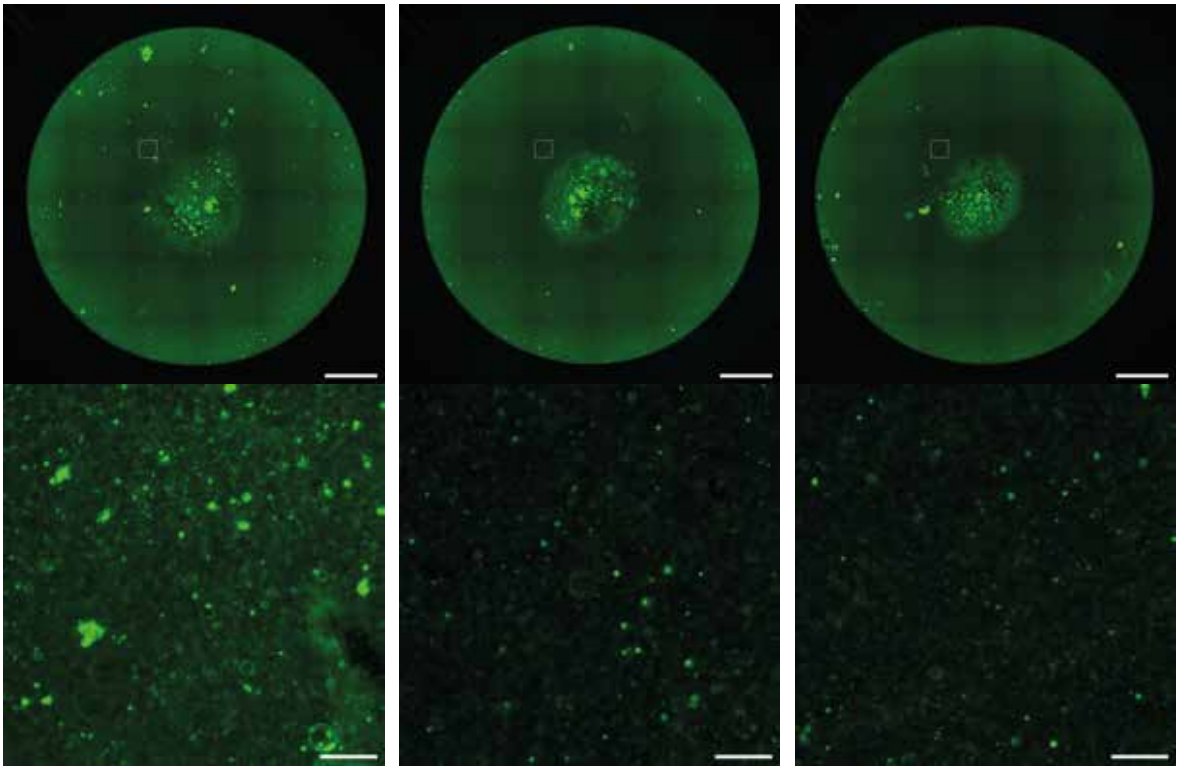


Figure 6.35: Fluorescent microscope images of ATTO 488-labeled GUVs with calcium ions.

GUV-GUV interactions using E-cadherins (with Ni(II) ion, with Ca(II) ion, without E-cadherin, Atto488)

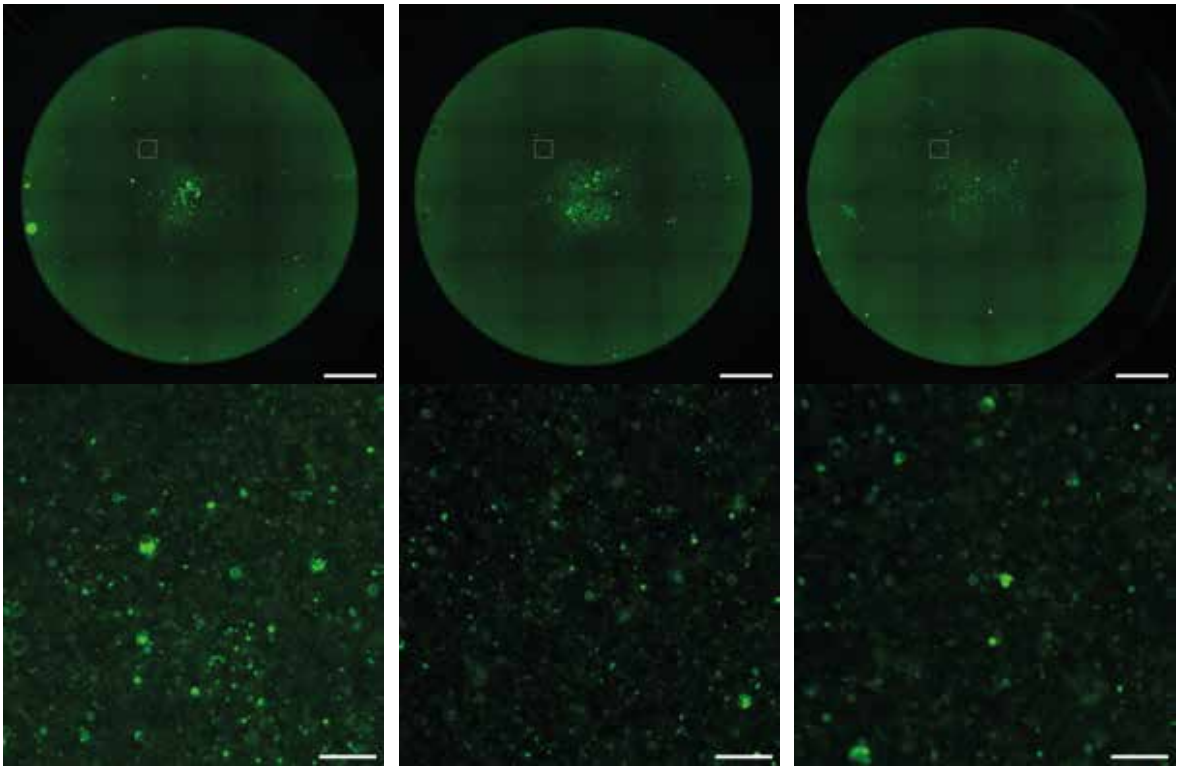


Figure 6.36: Fluorescent microscope images of ATTO 488-labeled GUVs with nickel(II) and calcium ions.

GUV-GUV interactions using E-cadherins (without Ni(II) ion, without Ca(II) ion, with E-cadherin, Atto488)

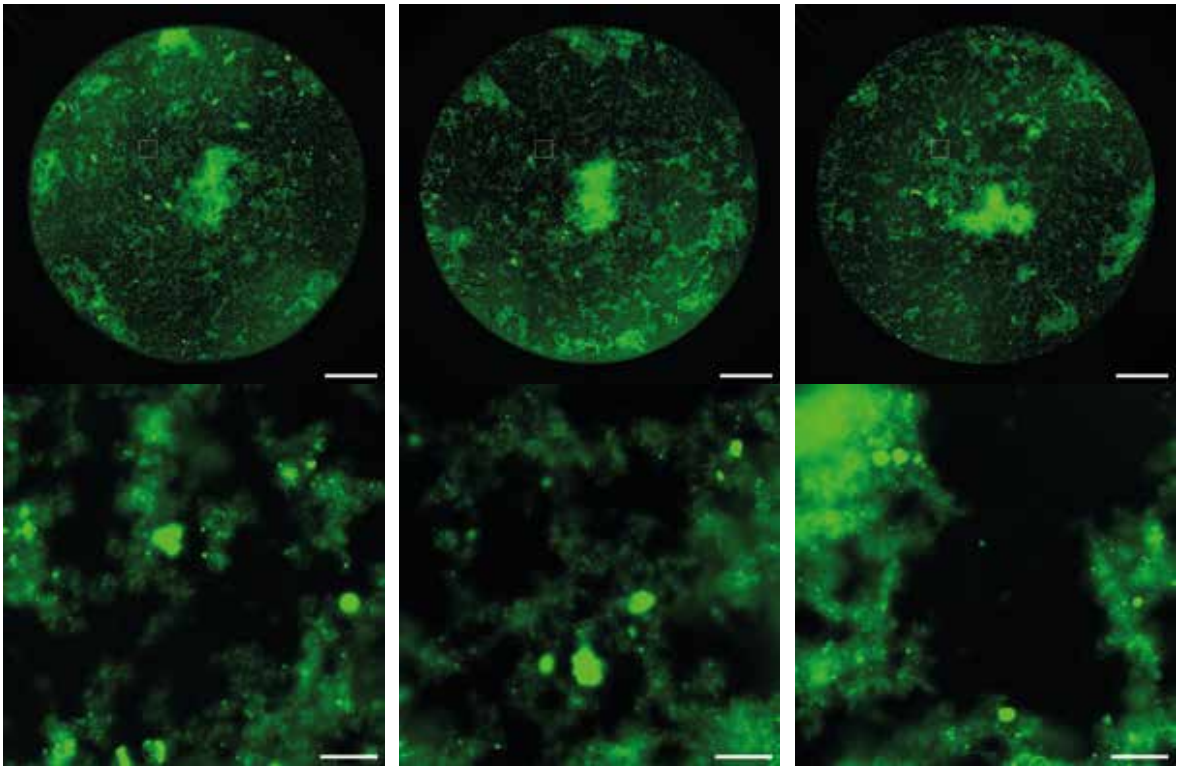


Figure 6.37: Fluorescent microscope images of ATTO 488-labeled GUVs with E-cadherin.

GUV-GUV interactions using E-cadherins (with Ni(II) ion, without Ca(II) ion, with E-cadherin, Atto488)

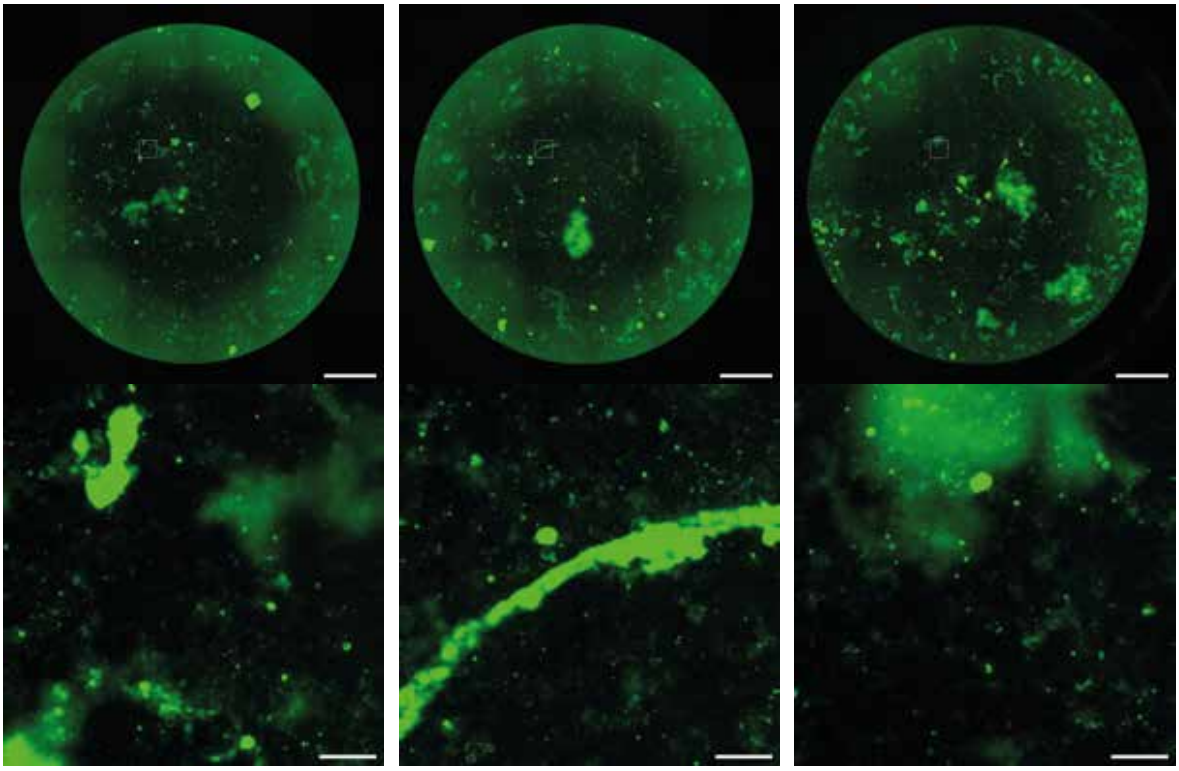


Figure 6.38: Fluorescent microscope images of ATTO 488-labeled GUVs with E-cadherin and nickel(II) ions.

GUV-GUV interactions using E-cadherins (without Ni(II) ion, with Ca(II) ion, with E-cadherin, Atto488)

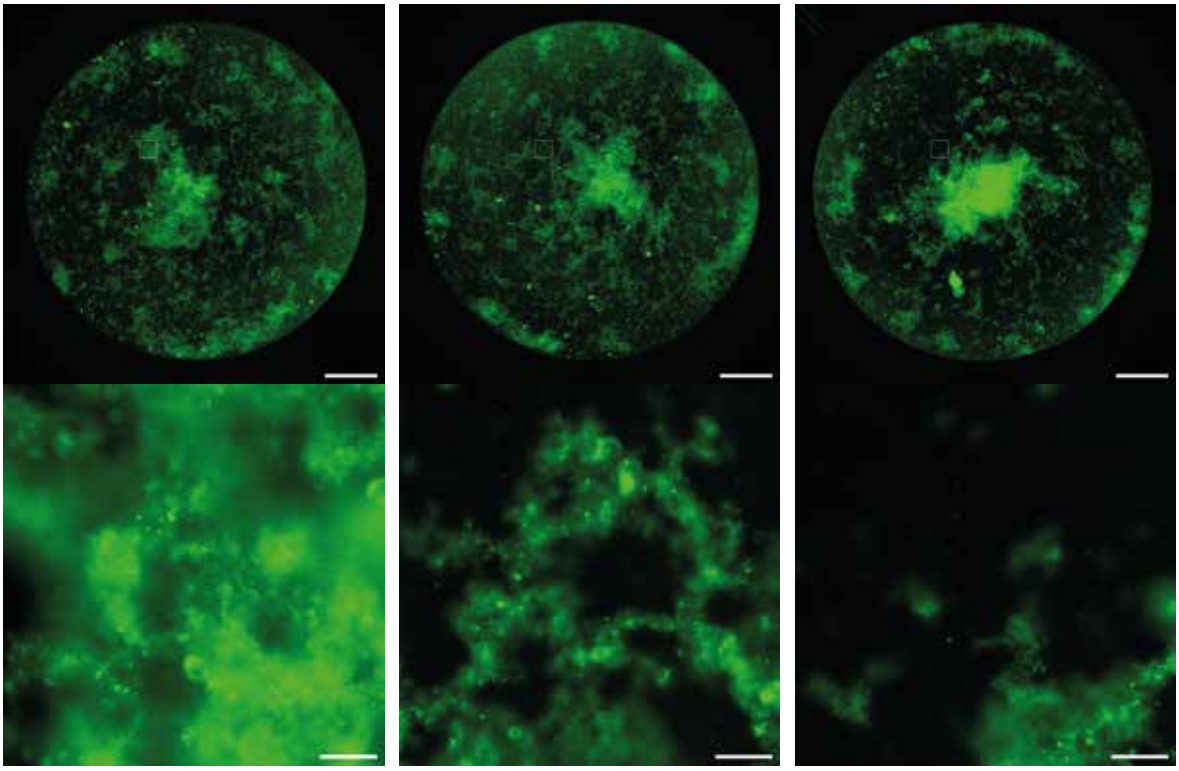


Figure 6.39: Fluorescent microscope images of ATTO 488-labeled GUVs with E-cadherin and calcium ions.

GUV-GUV interactions using E-cadherins (with Ni(II) ion, with Ca(II) ion, with E-cadherin, Atto488)

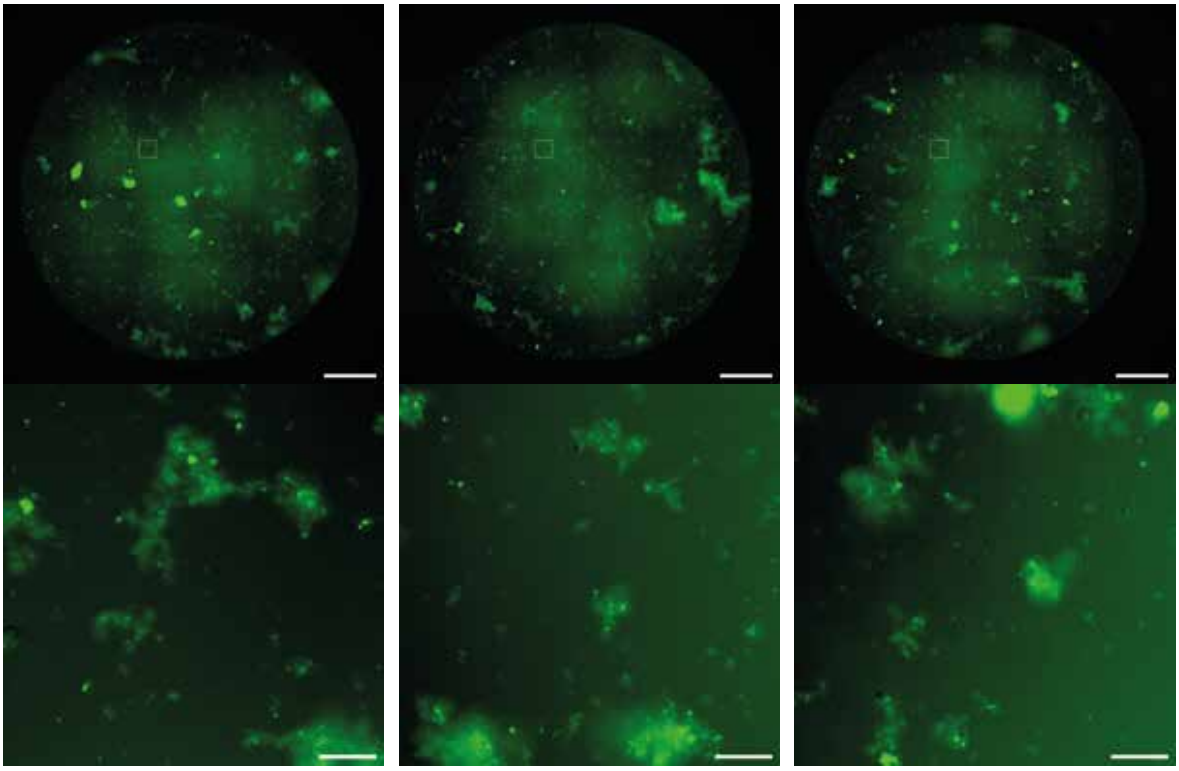


Figure 6.40: Fluorescent microscope images of ATTO 488-labeled GUVs with E-cadherin, nickel(II) and calcium ions.

GUV-GUV interactions using palindromic DNA (without DNA)

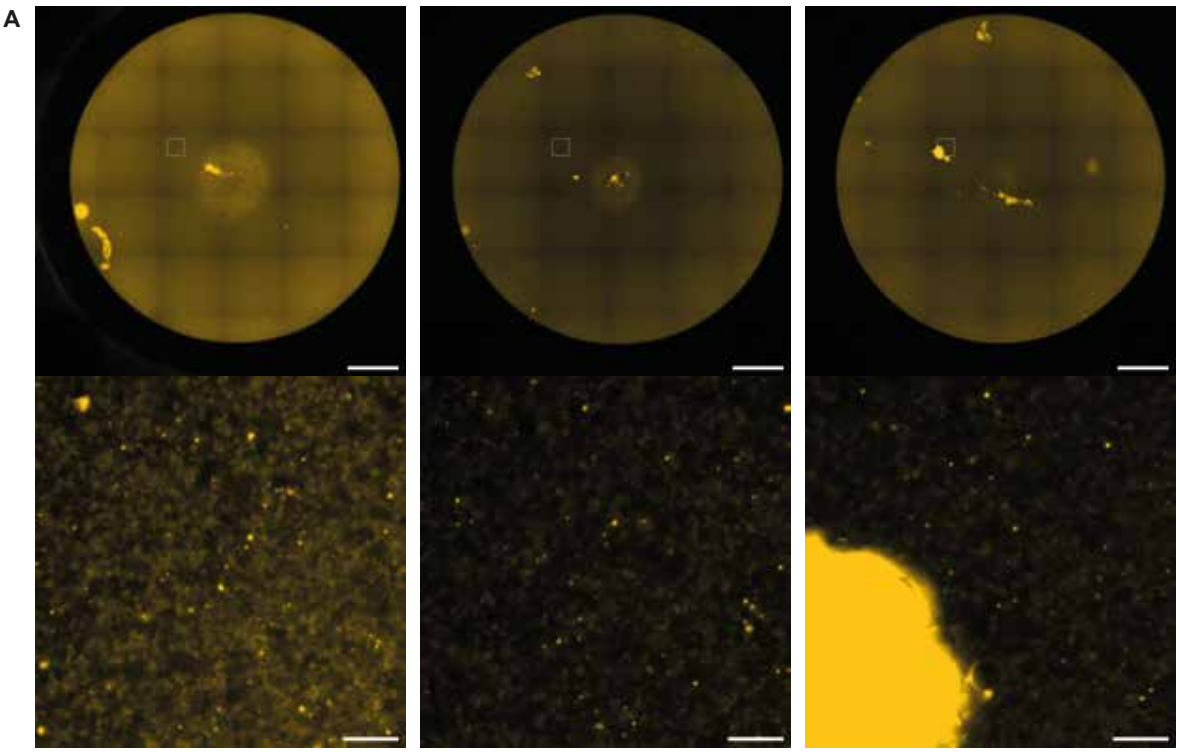


Figure 6.41: Fluorescent microscope images of Liss Rhodamine-labeled GUVs.

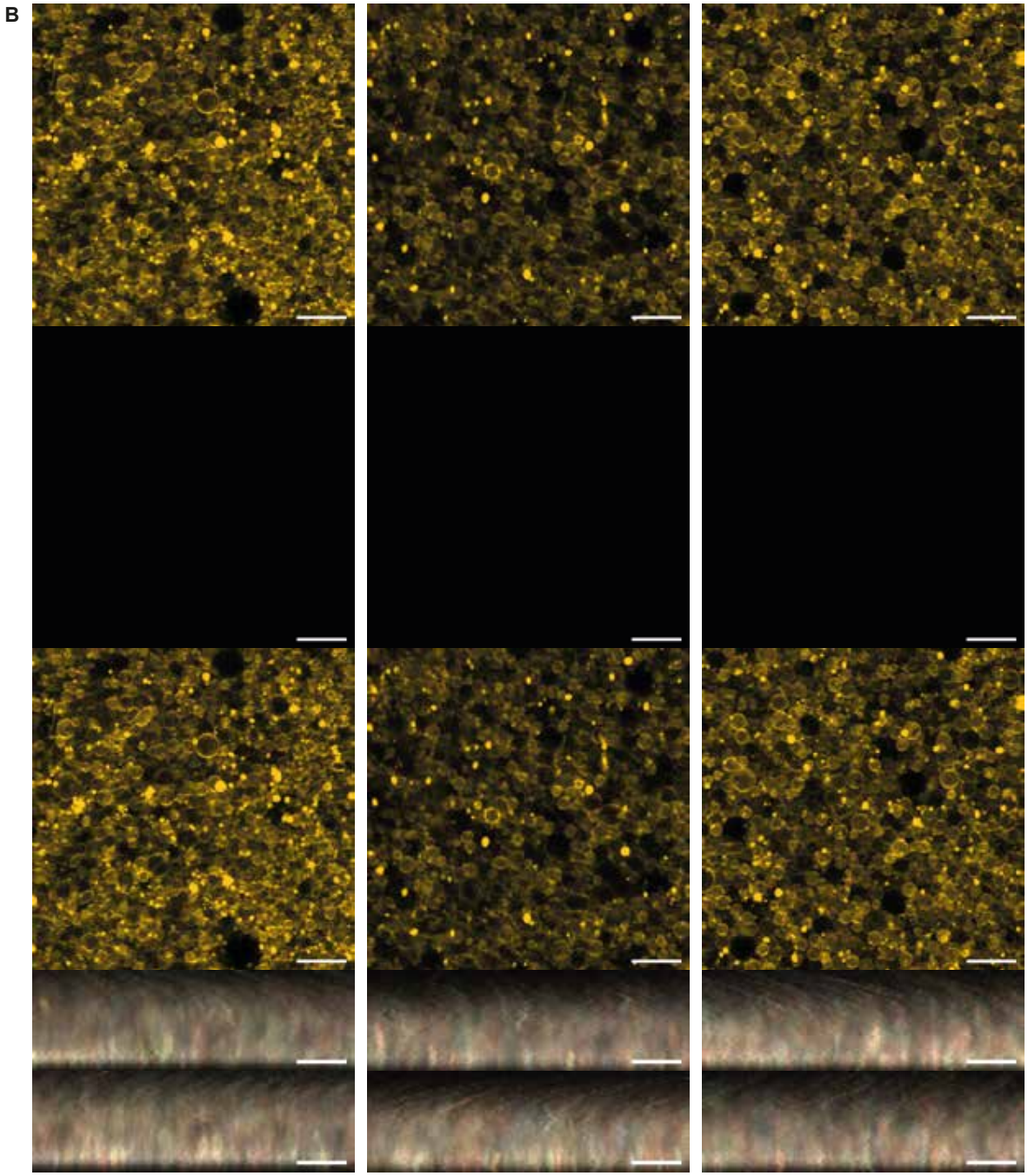


Figure 6.42: Confocal Z-stack (XZ- and YZ-projection) images of Liss Rhodamine-labeled GUVs.

GUV-GUV interactions using palindromic DNA (with DNA)

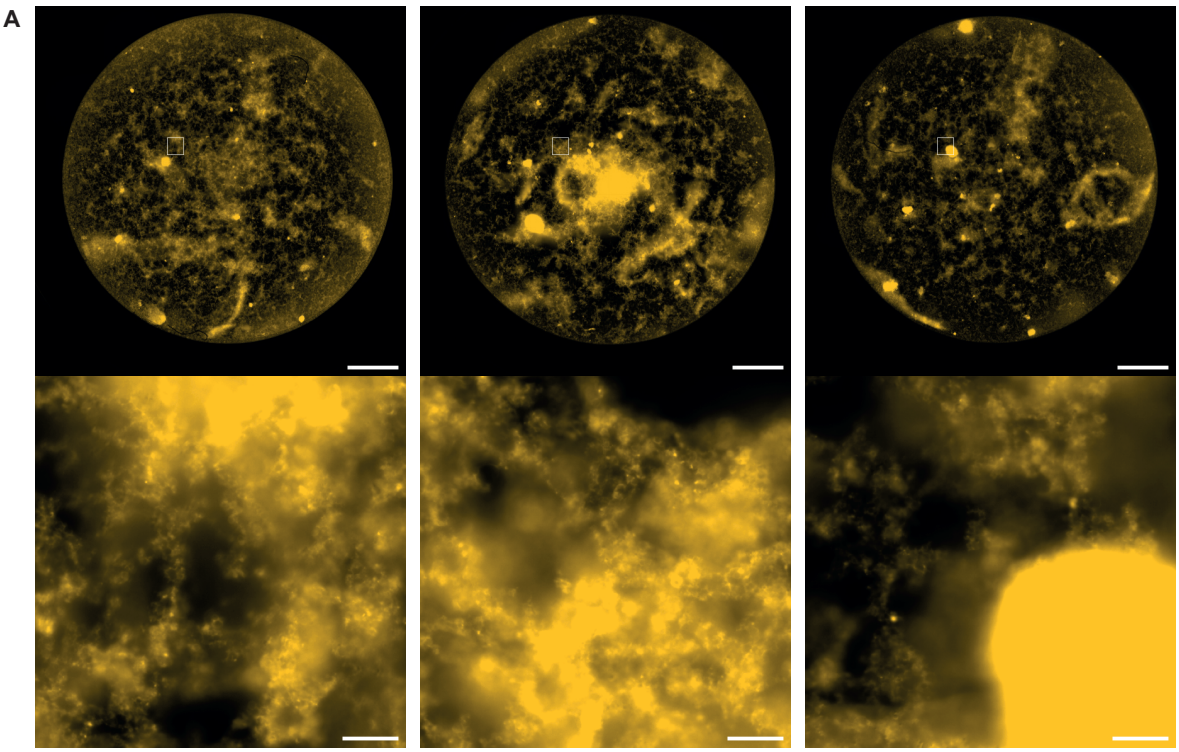


Figure 6.43: Fluorescent microscope images of Liss Rhodamine-labeled GUVs with palindromic DNA.

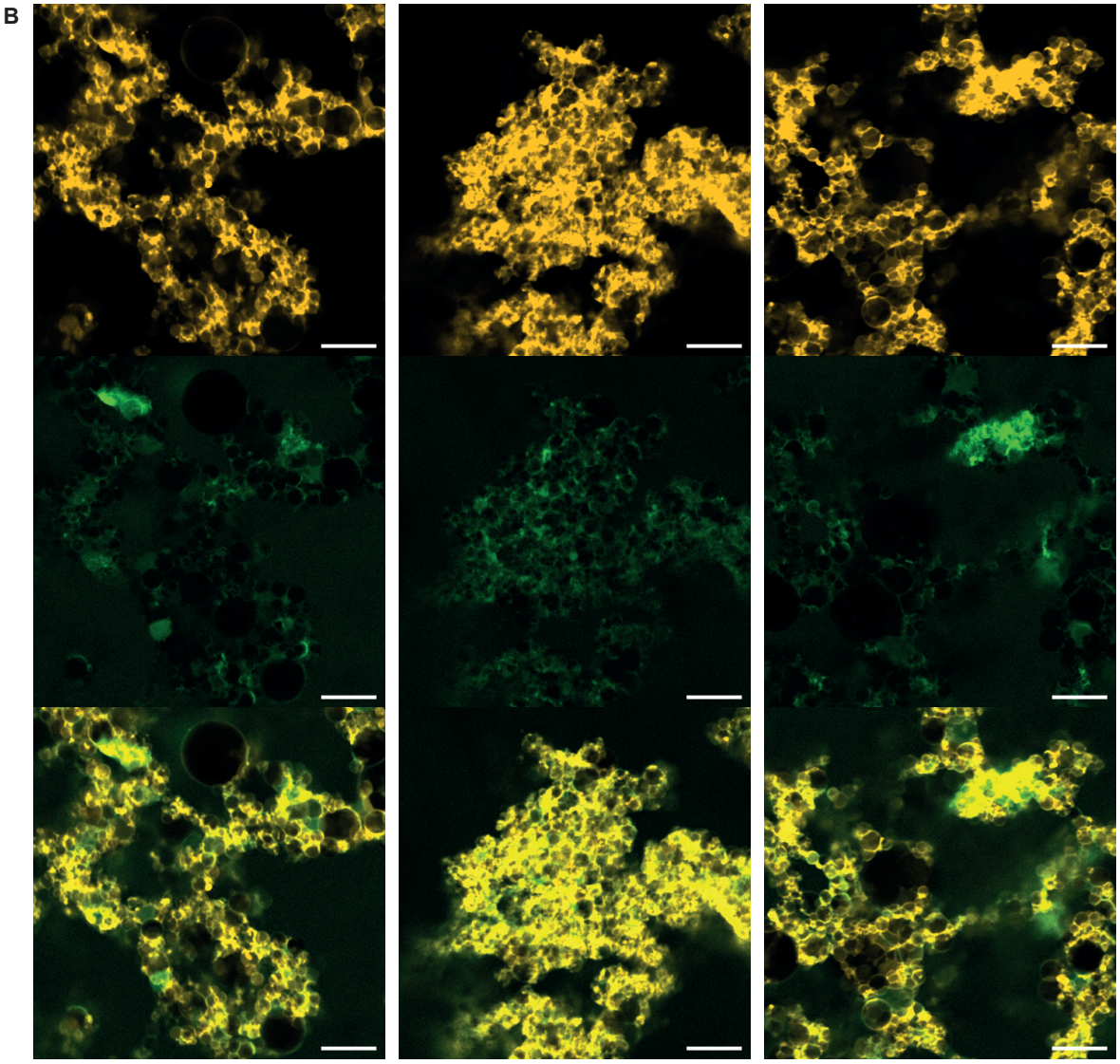


Figure 6.44: Representative confocal images of Liss Rhodamine-labeled GUVs with palindromic DNA.

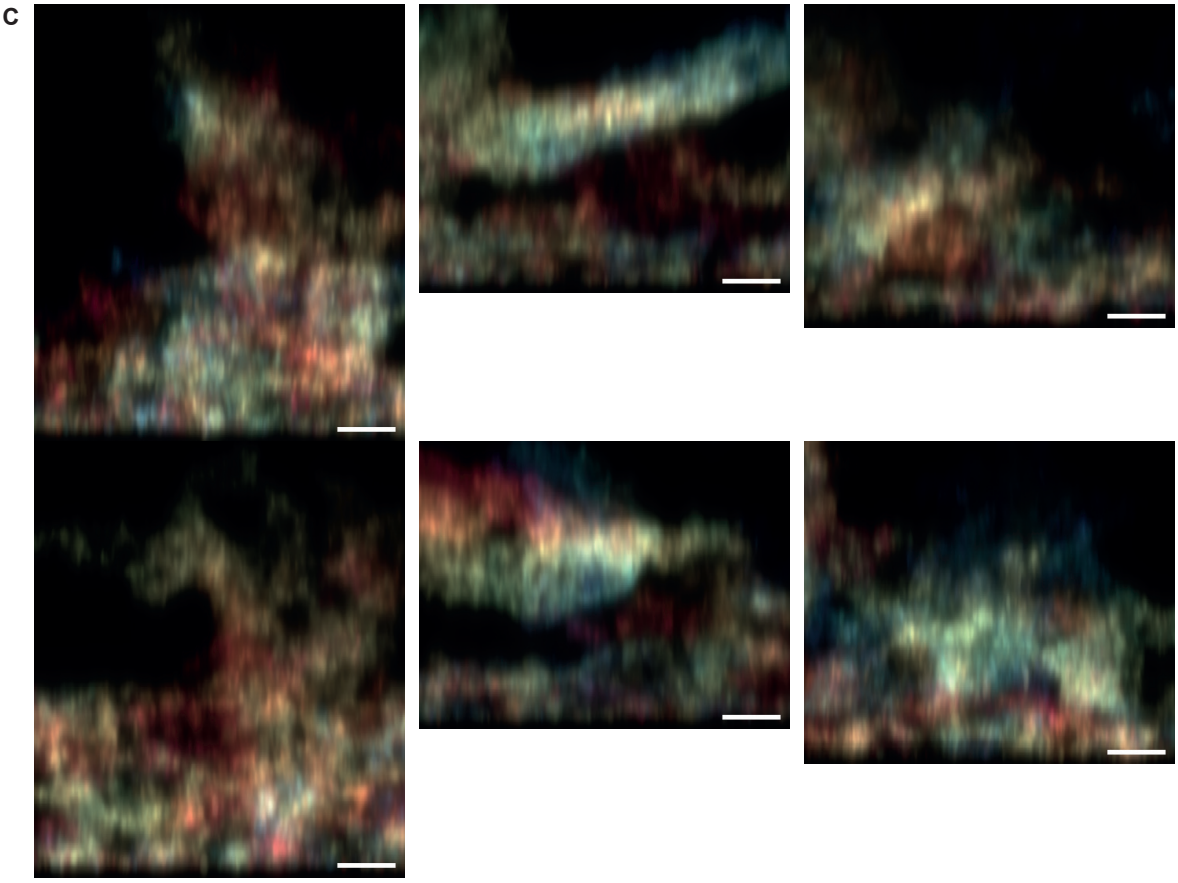


Figure 6.45: Confocal Z-stack (XZ- and YZ-projection) images of Liss Rhodamine-labeled GUVs with palindromic DNA.

Bibliography

1. Sauer, F., Haas, M., Siegle, A. F., Lauer, C. A. & Trapp, O. From amino acid mixtures to peptides in liquid sulphur dioxide on early Earth. *Nature Communications* **12,** 7182. ISSN: 2041-1723. https://doi.org/10.1038/s41467-021-27527-7 (2021).

2. Teichert, J. S., Kruse, F. M. & Trapp, O. Direct Prebiotic Pathway to DNA Nucleosides. *Angewandte Chemie International Edition* **58,** 9944–9947. ISSN: 1433-7851. https://doi.org/10.1002/anie.201903400 (2019).

3. Paschek, K. *et al.* Possible Ribose Synthesis in Carbonaceous Planetesimals. *Life* **12.** ISSN: 2075-1729 (2022).

4. Neveu, M., Hays, L. E., Voytek, M. A., New, M. H. & Schulte, M. D. The Ladder of Life Detection. *Astrobiology* **18,** 1375–1402. ISSN: 1531-1074. https://doi.org/10.1089/ast.2017.1773%20https://www.liebertpub.com/doi/pdf/10.1089/ast.2017.1773?download=true (2018).

5. Green, J. *et al.* Call for a framework for reporting evidence for life beyond Earth. *Nature* **598,** 575–579. ISSN: 1476-4687. https://doi.org/10.1038/s41586-021-03804-9 (2021).

6. Damiano, L. & Stano, P. On the "Life-Likeness" of Synthetic Cells. *Frontiers in Bioengineering and Biotechnology* **8.** ISSN: 2296-4185. https://www.frontiersin.org/article/10.3389/fbioe.2020.00953 (2020).

7. Wang, C., Yang, J. & Lu, Y. Modularize and Unite: Toward Creating a Functional Artificial Cell. *Frontiers in Molecular Biosciences* **8.** ISSN: 2296-889X. https://www.frontiersin.org/article/10.3389/fmolb.2021.781986 (2021).

8. Browning, S. T. & Shuler, M. L. Towards the development of a minimal cell model by generalization of a model of Escherichia coli: use of dimensionless rate parameters. *Biotechnol Bioeng* **76,** 187–92. ISSN: 0006-3592 (Print) 0006-3592 (2001).

9. Hicks, M., Bachmann, T. T. & Wang, B. Synthetic Biology Enables Programmable Cell-Based Biosensors. *Chemphyschem* **21,** 132–144. ISSN: 1439-4235 (Print) 1439-4235 (2020).

10. Gonzales, D. T., Yandrapalli, N., Robinson, T., Zechner, C. & Tang, T. Y. D. Cell-Free Gene Expression Dynamics in Synthetic Cell Populations. *ACS Synthetic Biology* **11,** 205–215. https://doi.org/10.1021/acssynbio.1c00376 (2022).

11. Weiss, M. *et al.* Sequential bottom-up assembly of mechanically stabilized synthetic cells by microfluidics. *Nature Materials* **17,** 89–96. ISSN: 1476-4660. https://doi.org/10.1038/nmat5005%20https://www.nature.com/articles/nmat5005 (2018).

12. Sauter, D. *PNIPAM-containing droplets : The route towards an artificial cytoskeleton assembly based on synthetic and natural components* Thesis (2021). http://nbn-resolving.de/urn:nbn:de:bsz:16-heidok-305070%20http://dx.doi.org/10.11588/heidok.00030507%20https://nbn-resolving.de/urn:nbn:de:bsz:16-heidok-305070%20https://doi.org/10.11588/heidok.00030507%20https://nbn-resolving.org/urn:nbn:de:bsz:16-heidok-305070.

13. Elangbam, C. S., Qualls C. W., J. & Dahlgren, R. R. Cell adhesion molecules–update. *Vet Pathol* **34,** 61–73. ISSN: 0300-9858 (Print) 0300-9858. https://journals.sagepub.com/doi/pdf/10.1177/030098589703400113 (1997).

14. Horne-Badovinac, S. Cell-cell and cell-matrix interactions. *Molecular biology of the cell* **25,** 731–731. ISSN: 1939-4586 1059-1524. https://pubmed.ncbi.nlm.nih.gov/24626845%20https://www.ncbi.nlm.nih.gov/pmc/articles/PMC3952839/ (2014).

15. Garcia, M. A., Nelson, W. J. & Chavez, N. Cell-Cell Junctions Organize Structural and Signaling Networks. *Cold Spring Harbor perspectives in biology* **10,** a029181. ISSN: 1943-0264. https://pubmed.ncbi.nlm.nih.gov/28600395%20https://www.ncbi.nlm.nih.gov/pmc/articles/PMC5773398/%20https://www.ncbi.nlm.nih.gov/pmc/articles/PMC5773398/pdf/cshperspect-JCT-a029181.pdf (2018).

16. Kutova, O. M. *et al.* Comparative Analysis of Cell–Cell Contact Abundance in Ovarian Carcinoma Cells Cultured in Two- and Three-Dimensional In Vitro Models. *Biology* **9.** ISSN: 2079-7737 (2020).

17. Wu, H., Xiong, W. C. & Mei, L. To build a synapse: signaling pathways in neuromuscular junction assembly. *Development* **137,** 1017–1033. ISSN: 0950-1991. https://doi.org/10.1242/dev.038711 (2010).

18. Bachmann, M., Kukkurainen, S., Hytönen, V. P. & Wehrle-Haller, B. Cell Adhesion by Integrins. *Physiological Reviews* **99,** 1655–1699. ISSN: 0031-9333. https://doi.org/10.1152/physrev.00036.2018 (2019).

19. Hartsock, A. & Nelson, W. J. Adherens and tight junctions: structure, function and connections to the actin cytoskeleton. *Biochimica et biophysica acta* **1778,** 660–669. ISSN: 0006-3002. https://pubmed.ncbi.nlm.nih.gov/17854762%20https://www.ncbi.nlm.nih.gov/pmc/articles/PMC2682436/ (2008).

20. Yamada, K. M. & Miyamoto, S. Integrin transmembrane signaling and cytoskeletal control. *Current Opinion in Cell Biology* **7,** 681–689. ISSN: 0955-0674. https://www.sciencedirect.com/science/article/pii/0955067495801103 (1995).

21. Ko, Y. K. *et al.* Characterization of junctional structures in the gingival epithelium as barriers against bacterial invasion. *J Periodontal Res.* ISSN: 0022-3484 (2022).

22. Guo, R., Sakamoto, H., Sugiura, S. & Ogawa, M. Endothelial cell motility is compatible with junctional integrity. *Journal of Cellular Physiology* **211,** 327–335. ISSN: 0021-9541. https://doi.org/10.1002/jcp.20937 (2007).

23. Evans, W. H. & Martin, P. E. Gap junctions: structure and function (Review). *Mol Membr Biol* **19,** 121–36. ISSN: 0968-7688 (Print) 0968-7688 (2002).

24. Banerjee, S., Sousa, A. D. & Bhat, M. A. Organization and function of septate junctions. *Cell Biochemistry and Biophysics* **46,** 65–77. ISSN: 1559-0283. https://doi.org/10.1385/CBB:46:1:65 (2006).

25. Takeichi, M. Cadherin Cell Adhesion Receptors as a Morphogenetic Regulator. *Science* **251,** 1451–1455. https://doi.org/10.1126/science.2006419 (1991).

26. Harris, T. J. C. & Tepass, U. Adherens junctions: from molecules to morphogenesis. *Nature Reviews Molecular Cell Biology* **11,** 502–514. ISSN: 1471-0080. https://doi.org/10.1038/nrm2927 (2010).

27. Gumbiner, B. M. Regulation of cadherin-mediated adhesion in morphogenesis. *Nature Reviews Molecular Cell Biology* **6,** 622–634. ISSN: 1471-0080. https://doi.org/10.1038/nrm1699 (2005).

28. Patel, S. D., Chen, C. P., Bahna, F., Honig, B. & Shapiro, L. Cadherin-mediated cell–cell adhesion: sticking together as a family. *Current Opinion in Structural Biology* **13,** 690–698. ISSN: 0959-440X. https://www.sciencedirect.com/science/article/pii/S0959440X03001659 (2003).

29. Yagi, T. & Takeichi, M. Cadherin superfamily genes: functions, genomic organization, and neurologic diversity. *Genes Dev* **14,** 1169–80. ISSN: 0890-9369 (Print) 0890-9369 (2000).

30. Nollet, F., Kools, P. & van Roy, F. Phylogenetic analysis of the cadherin superfamily allows identification of six major subfamilies besides several solitary members11Edited by M. Yaniv. *Journal of Molecular Biology* **299,** 551–572. ISSN: 0022-2836. https://www.sciencedirect.com/science/article/pii/S002228360093777X (2000).

31. Takeichi, M. Morphogenetic roles of classic cadherins. *Current Opinion in Cell Biology* **7,** 619–627. ISSN: 0955-0674. https://www.sciencedirect.com/science/article/pii/0955067495801022 (1995).

32. Fichtner, D. *et al.* Covalent and Density-Controlled Surface Immobilization of E-Cadherin for Adhesion Force Spectroscopy. *PLOS ONE* **9,** e93123. https://doi.org/10.1371/journal.pone.0093123 (2014).

33. Pokutta, S., Herrenknecht, K., Kemler, R. & Engel, J. Conformational changes of the recombinant extracellular domain of E-cadherin upon calcium binding. *Eur J Biochem* **223,** 1019–26. ISSN: 0014-2956 (Print) 0014-2956 (1994).

34. Curtis, M. W., Johnson, K. R. & Wheelock, M. J. E-cadherin/catenin complexes are formed cotranslationally in the endoplasmic reticulum/Golgi compartments. *Cell communication & adhesion* **15,** 365–378. ISSN: 1543-5180 1541-9061. https://pubmed.ncbi.nlm.nih.gov/18937087%20https://www.ncbi.nlm.nih.gov/pmc/articles/PMC2742162/%20https://www.tandfonline.com/doi/pdf/10.1080/15419060802460748?needAccess=true (2008).

35. Halbleib, J. M. & Nelson, W. J. Cadherins in development: cell adhesion, sorting, and tissue morphogenesis. *Genes Dev* **20,** 3199–214. ISSN: 0890-9369 (Print) 0890-9369 (2006).

36. Perez-Moreno, M. & Fuchs, E. Catenins: keeping cells from getting their signals crossed. *Dev Cell* **11,** 601–12. ISSN: 1534-5807 (Print) 1534-5807 (2006).

37. D'Souza-Schorey, C. Disassembling adherens junctions: breaking up is hard to do. *Trends Cell Biol* **15,** 19–26. ISSN: 0962-8924 (Print) 0962-8924 (2005).

38. Moreno, M. R., Boswell, K., Casbolt, H. L. & Bulgakova, N. A. Multifaceted control of E-cadherin dynamics by the Adaptor Protein Complex 1 during epithelial morphogenesis. *Mol Biol Cell,* mbcE21120598. ISSN: 1059-1524 (2022).

39. Sisto, M., Ribatti, D. & Lisi, S. E-Cadherin Signaling in Salivary Gland Development and Autoimmunity. *J Clin Med* **11.** ISSN: 2077-0383 (Print) 2077-0383 (2022).

40. Beavon, I. R. G. The E-cadherin–catenin complex in tumour metastasis: structure, function and regulation. *European Journal of Cancer* **36,** 1607–1620. ISSN: 0959-8049. https://www.sciencedirect.com/science/article/pii/S0959804900001581 (2000).

41. Zhou, J. Z. & Jiang, J. X. Gap junction and hemichannel-independent actions of connexins on cell and tissue functions–an update. *FEBS Lett* **588,** 1186–92. ISSN: 0014-5793 (Print) 0014-5793 (2014).

42. Cao, F. *et al.* A quantitative analysis of connexin-specific permeability differences of gap junctions expressed in HeLa transfectants and Xenopus oocytes. *J Cell Sci* **111 (Pt 1),** 31–43. ISSN: 0021-9533 (Print) 0021-9533 (1998).

43. Elfgang, C. *et al.* Specific permeability and selective formation of gap junction channels in connexin-transfected HeLa cells. *J Cell Biol* **129,** 805–17. ISSN: 0021-9525 (Print) 0021-9525 (1995).

44. Nicholson, B. J. *et al.* The molecular basis of selective permeability of connexins is complex and includes both size and charge. *Braz J Med Biol Res* **33,** 369–78. ISSN: 0100-879X (Print) 0100-879x (2000).

45. Alberts, B. *Molecular biology of the cell* 4. ed. (Garland Science, New York, NY [u.a.], 2002).

46. Chalcroft, J. P. & Bullivant, S. AN INTERPRETATION OF LIVER CELL MEMBRANE AND JUNCTION STRUCTURE BASED ON OBSERVATION OF FREEZE-FRACTURE REPLICAS OF BOTH SIDES OF THE FRACTURE. *Journal of Cell Biology* **47,** 49–60. ISSN: 0021-9525. https://doi.org/10.1083/jcb.47.1.49 (1970).

47. Guo, P., Weinstein, A. M. & Weinbaum, S. A dual-pathway ultrastructural model for the tight junction of rat proximal tubule epithelium. *American Journal of Physiology-Renal Physiology* **285,** F241–F257. ISSN: 1931-857X. https://doi.org/10.1152/ajprenal.00331.2002 (2003).

48. Wolburg, H., Lippoldt, A. & Ebnet, K. in *Tight Junctions* (ed Gonzalez-Mariscal, L.) 175–195 (Springer US, Boston, MA, 2006). https://doi.org/10.1007/0-387-36673-3_13.

49. Schneeberger, E. E. & Lynch, R. D. The tight junction: a multifunctional complex. *American Journal of Physiology-Cell Physiology* **286,** C1213–C1228. ISSN: 0363-6143. https://doi.org/10.1152/ajpcell.00558.2003 (2004).

50. Furuse, M. *et al.* Occludin: a novel integral membrane protein localizing at tight junctions. *The Journal of cell biology* **123,** 1777–1788. ISSN: 0021-9525 1540-8140. https://pubmed.ncbi.nlm.nih.gov/8276896%20https://www.ncbi.nlm.nih.gov/pmc/articles/PMC2290891/ (1993).

51. Van Itallie, C. M. & Anderson, J. M. Claudins and epithelial paracellular transport. *Annu Rev Physiol* **68,** 403–29. ISSN: 0066-4278 (Print) 0066-4278 (2006).

52. Furuse, M., Fujita, K., Hiiragi, T., Fujimoto, K. & Tsukita, S. Claudin-1 and -2: novel integral membrane proteins localizing at tight junctions with no sequence similarity to occludin. *J Cell Biol* **141,** 1539–50. ISSN: 0021-9525 (Print) 0021-9525 (1998).

53. Mohandas, T. K. *et al.* Localization of the Tight Junction Protein Gene TJP1 to Human Chromosome 15q13, Distal to the Prader-Willi/Angelman Region, and to Mouse Chromosome 7. *Genomics* **30,** 594–597. ISSN: 0888-7543. https://www.sciencedirect.com/science/article/pii/S0888754385712815 (1995).

54. Rajasekaran, A. K., Hojo, M., Huima, T. & Rodriguez-Boulan, E. Catenins and zonula occludens-1 form a complex during early stages in the assembly of tight junctions. *J Cell Biol* **132,** 451–63. ISSN: 0021-9525 (Print) 0021-9525 (1996).

55. Siliciano, J. D. & Goodenough, D. A. Localization of the tight junction protein, ZO-1, is modulated by extracellular calcium and cell-cell contact in Madin-Darby canine kidney epithelial cells. *J Cell Biol* **107,** 2389–99. ISSN: 0021-9525 (Print) 0021-9525 (1988).

56. Berrier, A. L. & Yamada, K. M. Cell–matrix adhesion. *Journal of Cellular Physiology* **213,** 565–573. ISSN: 0021-9541. https://doi.org/10.1002/jcp.21237 (2007).

57. Hynes, R. O. Integrins: bidirectional, allosteric signaling machines. *Cell* **110,** 673–87. ISSN: 0092-8674 (Print) 0092-8674. https://www.cell.com/cell/pdf/S0092-8674(02)00971-6.pdf (2002).

58. Ye, F., Kim, C. & Ginsberg, M. H. Reconstruction of integrin activation. *Blood* **119,** 26–33. ISSN: 0006-4971. https://doi.org/10.1182/blood-2011-04-292128 (2012).

59. Cheah, M. & Andrews, M. R. Integrin Activation: Implications for Axon Regeneration. *Cells* **7.** ISSN: 2073-4409 (2018).

60. Vorup-Jensen, T., Ostermeier, C., Shimaoka, M., Hommel, U. & Springer Timothy, A. Structure and allosteric regulation of the $\alpha X\beta 2$ integrin I domain. *Proceedings of the National Academy of Sciences* **100,** 1873–1878. https://doi.org/10.1073/pnas.0237387100 (2003).

61. Ye, F., Liu, J., Winkler, H. & Taylor, K. A. Integrin alpha IIb beta 3 in a membrane environment remains the same height after Mn2+ activation when observed by cryoelectron tomography. *Journal of molecular biology* **378,** 976–986. ISSN: 1089-8638 0022-2836. https://pubmed.ncbi.nlm.nih.gov/18405917%20https://www.ncbi.nlm.nih.gov/pmc/articles/PMC2614134/ (2008).

62. Ye, F. *et al.* Recreation of the terminal events in physiological integrin activation. *Journal of Cell Biology* **188,** 157–173. ISSN: 0021-9525. https://doi.org/10.1083/jcb.200908045 (2010).

63. Wickstead, B. & Gull, K. The evolution of the cytoskeleton. *Journal of Cell Biology* **194,** 513–525. ISSN: 0021-9525. https://doi.org/10.1083/jcb.201102065 (2011).

64. Huber, F. *et al.* Emergent complexity of the cytoskeleton: from single filaments to tissue. *Advances in Physics* **62,** 1–112. ISSN: 0001-8732. https://doi.org/10.1080/00018732.2013.771509 (2013).

65. Schaks, M., Giannone, G. & Rottner, K. Actin dynamics in cell migration. *Essays in biochemistry* **63,** 483–495. ISSN: 1744-1358 0071-1365. https://pubmed.ncbi.nlm.nih.gov/31551324%20https://www.ncbi.nlm.nih.gov/pmc/articles/PMC6823167/ (2019).

66. Khaitlina, S. Y. Intracellular transport based on actin polymerization. *Biochemistry (Mosc)* **79,** 917–27. ISSN: 0006-2979 (2014).

67. Nürnberg, A., Kitzing, T. & Grosse, R. Nucleating actin for invasion. *Nature Reviews Cancer* **11,** 177–187. ISSN: 1474-1768. https://doi.org/10.1038/nrc3003 (2011).

68. Dominguez, R. & Holmes, K. C. Actin Structure and Function. *Annual Review of Biophysics* **40,** 169–186. ISSN: 1936-122X. https://doi.org/10.1146/annurev-biophys-042910-155359%20https://www.annualreviews.org/doi/pdf/10.1146/annurev-biophys-042910-155359 (2011).

69. Parigoris, E. *et al.* Facile generation of giant unilamellar vesicles using polyacrylamide gels. *Scientific reports* **10,** 4824–4824. ISSN: 2045-2322. https://pubmed.ncbi.nlm.nih.gov/32179778%20https://www.ncbi.nlm.nih.gov/pmc/articles/PMC7075891/ (2020).

70. Walde, P., Cosentino, K., Engel, H. & Stano, P. Giant Vesicles: Preparations and Applications. *ChemBioChem* **11,** 848–865. ISSN: 1439-4227. https://doi.org/10.1002/cbic.201000010 (2010).

71. Hu, P. C., Li, S. & Malmstadt, N. Microfluidic fabrication of asymmetric giant lipid vesicles. *ACS Appl Mater Interfaces* **3,** 1434–40. ISSN: 1944-8244 (Print) 1944-8244 (2011).

72. Akbarzadeh, A. *et al.* Liposome: classification, preparation, and applications. *Nanoscale Research Letters* **8,** 102. ISSN: 1556-276X. https://doi.org/10.1186/1556-276X-8-102 (2013).

73. Van Swaay, D. & deMello, A. Microfluidic methods for forming liposomes. *Lab on a Chip* **13,** 752–767. ISSN: 1473-0197. http://dx.doi.org/10.1039/C2LC41121K (2013).

74. Patil, Y. P. & Jadhav, S. Novel methods for liposome preparation. *Chemistry and Physics of Lipids* **177,** 8–18. ISSN: 0009-3084. https://www.sciencedirect.com/science/article/pii/S0009308413001497 (2014).

75. Arriaga, L. R. *et al.* Ultrathin Shell Double Emulsion Templated Giant Unilamellar Lipid Vesicles with Controlled Microdomain Formation. *Small* **10,** 950–956. ISSN: 1613-6810. https://doi.org/10.1002/smll.201301904 (2014).

76. Beales, P. A., Ciani, B. & Cleasby, A. J. Nature's lessons in design: nanomachines to scaffold, remodel and shape membrane compartments. *Physical Chemistry Chemical Physics* **17,** 15489–15507. ISSN: 1463-9076. http://dx.doi.org/10.1039/C5CP00480B (2015).

77. Darszon, A. *et al.* Reassembly of protein-lipid complexes into large bilayer vesicles: Perspectives for membrane reconstitution. *Proceedings of the National Academy of Sciences* **77,** 239–243. https://doi.org/10.1073/pnas.77.1.239 (1980).

78. Needham, D., McIntosh, T. J. & Evans, E. Thermomechanical and transition properties of dimyristoylphosphatidylcholine/cholesterol bilayers. *Biochemistry* **27,** 4668–4673. ISSN: 0006-2960. https://doi.org/10.1021/bi00413a013 (1988).

79. Rodriguez, N., Pincet, F. & Cribier, S. Giant vesicles formed by gentle hydration and electroformation: A comparison by fluorescence microscopy. *Colloids and Surfaces B: Biointerfaces* **42,** 125–130. ISSN: 0927-7765. https://www.sciencedirect.com/science/article/pii/S0927776505000603 (2005).

80. Reeves, J. P. & Dowben, R. M. Formation and properties of thin-walled phospholipid vesicles. *Journal of Cellular Physiology* **73,** 49–60. ISSN: 0021-9541. https://doi.org/10.1002/jcp.1040730108 (1969).

81. Pereno, V. *et al.* Electroformation of Giant Unilamellar Vesicles on Stainless Steel Electrodes. *ACS omega* **2,** 994–1002. ISSN: 2470-1343. https://pubmed.ncbi.nlm.nih.gov/28393132%20https://www.ncbi.nlm.nih.gov/pmc/articles/PMC5377273/ (2017).

82. Méléard, P., Bagatolli, L. A. & Pott, T. Giant unilamellar vesicle electroformation from lipid mixtures to native membranes under physiological conditions. *Methods Enzymol* **465,** 161–76. ISSN: 0076-6879 (2009).

83. Angelova, M. I. & Dimitrov, D. S. Liposome electroformation. *Faraday Discussions of the Chemical Society* **81,** 303–311. ISSN: 0301-7249. http://dx.doi.org/10.1039/DC9868100303 (1986).

84. Peruzzi, J., Gutierrez, M. G., Mansfield, K. & Malmstadt, N. Dynamics of Hydrogel-Assisted Giant Unilamellar Vesicle Formation from Unsaturated Lipid Systems. *Langmuir* **32,** 12702–12709. ISSN: 0743-7463 (2016).

85. Weinberger, A. *et al.* Gel-assisted formation of giant unilamellar vesicles. *Biophysical journal* **105,** 154–164. ISSN: 1542-0086 0006-3495. https://pubmed.ncbi.nlm.nih.gov/23823234%20https://www.ncbi.nlm.nih.gov/pmc/articles/PMC3699747/ (2013).

86. Schultze, J. *et al.* Preparation of Monodisperse Giant Unilamellar Anchored Vesicles Using Micropatterned Hydrogel Substrates. *ACS Omega* **4,** 9393–9399. https://doi.org/10.1021/acsomega.9b00912 (2019).

87. Traïkia, M., Warschawski, D. E., Recouvreur, M., Cartaud, J. & Devaux, P. F. Formation of unilamellar vesicles by repetitive freeze-thaw cycles: characterization by electron microscopy and 31P-nuclear magnetic resonance. *European Biophysics Journal* **29,** 184–195. ISSN: 1432-1017. https://doi.org/10.1007/s002490000077 (2000).

88. Qiao, H. *et al.* Encapsulation of Nucleic Acids into Giant Unilamellar Vesicles by Freeze-Thaw: a Way Protocells May Form. *Orig Life Evol Biosph* **47,** 499–510. ISSN: 0169-6149 (2017).

89. Moga, A., Yandrapalli, N., Dimova, R. & Robinson, T. Optimization of the Inverted Emulsion Method for High-Yield Production of Biomimetic Giant Unilamellar Vesicles. *Chembiochem : a European journal of chemical biology* **20,** 2674–2682. ISSN: 1439-7633 1439-4227. https://pubmed.ncbi.nlm.nih.gov/31529570%20https://www.ncbi.nlm.nih.gov/pmc/articles/PMC6856842/ (2019).

90. Yandrapalli, N., Seemann, T. & Robinson, T. On-Chip Inverted Emulsion Method for Fast Giant Vesicle Production, Handling, and Analysis. *Micromachines* **11.** ISSN: 2072-666X (2020).

91. Blosser, M. C., Horst, B. G. & Keller, S. L. cDICE method produces giant lipid vesicles under physiological conditions of charged lipids and ionic solutions. *Soft matter* **12,** 7364–7371. ISSN: 1744-6848 1744-683X. https://pubmed.ncbi.nlm.nih.gov/27510092%20https://www.ncbi.nlm.nih.gov/pmc/articles/PMC5008994/ (2016).

92. Van de Cauter, L. *et al.* Optimized cDICE for Efficient Reconstitution of Biological Systems in Giant Unilamellar Vesicles. *ACS Synth Biol* **10,** 1690–1702. ISSN: 2161-5063 (2021).

93. Van Buren, L., Koenderink, G. H. & Martinez-Torres, C. DisGUVery: a versatile open-source software for high-throughput image analysis of Giant Unilamellar Vesicles. *bioRxiv,* 2022.01.25.477663. http://biorxiv.org/content/early/2022/01/25/2022.01.25.477663.abstract (2022).

94. Stachowiak Jeanne, C. *et al.* Unilamellar vesicle formation and encapsulation by microfluidic jetting. *Proceedings of the National Academy of Sciences* **105,** 4697–4702. https://doi.org/10.1073/pnas.0710875105 (2008).

95. Armstrong, M., Vahey, M. D., Hunt, T. P. & Fletcher, D. A. Forming and loading giant unilamellar vesicles with acoustic jetting. *Biomicrofluidics* **14,** 064105. https://doi.org/10.1063/5.0021742 (2020).

96. Haller, B. *et al.* Charge-controlled microfluidic formation of lipid-based single- and multicompartment systems. *Lab on a Chip* **18,** 2665–2674. ISSN: 1473-0197. http://dx.doi.org/10.1039/C8LC00582F%20https://pubs.rsc.org/en/content/articlepdf/2018/lc/c8lc00582f (2018).

97. Göpfrich, K. *et al.* Ion Channels Made from a Single Membrane-Spanning DNA Duplex. *Nano Letters* **16,** 4665–4669. ISSN: 1530-6984. https://doi.org/10.1021/acs.nanolett.6b02039 (2016).

98. Staufer, O. *et al.* Microfluidic production and characterization of biofunctionalized giant unilamellar vesicles for targeted intracellular cargo delivery. *Biomaterials* **264,** 120203. ISSN: 0142-9612. https://www.sciencedirect.com/science/article/pii/S014296122030449X (2021).

99. Heuberger, L. & Palivan, C. Block Copolymer Giant Unilamellar Vesicles for High-Throughput Screening. *CHIMIA* **76,** 350. https://chimia.ch/chimia/article/view/2022_350 (2022).

100. Staufer, O., Schröter, M., Platzman, I. & Spatz, J. P. Bottom-Up Assembly of Functional Intracellular Synthetic Organelles by Droplet-Based Microfluidics. *Small* **16,** 1906424. ISSN: 1613-6810. https://onlinelibrary.wiley.com/doi/abs/10.1002/smll.201906424%20https://onlinelibrary.wiley.com/doi/pdfdirect/10.1002/smll.201906424?download=true (2020).

101. Göpfrich, K. *et al.* One-Pot Assembly of Complex Giant Unilamellar Vesicle-Based Synthetic Cells. *ACS Synthetic Biology* **8,** 937–947. https://doi.org/10.1021/acssynbio.9b00034%20https://pubs.acs.org/doi/pdf/10.1021/acssynbio.9b00034 (2019).

102. Lussier, F. *et al.* pH-Triggered Assembly of Endomembrane Multicompartments in Synthetic Cells. *ACS Synthetic Biology.* https://doi.org/10.1021/acssynbio.1c00472,%20https://pubs.acs.org/doi/pdf/10.1021/acssynbio.1c00472 (2021).

103. Karamdad, K., Law, R. V., Seddon, J. M., Brooks, N. J. & Ces, O. Preparation and mechanical characterisation of giant unilamellar vesicles by a microfluidic method. *Lab on a Chip* **15,** 557–562. ISSN: 1473-0197. http://dx.doi.org/10.1039/C4LC01277A (2015).

104. Krafft, D. *et al.* Compartments for Synthetic Cells: Osmotically Assisted Separation of Oil from Double Emulsions in a Microfluidic Chip. *ChemBioChem* **20,** 2604–2608. ISSN: 1439-4227. https://doi.org/10.1002/cbic.201900152 (2019).

105. Ahmed, I., Iqbal, H. M. N. & Akram, Z. Microfluidics Engineering: Recent Trends, Valorization, and Applications. *Arabian Journal for Science and Engineering* **43,** 23–32. ISSN: 2191-4281. https://doi.org/10.1007/s13369-017-2662-4 (2018).

106. Beebe, D. J., Mensing, G. A. & Walker, G. M. Physics and applications of microfluidics in biology. *Annu Rev Biomed Eng* **4,** 261–86. ISSN: 1523-9829 (Print) 1523-9829 (2002).

107. Elvira, K. S., i Solvas, X. C., Wootton, R. C. R. & deMello, A. J. The past, present and potential for microfluidic reactor technology in chemical synthesis. *Nature Chemistry* **5,** 905–915. ISSN: 1755-4349. https://doi.org/10.1038/nchem.1753 (2013).

108. Wu, J., He, Z., Chen, Q. & Lin, J.-M. Biochemical analysis on microfluidic chips. *TrAC Trends in Analytical Chemistry* **80,** 213–231. ISSN: 0165-9936. https://www.sciencedirect.com/science/article/pii/S016599361530145X (2016).

109. Rabiee, N. *et al.* Nanotechnology-assisted microfluidic systems: from bench to bedside. *Nanomedicine* **16,** 237–258. ISSN: 1743-5889. https://doi.org/10.2217/nnm-2020-0353 (2021).

110. Barry, R. & Ivanov, D. Microfluidics in biotechnology. *J Nanobiotechnology* **2,** 2. ISSN: 1477-3155 (2004).

111. Teh, S.-Y., Lin, R., Hung, L.-H. & Lee, A. P. Droplet microfluidics. *Lab on a Chip* **8,** 198–220. ISSN: 1473-0197. http://dx.doi.org/10.1039/B715524G (2008).

112. Seemann, R., Brinkmann, M., Pfohl, T. & Herminghaus, S. Droplet based microfluidics. *Reports on Progress in Physics* **75,** 016601. ISSN: 0034-4885 1361-6633. http://dx.doi.org/10.1088/0034-4885/75/1/016601 (2011).

113. Sesen, M., Alan, T. & Neild, A. Droplet control technologies for microfluidic high throughput screening (μHTS). *Lab on a Chip* **17,** 2372–2394. ISSN: 1473-0197. http://dx.doi.org/10.1039/C7LC00005G (2017).

114. Song, H., Tice, J. D. & Ismagilov, R. F. A Microfluidic System for Controlling Reaction Networks in Time. *Angewandte Chemie International Edition* **42,** 768–772. ISSN: 1433-7851. https://doi.org/10.1002/anie.200390203 (2003).

115. Garstecki, P., Fuerstman, M. J., Stone, H. A. & Whitesides, G. M. Formation of droplets and bubbles in a microfluidic T-junction—scaling and mechanism of break-up. *Lab on a Chip* **6,** 437–446. ISSN: 1473-0197. http://dx.doi.org/10.1039/B510841A (2006).

116. Sackmann, E. K., Fulton, A. L. & Beebe, D. J. The present and future role of microfluidics in biomedical research. *Nature* **507,** 181–189. ISSN: 1476-4687. https://doi.org/10.1038/nature13118 (2014).

117. Squires, T. M. & Quake, S. R. Microfluidics: Fluid physics at the nanoliter scale. *Reviews of Modern Physics* **77,** 977–1026. https://link.aps.org/doi/10.1103/RevModPhys.77.977 (2005).

118. Reynolds, O. XXIX. An experimental investigation of the circumstances which determine whether the motion of water shall be direct or sinuous, and of the law of resistance in parallel channels. *Philosophical Transactions of the Royal Society of London* **174,** 935–982. https://doi.org/10.1098/rstl.1883.0029 (1883).

119. Hardt, S. & Schönfeld, F. in *Microfluidic Technologies for Miniaturized Analysis Systems* (eds Hardt, S. & Schönfeld, F.) 1–58 (Springer US, Boston, MA, 2007). https://doi.org/10.1007/978-0-387-68424-6_1.

120. Rapp, B. E. in *Microfluidics: Modelling, Mechanics and Mathematics* (ed Rapp, B. E.) 243–263 (Elsevier, Oxford, 2017). https://www.sciencedirect.com/science/article/pii/B9781455731411500095.

121. Stewart, K. M. & Atkinson, J. F. in *Encyclopedia of Inland Waters (Second Edition)* (eds Mehner, T. & Tockner, K.) 45–52 (Elsevier, Oxford, 2022). https://www.sciencedirect.com/science/article/pii/B9780128191668001365.

122. Berry, J. D., Neeson, M. J., Dagastine, R. R., Chan, D. Y. C. & Tabor, R. F. Measurement of surface and interfacial tension using pendant drop tensiometry. *Journal of Colloid and Interface Science* **454,** 226–237. ISSN: 0021-9797. https://www.sciencedirect.com/science/article/pii/S002197971500466X (2015).

123. Schroën, K., de Ruiter, J. & Berton-Carabin, C. The Importance of Interfacial Tension in Emulsification: Connecting Scaling Relations Used in Large Scale Preparation with Microfluidic Measurement Methods. *ChemEngineering* **4.** ISSN: 2305-7084 (2020).

124. Simon, M. G., Lin, R., Fisher, J. S. & Lee, A. P. A Laplace pressure based microfluidic trap for passive droplet trapping and controlled release. *Biomicrofluidics* **6,** 14110–1411013. ISSN: 1932-1058. https://pubmed.ncbi.nlm.nih.gov/22662095%20https://www.ncbi.nlm.nih.gov/pmc/articles/PMC3365347/ (2012).

125. Ostwald, W. Studien über die Bildung und Umwandlung fester Körper: 1. Abhandlung: Übersättigung und Überkaltung. *Zeitschrift für Physikalische Chemie* **22U,** 289–330. https://doi.org/10.1515/zpch-1897-2233 (1897).

126. Taylor, P. Ostwald ripening in emulsions. *Advances in Colloid and Interface Science* **75,** 107–163. ISSN: 0001-8686. https://www.sciencedirect.com/science/article/pii/S0001868698000359 (1998).

127. Garti, N. & Lutz, R. in *Interface Science and Technology* (ed Petsev, D. N.) 557–605 (Elsevier, 2004). https://www.sciencedirect.com/science/article/pii/S1573428504800164.

128. Viana, C., Bohrer, D., de Carvalho, L. M., do Nascimento, P. C. & da Rosa, M. B. Emulsified systems for metal determination by spectrometric methods. *TrAC Trends in Analytical Chemistry* **53,** 49–59. ISSN: 0165-9936. https://www.sciencedirect.com/science/article/pii/S0165993613002355 (2014).

129. Baret, J.-C. Surfactants in droplet-based microfluidics. *Lab on a Chip* **12,** 422–433. ISSN: 1473-0197. http://dx.doi.org/10.1039/C1LC20582J (2012).

130. Jin, F., Balasubramaniam, R. & Stebe, K. J. SURFACTANT ADSORPTION TO SPHERICAL PARTICLES: THE INTRINSIC LENGTH SCALE GOVERNING THE SHIFT FROM DIFFUSION TO KINETIC-CONTROLLED MASS TRANSFER. *The Journal of Adhesion* **80,** 773–796. ISSN: 0021-8464. https://doi.org/10.1080/00218460490480770 (2004).

131. McDonald, J. C. & Whitesides, G. M. Poly(dimethylsiloxane) as a Material for Fabricating Microfluidic Devices. *Accounts of Chemical Research* **35,** 491–499. ISSN: 0001-4842. https://doi.org/10.1021/ar010110q (2002).

132. Duffy, D. C., McDonald, J. C., Schueller, O. J. A. & Whitesides, G. M. Rapid Prototyping of Microfluidic Systems in Poly(dimethylsiloxane). *Analytical Chemistry* **70,** 4974–4984. ISSN: 0003-2700. https://doi.org/10.1021/ac980656z (1998).

133. Ng, J. M., Gitlin, I., Stroock, A. D. & Whitesides, G. M. Components for integrated poly(dimethylsiloxane) microfluidic systems. *Electrophoresis* **23,** 3461–73. ISSN: 0173-0835 (Print) 0173-0835 (2002).

134. Raj M, K. & Chakraborty, S. PDMS microfluidics: A mini review. *Journal of Applied Polymer Science* **137,** 48958. ISSN: 0021-8995. https://doi.org/10.1002/app.48958 (2020).

135. Thorsen, T., Roberts, R. W., Arnold, F. H. & Quake, S. R. Dynamic Pattern Formation in a Vesicle-Generating Microfluidic Device. *Physical Review Letters* **86,** 4163–4166. https://link.aps.org/doi/10.1103/PhysRevLett.86.4163 (2001).

136. Anna, S. L., Bontoux, N. & Stone, H. A. Formation of dispersions using "flow focusing" in microchannels. *Applied Physics Letters* **82,** 364–366. ISSN: 0003-6951. https://doi.org/10.1063/1.1537519 (2003).

137. Ahn, K. *et al.* Dielectrophoretic manipulation of drops for high-speed microfluidic sorting devices. *Applied Physics Letters* **88,** 024104. ISSN: 0003-6951. https://doi.org/10.1063/1.2164911 (2006).

138. Frenz, L., Blank, K., Brouzes, E. & Griffiths, A. D. Reliable microfluidic on-chip incubation of droplets in delay-lines. *Lab on a Chip* **9,** 1344–1348. ISSN: 1473-0197. http://dx.doi.org/10.1039/B816049J (2009).

139. Holtze, C. *et al.* Biocompatible surfactants for water-in-fluorocarbon emulsions. *Lab on a Chip* **8,** 1632–1639. ISSN: 1473-0197. http://dx.doi.org/10.1039/B806706F,%20https://pubs.rsc.org/en/content/articlepdf/2008/lc/b806706f.

140. Abate Adam, R., Hung, T., Mary, P., Agresti Jeremy, J. & Weitz David, A. High-throughput injection with microfluidics using picoinjectors. *Proceedings of the National Academy of Sciences* **107,** 19163–19166. https://doi.org/10.1073/pnas.1006888107 (2010).

141. Niederholtmeyer, H., Stepanova, V. & Maerkl Sebastian, J. Implementation of cell-free biological networks at steady state. *Proceedings of the National Academy of Sciences* **110,** 15985–15990. https://doi.org/10.1073/pnas.1311166110 (2013).

142. Niederholtmeyer, H. *et al.* Rapid cell-free forward engineering of novel genetic ring oscillators. *eLife* **4,** e09771. ISSN: 2050-084X. https://doi.org/10.7554/eLife.09771 (2015).

143. Dave, N. & Joshi, T. A Concise Review on Surfactants and Its Significance. *International Journal of Applied Chemistry* **13,** 663–672 (2017).

144. Hu, Z., Verheijen, W., Hofkens, J., Jonas, A. M. & Gohy, J.-F. Formation of Vesicles in Block Copolymer-Fluorinated Surfactant Complexes. *Langmuir* **23,** 116–122. ISSN: 0743-7463. https://doi.org/10.1021/la061532h (2007).

145. Muller, P. Glossary of terms used in physical organic chemistry (IUPAC Recommendations 1994). *Pure and Applied Chemistry* **66,** 1077–1184. https://doi.org/10.1351/pac199466051077 (1994).

146. Skhiri, Y. *et al.* Dynamics of molecular transport by surfactants in emulsions. *Soft Matter* **8,** 10618–10627. ISSN: 1744-683X. http://dx.doi.org/10.1039/C2SM25934F (2012).

147. Brosseau, Q., Vrignon, J. & Baret, J.-C. Microfluidic Dynamic Interfacial Tensiometry (μDIT). *Soft Matter* **10,** 3066–3076. ISSN: 1744-683X. http://dx.doi.org/10.1039/C3SM52543K%20https://pubs.rsc.org/en/content/articlepdf/2014/sm/c3sm52543k (2014).

148. Griffin, W. C. Classification of Surface-Active Agents by 'HLB'. *Journal of the Society of Cosmetic Chemists* **1,** 311–26 (1949).

149. Racz, I. The hydrophile-lipophile balance. *Gyogyszereszet* **7,** 43–6. ISSN: 0017-6036 (1963).

150. Platzman, I., Janiesch, J.-W. & Spatz, J. P. Synthesis of Nanostructured and Biofunctionalized Water-in-Oil Droplets as Tools for Homing T Cells. *Journal of the American Chemical Society* **135,** 3339–3342. ISSN: 0002-7863. https://doi.org/10.1021/ja311588c%20https://pubs.acs.org/doi/pdf/10.1021/ja311588c (2013).

151. Clayden, J., Greeves, N. & Warren, S. G. *Organic chemistry* 2. ed. (Oxford Univ. Press, Oxford [u.a.], 2012).

152. O'Shaughnessy, B. & Sawhney, U. Reaction Kinetics at Polymer-Polymer Interfaces. *Macromolecules* **29,** 7230–7239. ISSN: 0024-9297. https://doi.org/10.1021/ma9601171 (1996).

153. Worrell, B. T., Malik, J. A. & Fokin, V. V. Direct Evidence of a Dinuclear Copper Intermediate in Cu(I)-Catalyzed Azide-Alkyne Cycloadditions. *Science* **340,** 457–460. https://doi.org/10.1126/science.1229506 (2013).

154. Scanga, R. *et al.* Click chemistry approaches to expand the repertoire of PEG-based fluorinated surfactants for droplet microfluidics. *RSC Advances* **8,** 12960–12974. http://dx.doi.org/10.1039/C8RA01254G%20https://www.ncbi.nlm.nih.gov/pmc/articles/PMC6779154/pdf/nihms-1052133.pdf (2018).

155. Case, D. R., Zubieta, J. & P Doyle, R. The Coordination Chemistry of Bio-Relevant Ligands and Their Magnesium Complexes. *Molecules (Basel, Switzerland)* **25,** 3172. ISSN: 1420-3049. https://pubmed.ncbi.nlm.nih.gov/32664540%20https://www.ncbi.nlm.nih.gov/pmc/articles/PMC7397051/ (2020).

156. Kondoh, A. & Oi, T. Interaction of Alkaline Earth Metal Ions with Carboxylic Acids in Aqueous Solutions studied by 13C NMR Spectroscopy. *Zeitschrift für Naturforschung A* **53,** 77–91. https://doi.org/10.1515/zna-1998-1-212 (1998).

157. Chowdhury, M. S. *et al.* Dendronized fluorosurfactant for highly stable water-in-fluorinated oil emulsions with minimal inter-droplet transfer of small molecules. *Nature Communications* **10,** 4546. ISSN: 2041-1723. https://doi.org/10.1038/s41467-019-12462-5 (2019).

158. An, C. *et al.* Thermo-responsive fluorinated surfactant for on-demand demulsification of microfluidic droplets. *Lab on a Chip* **21,** 3412–3419. ISSN: 1473-0197. http://dx.doi.org/10.1039/D1LC00450F%20https://pubs.rsc.org/en/content/articlelanding/2021/LC/D1LC00450F%20https://pubs.rsc.org/en/content/articlepdf/2021/lc/d1lc00450f (2021).

159. Chowdhury, M. S. *et al.* Functional Surfactants for Molecular Fishing, Capsule Creation, and Single-Cell Gene Expression. *Nano-Micro Letters* **13,** 147. ISSN: 2150-5551. https://doi.org/10.1007/s40820-021-00663-x%20https://www.ncbi.nlm.nih.gov/pmc/articles/PMC8214653/pdf/40820_2021_Article_663.pdf (2021).

160. Schwille, P. & Diez, S. Synthetic biology of minimal systems. *Critical Reviews in Biochemistry and Molecular Biology* **44,** 223–242. ISSN: 1040-9238. https://doi.org/10.1080/10409230903074549 (2009).

161. Ishmukhametov, R. R., Russell, A. N. & Berry, R. M. A modular platform for one-step assembly of multi-component membrane systems by fusion of charged proteoliposomes. *Nature Communications* **7,** 13025. ISSN: 2041-1723. https://doi.org/10.1038/ncomms13025 (2016).

162. Benk, L. T. *et al.* Integrin αIIbβ3 Activation and Clustering in Minimal Synthetic Cells. *Advanced NanoBiomed Research* **2,** 2100094. ISSN: 2699-9307. https://doi.org/10.1002/anbr.202100094 (2022).

163. Carnarius, C. *et al.* Green Fluorescent Protein Changes the Conductance of Connexin 43 (Cx43) Hemichannels Reconstituted in Planar Lipid Bilayers*. *Journal of Biological Chemistry* **287,** 2877–2886. ISSN: 0021-9258. https://www.sciencedirect.com/science/article/pii/S0021925820532468 (2012).

164. Gaßmann, O. *et al.* The M34A mutant of Connexin26 reveals active conductance states in pore-suspending membranes. *Journal of Structural Biology* **168,** 168–176. ISSN: 1047-8477. https://www.sciencedirect.com/science/article/pii/S1047847709000549 (2009).

165. Saito, H. *et al.* Time-Resolved Tracking of a Minimum Gene Expression System Reconstituted in Giant Liposomes. *ChemBioChem* **10,** 1640–1643. ISSN: 1439-4227. https://doi.org/10.1002/cbic.200900205 (2009).

166. Dreher, Y., Jahnke, K., Schröter, M. & Göpfrich, K. Light-Triggered Cargo Loading and Division of DNA-Containing Giant Unilamellar Lipid Vesicles. *Nano Letters* **21,** 5952–5957. ISSN: 1530-6984. https://doi.org/10.1021/acs.nanolett.1c00822%20https://pubs.acs.org/doi/pdf/10.1021/acs.nanolett.1c00822 (2021).

167. Jahnke, K., Huth, V., Mersdorf, U., Liu, N. & Göpfrich, K. Bottom-Up Assembly of Synthetic Cells with a DNA Cytoskeleton. *ACS Nano* **16,** 7233–7241. ISSN: 1936-0851. https://doi.org/10.1021/acsnano.1c10703 (2022).

168. Bujara, M., Schümperli, M., Pellaux, R., Heinemann, M. & Panke, S. Optimization of a blueprint for in vitro glycolysis by metabolic real-time analysis. *Nature Chemical Biology* **7,** 271–277. ISSN: 1552-4469. https://doi.org/10.1038/nchembio.541 (2011).

169. Litschel, T. *et al.* Reconstitution of contractile actomyosin rings in vesicles. *Nature Communications* **12,** 2254. ISSN: 2041-1723. https://doi.org/10.1038/s41467-021-22422-7 (2021).

170. Ganzinger, K. A. & Schwille, P. More from less – bottom-up reconstitution of cell biology. *Journal of Cell Science* **132,** jcs227488. ISSN: 0021-9533. https://doi.org/10.1242/jcs.227488 (2019).

171. Bieling, P. *et al.* Reconstitution of a microtubule plus-end tracking system in vitro. *Nature* **450,** 1100–1105. ISSN: 1476-4687. https://doi.org/10.1038/nature06386 (2007).

172. Mulla, Y., Aufderhorst-Roberts, A. & Koenderink, G. Shaping up synthetic cells. *Physical Biology* **15** (2018).

173. Streicher, P. *et al.* Integrin reconstituted in GUVs: a biomimetic system to study initial steps of cell spreading. *Biochim Biophys Acta* **1788,** 2291–300. ISSN: 0006-3002 (Print) 0006-3002. https://www.sciencedirect.com/science/article/pii/S0005273609002533?via%3Dihub (2009).

174. Nourian, Z., Roelofsen, W. & Danelon, C. Triggered Gene Expression in Fed-Vesicle Microreactors with a Multifunctional Membrane. *Angewandte Chemie International Edition* **51,** 3114–3118. ISSN: 1433-7851. https://doi.org/10.1002/anie.201107123 (2012).

175. Chiarabelli, C., Stano, P. & Luisi, P. L. Chemical approaches to synthetic biology. *Current Opinion in Biotechnology* **20,** 492–497. ISSN: 0958-1669. https://www.sciencedirect.com/science/article/pii/S0958166909000974 (2009).

176. Kuruma, Y. & Ueda, T. The PURE system for the cell-free synthesis of membrane proteins. *Nature Protocols* **10,** 1328–1344. ISSN: 1750-2799. https://doi.org/10.1038/nprot.2015.082 (2015).

177. Yao, Z. *et al.* Visual Detection of Copper(II) Ions Based on an Anionic Polythiophene Derivative Using Click Chemistry. *Analytical Chemistry* **85,** 5650–5653. ISSN: 0003-2700. https://doi.org/10.1021/ac401386v%20https://pubs.acs.org/doi/pdf/10.1021/ac401386v (2013).

178. Jochyms, Q., Mignard, E. & Vincent, J.-M. Fluorosurfactants for applications in catalysis. *Journal of Fluorine Chemistry* **177,** 11–18. ISSN: 0022-1139. https://www.sciencedirect.com/science/article/pii/S002211391500024X (2015).

179. Riechers, B. *Dynamics of Surfactants at Soft Interfaces using Droplet-Based Microfluidics* Thesis (2016). http://dx.doi.org/10.53846/goediss-5483.

180. Riechers, B. *et al.* Surfactant adsorption kinetics in microfluidics. *Proceedings of the National Academy of Sciences* **113,** 11465–11470. https://www.pnas.org/doi/abs/10.1073/pnas.1604307113 (2016).

181. Schubert, D. & Boss, K. Analytical Ultracentrifugation of Proteins in Solutions of Triton X-100 Using Absorption Optics. *Zeitschrift für Naturforschung C* **40,** 908–911. https://doi.org/10.1515/znc-1985-11-1226%20https://www.degruyter.com/document/doi/10.1515/znc-1985-11-1226/pdf (1985).

182. Arnold, J. C. & Sawin, H. H. Charging of pattern features during plasma etching. *Journal of Applied Physics* **70,** 5314–5317. ISSN: 0021-8979. https://doi.org/10.1063/1.350241%20https://aip.scitation.org/doi/10.1063/1.350241 (1991).

183. Van der Walt, S. *et al.* scikit-image: image processing in Python. *PeerJ* **2,** e453. ISSN: 2167-8359. https://doi.org/10.7717/peerj.453 (June 2014).

184. Web Page. 2019. https://docs.opencv.org/2.4/modules/imgproc/doc/miscellaneous_transformations.html.

185. Sobel, I. & Feldman, G. M. *An Isotropic 3×3 image gradient operator* in (1990).

186. Zack, G. W., Rogers, W. E. & Latt, S. A. Automatic measurement of sister chromatid exchange frequency. *Journal of Histochemistry & Cytochemistry* **25,** 741–753. https://journals.sagepub.com/doi/abs/10.1177/25.7.70454%20https://journals.sagepub.com/doi/pdf/10.1177/25.7.70454 (1977).

187. Tan, Y.-C., Fisher, J. S., Lee, A. I., Cristini, V. & Lee, A. P. Design of microfluidic channel geometries for the control of droplet volume, chemical concentration, and sorting. *Lab on a Chip* **4,** 292–298. ISSN: 1473-0197. http://dx.doi.org/10.1039/B403280M%20https://pubs.rsc.org/en/content/articlepdf/2004/lc/b403280m (2004).

188. Tan, Y.-C. & Lee, A. P. Microfluidic separation of satellite droplets as the basis of a monodispersed micron and submicron emulsification system. *Lab on a Chip* **5,** 1178–1183. ISSN: 1473-0197. http://dx.doi.org/10.1039/B504497A%20https://pubs.rsc.org/en/content/articlepdf/2005/lc/b504497a (2005).

189. Link, D. R. *et al.* Electric Control of Droplets in Microfluidic Devices. *Angewandte Chemie International Edition* **45,** 2556–2560. ISSN: 1433-7851. https://onlinelibrary.wiley.com/doi/abs/10.1002/anie.200503540%20https://onlinelibrary.wiley.com/doi/pdfdirect/10.1002/anie.200503540?download=true (2006).

190. Sohrabi, S., Kassir, N. & Keshavarz Moraveji, M. Droplet microfluidics: fundamentals and its advanced applications. *RSC Advances* **10,** 27560–27574. http://dx.doi.org/10.1039/D0RA04566G%20https://pubs.rsc.org/en/content/articlepdf/2020/ra/d0ra04566g (2020).

191. Kaiser, E. M. & Woodruff, R. A. Synthesis of esters of acid-unstable alcohols by means of n-butyllithium. *The Journal of Organic Chemistry* **35,** 1198–1199. ISSN: 0022-3263. https://doi.org/10.1021/jo00829a084%20https://pubs.acs.org/doi/pdf/10.1021/jo00829a084 (1970).

192. Li, M. *et al.* Phase Behavior and Thermodynamic Model Parameters in Simulations of Extractive Distillation for Azeotrope Separation. *Scientific reports* **7,** 9497–9497. ISSN: 2045-2322. https://pubmed.ncbi.nlm.nih.gov/28842579%20https://www.ncbi.nlm.nih.gov/pmc/articles/PMC5573411/ (2017).

193. Kolb, H. C., Finn, M. G. & Sharpless, K. B. Click Chemistry: Diverse Chemical Function from a Few Good Reactions. *Angewandte Chemie International Edition* **40,** 2004–2021. ISSN: 1433-7851. https://onlinelibrary.wiley.com/doi/abs/10.1002/1521-3773%2820010601%2940%3A11%3C2004%3A%3AAID-ANIE2004%3E3.0.CO%3B2-5%20https://onlinelibrary.wiley.com/doi/pdfdirect/10.1002/1521-3773%2820010601%2940%3A11%3C2004%3A%3AAID-ANIE2004%3E3.0.CO%3B2-5?download=true (2001).

194. Berg, R. & Straub, B. F. Advancements in the mechanistic understanding of the copper-catalyzed azide-alkyne cycloaddition. *Beilstein journal of organic chemistry* **9,** 2715–2750. ISSN: 1860-5397. https://pubmed.ncbi.nlm.nih.gov/24367437%20https://www.ncbi.nlm.nih.gov/pmc/articles/PMC3869285/ (2013).

195. Teyssot, M.-L. *et al.* Aromatic Nitrogen Donors for Efficient Copper(I)–NHC CuAAC under Reductant-Free Conditions. *European Journal of Organic Chemistry* **2010,** 3507–03515. ISSN: 1434-193X. https://chemistry-europe.onlinelibrary.wiley.com/doi/abs/10.1002/ejoc.201000046 (2010).

196. Karis, T. E., Marchon, B., Hopper, D. A. & Siemens, R. L. Perfluoropolyether characterization by nuclear magnetic resonance spectroscopy and gel permeation chromatography. *Journal of Fluorine Chemistry* **118,** 81–94. ISSN: 0022-1139. https://www.sciencedirect.com/science/article/pii/S0022113902001975%20https://www.sciencedirect.com/science/article/pii/S0022113902001975?via%3Dihub (2002).

197. Chen, R., Sun, Z. & Chen, D. in *Microfluidics for Pharmaceutical Applications* (eds Santos, H. A., Liu, D. & Zhang, H.) 307–335 (William Andrew Publishing, 2019). https://www.sciencedirect.com/science/article/pii/B9780128126592000119.

198. Antona, S., Platzman, I. & Spatz, J. P. Droplet-Based Cytotoxicity Assay: Implementation of Time-Efficient Screening of Antitumor Activity of Natural Killer Cells. *ACS Omega* **5,** 24674–24683. https://doi.org/10.1021/acsomega.0c03264%20https://pubs.acs.org/doi/pdf/10.1021/acsomega.0c03264 (2020).

199. Shao, F. *et al.* Microfluidic Encapsulation of Single Cells by Alginate Microgels Using a Trigger-Gellified Strategy. *Frontiers in Bioengineering and Biotechnology* **8.** ISSN: 2296-4185. https://www.frontiersin.org/article/10.3389/fbioe.2020.583065 (2020).

200. Carrión, F. J., De La Maza, A. & Parra, J. L. The Influence of Ionic Strength and Lipid Bilayer Charge on the Stability of Liposomes. *Journal of Colloid and Interface Science* **164,** 78–87. ISSN: 0021-9797. https://www.sciencedirect.com/science/article/pii/S0021979784711453 (1994).

201. Claessens, M. M. A. E., van Oort, B. F., Leermakers, F. A. M., Hoekstra, F. A. & Cohen Stuart, M. A. Charged lipid vesicles: effects of salts on bending rigidity, stability, and size. *Biophysical journal* **87,** 3882–3893. ISSN: 0006-3495 1542-0086. https://pubmed.ncbi.nlm.nih.gov/15377511%20https://www.ncbi.nlm.nih.gov/pmc/articles/PMC1304899/%20https://www.cell.com/biophysj/pdf/S0006-3495(04)73854-0.pdf (2004).

202. Šegota, S., Vojta, D., Pletikapić, G. & Baranović, G. Ionic strength and composition govern the elasticity of biological membranes. A study of model DMPC bilayers by force- and transmission IR spectroscopy. *Chemistry and Physics of Lipids* **186,** 17–29. ISSN: 0009-3084. https://www.sciencedirect.com/science/article/pii/S0009308414001340 (2015).

203. Pashapour, S. *Generation of extracellular matrix protein-based microcapsules for invetigating single cells* Thesis (2021).

204. LeValley, P. J. *et al.* Photolabile Linkers: Exploiting Labile Bond Chemistry to Control Mode and Rate of Hydrogel Degradation and Protein Release. *Journal of the American Chemical Society* **142,** 4671–4679. ISSN: 1520-5126 0002-7863. https://pubmed.ncbi.nlm.nih.gov/32037819%20https://www.ncbi.nlm.nih.gov/pmc/articles/PMC7267699/%20https://www.ncbi.nlm.nih.gov/pmc/articles/PMC7267699/pdf/nihms-1593780.pdf (2020).

205. Ollech, D. *et al.* An optochemical tool for light-induced dissociation of adherens junctions to control mechanical coupling between cells. *Nature communications* **11,** 472–472. ISSN: 2041-1723. https://pubmed.ncbi.nlm.nih.gov/31980653%20https://www.ncbi.nlm.nih.gov/pmc/articles/PMC6981158/%20https:

//www.ncbi.nlm.nih.gov/pmc/articles/PMC6981158/pdf/41467_2020_Article_14390.pdf (2020).

206. Bochet, C. G. Photolabile protecting groups and linkers. *Journal of the Chemical Society, Perkin Transactions 1,* 125–142. ISSN: 1472-7781. http://dx.doi.org/10.1039/B009522M%20https://pubs.rsc.org/en/content/articlelanding/2002/P1/b009522m (2002).

207. Wang, P. Photolabile Protecting Groups: Structure and Reactivity. *Asian Journal of Organic Chemistry* **2,** 452–464. ISSN: 2193-5807. https://onlinelibrary.wiley.com/doi/abs/10.1002/ajoc.201200197%20https://onlinelibrary.wiley.com/doi/10.1002/ajoc.201200197 (2013).

208. Bamford, C. H. & Norrish, R. G. W. 359. Primary photochemical reactions. Part VII. Photochemical decomposition of isovaleraldehyde and di-n-propyl ketone. *Journal of the Chemical Society (Resumed),* 1504–1511. ISSN: 0368-1769. http://dx.doi.org/10.1039/JR9350001504%20https://pubs.rsc.org/en/content/articlelanding/1935/JR/jr9350001504 (1935).

209. Klán, P. *et al.* Photoremovable Protecting Groups in Chemistry and Biology: Reaction Mechanisms and Efficacy. *Chemical Reviews* **113,** 119–191. ISSN: 0009-2665. https://doi.org/10.1021/cr300177k%20https://www.ncbi.nlm.nih.gov/pmc/articles/PMC3557858/pdf/cr300177k.pdf (2013).

210. Schmierer, T. *et al.* Femtosecond spectroscopy on the photochemistry of ortho-nitrotoluene. *Physical Chemistry Chemical Physics* **12,** 15653–15664. ISSN: 1463-9076. http://dx.doi.org/10.1039/C004025H (2010).

211. Aujard, I. *et al.* o-Nitrobenzyl Photolabile Protecting Groups with Red-Shifted Absorption: Syntheses and Uncaging Cross-Sections for One- and Two-Photon Excitation. *Chemistry – A European Journal* **12,** 6865–6879. ISSN: 0947-6539. https://doi.org/10.1002/chem.200501393 (2006).

212. Li, P. & Xu, J. C. The development of highly efficient onium-type peptide coupling reagents based upon rational molecular design. *The Journal of Peptide Research* **58,** 129–139. ISSN: 1397-002X. https://doi.org/10.1034/j.1399-3011.2001.00867.x%20https://onlinelibrary.wiley.com/doi/abs/10.1034/j.1399-3011.2001.00867.x?sid=nlm%3Apubmed (2001).

213. Web Page. 2022. https://multimedia.3m.com/mws/media/654960/3m-novec-7500-engineered-fluid.pdf.

214. *CRC handbook of chemistry and physics. a ready-reference book of chemical and physical data* 100th edition. eng (eds Rumble, J. R., Lide, D. R. & Bruno, T. J.) Literaturangaben, 1 Band (verschiedene Seitenzählungen). ISBN: 978-1-138-36729-6 (CRC Press, Taylor and Francis Group, Boca Raton ; London ; New York, 2019).

215. Costigliola, L., Heyes, D. M., Schrøder, T. B. & Dyre, J. C. Revisiting the Stokes-Einstein relation without a hydrodynamic diameter. *The Journal of Chemical Physics* **150,** 021101. ISSN: 0021-9606. https://doi.org/10.1063/1.5080662 (2019).

216. Cui, S. *et al.* Correlation of the cytotoxic effects of cationic lipids with their headgroups. *Toxicology Research* **7,** 473–479. ISSN: 2045-452X. http://dx.doi.org/10.1039/C8TX00005K%20https://www.ncbi.nlm.nih.gov/pmc/articles/PMC6062336/pdf/TX-007-C8TX00005K.pdf (2018).

217. Schreier, H. *et al.* Physicochemical properties and in vitro toxicity of cationic liposome cDNA complexes. *Pharm Acta Helv* **72,** 215–23. ISSN: 0031-6865 (Print) 0031-6865 (1997).

218. Midekessa, G. *et al.* Zeta Potential of Extracellular Vesicles: Toward Understanding the Attributes that Determine Colloidal Stability. *ACS Omega* **5,** 16701–16710. https://doi.org/10.1021/acsomega.0c01582%20https://pubs.acs.org/doi/pdf/10.1021/acsomega.0c01582 (2020).

219. Martin, M. M. & Lindqvist, L. The pH dependence of fluorescein fluorescence. *Journal of Luminescence* **10,** 381–390. ISSN: 0022-2313. https://www.sciencedirect.com/science/article/pii/0022231375900034 (1975).

220. Takeichi, M. Dynamic contacts: rearranging adherens junctions to drive epithelial remodelling. *Nat Rev Mol Cell Biol* **15,** 397–410. ISSN: 1471-0072. https://www.nature.com/articles/nrm3802 (2014).

221. Shapiro, L. & Weis, W. I. Structure and biochemistry of cadherins and catenins. *Cold Spring Harb Perspect Biol* **1,** a003053. ISSN: 1943-0264. https://www.ncbi.nlm.nih.gov/pmc/articles/PMC2773639/pdf/cshperspect-JCT-a003053.pdf (2009).

222. Maker, A. & Gumbiner, B. M. Reconstitution of the full transmembrane cadherin-catenin complex. *Protein Expression and Purification* **193,** 106056. ISSN: 1046-5928. https://www.sciencedirect.com/science/article/pii/S1046592822000134 (2022).

223. Green, N. M. in *Advances in Protein Chemistry* (eds Anfinsen, C. B., Edsall, J. T. & Richards, F. M.) 85–133 (Academic Press, 1975). https://www.sciencedirect.com/science/article/pii/S0065323308604118.

224. Anderegg, G. Critical survey of stability constants of NTA complexes. *Pure and Applied Chemistry* **54,** 2693–2758. https://doi.org/10.1351/pac198254122693%20https://www.degruyter.com/document/doi/10.1351/pac198254122693/pdf (1982).

225. Galkin, M. A., Russell, A. N., Vik, S. B., Berry, R. M. & Ishmukhametov, R. R. Detergent-free Ultrafast Reconstitution of Membrane Proteins into Lipid Bilayers Using Fusogenic Complementary-charged Proteoliposomes. *JoVE,* e56909. ISSN: 1940-087X. https://www.jove.com/t/56909%20https://www.jove.com/de/pdf/56909/jove-protocol-56909-detergent-free-ultrafast-reconstitution-membrane-proteins-into-lipid (2018).

226. Erb, E.-M., Tangemann, K., Bohrmann, B., Müller, B. & Engel, J. Integrin αIIbβ3 Reconstituted into Lipid Bilayers Is Nonclustered in Its Activated State but Clusters after Fibrinogen Binding. *Biochemistry* **36,** 7395–7402. ISSN: 0006-2960. https://doi.org/10.1021/bi9702187%20https://pubs.acs.org/doi/10.1021/bi9702187 (1997).

227. Liu, P.-F., Avramova, L. V. & Park, C. Revisiting absorbance at 230nm as a protein unfolding probe. *Analytical Biochemistry* **389,** 165–170. ISSN: 0003-2697. https://www.sciencedirect.com/science/article/pii/S0003269709001894 (2009).

228. Stengel, G., Zahn, R. & Höök, F. DNA-Induced Programmable Fusion of Phospholipid Vesicles. *Journal of the American Chemical Society* **129,** 9584–9585. ISSN: 0002-7863. https://doi.org/10.1021/ja073200k%20https://pubs.acs.org/doi/pdf/10.1021/ja073200k (2007).

229. Löffler, P. M. G. *et al.* A DNA-Programmed Liposome Fusion Cascade. *Angewandte Chemie International Edition* **56,** 13228–13231. ISSN: 1433-7851. https://doi.org/10.1002/anie.201703243%20https://onlinelibrary.wiley.com/doi/pdfdirect/10.1002/anie.201703243?download=true (2017).

230. Gaut, N. J. *et al.* Programmable Fusion and Differentiation of Synthetic Minimal Cells. *ACS Synthetic Biology* **11,** 855–866. https://doi.org/10.1021/acssynbio.1c00519%20https://pubs.acs.org/doi/10.1021/acssynbio.1c00519%20https://pubs.acs.org/doi/pdf/10.1021/acssynbio.1c00519 (2022).

231. Peruzzi, J. A., Jacobs, M. L., Vu, T. Q., Wang, K. S. & Kamat, N. P. Barcoding Biological Reactions with DNA-Functionalized Vesicles. *Angewandte Chemie International Edition* **58,** 18683–18690. ISSN: 1433-7851. https://doi.org/10.1002/anie.201911544 (2019).

232. Bashirzadeh, Y. *et al.* Actin crosslinker competition and sorting drive emergent GUV size-dependent actin network architecture. *Communications Biology* **4,** 1136. ISSN: 2399-3642. https://doi.org/10.1038/s42003-021-02653-6 (2021).

233. Perrier, D. L. *et al.* Response of an actin network in vesicles under electric pulses. *Scientific reports* **9,** 8151–8151. ISSN: 2045-2322. https://pubmed.ncbi.nlm.nih.gov/31148577%20https://www.ncbi.nlm.nih.gov/pmc/articles/PMC6544639/ (2019).

234. Wubshet, N. H., Wu, B., Veerapaneni, S. & Liu, A. P. Differential regulation of GUV mechanics via actin network architectures. *bioRxiv,* 2022.05.01.490228. http://biorxiv.org/content/early/2022/05/01/2022.05.01.490228.abstract (2022).

235. Angelini Thomas, E. *et al.* Counterions between charged polymers exhibit liquid-like organization and dynamics. *Proceedings of the National Academy of Sciences* **103,** 7962–7967. https://doi.org/10.1073/pnas.0601435103 (2006).

236. Bekard, I. B., Asimakis, P., Bertolini, J. & Dunstan, D. E. The effects of shear flow on protein structure and function. *Biopolymers* **95,** 733–745. ISSN: 0006-3525. https://doi.org/10.1002/bip.21646 (2011).

237. Macek, B. *et al.* Protein post-translational modifications in bacteria. *Nature Reviews Microbiology* **17,** 651–664. ISSN: 1740-1534. https://doi.org/10.1038/s41579-019-0243-0 (2019).

238. Thomsen, R. P. *et al.* A large size-selective DNA nanopore with sensing applications. *Nature Communications* **10,** 5655. ISSN: 2041-1723. https://doi.org/10.1038/s41467-019-13284-1 (2019).

239. Platzman, I. *et al.* Surface properties of nanostructured bio-active interfaces: impacts of surface stiffness and topography on cell–surface interactions. *RSC Advances* **3,** 13293–13303. http://dx.doi.org/10.1039/C3RA41579A (2013).

240. Lang, M. J., Fordyce, P. M., Engh, A. M., Neuman, K. C. & Block, S. M. Simultaneous, coincident optical trapping and single-molecule fluorescence. *Nature Methods* **1,** 133–139. ISSN: 1548-7105. https://doi.org/10.1038/nmeth714 (2004).

241. Wiegand, T. *et al.* Forces during cellular uptake of viruses and nanoparticles at the ventral side. *Nat Commun* **11,** 32. ISSN: 2041-1723 (2020).

242. Li, I. T. S., Ha, T. & Chemla, Y. R. Mapping cell surface adhesion by rotation tracking and adhesion footprinting. *Scientific Reports* **7,** 44502. ISSN: 2045-2322. https://doi.org/10.1038/srep44502 (2017).

243. Staufer, O. *et al.* Bottom-up assembly of biomedical relevant fully synthetic extracellular vesicles. *Science Advances* **7,** eabg6666. https://www.science.org/doi/abs/10.1126/sciadv.abg6666%20https://www.ncbi.nlm.nih.gov/pmc/articles/PMC8442894/pdf/sciadv.abg6666.pdf (2021).

244. Staufer, O. *et al.* Vesicle Induced Receptor Sequestration: Mechanisms behind Extracellular Vesicle-Based Protein Signaling. *Advanced Science* **9,** 2200201. ISSN: 2198-3844. https://doi.org/10.1002/advs.202200201 (2022).

245. Hansen, M. J., Velema, W. A., Lerch, M. M., Szymanski, W. & Feringa, B. L. Wavelength-selective cleavage of photoprotecting groups: strategies and applications in dynamic systems. *Chemical Society Reviews* **44,** 3358–3377. ISSN: 0306-0012. http://dx.doi.org/10.1039/C5CS00118H (2015).

246. Kördel, C., Popeney, C. S. & Haag, R. Photoresponsive amphiphiles based on azobenzene-dendritic glycerol conjugates show switchable transport behavior. *Chemical Communications* **47,** 6584–6586. ISSN: 1359-7345. http://dx.doi.org/10.1039/C1CC11673H%20https://pubs.rsc.org/en/content/articlepdf/2011/cc/c1cc11673h (2011).

247. Langecker, M. *et al.* Synthetic Lipid Membrane Channels Formed by Designed DNA Nanostructures. *Science* **338,** 932–936. https://doi.org/10.1126/science.1225624 (2012).

248. Yoshina-Ishii, C., Miller, G. P., Kraft, M. L., Kool, E. T. & Boxer, S. G. General Method for Modification of Liposomes for Encoded Assembly on Supported Bilayers. *Journal of the American Chemical Society* **127,** 1356–1357. ISSN: 0002-7863. https://doi.org/10.1021/ja043299k (2005).

249. Falk, M. M., Buehler, L. K., Kumar, N. M. & Gilula, N. B. Cell-free synthesis and assembly of connexins into functional gap junction membrane channels. *The EMBO Journal* **16,** 2703–2716. ISSN: 0261-4189. https://doi.org/10.1093/emboj/16.10.2703 (1997).

250. Belardi, B. *et al.* Claudin-4 reconstituted in unilamellar vesicles is sufficient to form tight interfaces that partition membrane proteins. *Journal of Cell Science* **132,** jcs221556. ISSN: 0021-9533. https://doi.org/10.1242/jcs.221556 (2018).

251. Belardi, B. *et al.* A Weak Link with Actin Organizes Tight Junctions to Control Epithelial Permeability. *Developmental Cell* **54,** 792–804.e7. ISSN: 1534-5807. https://www.sciencedirect.com/science/article/pii/S1534580720305979 (2020).

Scientific Contribution

Charge-controlled microfluidic formation of lipid-based single- and multicompartment systems. B. Haller, K. Göpfrich, M. Schröter, J.-W. Janiesch, I. Platzman, J. P. Spatz, *Lab on a Chip* **2018**, *18*, 2665–2674.



A Novel NAD-RNA Decapping Pathway Discovered by Synthetic Light-Up NAD-RNAs. F. Abele, K. Höfer, P. Bernhard, J. Grawenhoff, M. Seidel, A. Krause, S. Kopf, M. Schröter, A. Jäschke, *Biomolecules* **2020**, *10*, 513.



Bottom-Up Assembly of Functional Intracellular Synthetic Organelles by Droplet-Based Microfluidics. O. Staufer, M. Schröter, I. Platzman, J. P. Spatz, *Small* **2020**, *16*, 1906424.



Light-Triggered Cargo Loading and Division of DNA-Containing Giant Unilamellar Lipid Vesicles. Y. Dreher, K. Jahnke, M. Schröter, K. Göpfrich, *Nano Letters* **2021**, *21*, 5952–5957.



pH-Triggered Assembly of Endomembrane Multicompartments in Synthetic Cells. F. Lussier, M. Schröter, N. J. Diercks, K. Jahnke, C. Weber, C. Frey, I. Platzman, J. P. Spatz, *ACS Synthetic Biology* **2021**.



Microfluidic production and characterization of biofunctionalized giant unilamellar vesicles for targeted intracellular cargo delivery. O. Staufer, S. Antona, D. Zhang, J. Csatári, M. Schröter, J.-W. Janiesch, S. Fabritz, I. Berger, I. Platzman, J. P. Spatz, *Biomaterials* **2021**, *264*, 120203.



Bottom-up assembly of biomedical relevant fully synthetic extracellular vesicles. O. Staufer, F. Dietrich, R. Rimal, M. Schröter, S. Fabritz, H. Boehm, S. Singh, M. Möller, I. Platzman, J. P. Spatz, *Science Advances* **2021**, *7*, eabg6666.



Vesicle Induced Receptor Sequestration: Mechanisms behind Extracellular Vesicle-Based Protein Signaling. O. Staufer, J. E. Hernandez Bücher, J. Fichtler, M. Schröter, I. Platzman, J. P. Spatz, *Advanced Science* **2022**, *9*, 2200201.



PNIPAM-containing droplets: The route towards an artificial cytoskeleton assembly for synthetic cell motility. D. Sauter, M. Schröter, C. Frey, C. Weber, U. Mersdorf, J. Janiesch, I. Platzman and J. P. Spatz, *in preparation*

Towards the assembly of extracellular matrix-based protein microcapsules as a versatile tool to investigate bacterial infections. S. Pashapour, M. Schröter, S. Seneca, F. Frischknecht, I. Platzman, and J. P. Spatz, *in preparation*

Positively-charged surfactant. M. Schröter, J. E. Hernandez Büche, S. Pashapour, S. Fabritz, I. Platzman, and J. P. Spatz, *in preparation*

Hybrid system. J. De Lora, M. Schröter, S. Pashapour, I. Platzman, and J. P. Spatz, *in preparation*

GESAMTFAKULTÄT FÜR MATHEMATIK, INGENIEUR- UND NATURWISSENSCHAFTEN

COMBINED FACULTY OF MATHEMATICS, ENGINEERING AND NATURAL SCIENCES

RUPRECHT-KARLS-
UNIVERSITÄT
HEIDELBERG

Eidesstattliche Versicherung gemäß § 8 der Promotionsordnung für die Gesamtfakultät für Mathematik, Ingenieur- und Naturwissenschaften der Universität Heidelberg /
Sworn Affidavit according to § 8 of the doctoral degree regulations of the Combined Faculty of Mathematics, Engineering and Natural Sciences at Heidelberg University

1. Bei der eingereichten Dissertation zu dem Thema / The thesis I have submitted entitled

   Development of next-generation fluorinated block copolymers and bottom-up assembly of biomimetic cell interaction modules

   handelt es sich um meine eigenständig erbrachte Leistung / is my own work.

2. Ich habe nur die angegebenen Quellen und Hilfsmittel benutzt und mich keiner unzulässigen Hilfe Dritter bedient. Insbesondere habe ich wörtlich oder sinngemäß aus anderen Werken übernommene Inhalte als solche kenntlich gemacht. / I have only used the sources indicated and have not made unauthorised use of services of a third party. Where the work of others has been quoted or reproduced, the source is always given.

3. Die Arbeit oder Teile davon habe ich wie folgt/bislang nicht[1)] an einer Hochschule des In- oder Auslands als Bestandteil einer Prüfungs- oder Qualifikationsleistung vorgelegt. / I have not yet/have already[1)] presented this thesis or parts thereof to a university as part of an examination or degree.

   Titel der Arbeit / Title of the thesis: ……

   Hochschule und Jahr / University and year: ……

   Art der Prüfungs- oder Qualifikationsleistung / Type of examination or degree: ……

4. Die Richtigkeit der vorstehenden Erklärungen bestätige ich. / I confirm that the declarations made above are correct.

5. Die Bedeutung der eidesstattlichen Versicherung und die strafrechtlichen Folgen einer unrichtigen oder unvollständigen eidesstattlichen Versicherung sind mir bekannt. / I am aware of the importance of a sworn affidavit and the criminal prosecution in case of a false or incomplete affidavit.

Ich versichere an Eides statt, dass ich nach bestem Wissen die reine Wahrheit erklärt und nichts verschwiegen habe. / I affirm that the above is the absolute truth to the best of my knowledge and that I have not concealed anything.

Heidelberg, 09. Juni 2022 ……

Ort und Datum / Place and date

…… Unterschrift / Signature

[1)] Nicht Zutreffendes streichen. Bei Bejahung sind anzugeben: der Titel der andernorts vorgelegten Arbeit, die Hochschule, das Jahr der Vorlage und die Art der Prüfungs- oder Qualifikationsleistung. / Please cross out what is not applicable. If applicable, please provide: the title of the thesis that was presented elsewhere, the name of the university, the year of presentation and the type of examination or degree.

The German text is legally binding.